AEROSOL DYNAMICS OF AGGLOMERATES

Thesis by

Steven Nicholas Rogak

In Partial Fulfillment of the Requirements

for the Degree of

Doctor of Philosophy

California Institute of Technology

Pasadena, California

1991

(Submitted April 23, 1991)

ACKNOWLEDGEMENTS

To my adviser, Dr. Richard Flagan, I am grateful for constant encouragement in the undertaking of difficult investigations. I also thank him for igniting my interest in the physics of invisibly small things.

Thanks also go to Dr. Kikuo Okuyama for showing me the "Japanese way" of doing experiments. At the end of my stay at Caltech, I am beginning to understand what he was talking about. I am also thankful to have been able to collaborate with Dr. Urs Baltensperger. My research would have been poorer and less enjoyable without his stimulating discussions and high standards.

Many other people contributed directly to this thesis by either proofreading drafts, collaborating in experiments, or pointing out glaring errors in my thinking: B. Dominik, R. Harley, B. Wyslouzil, Dr. H.V. Nguyen, M. Richmond, L. Yan, B. Wong, C. Chan, X-M Li., C. Garland, and D. Dabdub. I greatly appreciate patience and help from my committee, Drs. B. Fultz, G. Gavalas, J. Morgan and J. Seinfeld. Less direct but no less important was the contribution of other members of the air pollution group and the Caltech community, who kept me interested in other matters.

Finally, I thank my parents, who educated me.

To my family, Earl, Helen, Zena and Barbara.

ABSTRACT

The mobility, charging, coagulation and mass-transfer properties of aerosol agglomerates were related to the particle and the background gas mean free path λ. The mobility-equivalent diameter d_m of a self-similar cluster of spheres in the continuum regime ($\lambda << d_m$) was calculated to be proportional to the radius of gyration R_g of the cluster for fractal dimension $D_f > 1.3$. Slender-body behavior is approached for $D_f < 1.3$. In the free-molecule regime ($d_m << \lambda$), d_m is nearly equal to the projected-area diameter d_A. In the transition regime ($d_m \sim \lambda$), d_m depends on both d_A and R_g. In general, there is a divergence of d_A and R_g as the agglomerate size increases, but it is very gradual for typical aerosol agglomerates, for which $d_m \sim d_A$ in the transition regime.

The mass transfer of nanometer-sized ^{211}Pb clusters to TiO_2 agglomerates was investigated with an Epiphaniometer. The measured mass-transfer-equivalent diameters of the agglomerates were within 10% of d_m. The lead cluster mean free path was nearly the same as λ. For an analogous phenomenon, the bipolar diffusion charging of agglomerates, it was found that the charging-equivalent diameter of the agglomerates was ~ 10% larger than d_m.

These measurements were incorporated into a model describing the coagulation of agglomerates in the transition regime. Particles smaller than the primary particle diameter d_1 were assumed to coalesce rapidly, while large particles were assumed to be solid with a fractal structure. In the transition regime, the agglomerate mean free paths are much smaller than d_m even when $d_m < \lambda$. This leads to distinctly different dynamic behavior than predicted by previous models developed for the continuum or free-molecule regimes. The enhancement of coagulation over that of dense spheres is large for aerosols with median diameters slightly greater than d_1 but smaller for aerosols consisting of much larger particles.

TABLE OF CONTENTS

LIST OF FIGURES

Chapter 2

Chapter 3

Chapter 4

Chapter 5

Chapter 6

Chapter 7

Chapter 8

List of Tables

CHAPTER 1
INTRODUCTION

Suspensions of fine particles in a gas, or aerosols, are produced by natural and artificial phenomena. Many of the particles are formed from liquids, and therefore are spherical. Common examples include cloud droplets, sea spray, cigarette tar particles and other aerosols formed from organic liquids. An equally important class of aerosols is formed from solid materials such as soot, metal oxides and metals. Such particles are often irregular agglomerates of uniformly sized primary spheres. The irregular structure considerably complicates the prediction of the dynamic behavior of the aerosol because no rigorous treatment of non-spherical particles has been developed. The problem is twofold. Given a precise description of the particle shape, one must solve the relevant governing equations with complicated boundary conditions. Even if this can be done, there is the additional problem of characterizing the shape of real aerosol particles correctly and adequately. These problems are closely related since aerosol measurements and shape characterizations are often based on the measurement of dynamic properties; the nature of the aerosol is inferred from the data, using the appropriate theory.

A realistic model of the particle geometry is essential to the study of non-spherical particles. A balance between simplicity and accuracy is necessary. For example, a particle might be characterized by the diameter of a sphere having the same volume. Such a geometric model does not allow the prediction of the projected area of the particle, which is more relevant to transport properties such as the aerodynamic drag. Another approach, well developed in the literature, is to characterize the aerosol by a "dynamic shape factor", which is the ratio of the drag forces acting on the particle and a sphere of the same volume. Neither of these characterizations is based on any insight into the particle formation process. Recent computer simulations of particle aggregation have indicated that fractal models may be useful in characterizing agglomerate structure, but it can be difficult to relate these simulations to real aerosol systems.

The objective of this study is to develop a more complete structural model that can not only be used to predict the relevant aerosol properties, but can also be related to aerosol formation mechanisms. Chapter 2 discusses the agglomerate aerosol formation process. The use of fractal models to characterize these agglomerates, the justification of such models and their relation to measurements of real aerosols are discussed in Chapter 3.

Having developed reasonable models of the particle structure, it is possible to make verifiable predictions of the aerosol properties. The aerodynamic drag, charging behavior, mass transfer and coagulation kinetics (i.e., particle growth by agglomeration) are among the most important phenomena related to aerosols, as they directly affect the measurement of aerosols and the evolution of aerosols in ambient and industrial environments.

An understanding of the relation between particle structure and aerodynamic drag is necessary before making measurements of particle coagulation kinetics, since the interpretation of coagulation data inevitably requires a knowledge of the drag-structure relation. The drag on a particle generally depends on its velocity, shape and the properties of the background gas. The particles of interest here are sufficiently small and move slowly enough that fluid inertia and compressibility may be neglected. In this case, the fluid dynamics are governed by creeping flow, so the drag force is proportional to the particle speed. The particles of interest may be much larger than the gas mean free path so the Stokes flow or continuum creeping flow equations may be used to predict the aerodynamic drag. The Stokes flow problem is discussed in Chapter 4. In most practical situations, the agglomerate particles are comparable in size to the gas mean free path, so the gas cannot be treated as a continuum. This transition regime flow is considerably more complicated than Stokes flow and rigorous solutions are unavailable even for spheres. Chapter 5 describes experiments conducted to measure the effect of particle structure on the drag in the transition regime .

Measurements of the attachment rate of ultrafine lead clusters to agglomerate particles provides additional information relevant to the coagulation process. Such mass-

transfer properties of agglomerates are also relevant to the attachment of radionucleides to ambient aerosol or the transport of gaseous species to particles. Chapter 6 discusses the procedures and results of this study.

The attachment of ions to particles is closely related to the mass-transfer process. However, the analogy between mass transfer and charging is not exact, because of electrostatic interactions. Since the charging phenomenon is particularly relevant to the interpretation of many aerosol measurements, the study discussed in Chapter 7 was undertaken to characterize the charging of non-spherical particles.

The work of the above chapters investigates particle motion and the interaction of small particles or ions with agglomerate aerosols. Many of the results of the drag and mass-transfer studies can be extrapolated to predict the frequency of collisions between agglomerates, i.e., the coagulation kinetics. Chapter 8 integrates the results of the earlier chapters to obtain a model capable of predicting the evolution of an aerosol size distribution, for particles of variable size and shape.

The present work on the effect of particle structure on aerosol dynamics may be useful in future investigations of complex agglomerate aerosol systems where chemical reactions, interparticle forces and particle restructuring are important.

CHAPTER 2

FORMATION OF AEROSOL AGGLOMERATES

Aerosol particles produced in many high-temperature environments are agglomerates of 10-100 nm spherules. This structure is often attributed to particle growth by Brownian coagulation without coalescence. Although the arrangement of the primary particles is remarkably similar for particles generated under a wide range of conditions, the structure of the primary particles comprising the agglomerate varies from one system to another.

The formation of aerosol agglomerates generally starts with the creation of a supersaturated vapor, either by chemical reaction or by rapid cooling (Figure 1). In many systems, the particles are metal oxides or other materials with extremely low vapor pressures. As a result, the supersaturation ratios of the condensing vapors may be so high that the usual thermodynamic barrier to nucleation is negligible and nucleation rates may be limited by the gas collision frequency. Nuclation on ions may be significant some high temperature systems (Calcote and Olson, 1987; Rabeony and Mirabel, 1987).

Particles form by nucleation and grow by coagulation (collisions of particles) and condensation (deposition of molecules on particles). Eventually, the condensing vapor is depleted and the aerosol evolves by coagulation. In addition to these growth processes, restructuring by sintering occurs. While coagulation produces irregular agglomerates, condensation and sintering produce rounded particles. The ultimate structure of the particle depends on the characteristic time scales for these three processes (Figure 2).

For aerosols evolving by coagulation, the particle concentration $n(t)$ decays from the initial concentration $n(0)$ according to

$$\frac{dn(t)}{dt} = -\frac{1}{2} K(d)\, n^2(t) \quad , \tag{1}$$

where $K(d)$ is the size-dependent coagulation rate coefficient (Seinfeld, 1986). For $n(t) << n(0)$, neglecting the size dependence of K, (1) implies that the diameter grows as $d \sim (K\, n(0)\, t)^{1/3}$. The characteristic time for a doubling of the particle diameter would therefore scale as $\tau_{coag} \sim d^3$.

For condensation, the particle diameter grows according to

$$d^2 \frac{dd}{dt} = K_{cond}\,(d)\; n_0 \quad , \tag{2}$$

where n_0 is the concentration of the condensing vapor and K_{cond} is a kinetic parameter analogous to the coagulation coefficient. Using the form of K_{cond} appropriate for d smaller than the gas mean free path and assuming that n_0 is constant, it follows from (2) that the time for diameter-doubling scales as $\tau_{cond} \sim d$ (Seinfeld, 1986). Thus, coagulation is expected to decelerate more quickly than condensation, suggesting that condensation would dominate particle growth after a sufficiently long time, resulting in spherical particles. In practice, the reactions that produce condensible vapor may last for such a short duration τ_{react} that condensation rarely dominates the particle growth. Numerical models of simultaneous nucleation, condensation, and coagulation show that as τ_{react} decreases, nucleation and coagulation become increasingly important, resulting in smaller and more numerous particles (Girshick and Chiu, 1989; Nguyen, 1989; Wu et al., 1987). The relative importance of condensation and coagulation also affects the particle size distribution. Condensation produces aerosols with a narrow size distribution while coagulation tends to produce particle distributions with a characteristic width (Friedlander and Wang, 1966). Distributions from coagulation are approximately log-normal with 67% of the particle diameters between d / σ_g and $\sigma_g d$, where d is the median diameter and σ_g is the geometric standard deviation which ranges from 1.4 to 1.6 (Seinfeld, 1986; Okuyama et al., 1989; Chapter 8). Simultaneous nucleation, condensation and coagulation can result in broad, bimodal size distributions.

Sintering can be defined as the restructuring of particles to minimize surface energy (Herring, 1950). Material may be transferred by volume diffusion, surface migration, viscous flow or vapor transport. The characteristic time τ_{sinter} required to form a "neck" of diameter d between two spheres (Figure 2) scales as d^4 for surface diffusion, d^3 for volume diffusion, d^2 for vapor transport and d for viscous flow (Herring, 1950). These scaling laws assume that material properties are independent of particle size, which is probably not true for the extremely small particles involved in the early stages of agglomerate formation. For $d < 10$ nm, crystal defect densities may increase, resulting in accelerated sintering (Hayashi, 1987; Horvath et al., 1987). Further complications are introduced by trace species adsorbed onto the particle surface.

After some time τ_{react}, nucleation and condensation cease and the particle structure is determined by a competition between coagulation and sintering. The scaling arguments suggest that the coagulation time increases faster than the characteristic times for sintering by viscous flow or vapor transport. However, for many systems these two sintering mechanisms may be neglected, so τ_{sinter} increases faster than d^3, i.e., faster than τ_{coag}. In this case, irregular agglomerates would result. Even in this case one expects sintering to remove structural features smaller than some characteristic size determined by the material properties, temperature and time.

The effect of temperature variations on sintering and nucleation during agglomerate formation is important. For example, flame-generated particles are formed at high temperatures and grow in the cooler exhaust gases. Koch and Friedlander (1990) have developed a model to predict the primary particle size of coagulating systems with constant cooling rates, but a simple two-step particle formation model may be nearly as accurate for systems in which the sintering rate decreases rapidly. In the high-temperature stage, sintering is rapid and spherical primary particles are formed. In the low-temperature stage, the primary particles agglomerate without sintering.

It will be shown that depending on the agglomerate formation conditions, sintering and aerosol dynamics influence the particle structure. Conversely, consideration of the structure may yield important information on the origins of the aerosol.

MINERAL AGGLOMERATES

Flame-Generated Particles

Ultrafine particles from a wide range of materials can be generated in flames (Juillet et al., 1973; Nielson et al., 1961). Kasper et al., (1980) produced magnetic iron oxide (α-Fe_2O_3 hematite) aerosols by decomposing iron penta carbonyl $Fe(CO)_5$ in an O_2 - CO flame. The resulting agglomerates are nearly straight chains (Figure 3), indicating that coagulation of the primary particles occurred at temperatures below 680°C, where hematite is strongly magnetic (Fuchs, 1964). There are no visible necks joining the primary particles, further evidence that there was very little sintering or condensation occurring during the chain formation. The primary particle size distribution was affected by changing the concentration of the atomized solution and the flame characteristics (Table I). Increasing the oxygen concentration (i.e., increasing the temperature and decreasing the flame residence time) resulted in smaller, more polydisperse primary particles. Increasing the mass concentration by a factor of 3 increased the primary particle volume by a similar factor. Similar variations in primary particle size were obtained in the synthesis of Al_2O_3 by flame pyrolysis (Sokolowski et al., 1977). These results suggest that aerosol dynamics control the primary particle size. If sintering rates controlled the primary particle size, one would expect to see larger particles at higher temperatures.

Table I. Hematite Agglomerate Generation from [$Fe(CO)_5$] flame decomposition (Kasper et al., 1980).

[$Fe(CO)_5$] %	Temperature range °C	d_1 nm	σ_g	Comments
2	450 - 1050	75	1.3	laminar CO air
2	~ 1300	20- 30	1.7	turbulent O_2:CO ratio ~3
2	~ 1200	45 -60	~ 1.5	O_2:CO ratio ~1
1	~ 1200	40 - 50	~ 1.5	O_2:CO ratio ~1
0.7	~ 1200	35 -45	~ 1.5	O_2:CO ratio ~1

A persistent environmental problem associated with coal combustion is the generation of submicron coal ash (Saxena et al., 1985; Markowski et al, 1980) by the vaporization and nucleation of coal-borne mineral matter (Sarofim et al., 1977; Flagan, 1979). The process is extremely complex, probably involving reduction and oxidation reactions in addition to physical vaporization. Heating and cooling may occur extremely rapidly in the vicinity of a burning coal particle (Senior and Flagan, 1982). The sintering behavior is complicated by the fluxing effect of certain minerals on the largely silicate ashes.

In order to understand the factors affecting primary particle size, Helble and Sarofim (1989) measured the primary particle sizes in agglomerates produced by the combustion of real and synthetic coal chars. The background gas temperature during combustion was varied from 1500 K to 1750 K, while the char combustion temperature was controlled by varying the oxygen concentration. Larger primary particles were produced at higher temperatures, partly because of increased vaporization of mineral matter. After correcting for the variations in the amount of material vaporized, there remained a correlation between the primary particle size and predicted sintering rates. For this reason, Helble and Sarofim concluded that sintering rates control the primary particle size. Examination of published micrographs of Fe_2O_3 agglomerates lead to other interpretations. The micrographs show agglomerates with distinct primary particles

(similar to those in Figure 3, although less straight) with almost no visible "necking" between the particles in the agglomerates. The two-stage agglomerate formation mechanism discussed above may apply to this system since the char combustion occurs for a very short time compared to the time available for coagulation. The geometric standard deviation of the primary particles was approximately σ_g =2.0, suggesting that nucleation occurred for a substantial fraction of the primary particle formation period.

Laser and Electrical-Arc Particle Generation

Agglomerates may be produced by the rapid vaporization of materials by high electrical currents. While arc welding fumes are a health concern (Kalliomäki et al., 1987), ultrafine particles produced in electric-arc furnaces may be useful as engineering materials (Kuhn et al., 1961). In such systems, material properties, arc energies and quenching rates influence the size, appearance and degree of agglomeration of the primary particles. Lower concentrations and higher melting points result in smaller primary particles. For laboratory studies, agglomerates have been produced by the "exploding wire" technique, in which a high voltage is used to vaporize a wire made of the desired sample material. Kops et al. (1975) vaporized iron to form Fe_2O_3 particles, which were then allowed to coagulate for several hours. Since the coagulation time was many orders of magnitude larger than the explosion time, it is not surprising that the agglomerates were composed of crystalline, unsintered primary particles. Increasing the explosion energy decreased the primary particle diameter (Allen and Briant, 1978) from 47 to 20 nm, with a geometric standard deviation of $\sigma_g \sim 1.8$.

Lushnikov et al. (1987) generated iron and titanium agglomerates by heating the metals with high-energy laser pulses. Increasing the laser power did not affect the primary particle size, though it did increase the overall agglomerate size. However, when the background gas was changed from argon to helium, the primary particle size was reduced by a factor of 2. Reducing the argon pressure to 1 torr caused a primary particle size

reduction of a factor of 3 to 4. In an earlier study, laser vaporization of nuclear-reactor fuel pellets was used to produce agglomerates of uranium and polonium oxide (Allen and Briant, 1978; Allen et al., 1979). Increasing the laser pulse energy by a factor of 10 increased the primary particle diameter several fold, in contrast to Lushnikov's results. The primary particles ranged from 20 to 60 nm with standard deviations ranging from 1.35 to 1.46.

Agglomerates Produced in Externally Heated Furnaces

TiO_2 -Previous Studies

For many years, fine TiO_2 particles used in pigments have been produced by pyrolysis of titanium compounds such as $TiCl_4$ or titanium alkoxides. Although flame pyrolysis is usually used for commercial pigment manufacture, pyrolysis in well-characterized electric furnaces has been used in laboratory studies. The alkoxide method was used for the particle generation in this study.

Titanium tetraisopropoxide $Ti(OC_3H_7)_4$ is a clear liquid at room temperature, whose vapor decomposes in nitrogen at temperatures $T > 400°C$,

$$Ti(OC_3H_7)_4 \longrightarrow TiO_2 + 4\,C_3H_6 + 2\,H_2O \ . \qquad (3)$$

The reaction may be self-catalysed under certain conditions (Komiyama et al., 1984) and is probably complicated by reactions with water vapor, since the alkoxide is hygroscopic. Nevertheless, the aerosol yield data of Okuyama et al. (1986,1989) are consistent with a first order decomposition with a rate constant

$$k_R = 9.56 \times 10^{12} \exp\left(- \frac{185\ kJ}{RT} \right) \quad s^{-1} \ . \qquad (4)$$

In that study, alkoxide vapor in nitrogen was introduced at the centerline of a preheated sheath flow in a small electrically heated tube furnace at 400-600°C.

The agglomerates produced by the system contained 1-10 primary particles. On the basis of micrographs, the primary particle diameters were 10 to 50 nm with an average of ~27 nm. Particles produced at 400 °C were amorphous while those produced at higher temperatures were anatase. There were substantial necks joining many of the primaries, suggesting that condensation or sintering was occurring as the chains were forming, even though the furnace temperature was well below the 1830-1840 °C melting temperature of TiO_2. The role of sintering in these experiments can be understood by considering published data on the sintering of TiO_2.

Hahn et al. (1990) found that 20 nm grains of TiO_2 (rutile) could exist stably for several hours at temperatures well above 400 °C. This was also observed in studies of the initial sintering of anatase particles (Hébrard et al., 1990). Anatase powder, initially spherical with an area-mean diameter of 15 nm, was sintered at 575°C under various atmospheres. Surface area measurements showed that the area-mean diameter doubled after several hours. Water vapor and oxygen accelerated the process, which was shown to be consistent with surface diffusion of hydroxyl groups as the rate-limiting step in the sintering process.

Thus, at the temperatures in the reactor used by Okuyama et al., significant sintering of 15 nm particles should have occurred only after about 2 hours, while the residence time was ~2 seconds. From Herring's scaling laws for surface diffusion, $\tau_{sinter} \sim d^4$. The diameter of a particle that would have sintered substantially in 2 seconds is therefore $d \sim$ 2 nm. Structures in the agglomerate that were smaller than this size might have existed during the entire formation process, but would have been lost by the time the particles were sampled and photographed.

Fast Mixing TiO_2 Reactor

In the reactor used by Okuyama et al. (1986), the heating and subsequent reaction of the alkoxide were limited by heat conduction in the laminar flow. To avoid the necessity

of characterizing this heat transfer-reaction process, a "fast-mixing" reactor was built, in which high-velocity jets of preheated nitrogen were mixed rapidly with a smaller vapor-laden flow. The mixing occurred in a small machinable glass (MACOR, Corning, NY) chamber that was inserted into the stainless steel reactor (Figure 4). In the first versions of the apparatus, the vapor concentration was controlled by bubbling nitrogen through the liquid alkoxide. The vapor stream was carried into the furnace by a water-cooled injection probe (Figure 4) which prevented premature heating and reaction of the vapor. Coagulation of the aerosol occurred downstream of the mixer in a 47.5 mm I.D. stainless steel tube. A fraction of the flow was sampled with a water-cooled dilution probe. The residence time could be varied by changing the probe position in the reactor. Because of the dilution and cooling of the probe, it could be assumed that no significant coagulation or particle formation occurred downstream of the furnace. The reactor output was characterized using a condensation nucleus counter (CNC, model E-1033A-01G, Environment One Corp., Schenectady, NY) and transmission electron micrographs (TEM, model 301, Phillips) of particles collected with a thermophoretic precipitator. Gas flow rates and temperatures are shown in Figure 5. Three samples were taken on three separate TEM grids corresponding to the conditions and plate numbers of Table II.

The main difference between the three samples was the thermophoretic sampling method used. For the first TEM grid, the aerosol was sampled for 5 minutes with the sample stream heated to ~100°C before deposition on the room-temperature grid. For the second sample the aerosol was not heated, with the expected result that the grid coverage was poor. The third sample was collected from a heated aerosol over 2 minutes. The number concentration in the sampled aerosol was 3 - 4 $x10^6$ particles/cm^3.

Table II. Conditions for TEM grids 1-3, March 23, 1988 Experiment using the Fast-Mixing Reactor I.

TEM grid	Negative #	kX	d_1 (nm) Min-Max	Comments
1	2693	82	16-55	1 small agglomerate with d_1~15 nm
1	2694	30		1 larger agglomerate with fused d_1 same field of view as above. Agglomerate lengths ~ 80 nm
1	2695	62	14 -94	L ~ 50 nm
1	2696	140	13 -100	Crystalline structure shown by plate 2697
1	2698	4.3	-	Non-agglomerate crystal contamination
1	2699	82	10 -114	Agglomeration on grid possible
1	2700	3.6		Contamination with 0.5 μm sphere
2	2701	82	20 -45	Agglomerates longer than 1 μm
3	2702	82	12 -52	
3	2703	30		Same particle as 2702
3	2704	36	11 -50	Agglomerate 2000 nm long
3	2705	105	14 -51	Same particle as 2704

Figures 6 to 9 show typical agglomerates from the reactor. It is not surprising that the primaries appear to be fused since most of the coagulation should have occurred during the several seconds that the particles were in the 500°C furnace. At this temperature, the decomposition of the alkoxide may have taken several hundred milliseconds, so both sintering and condensation may have occurred during the agglomerate formation. Measurement of the primary particle size distribution is difficult because most of the primaries are well fused together. For this reason, the primary particles have been characterized by the minimum and maximum measured diameters. Although the primary diameters probably are not log-normally distributed, the median diameters and geometric standard deviation were estimated for comparison with previous studies. For Figure 8, d_1=36 nm and σ_g=1.5 while for Figure 9, d_1=33 nm and σ_g=1.3.

Convection currents produced by the cool sampling probe resulted in unsteady particle concentrations and uncertain residence times. Cleaning and leak testing also proved

difficult as the seals were located inside the hot furnace. To remedy these problems, the diameter of the main coagulation tube was reduced and all seals were moved outside the furnace (Figure 10). TEM samples were taken by inserting a TEM grid through the sampling probe into the hot furnace. The transient temperature differential resulted in very high sampling efficiencies and allowed sampling at shorter residence times. Size (mobility diameter) distributions were measured with an electrostatic aerosol analyzer (EAA, model 3030, TSI inc., St. Paul, MN).

In the second series of experiments, the average primary particle size appears to be slightly smaller than in the first study. It is possible that the longer residence time of the first apparatus contributed to this difference. Within the second series of samples, there is no clear trend in the fine-scale size with increasing residence time or temperature. There are changes in the appearance of the particles, however which cannot be characterized by the primary particle diameter, as will be shown below.

Table III. Particles from the Fast Mixing Reactor II

Grid	Plate	Mag	Run	T	t_{res}	d_m	d_1	Comments
		KX		°C	s	nm	nm	
6A	2737	62	1	530	0.13	15	13 -16	no agglomerates
6A	2738	62	1	530	0.13	15		77 nm spheres visible
6A	2739	62	1	530	0.13	15		7 nm specks
6A	2740	169	1	530	0.13	15		100 nm spheres
8B	2741	62	7	650	1.8	24	9 -16	Agglomerate length ~150 nm
8B	2742	169	7	650	1.8	24	6 -12	
8B	2743	30	7	650	1.8	24		re-suspended deposit
8C	2744	62	7	650	1.8	24	10 -32	1-500 primaries
8C	2745	169	7	650	1.8	24	21 -40	1-20 primaries
7A	2746	169	4	530	1.1	24	7 -24	1-10 primaries
7B	2747	169	4	530	1.1	24	9 -24	
7B	2748	62	4	530	1.1	24	7 -32	
7D	2749	62	5	650	0.9	19		
7D	2750	169	5	650	0.9	19	9 -16	
8A	2751	62	6	650	1.2	24		
8A	2752	169	6	650	1.2	24	7 -18	

When the sampling probe was fully inserted, the residence time in the furnace was ~0.13 second. From (4), the reaction time at 530 °C is ~1 second. Thus, it is not surprising that agglomerates were not seen in run #1. Even with a residence time of 1.1 seconds, the primary particles are indistinct (Figure 11). This contrasts with the particles formed at 650 °C within 0.9s (Figures 12, 13). At this temperature, the alkoxide decomposition is ~10 times faster than at 530 °C, so the vapor concentration is very small during most of the agglomerate formation, and condensational growth is minimal.

The EAA measurements of the peak mobility diameter (Table III) show that larger particles are produced with longer residence times. The effect of temperature is not measurable by the EAA. It is also noted that the peak mobility diameter is generally smaller than the particle sizes measured from TEM. This difference may be due to several factors such as size-selective particle sampling or non-ideal EAA response for non-spherical particles. These questions are considered in more detail in Chapters 5 -7.

Because of thermophoretic losses or problems in the alkoxide bubbler, the apparent yield of the first two generators was ~1%. The yield was increased with the final version of the faster mixing reactor, described in Chapters 5 and 6. The mixing chamber and growth tube of this reactor were the same as in the previous reactor, but the TEM sampling occurred outside the furnace. The furnace was also inverted, allowing flow rates to be decreased without causing buoyancy flows. Thus, the residence time could be increased above 4 seconds. The particles produced in this system are discussed in Chapter 5, so only a few features will be noted here. All of the agglomerates were formed at 500 °C. The residence time varied from 1.5 to 4.2 seconds, while the TiO_2 concentration varied from 17 to 400 moles TiO_2 per million moles N_2 (Table IV).

It can be seen from Table IV and Figures 14 to 16 that the primary particle size increases as the mass concentration and residence time increase, although it is difficult to determine which factor is more important. From the arguments given earlier, if the time

available for sintering increases by a factor of 3, the characteristic diameter should increase by a factor of $3^{1/4}$ =1.3 to $3^{1/3}$=1.4, depending on the sintering mechanism. On the other hand, if mass concentration increases by a factor of 20, the particle diameters should increase by $20^{1/3}$=2.7. Thus, the observed increases in primary particle size appear to be larger than expected from sintering considerations, but smaller than expected from the concentration changes. Considering the uncertainties in the alkoxide decomposition rates, a more rigorous analysis is difficult.

Table IV. Particles produced in Fast-Mixing Reactor III

Grid	Plates	Mag	[TiO2]	Q_{alk}	Q_H	t_{res}	d_1	Comments
		KX	ppm	lpm	lpm	s	min	
B2	3832	105	17	0.41	5.7	1.5	6 -24	amorphous
A1	3071	25	22	0.41	2.5	6.0	20 -46	peak mobility $d \sim 70$ nm
K8	5478		44	0.21	2.2	3.8		crystalline
	-5481		44	0.21	2.2	3.8	9 -200	
O10	5488	6	400	0.91	1.2	4.2	11- 200	
	-5493					4.2		

Particles produced in the shortest residence time were amorphous, given the TEM diffraction patterns. This is surprising, since Okuyama et al. (1986) found that all particles formed above 400 °C were anatase; however, the furnace residence time in that study was slightly over 2 seconds. With longer residence times, the fast-mixing reactor also produced crystalline material, as shown by TEM diffraction. Large crystals are evident in the micrographs of these agglomerates (Figures 15,16).

Compact TiO_2 Reactor

A simpler and smaller reactor was built for later charging experiments (Chapter 7, Figure 5). The basic principle was the same as used in the earlier devices, but the residence time in the small reactor was much shorter. As a result, heating and mixing times were

comparable to the residence time. Most of the coagulation occurred at room-temperature in a large chamber.

The agglomerates produced in this reactor (Figures 17, 18) were significantly different from those described previously. The primary particles from the compact reactor ranged from 7 to 30 nm (d_1 =11 nm, σ_g=1.3), even for high mass concentrations. X-ray diffraction showed that the particles were anatase; there were no crystals visible in the TEM micrographs.

Production of Silicon Particles from Silane Decomposition

The TEM plates of Chapter 5 show silicon agglomerates produced from the pyrolysis of silane. A major difference between the titania and silicon reactors was the use of a second furnace to sinter the silicon particles (Chapter 5, Figure 4). In the "seed" reactor (residence time ~1 second, temperature ~950°C) silane was reacted to produce a fine aerosol. This aerosol then passed through a long, room-temperature aging coil (residence time ~30 to 60 seconds) before entering the second furnace (residence time 1 to 2 seconds). Coagulation in the sintering furnace was negligible compared to coagulation in the aging coil.

With the sintering furnace at 900°C, the agglomerates formed in the aging coil passed unchanged. Micrographs (Chapter 5, Figure 11) show that most of the primaries are distinct, evidence of agglomeration without sintering. The primary particles themselves are not perfectly spherical, possibly because of agglomeration and partial fusion in the seed reactor.

Increasing the furnace temperature to 1100°C produced a remarkable change in the particle structure (Chapter 5, Figure 12). Nearly all of the primary particles were fused, indicating that all bonds between the primary particles were of a similar age. These particles differ markedly from the TiO_2, in which there appeared to be a random mixture of fused and unfused primary particles.

CARBONACEOUS AGGLOMERATES

Agglomerates may be formed from organic material as well as from mineral matter. The most common example is soot, which is formed in fuel-rich regions of hydrocarbon flames. There is considerable debate concerning the nature of the species involved in soot inception, since complex hydrocarbons may be broken into many intermediate compounds before being oxidized to CO_2 or CO. Such factors as fuel composition, flame stoichiometry, temperature and trace minerals can have a profound influence on sooting in flames (Glassman, 1988). Soot appears to be formed from the polymerization of a fuel pyrolysis product (e.g., acetylene), followed by surface growth through other types of reactions. The sooting process occurs for only milliseconds before it is halted by changes in flame stoichiometry and temperature (Harris and Weiner, 1983). Eventually, oxidation may reduce the size of the soot particles. Micrographs of soot from many sources (Flagan and Seinfeld, 1987; Samson et al., 1987) show agglomerates of completely unfused, very uniformly-sized primary particles (d_1 ~ 10 to 60 nm, σ_g =1.1 to 1.2), consistent with condensational growth of the primary particles in the flame, followed by agglomerate formation in the cooler exhaust gases.

Carbonaceous agglomerates formed in smog chamber studies (Paulson et al., 1990) have relatively large (50-100 nm) primary particles (Figure 19). In these studies, 0.9 ppm NOx and 1.8 ppm beta-pinene in air were exposed to sunlight for six hours. After ~120 minutes, reactions of the hydrocarbons with ozone and other photochemical products produced a low vapor-pressure species that nucleated, forming particles over several minutes. At the same time, other liquid and solid material condensed on the newly formed surfaces. The time available for coagulation ranged from 20 minutes to several hours, long enough for agglomerates of 10-50 primary particles to form.

COLLOIDAL AGGLOMERATES

Agglomerates are often formed in the liquid phase. In many of the previous laboratory studies (Weitz and Huang, 1984; Lindsay et al., 1987; Tang et al., 1988), spherical solid particles were dispersed in a solvent under conditions in which the surface electrical double layer prevented coagulation. The colloid was made unstable by suddenly increasing the ionic strength or by changing the pH of the solution. If there is no interparticle repulsion, the coagulation is diffusion-limited, and the resulting floc has a structure similar to that seen in aerosol agglomerates.

Colloidal agglomerates may also form from reactions of precursor solutions. For example, TiO_2 (anatase) and ZnO agglomerates with 2-10 nm primary particles have been prepared using the hydrolysis of $TiCl_4$ and zinc acetate (Kormann et al., 1988; Bahnemann et al., 1987). In these studies it was found that the ZnO primary particles generally had primary diameters of 5 nm $\pm$ 0.5 nm (Figure 20) while the TiO_2 primary particles were typically 2.4 nm. It is interesting to note that crystalline TiO_2 can exist in particles with only 100 to 300 molecules and that such small crystals do not sinter instantaneously at room temperature or under the electron beam of the TEM. It was found that dried agglomerates could be broken up if samples were resuspended immediately after drying. After a period of minutes, however, the dried powder could no longer be resuspended completely (Hoffman, 1991). This is consistent with the sintering discussion above, but the presence of the solvent complicates considerably the interpretation of these observations.

The extremely uniform primary particle size ($\sigma_g \sim 1.1$) is consistent with particle growth by the deposition of single molecules. It is also likely that the electrical double layer repulsion had a strong effect on the reaction and aggregation kinetics.

CONCLUSIONS

Agglomerate formation in gas or liquid phase systems is a complex process depending on the chemical kinetics, particle dynamics and solid phase sintering. Growth by surface reactions or condensation is expected to produce dense spheres with a narrow size range. Coagulation produces particles with broader size distributions and also results in the formation of agglomerates, provided that restructuring by sintering or other processes is not important.

Agglomerates from different sources have primary particles with similar sizes, suggesting that the rate-limiting step in the formation process is the same for all of these systems. It has been hypothesized that primary particle size is determined by sintering kinetics. However, examination of agglomerates produced in a variety of systems indicates that this is not universally true. In some systems, the primary particles are formed at such high temperatures that coalescence is rapid compared to coagulation. Agglomerates are formed later, after the temperature decreases, and primary particles are distinct. In such systems, the primary particle size is determined by the mass concentration and the residence time at high temperature. On the other hand, sintering rates may be critical in low-temperature isothermal systems where coagulation and sintering occur at comparable rates. Agglomerates produced in such systems are characterized by highly fused primary particles.

The formation of agglomerates in typical aerosol systems is difficult to investigate experimentally, since it occurs typically at high temperatures, over time scales of milliseconds to seconds. The chemical reactions leading to the particle formation are often complex. Similarly, the solid-phase sintering of ultrafine particles is an area of active research. Thus, efforts to understand the early phase of agglomerate formation have been qualitative.

Although modeling may provide new insight into the agglomerate formation, such investigations require a detailed understanding of the sintering kinetics and aerosol dynamics of non-spherical particles. The latter question involves both the characterization of particle structure and an understanding of the effect of the structure on the particle transport properties, including condensation and coagulation.

REFERENCES

Allen, M.D. and Briant, J.K.(1978). *Health Physics* **35**:237-254.

Allen, M.D., Briant, J.K and Moss, O.R.(1979). *Am. Ind. Hyg. Assoc. J.* **40**:474-481.

Bahnemann, D.W., Kormann, C. and Hoffman, M.R.(1987). *J. Phys. Chem.* **91**:3789-3798.

Calcote, H.F. and Olson, D.B. (1987). *Abstracts from the American Chemical Society* **194**:69.

Flagan, R.C. (1979). in *Seventeenth Symposium (International) on Combustion*, The Combustion Institute, Pittsburgh, PA, pp.97-104.

Flagan, R.C. and Seinfeld, J.H.(1987). *Fundamentals of Air Pollution Engineering*. Prentice Hall, Engelwood Cliffs, p.374.

Friedlander, S.K. and Wang, C.S.(1966). *J. Colloid Interface Sci.*, **22**:126

Fuchs, N.A.(1964). *The Mechanics of Aerosols* , Pergamon, New York, p. 314.

Girshick, S.L. and Chiu, C-P.(1989). *Plasma Chemistry and Plasma Processing*, **9**:355-369.

Glassman, I.(1988). *Combustion*, Academic Press, San Diego.

Hahn, H., Logas, J. and Averback, R.S.(1990). *J. Mater. Res.* **5**:609-614.

Harris, S.J. and Weiner, A.M.(1983). *Comb. Sci. Technol.* **32**:267-275.

Hayashi, C.(1987). *Physics Today*. December, 44-51.

Hébrard, J-L., Nortier, P., Pijolat, M. and Soustelle, M.(1990). *J. Am. Ceram. Soc.*, **73**:79-84.

Helble, J.J. and Sarofim, A.F.(1989). *J. Colloid Interface Sci.* **128**:348-362.

Herring, C. (1950). *J. Appl. Physics* **21**:301-303.

Hoffman, A. (1991). Private Conversation.

Horvath, J., Birringer, R., and Gleiter, H.(1987). *Solid State Comm.* **62**:319-322.

Juillet, F., Lecomte, F., Mozzanega, H., Teichner, S.J., Thevenet, A., and Vergnon, P.(1973). *Faraday Symp. Chem. Soc.* **7**:57-61.

Kalliomäki , P.L., Grekula, A., Hagberg, J., and Sivonen, S.(1987). *J. Aerosol Sci.* **18**:781-784.

Kasper, G., Shon, S-N and Shaw, D.T.(1980). *Am. Ind. Hyg. Assoc. J.* **41**:288-296.

Koch, W. and Friedlander, S.K. (1990). *J. Aerosol Sci.* **21**:S73-76.

Komiyama, H., Kanai, T. and Inoue, H.(1984). *Chem. Lett.* 1283.

Kops, J., Dibbets, G., Hermans, L. and Van de Vate, J. (1975). *J. Aerosol Sci.* **6**:329-333.

Kormann, C., Bahnemann, D.W. and Hoffman, M.R.(1988). *J. Phys. Chem.* **92**:5196

Kuhn, W.E., Lamprey, H., and Sheer, C.(1961). *Ultrafine Particles.* John Wiley and Sons, New York.

Lindsay, H.M., Lin, M.Y., Weitz, D.A., Sheng, P.,Chen, Z., Klein, R. and Meakin, P.(1987). *Faraday Discuss. Chem. Soc.* **83**:153-165.

Lushnikov, A.A, Pakhomov, A.V. and Chernyaeva, G.A.(1987). *Sov. Phys. Dokl.* **32**:45-45.

Markowski, G.R., Ensor, D.S., Hooper, R.G. and Carr, R. (1980). *Environ. Sci. Technol.* **14**:1400-1402.

Nguyen, H.V.(1989). Ph.D. dissertation, California Institute of Technology.

Nielson, M.L., Hamilton, P.M., and Walsh, R.J. (1961). in *Ultrafine Particles.* (W.E. Kuhn, H. Lamprey, H., and C. Sheer, eds.). John Wiley, New York.

Okuyama, K., Kousaka, Y., Tohge, N., Yamamoto, S., Wu, J.J., Flagan, R.C. and Seinfeld, J.H.(1986). *AIChe. J.* **2**:2010-2019.

Okuyama, K., Jeung, J-K., Kousaka, Y., Nguyen, H.V., Wu, J.J, and Flagan, R.C.(1989). *Chem. Eng. Sci.* **44**:1369-1375.

Paulson, S.E., Pandis, S.N., Baltensperger, U., Seinfeld, J.H., Flagan, R.C., Palen, E.J., Allen, D.T., Schaffner, C., Giger, W., and Portmann, A. (1990). *J. Aerosol Sci.* **21:** S245-S248.

Rabeony, H. and Mirabel, P. (1987). *J. Chem. Phys.* **91:**1815-1818.

Samson, R.J., Mulholland, G.W. and Gentry, J.W.(1987). *Langmuir* **3**:272-281.

Sarofim, A.F., Howard, J.B. and Padia, A.S.(1977). *Combustion Sci. Technol.* **16**:187-204.

Saxena, S.C., Henry, W.F., and Podolski, W.F.(1985). *Prog. Energy Combust. Sci.* **11**:193-251.

Seinfeld, J.H.(1986). *Atmospheric Chemistry and Physics of Air Pollution.* John Wiley, New York, pp. 400-431.

Senior, C.L. and Flagan, R.C.(1982). *Aerosol Sci. Technol.* **1**:371:383.

Sokolowski, M., Sokolowska, A., Michalski, A., and Gokieli, B.(1977). *J. Aerosol Sci.* **8**:219-230.

Tang, P., Colflesh, D.E. and Chu, B.(1988). *J. Colloid Interface Sci.* **126**:304-313.

Weitz, D. and Huang, J.S. (1984). in *Kinetics of Aggregation and Gelation.* (F. Family and D.P. Landau, eds.). Elsevier-North Holland, Amsterdam. pp. 19-28.

Wu, J.J., Nguyen, H.V., and Flagan, R.C.(1987). *Langmuir* **3**:266-271.

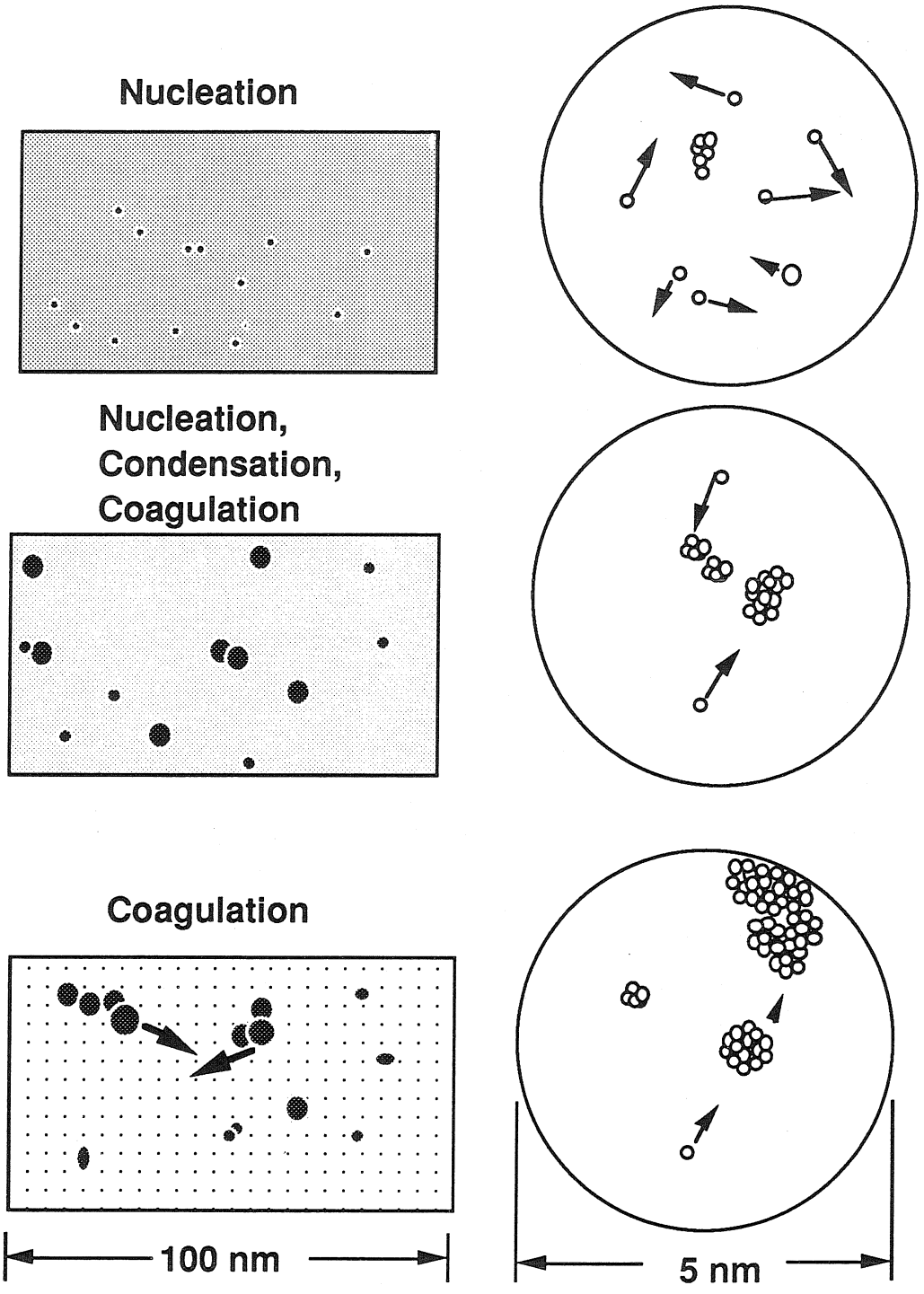

Figure 1. Agglomerate aerosols form by nucleation from a highly supersaturated vapor. Particles then grow by condensation and coagulation while the condensible vapor is depleted. At this point, coagulation dominates the growth.

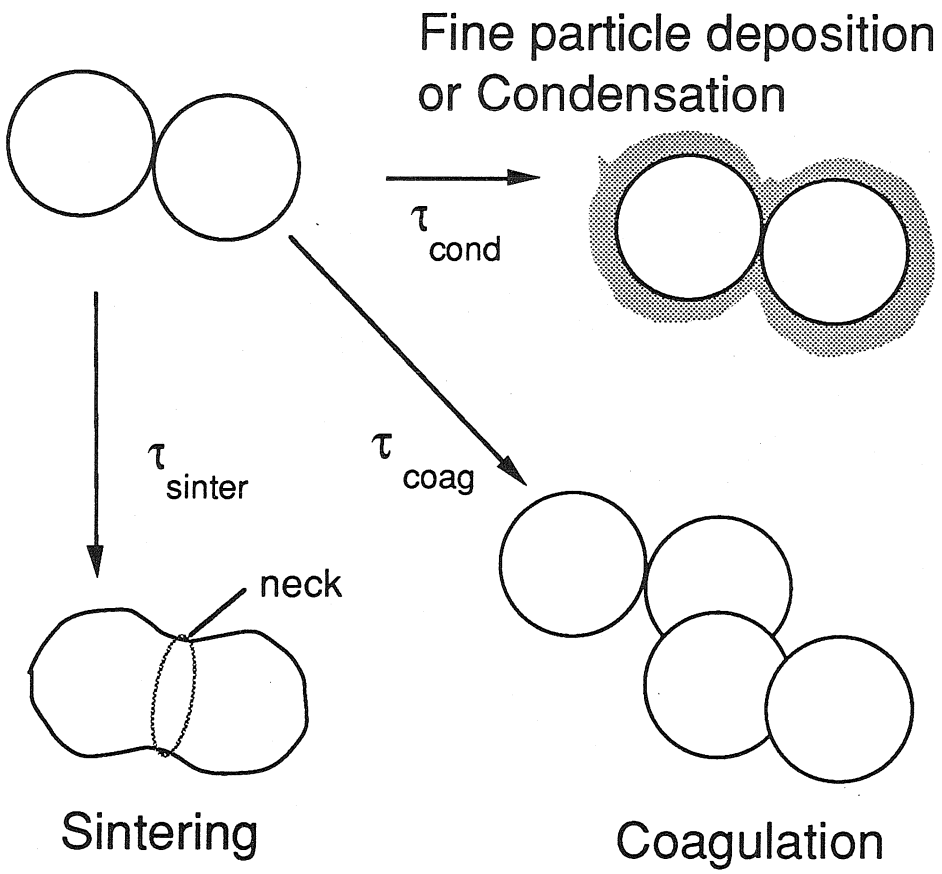

Figure 2. The structure of an aerosol particle is determined by the relative rates of sintering, coagulation and condensation.

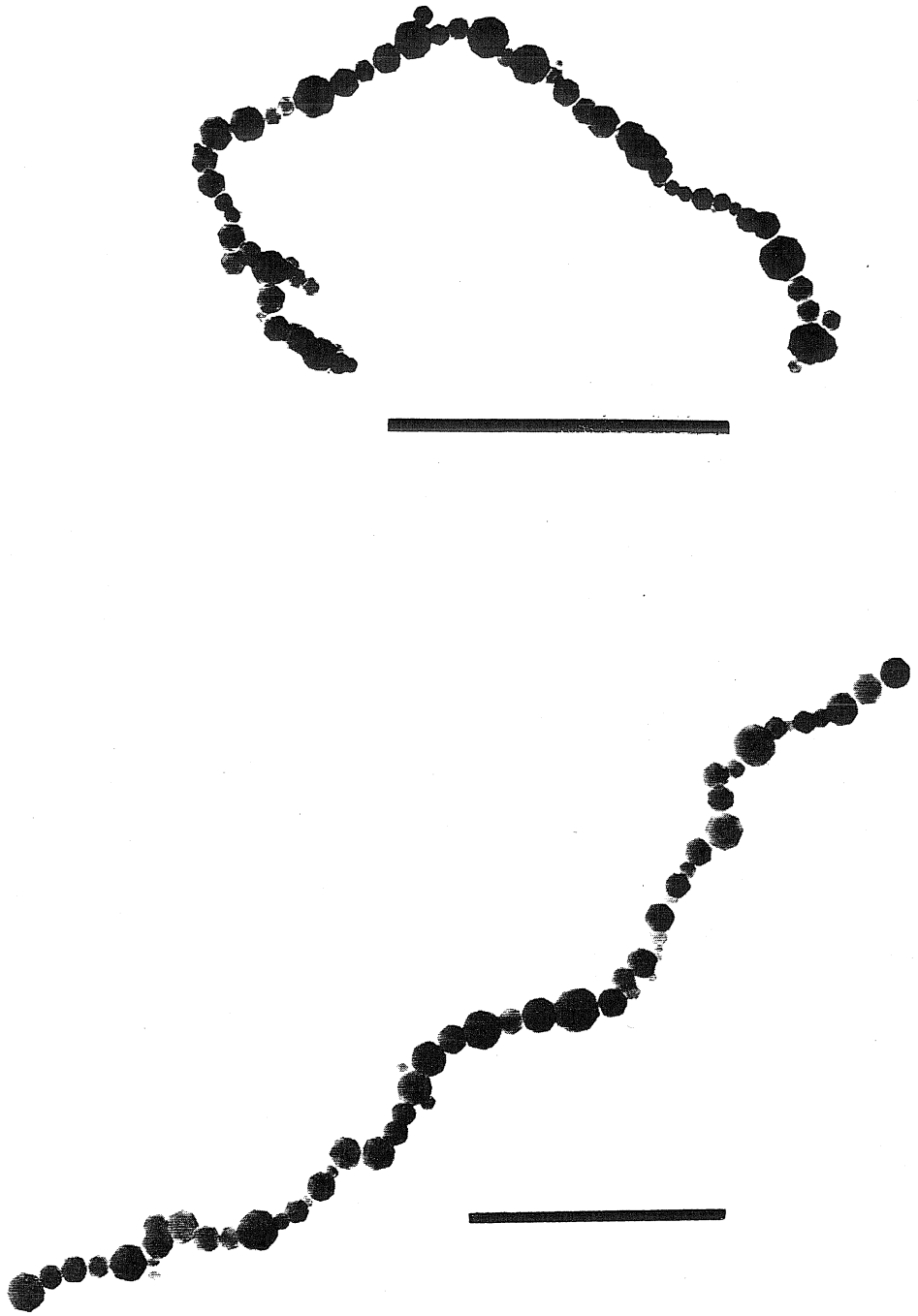

Figure 3. Hematite chains; bars=1000 nm. (Reprinted by permission of the publisher from G. Kasper, *Aerosol Sci. Technol.* vol. 1, pp. 201-215. Copyright 1982 by Elsevier Science Publishing Co., Inc.)

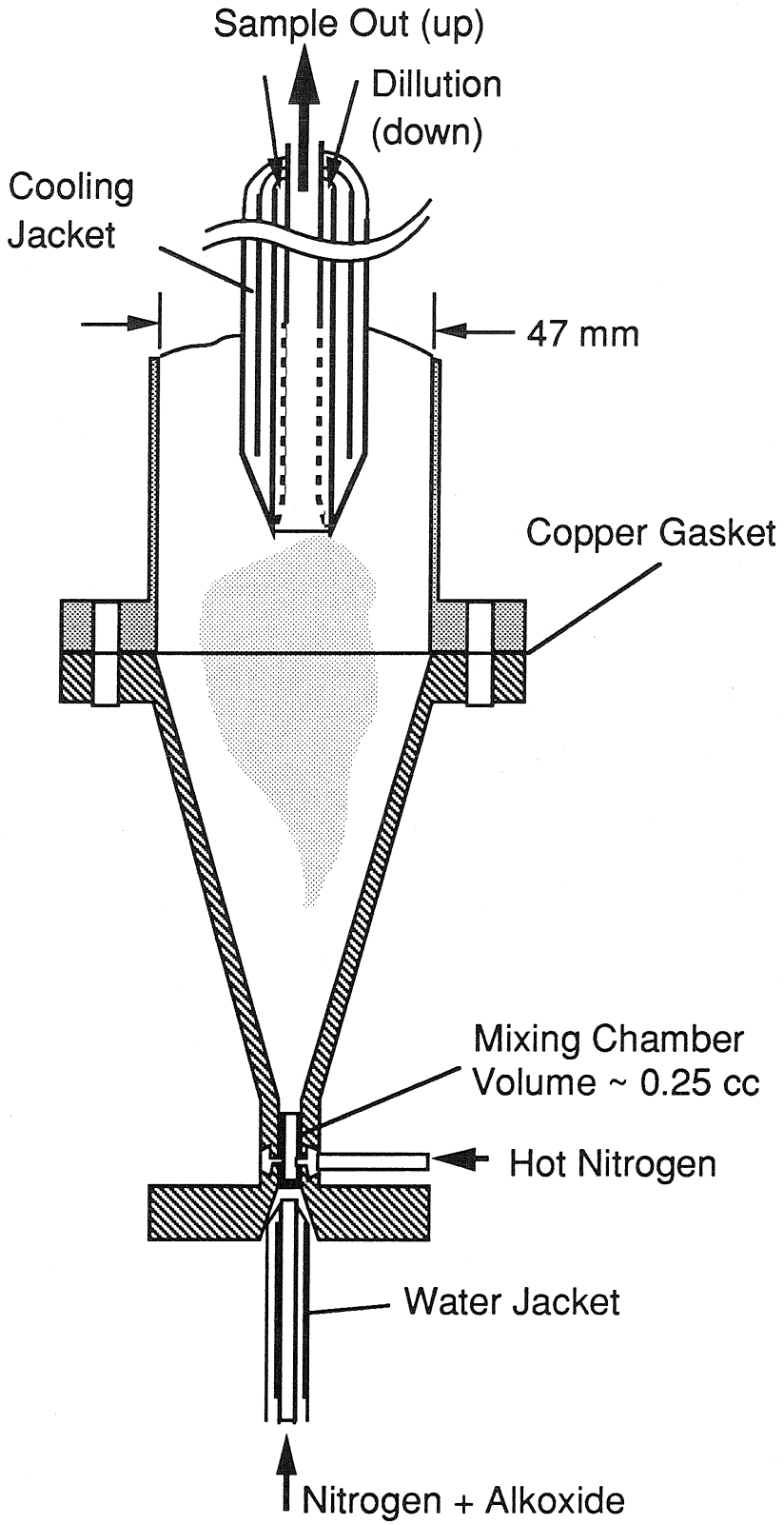

Figure 4. Detail of Mixing Nozzle used in the Fast-Mixing Reactor I.

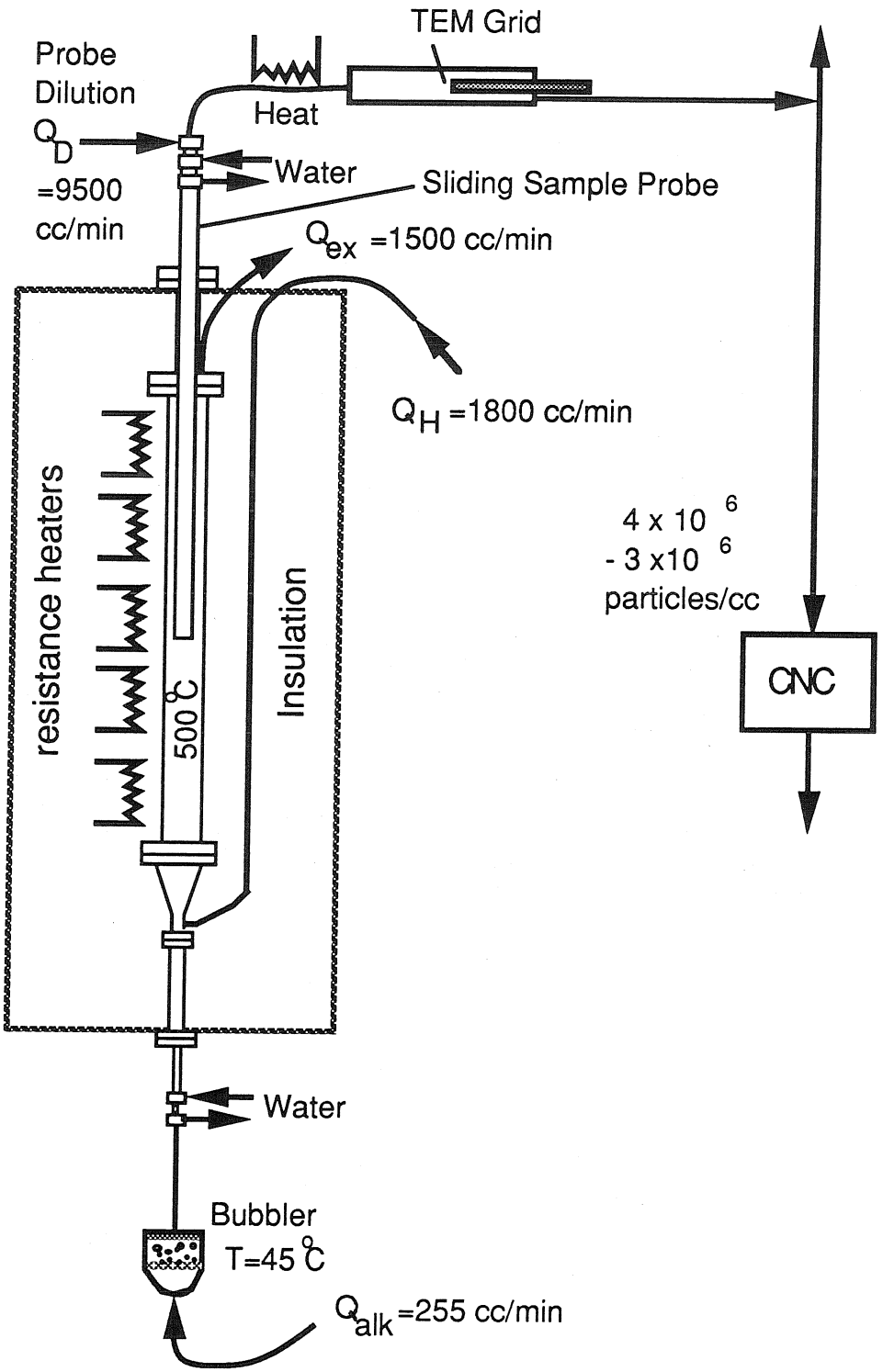

Figure 5. The Fast-Mixing Reactor I consists of an alkoxide vapor source (bubbler), a mixing chamber (Figure 4) and a long isothermal growth tube. Particles are collected on a transmission electron microscope (TEM) grid and counted by a condensation nucleus counter (CNC).

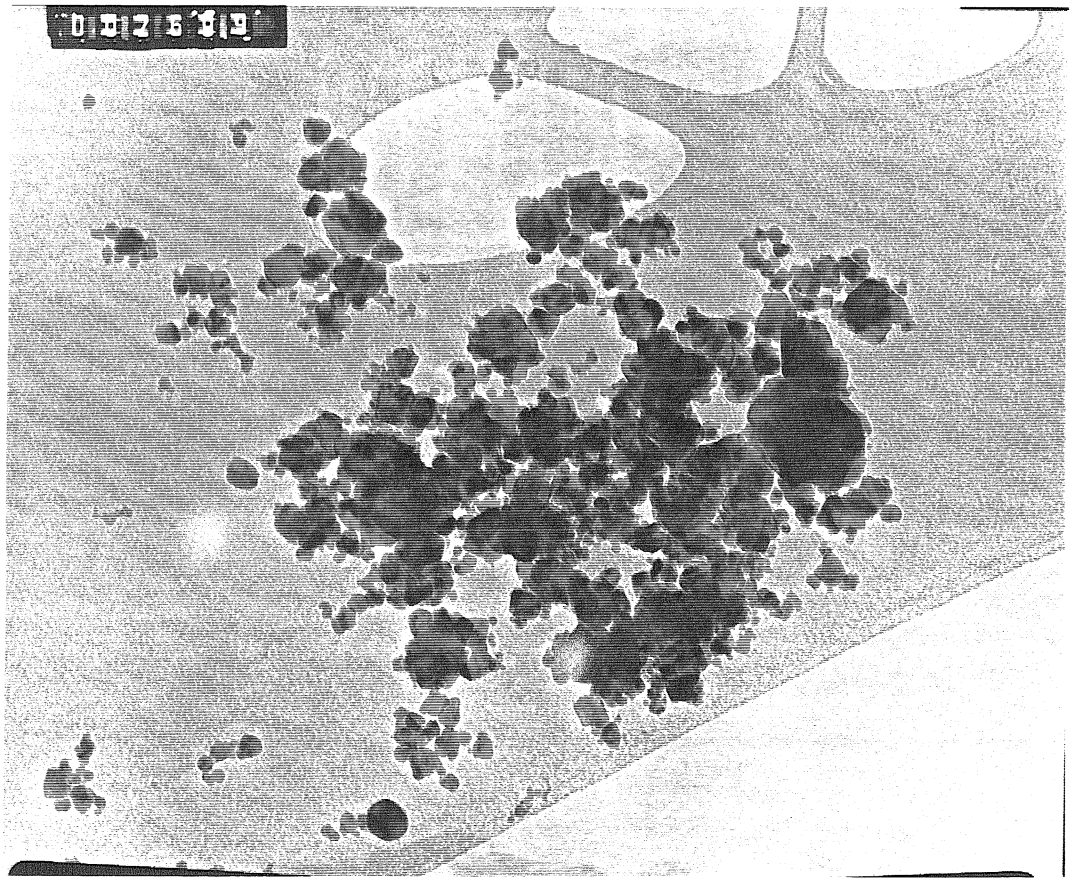

500 nm

Figure 6. TiO_2 from Fast-Mixing Reactor I, produced at 500 °C, Plate 2699.

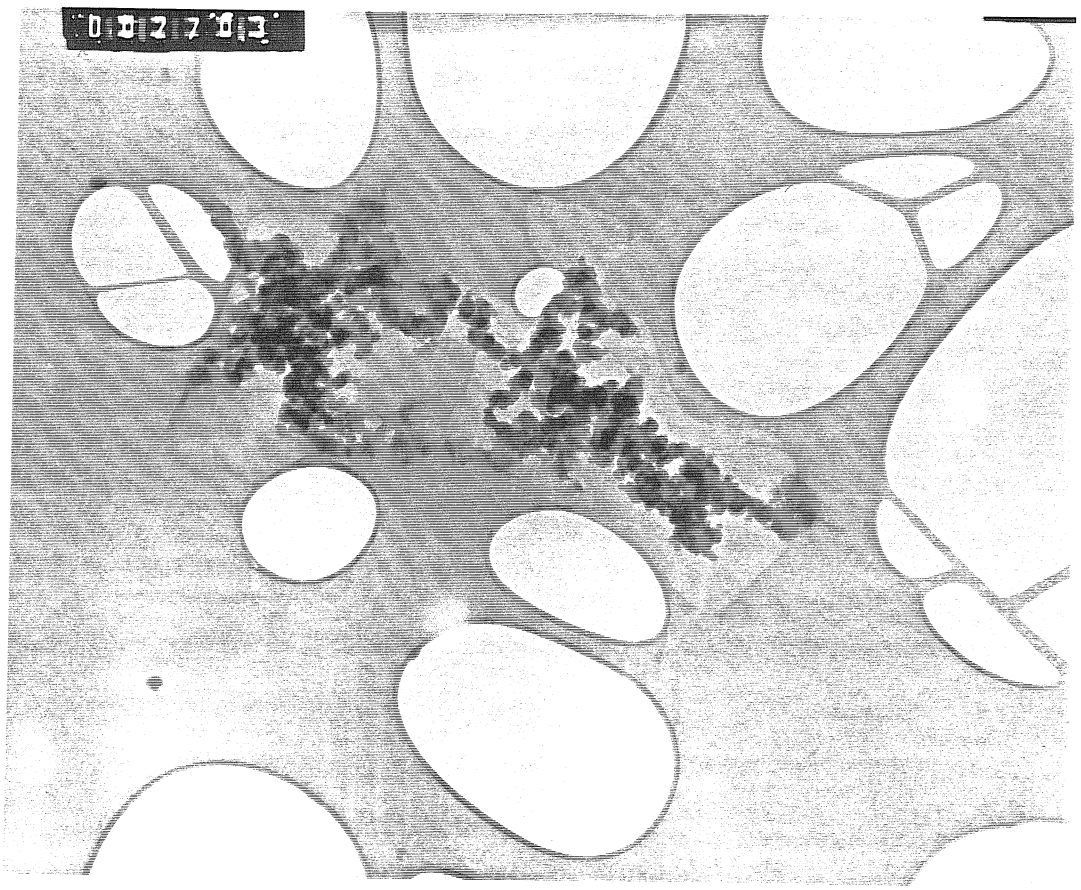

1000 nm

Figure 7. TiO_2 from Fast-Mixing Reactor I, Plate 2703.

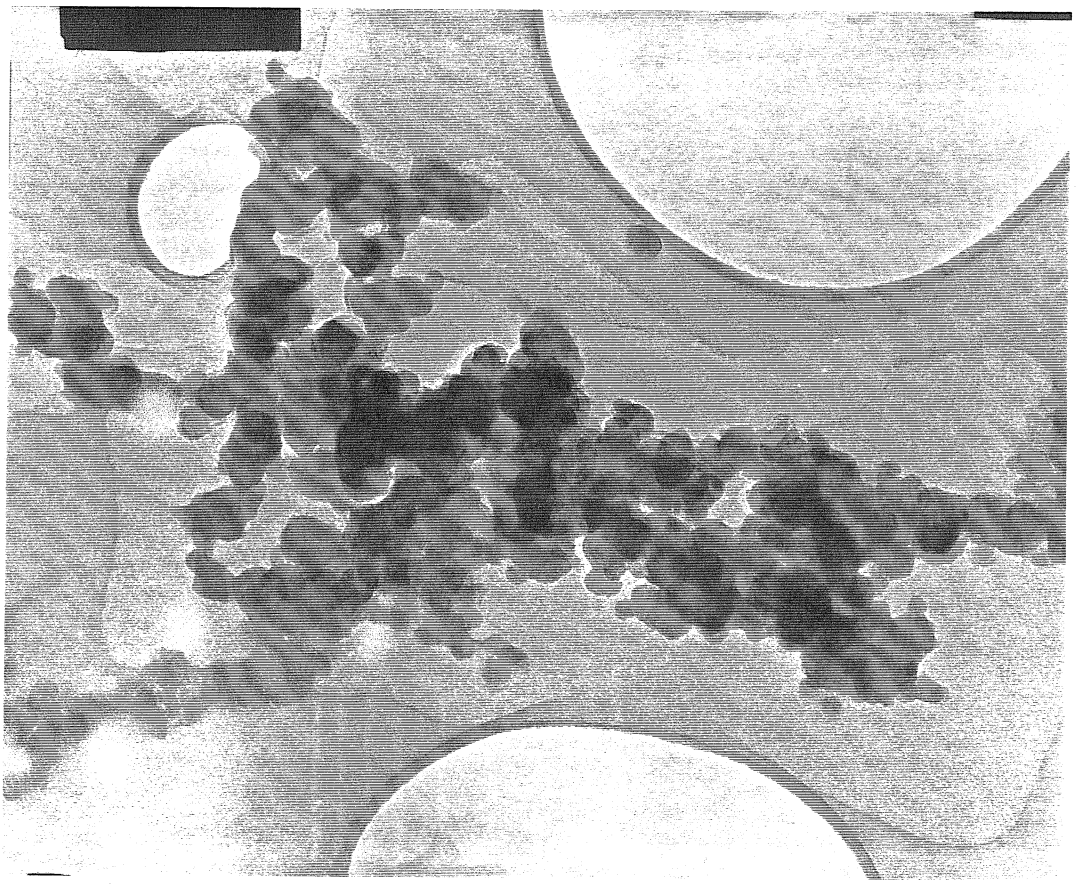

Figure 8. TiO_2 from Fast-Mixing Reactor I, Plate 2702, d_1=36 nm, σ_g=1.5.

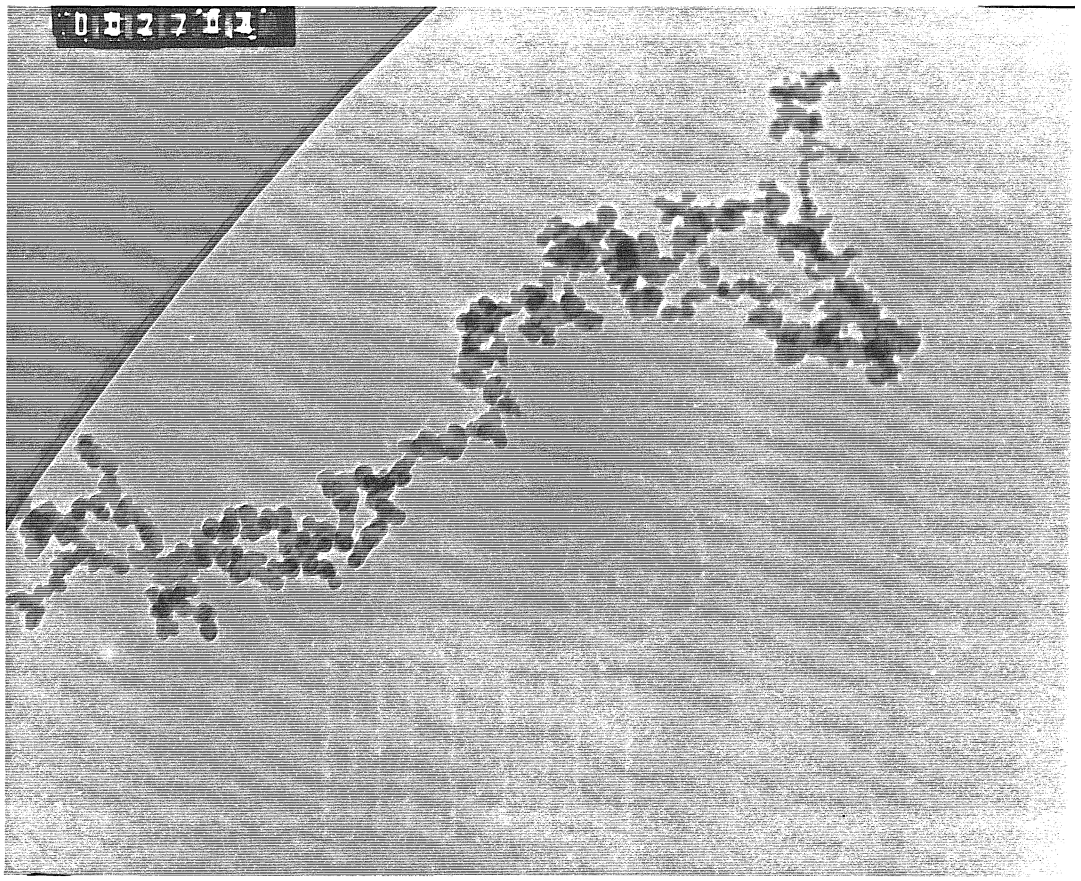

1000 nm

Figure 9. TiO_2 from Fast-Mixing Reactor I, Plate 2704, d_1=33 nm, σ_g=1.3.

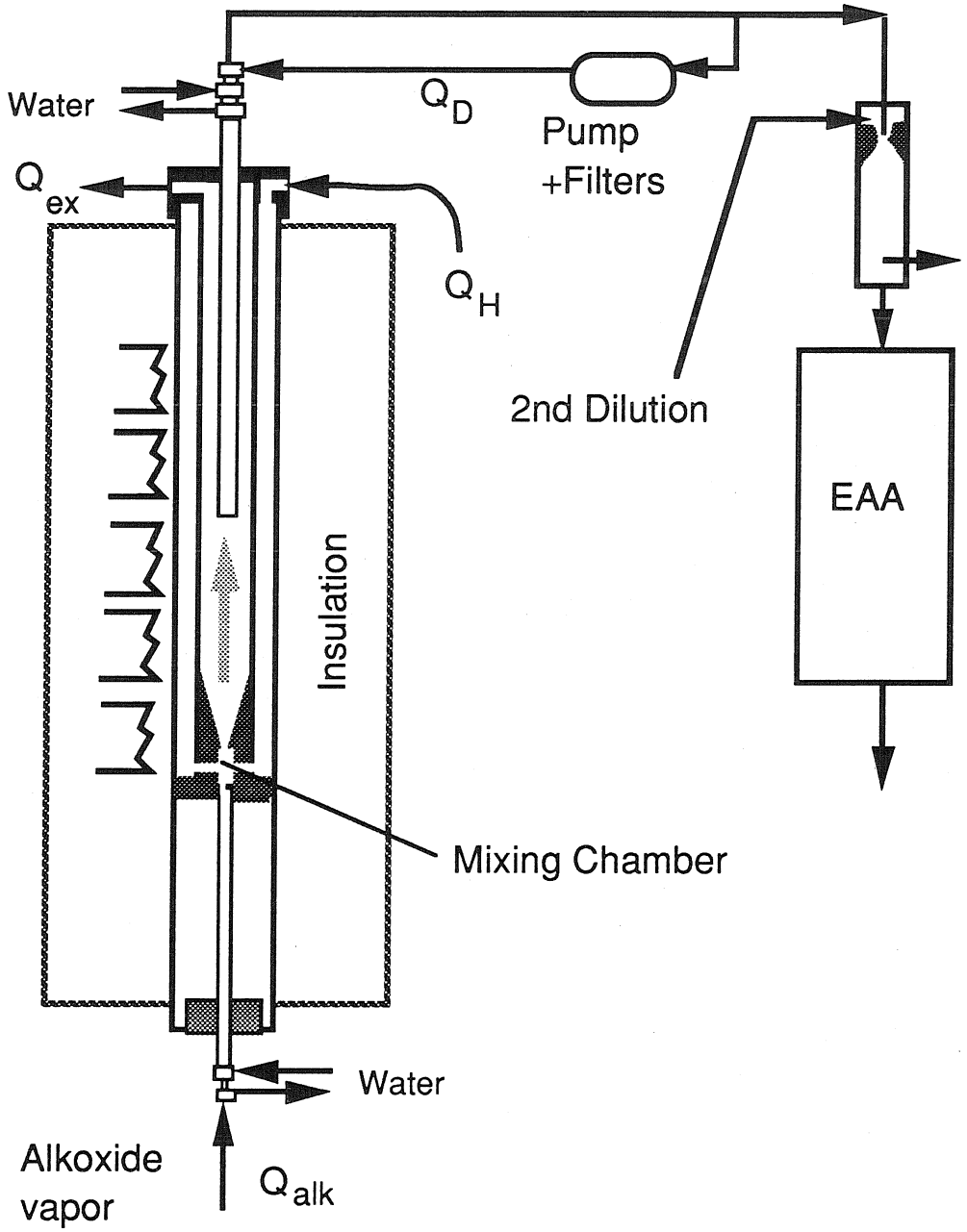

Figure 10. In the Fast-Mixing Reactor II, nitrogen is preheated in a down-flowing annular flow. The preheated nitrogen is then mixed with the alkoxide vapor, as in the Fast-Mixing Reactor I. The resulting aerosol flows upward to a sampling probe.

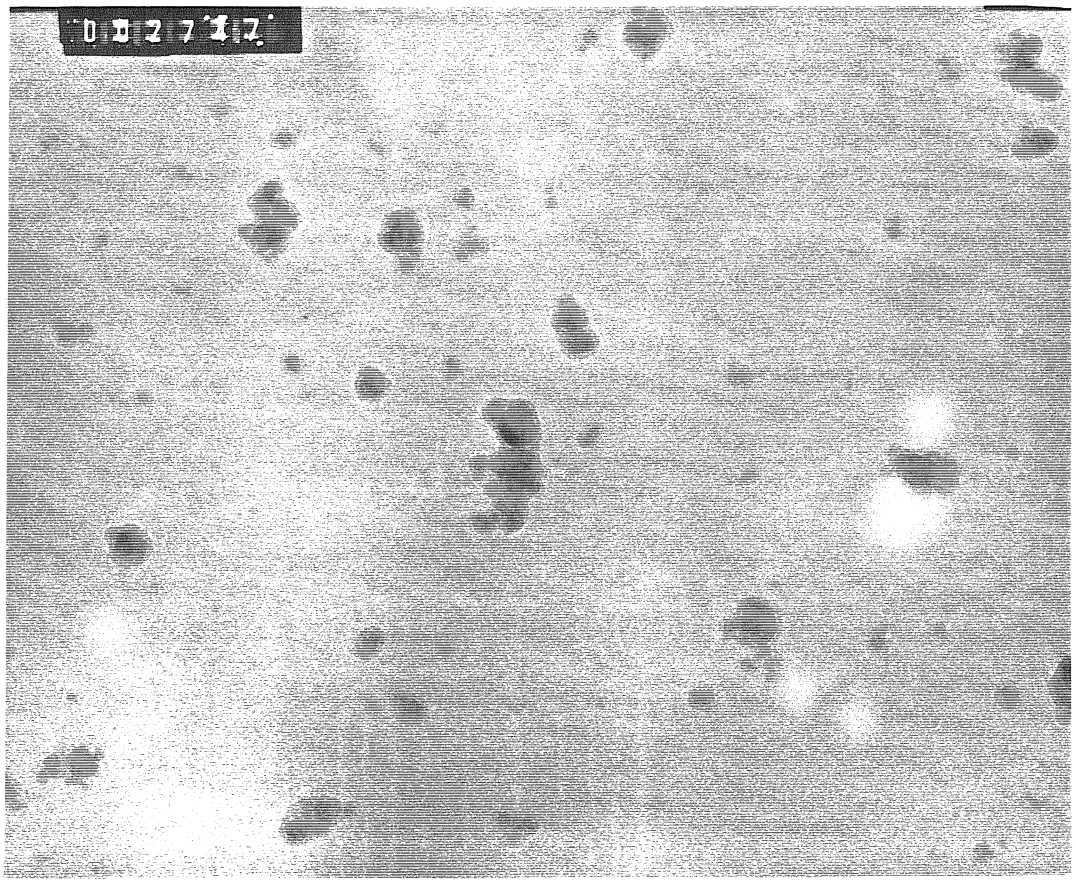

100 nm

Figure 11. TiO_2 from Fast-Mixing Reactor II, Plate 2747, T=530 °C, t_{res} =1.1 s.

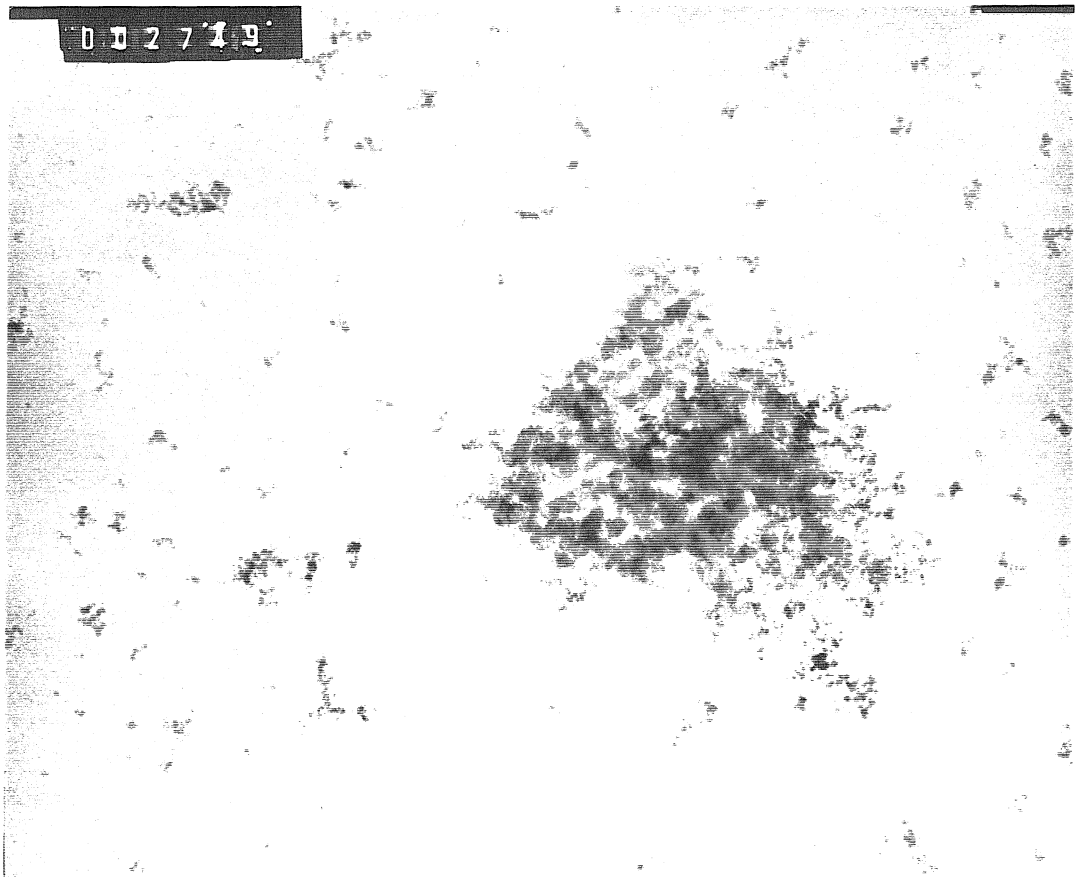

Figure 12. TiO_2 from Fast-Mixing Reactor II, Plate 2749, T=650 °C, t_{res} =0.9 s.

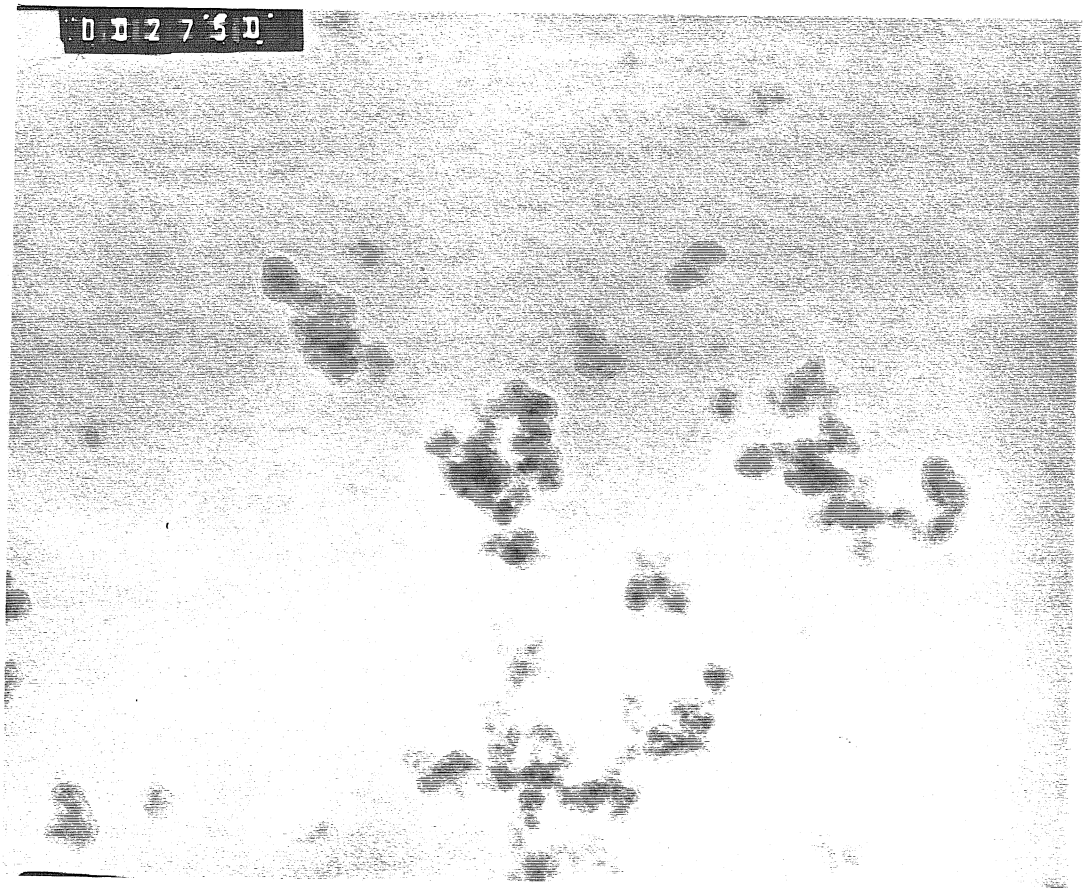

Figure 13. TiO_2 from Fast-Mixing Reactor II, Plate 2750, T=650 °C, t_{res} =0.9 s.

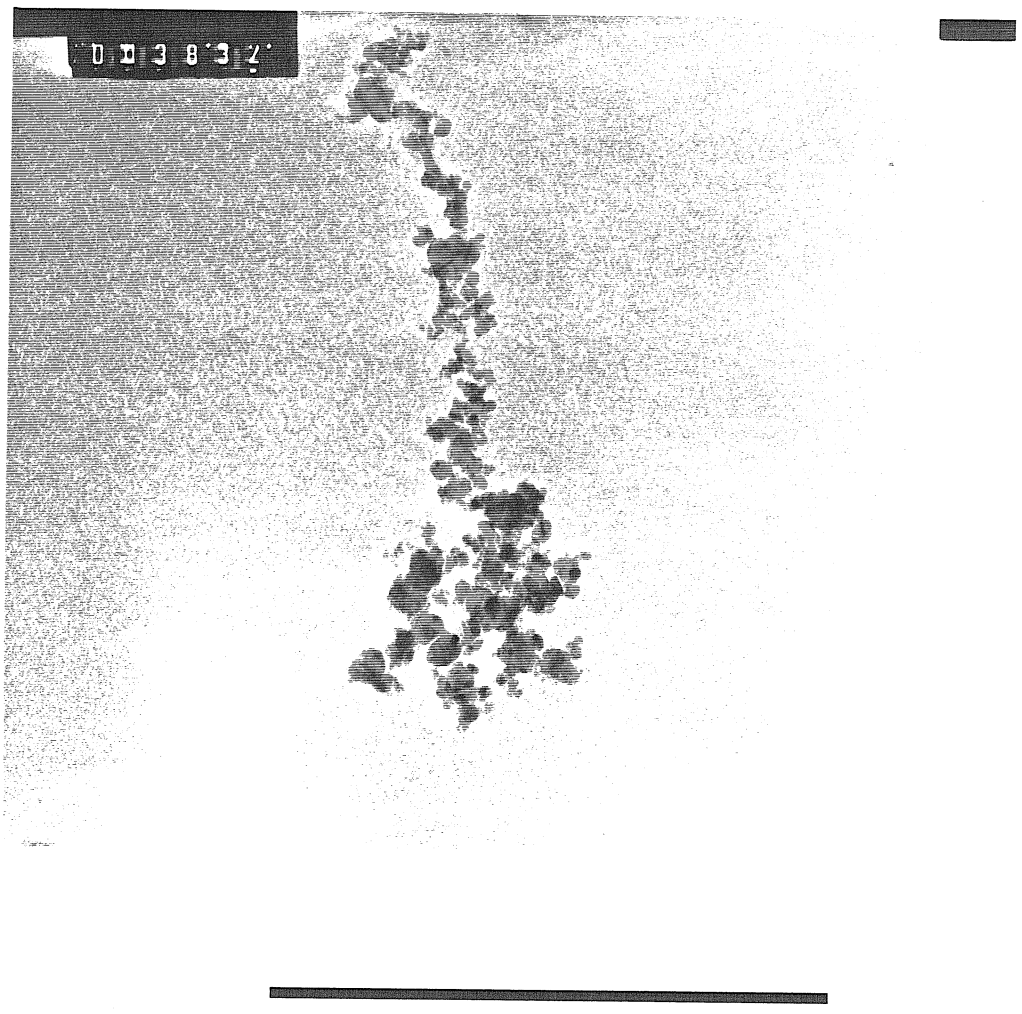

Figure 14. TiO_2 from Fast-Mixing Reactor III, Plate 3832, T=500 °C, t_{res} =1.5 s, 17 ppm TTIP.

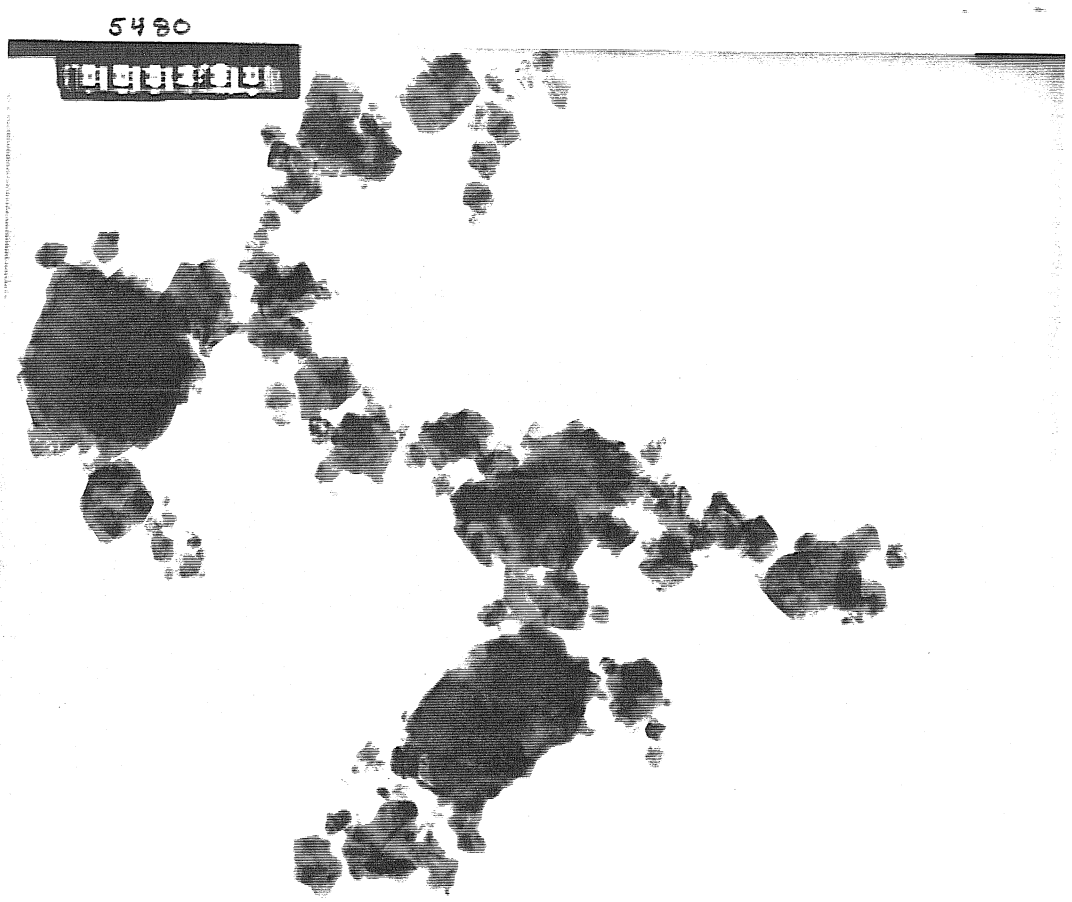

Figure 15. TiO_2 from Fast-Mixing Reactor III, Plate 5480, T=500 °C, t_{res} =3.8 s, 44 ppm TTIP.

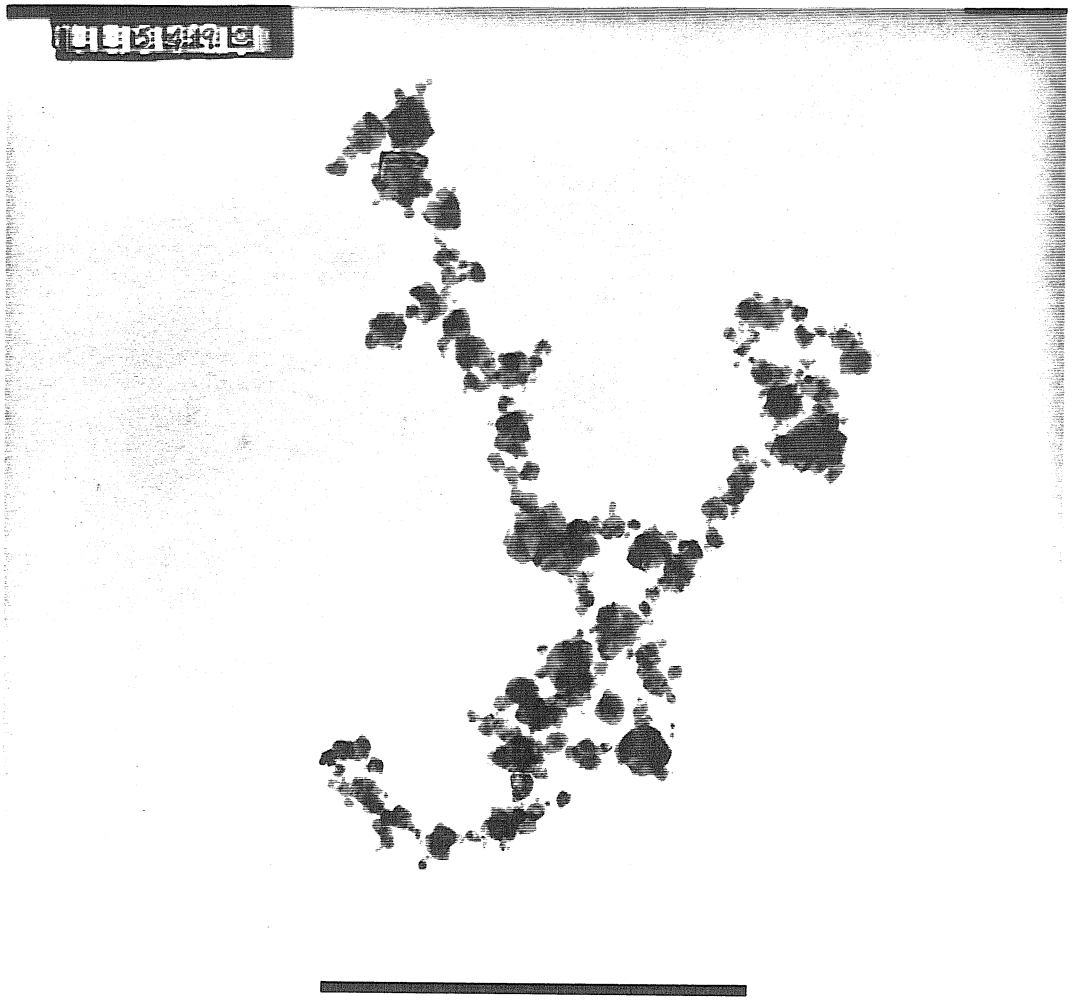

Figure 16. TiO_2 from Fast-Mixing Reactor III, Plate 5490, T=500 °C, t_{res} =4.2 s, 400 ppm TTIP.

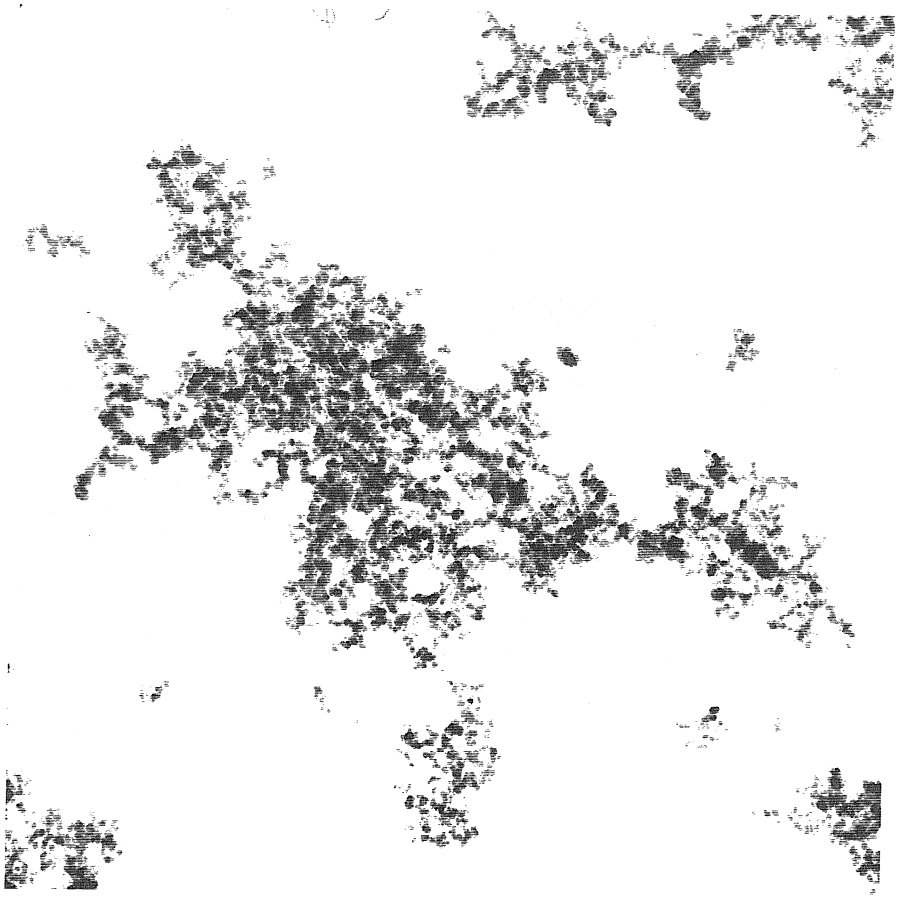

Figure 17. TiO_2 from Compact Reactor, T=530 °C.

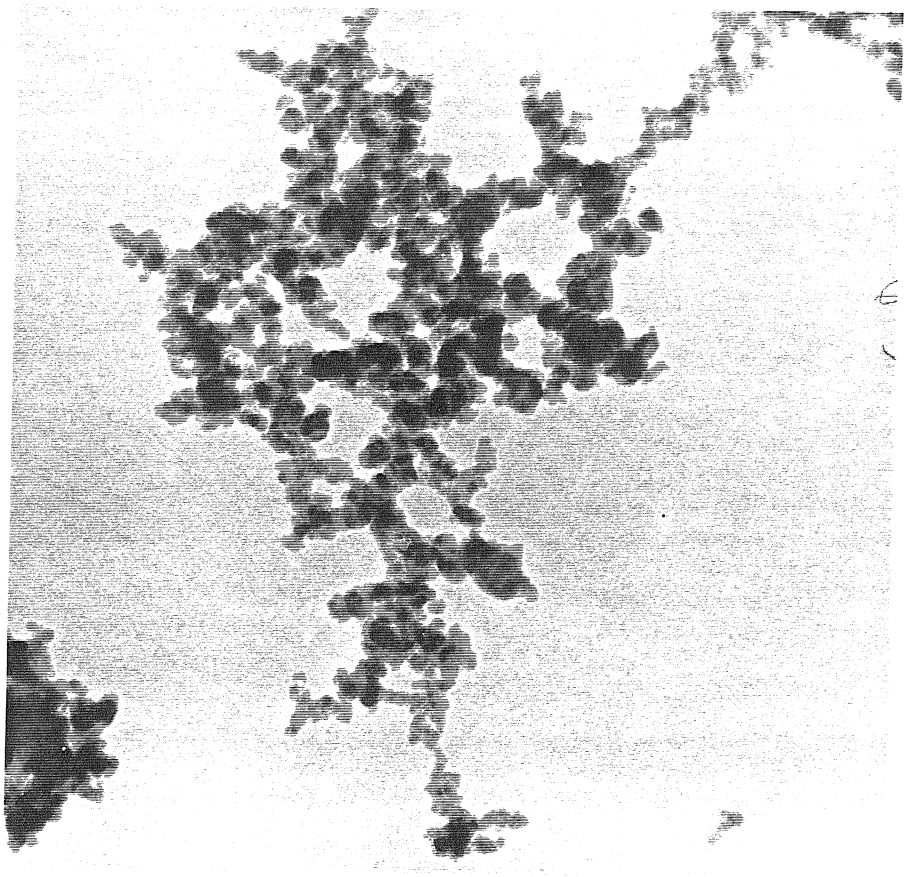

Figure 18. TiO_2 from Compact Reactor, T=530 °C, d_1=7 to 30 nm (median=11 nm, σ_g=1.3)

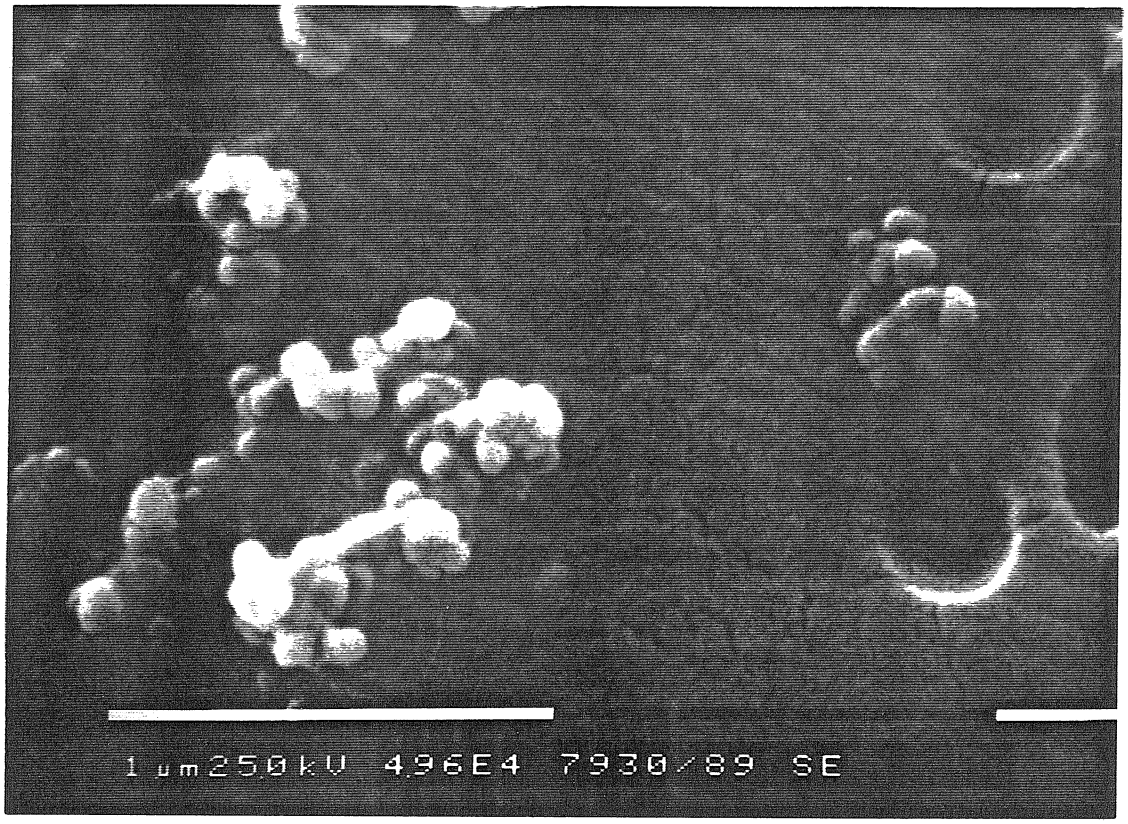

Figure 19. Agglomerate formed from photochemical smog chamber reactions of air, NOx and β-Pinene (Paulson et al., 1990).

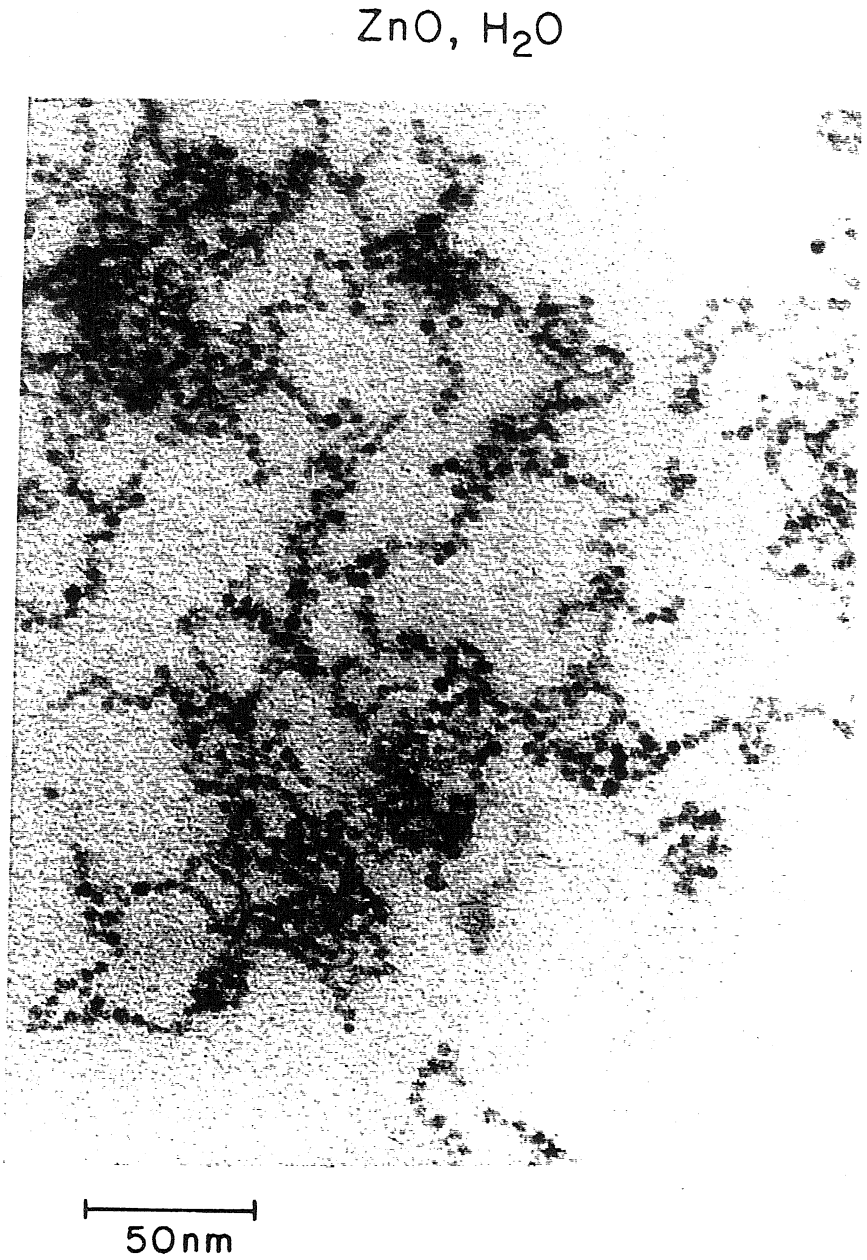

Figure 20. Colloidal ZnO agglomerate from the hydrolysis of zinc acetate in propanol (Bahnemann et al., 1987).

CHAPTER 3

CHARACTERIZATION OF THE STRUCTURE OF AGGLOMERATE PARTICLES

submitted to Particle Characterization and Particle Systems

ABSTRACT

Agglomerates of uniformly sized primary spheres are found in many aerosol and colloidal systems. Such particles have been described as fractal although they possess self-similarity over only a narrow range of length scales. Previous work suggests that for such objects, ideal fractal scaling laws may require substantial corrections. The problem is particularly acute for measurements of particle structure from 2d images. The relation between the structure of an agglomerate and the characteristics of its projection is investigated using simple analytical models and clusters generated by a modified cluster-cluster aggregation simulation. The morphology of the simulated clusters is varied by changing the ratio of masses of the colliding clusters. The fractal dimensions D_{f3} of the simulated clusters were typically 10 - 20% higher than those measured for the projections, D_{f2}, even though $D_{f3} < 2$. This difference decreases as the cluster size increases. It was found that the fraction of primary particles visible in the 2d image is more sensitive to cluster size than to fractal dimension for clusters with less than several thousand primary particles.

INTRODUCTION

Aerosol and colloidal particles produced in many systems are agglomerates of small, nearly spherical primary particles. The structure of the primary spheres themselves is an important problem, but only the arrangement of the primary particles within a cluster will be considered here. Computer simulations have been useful in understanding the

formation and structures of these agglomerates, but it has been difficult to compare the predicted structures with those observed experimentally.

In experimental studies involving agglomerate particles, one often desires three-dimensional (3d) structural information, such as the particle mass, the maximum length or the fractal dimension. However, many experimental techniques provide information about the two-dimensional (2d) projection of the cluster rather than the full 3d object. Microscopy is such a technique; even with the use of stereo pairs or dark-field transmission electron microscopy one cannot obtain the 3d coordinates of the primaries in an agglomerate [1]. Nevertheless, 3d structural information can often be inferred from 2d projections, given some additional information on the shape of the particles. For example, if the particles are known to be fibers deposited at random orientations on the microscope grid, the fiber lengths cannot be determined from a single micrograph but the statistics of the fiber lengths in a population can be found from a sufficiently large number of micrographs. In order to do this, one must be able to predict the appearance of micrographs for known 3d objects.

Fractal geometry has been used to characterize agglomerate particles; this, along with some important results from previous computer simulations, is reviewed below. Motivated by these simulations, analytical models are developed for simple fractals. Predictions from these models are then compared to results from simulations performed in this study. An algorithm that allows control of the cluster morphology is used to generate a variety of structures similar to those seen in particles produced in flames and high-temperature reactors. The 3d structures of computer-generated agglomerates are related to their 2d projections, aiding the interpretation of 2d characterizations of real particles.

FRACTALS

Forrest and Witten [2] found that metal oxide aerosol agglomerates exhibited scale invariant structures that have since been labeled fractal. The term "fractal" was coined by

Mandelbrot [3] to describe objects and mathematical sets with special scaling properties. The most striking feature of a fractal is its self-similarity or scale invariance. If any part of the object is magnified, it appears similar to the object as a whole. If each coordinate direction must be scaled by a different amount to produce similarity, the object is known as "self-affine" rather than self-similar. Fractal concepts have been applied in almost every branch of physics, to physical objects, abstract sets such as chaotic attractors, and velocity distributions in turbulent fluids. Recently there has been tremendous interest in the fractal properties of fine particles, as reviewed by Kaye et al. [4], Meakin [5] Smirnov [6] and Cleary et al. [7]. Here we are concerned with structures whose mass distribution may be described as fractal, specifically aerosol agglomerates. Figure 1 shows some clusters of spheres with exact self-similarity over a limited range of length scales. Real agglomerates have a random structure without exact self-similarity. However, if the scaling laws described below apply, then the agglomerates are known as statistical fractals [3].

Fractal clusters obey power-law scaling of the density with length. More explicitly, the mass m in a "measuring sphere" of radius l varies as

$$m(l) \sim l^{D_f} \quad , \tag{1}$$

where D_f is the fractal or Hausdorf-Besicovitch dimension [3]. For a true fractal with similarity at all length scales, the location and size of the measuring sphere are irrelevant. For finite objects such as those in Figure 1, Eq. (1) applies only for l between some upper and lower "cutoff" lengths. For example, the lower cutoff length for a fractal cluster of spheres would be somewhat larger than the primary sphere size. The upper cutoff length would be the radius of gyration or a similar measure of the overall cluster size. Rather than using Eq. (1), it is often convenient to work with the pair correlation function $C(l)$, which also obeys power-law scaling for l between the upper and lower cutoff lengths. The number of primary particles per unit volume n at position r is correlated to the number at $r+l$ by

$$C(l) = < n(r)\, n(r+l) > \sim |l|^{D_f - 3} , \qquad (2)$$

where $< >$ denotes averaging over all r and directions of l.

For a collection of similar fractals with masses M and radii of gyration R_g obeying Eqs. (1) or (2) ,

$$M(R_g) \sim R_g^{D_f} . \qquad (3)$$

Since D_f does not completely define the structure of an object, the connection between Eq. (3) and the previous relations requires that the clusters be similar and have primary spheres of the same size. This condition is satisfied by the objects in Figure 1; therefore, Eq. (3) can be used to compute D_f. Suppose that five Vicsec clusters are joined to form a larger Vicsec cluster. The mass is five times greater while the length is only three times larger, so $D_f = \log(5) / \log(3) = 1.49$. For statistical fractals with relatively narrow ranges of self-similarity, the conditions required for Eq.(3) to hold are less clear. For such clusters it is best to distinguish between the scaling of a collection of clusters and the scaling of the mass distribution within an individual cluster. The exponent in Eqs. (1) and (2) is often called D_α while D_β is used in Eq. (3) [5]. In this paper, D_f will refer to D_α.

It has often been assumed that if the fractal dimension D_{f3} of a 3d object is less than 2, then the projection of the object will also be a fractal with fractal dimension $D_{f2} = D_{f3}$ [3,8]. For a collection of such 3d objects with $D_\beta = D_{f3} < 2$, it is often assumed that the projected area is proportional to the mass [4,5,9,10] and that D_β can be determined from projections using Eq. (3). On the other hand, for sufficiently large 3d clusters with $D_{f3} > 2$, the projection appears to have a fairly uniform density, so that $D_{f2} = 2$ and the projected area scales as R_g^2 [3,10].

These relations (Table 1) must hold for infinitely large fractals, but it is clear that they are only approximate for finite objects, such as aerosol or colloidal agglomerates, which typically contain 10 - 2000 primary particles. Samson et al. [11] found that $D_{f2} < D_{f3}$ for computer-generated clusters even when $D_{f3} < 2$. Other simulations have shown that

the area-size relations of Table 1 are accurate only for clusters containing more than several thousand primary particles [12]. Thus, substantial corrections to the ideal fractal scaling laws may be required for such small clusters. After reviewing previous simulations, these corrections will be assessed using simple analytical models and computer simulations.

Table 1. Relations applicable to the projection of ideal fractals.

Fractal Dimension	Individual Object	Collection of Objects	
$D_{f3} < 2.0$	$D_{f2} = D_{f3}$	$area \sim mass$	D_β (2d) = D_β (3d)
$D_{f3} > 2.0$	$D_{f2} = 2.0$	$area \sim R_g^2$	D_β (2d) = 2.0

PREVIOUS SIMULATIONS OF AGGLOMERATE FORMATION

The formation of fractal agglomerates has been investigated primarily through computer simulations of the aggregation of uniformly sized spheres. Depending on the details of the growth algorithm, the clusters may be fractal and appear similar to colloidal or aerosol agglomerates.

In the first reported cluster growth simulations, single primary particles were added to a growing agglomerate. It was found that if the particles move on linear (ballistic) trajectories, dense clusters with $D_f \approx 3$ result [13]. Particles undergoing Brownian trajectories produce Diffusion Limited Aggregation (DLA) clusters with $D_f \approx 2.4$ [5, 14]. If the sticking probability of each collision is reduced, the density of the agglomerate is increased but D_f is unchanged for sufficiently large agglomerates. DLA simulations with finite particle mean free paths also produce denser structures, but this growth algorithm is not scale-invariant. Growth at scales smaller than the mean free path should result in $D_f \approx 3$, while $D_f \approx 2.4$ is expected for large clusters. DLA clusters that experience a Coulombic attraction develop an open, chainlike structure over length scales for which the

electrical interaction energy is larger than the thermal energy kT. For sufficiently large clusters D_f is unaffected by short-range interparticle forces [15].

Aerosol agglomerates are usually formed by collisions of comparably sized clusters. This process is known as cluster-cluster aggregation (CCA). In the first CCA models [13], the cluster added was either assumed to be the same size as the growing cluster, or chosen from a "library" of clusters. In the latter case, the clusters were chosen according to the probabilities predicted by the Smoluchowski equation. More recent CCA models have simulated the motion of large collections of particles moving on ballistic or Brownian trajectories within a control volume [5]. Brownian trajectories yield $D_f \approx 1.8$ while ballistic trajectories lead to $D_f \approx 1.9$ [5,9]. If the collision sticking probability is very low, "reaction limited" (RLCA) clusters with $D_f \approx 2.1$ are produced [16]. External forces causing rearrangement of the cluster may also result in denser clusters [5].

The DLA and CCA algorithms are similar except that the typical mass ratio β of the colliding particles is near zero for DLA and unity for CCA. This mass ratio is expected to depend on the cluster size distribution and the cluster mobilities. Thus, it is reasonable to expect that the mobility of the clusters will influence the structure of CCA agglomerates. However, in the CCA simulations, a cluster size distribution eventually develops in which most of the agglomerates have a similar size, regardless of the cluster mobilities. As a result, the fractal dimension is insensitive to the scaling of the cluster mobilities [5]. The CCA simulations performed previously have not investigated the effect of β on the agglomerate structure. The simulations of the present study will address this question and provide a convenient tool for studying the projections of fractal clusters.

MODEL AGGLOMERATES

Projections of Straight Chains

It is useful to begin with the simplest agglomerate, a straight chain of N unit-radius primary spheres. For sufficiently large N, both the 3d chain and its projections are

essentially line segments, with $D_{f3}=D_{f2}=1$. The projected area A, radius of gyration R_g, and aspect ratio α of the chain and its projection are found easily from geometry (Table 2).

Table 2. Orientation-Averaged Properties of the Projections of Chains (primary particle radius =1).

	2d Projection	3d Chain
Projected Area A	$\pi\ (1 + 0.849(N\text{-}1))$	$\max A = \pi N$
Fractal Dimension	$D_{f2} = 1.0$	$D_{f3} = 1.0$
Aspect Ratio α (N>>1)	$\frac{4}{\pi\sqrt{3}} N$	$\sqrt{\frac{5}{6}} N$
Radius of Gyration R_g (N>>1)	$\frac{2}{\pi\sqrt{3}} N$	$\frac{N}{\sqrt{3}}$

The radius of gyration of a solid body is defined as

$$R_{g3} = \frac{\int_{volume} (x^2+y^2+z^2)\ dx\ dy\ dz}{volume}\ , \tag{4}$$

while the corresponding radius for a plane figure is

$$R_{g2} = \frac{\int_{area} (x^2+y^2)\ dx\ dy}{area}\ . \tag{5}$$

The length-to-width ratio, or aspect ratio α, may be defined as the ratio of principal radii of gyration [14].

Some of the results obtained for chains are applicable to other shapes. For example, R_{g2} is generally smaller than R_{g3}. Also, for any 3d object there must be some primary particles that are "shielded" from view so that

$$\bar{A} = \frac{A}{\pi N} \leqq 1 \tag{7}$$

where $\bar{A}$ will be called the "area fraction". For randomly oriented long chains $\bar{A} \approx 0.85$ while for typical aerosol agglomerates the shielding is larger. For example, stereoscopic measurements have indicated that $\bar{A} \sim 0.64$ for soot agglomerates [17].

Monte-Carlo simulation was used to determine the projected area of straight chains with log-normally distributed primary particle diameters (Table 3). For each value of N and geometric standard deviation σ_g, 20 random chains were constructed. Each chain was projected at 100 random orientations to determine the average projected area, which was then normalized by the maximum possible projected area of the chain. As the width σ_g of the primary particle size distribution increases, the largest particles in the chain account for a larger fraction of the projected area, with the result that $\bar{A}$ increases. The computer program used for the simulation is given in Appendix A.

Table 3. Projections of straight chains comprised of N primary particles, which are distributed log-normally with geometric standard deviation σ_g and median diameter d_1. The normalized length $L = \frac{\text{length}}{Nd_1}$ and normalized maximum area $A_0 = \frac{4 \text{ maximum area}}{N\pi d_1^2}$ may be calculated from the properties of the log-normal distribution. The orientation-averaged projected area A is normalized by A_0 to give the area fraction $\bar{A}$.

	Theory		Simulation					
			N=100			N=500		
σ_g	L	A_0	L	A_0	$\bar{A}$ =A/A0	L	A_0	$\bar{A}$ =A/A_0
1.0	1	1	1	1.00±.01	0.86±.01	1	1.00±.01	0.85±.01
1.2	1.017	1.067	1.02±.01	1.07±.03	0.85±.02	1.02±.004	1.08±.02	0.85±.02
1.4	1.058	1.250	1.07±.02	1.30±.04	0.87±.01	1.06±.01	1.23±.03	0.88±.02
1.6	1.117	1.556	1.11±.03	1.54±.10	0.87±.02	1.12±.01	1.55±.06	0.90±.03
1.8	1.189	1.996	1.18±.03	1.99±.14	0.89±.02	1.20±.02	2.06±.08	0.87±.02
2.0	1.270	2.614	1.27±.05	2.55±.29	0.90±.02	1.26±.02	2.56±.12	0.90±.03

Projection of an Ideal Transparent Fractal

The geometry of projections is complicated by the shielding of primary particles in the cluster by other primaries. For very low D_f, it may be reasonable to neglect the shielding or to assume that it is the same for all primaries in the cluster. Shielding may also be neglected in particle characterizations with dark-field transmission electron microscopy where the mass of sufficiently small particles may be inferred from the scattered electron-beam intensity [1]. Analysis is considerably simplified in these situations in which all of the mass is visible in the projection.

Assume that the extreme surface of a fractal obeying Eqs. (1) and (2) is a sphere of radius R_f (Figure 2). This implies that the density n decreases with the distance r from the cluster centroid as

$$n(r) = \frac{N D_{f3}}{4\pi R_f^{D_{f3}}} \, r^{D_{f3}-3} . \tag{8}$$

The fractal dimension of a 3d cluster obeying Eq. (8) can be found from the mass m contained in measuring spheres of radius $r = yR_f$ centered on the cluster centroid,

$$m(y) = y^{D_{f3}} . \tag{9}$$

Fractal dimensions of 2d projections can be found in an analogous way, measuring the projected area $m'(y')$ enclosed by circles of radius y'. However, m' is not an exact power-law function of y'. Assuming that the fractal is transparent, Eq. (8) can be integrated to determine $m'(y')$,

$$m'(y') = 1.0 - \sin\theta_m + y'^{D_{f3}} \int_0^{\theta_m} \cos(x)^{1-D_{f3}} \, dx \tag{10}$$

$$y' = r'/R_f = \cos\theta_m$$

$$r' = r\cos\theta_m .$$

Figure 3 shows m and m' for spherically symmetric fractals of fractal dimensions 1.0 and 1.8. The fractal dimensions D_{f2} and D_{f3} are obtained from the slope of these curves. The 3d function m is a perfect power-law for all $y < 1$, but the 2d function m' is not a power-law, which implies that the projection is not fractal. For very small y, the slopes of the 2d and 3d functions are equal, suggesting that the correct fractal dimension would be obtained if only small length scales are considered. In practice the lower cutoff length, i.e., the primary particle diameter, determines the minimum values of y used in finding the fractal dimension. Moreover, if only small values of y are considered, only a small part of the cluster will be characterized by the measured fractal dimension. To be consistent with measurements made on real agglomerates, the fitting is done for y in the range $0<y<R_{g3}/R_f$. The points, which are spaced uniformly in y, are weighted according to

$m'(y)$. Using these procedures, an apparent fractal dimension of $D_{f2} = 1.41$ was obtained for $D_{f3} = 1.8$ (Figure 3).

Simulated Clusters

The model developed in the previous section has some important limitations. First, the clusters are assumed to be spherically symmetric, while typical aerosol agglomerates have aspect ratios of 1 to 3. Second, the model assumes that each of the constituent spheres has the same probability of being visible in the projection. Finally, real agglomerates are not exact fractals. More realistic results may be obtained by analyzing the structure of simulated clusters with shapes similar to real agglomerates. Such clusters were generated by "modified cluster-cluster aggregation" (MCCA). In order to calibrate the structural analysis of these MCCA clusters, several exact fractals were used.

Modified Cluster-Cluster Aggregation

The CCA algorithm [13] was modified so that the mass ratio β of the colliding clusters was constant for each simulation. Figure 4 illustrates the growth of clusters by this MCCA algorithm, for β=1 and β=0.5. A growing cluster of N_i primary particles (initially, N_i =1) is situated at the center of the control space. A cluster of mass N_a=max[1,βN_i] is then placed at a large distance from the growing cluster and allowed to move by Brownian motion (without rotation) until it either collides with the growing cluster (establishing a rigid bond) or travels far enough from the first cluster so that the process can be restarted. Single primaries are added until the number of primaries N_i exceeds β^{-1}, at which point clusters to be added are obtained from the coordinates of the growing cluster. If β=1, the added cluster is obtained by duplicating the growing cluster and giving it a random rotation. In real systems, colliding clusters are not correlated in this manner. Nevertheless, the MCCA procedure is scale-invariant for $N_i > \beta^{-1}$ so fractal agglomerates are expected. Figure 5 shows clusters generated by the MCCA algorithm for $\beta \sim 0$ and β=1.

The distinctly different appearances of the two clusters are reflected in the fractal dimensions, 2.2 for the first cluster and 1.98 for the second.

The algorithm was implemented using the BASIC program contained in Appendix A.

Exact Fractals

Clusters of known fractal dimension can be obtained by iterating a simple structure (Figure 1). One starts with a basic unit of P primary particles on a QxQxQ grid. Next, each of the primary particles is assumed to be composed of a miniature basic unit, reduced by a factor Q. Each of the primaries in the miniature basic unit may also be composed of still smaller basic units, and so on. The fractal dimension of such a structure is $D_{f3} = \log P/\log Q$, regardless of the exact arrangement of the basic unit [18]. Random rearrangements of the basic unit are used to obtain the random clusters used here and illustrated in Ref. [19].

ANALYSIS OF CLUSTER STRUCTURE

The simulated agglomerates were characterized by a variety of commonly measured parameters including the number of primaries, projected area, radius of gyration, aspect ratio, and fractal dimension.

In order to measure the projected area A, the cluster was projected onto the computer screen. The area fraction $\bar{A}$ was obtained as the number of object pixels normalized by the number of pixels in N non-overlapping primary spheres. For each cluster, $\bar{A}$ was determined by averaging over 4 randomly oriented projections.

Measurement of fractal dimension by the "successive-squares" algorithm [2] has become quite common. In that method, the projected area contained within a "measuring square" is determined as a function of the square size, and the fractal dimension is obtained using Eq. (9). We use a "modified successive-squares" procedure to determine D_{f3} and

D_{f2}, counting the number of primary particles (or pixels, for 2d images) within "measuring spheres" centered on the primary particle closest to the cluster centroid. Once the mass or area has been determined for each radius r, a power-law is fit to the function $m(r)$ for $1< r < R_g$, where R_{g2} or R_{g3} is used depending on whether the cluster or its projection is being considered.

A shortcoming of this methods is that the fine-scale information is based on a very small part of the object, i.e., the mass within a single, small measuring sphere. There is less statistical error in the fine-scale structural information obtained from the pair correlation function because it averages over all possible measuring sphere locations. For a body of N discrete particles, the pair correlation function $C(l)$ is

$$C(l) = \lim_{dl \to 0} \frac{1}{N} \frac{\sum_{i=1}^{N} \sum_{j=1}^{N} \theta(l < r_{ij} < l + dl)}{4 \pi l^2 \, dl} , \qquad (11)$$

where r_{ij} is the distance between particles i and j and $\theta = 1$ for $l < r_{ij} < l+dl$, zero otherwise. For computational efficiency, the summation is taken over N_{sample} random points within the cluster, creating a new cluster with N_{sample} point masses. The sample points may be arbitrarily close together so that the discrete correlation function will be statistically the same as the continuous function of Eq. (2) [8]. Once the correlation function is computed, the fractal dimension may be obtained from a power-law fit over some range of l, according to Eq. (2). For a 2d image of the cluster, N_{sample} points are generated by selecting points randomly from the image. Since the pixel spacing is generally much smaller than one primary particle diameter, the 2d function is essentially continuous for the range of length scales of interest. For each cluster, D_{f2} was taken as the median of the fractal dimensions of 4 randomly oriented projections.

A problem with the pair correlation approach is that points near the edge of the object give poor information on the long-range correlations [5,8,20]. The result is a

lowering of the measured fractal dimension. For this reason, Weitz and Huang [8] computed $C(l)$ only for points a distance l from the edge of the object. It is also possible to correct the correlation function after it is measured, as has been done in light scattering experiments [20]. Both methods require a model of the limiting surface of the cluster. The former approach is used here, assuming that the limiting surface is a sphere that completely contains the cluster and is centered on the primary particle closest to the centroid. The pair correlation function $C(r)$ and the modified successive-squares function, $m(r)$ are shown in Figure 6 for a straight chain, DLA cluster ($\beta = 0$, Figure 5) and an MCCA cluster ($\beta = 1.0$, Figure 5).

RESULTS

Exact Fractals

Figure 7 compares the true fractal dimension to the measured values for the exact fractals used here for calibration (Table 4). The clusters examined are self-similar over a very limited range of length scales, so some disagreement with the "true" values is expected. In general, the pair correlation results are in better agreement with the true values than are the modified successive-squares results. Both methods perform well on the large regular fractals (chains,vicsec cluster, 3d vicsec cluster, sierpinski gasket and 3d sierpinski gasket). The agreement of the expected and measured fractal dimensions depends largely on the range of length scales over which the fit is performed. The power-law regime for even the smallest chain (N=26) is broader than for the cube (N=1000), as indicated by the radius of gyration R_{g3} (Table 3).

Table 4. Results for fractal clusters of N primary particles, radius of gyration R_{g3} and aspect ratio α. For these shapes [a-i], the fractal dimension D_{ftrue} is known. The 2d projections of the clusters are described by the radius of gyration R_{g2}, the projected area fraction $\bar{A}$ and fractal dimensions D_f measured from the pair correlation function $C(r)$ and the modified successive-squares function $m(r)$.

					Aspect ratio α		D_f			
							Pair Corr.		Succ. Squ	
$D_{f\,true}$	N	R_{g3}	$\frac{R_{g2}}{R_{g3}}$	$\bar{A}$	3d	2d	3d	2d	3d	2d
3.0 [a]	1000	10	0.96	0.17	1.03	1.14	2.87	1.90	3.22	2.01
2.0 [b]	4096	45.3	0.83	0.48	1.04	1.05	2.06	1.79	1.95	1.99
2.0 [c]	16	3.6	0.81	0.78	1.22	1.11	1.86	1.72	2.00	2.20
2.0 [c]	256	14.7	0.83	0.56	1.20	1.20	1.84	1.67	2.13	1.99
2.0 [c]	4096	58.8	0.80	0.54	1.25	1.26	1.92	1.73	1.46	1.81
1.79 [d]	12	3	0.85	0.73	1.18	1.20	2.18	1.74	3.06	2.22
1.79 [d]	1728	47.9	0.85	0.66	1.24	1.26	1.88	1.75	1.87	1.68
1.79 [d]	144	12.4	0.87	0.71	1.41	1.50	1.88	1.56	2.73	1.84
1.79 [d]	12	3	0.87	0.76	1.17	1.22	2.36	1.59	2.83	1.90
1.79 [d]	143	12.1	0.81	0.59	1.20	1.29	1.88	1.60	2.17	1.85
1.77 [e]	343	17.7	0.86	0.58	1.03	1.05	2.01	1.69	1.75	1.67
1.77 [e]	49	5.9	0.85	0.66	1.02	1.06	2.15	1.82	1.68	1.74
1.58 [f]	729	42.7	0.81	0.76	1.43	2.10	1.58	1.59	1.57	1.70
1.49 [g]	125	17.1	0.76	0.69	1.44	3.55	1.55	1.41	1.51	1.59
1.0 [h]	181	35.4	0.88	0.83	1.02	1.07	1.36	1.25	1.28	1.20
1.0 [i]	26	15	0.85	0.88	24	22.2	0.95	0.94	1.06	1.03
1.0 [i]	51	29.4	0.90	0.93	47.8	48.5	0.96	0.94	0.94	1.08
1.0 [i]	100	57.7	0.71	0.82	89.7	76.8	0.97	0.96	1.00	1.04

[a] 1000 spheres arranged as a cube, [b] 3d Sierpinski gasket, [c] random cluster, [d] random cluster, [e] 3d Vicsec cluster, [f] 2d Sierpinski gasket, [g] 2d Vicsec cluster, [h] three mutually orthogonal chains intersecting at their midpoints, [i] straight chain.

Modified Cluster-Cluster Aggregation

Variation of Structure with Collision Mass Ratio

Table 5 summarizes the averages of structural measurements made on the MCCA clusters. Two clusters were analyzed for β=0, while 8-12 clusters were generated for each of the other values of β. As β increases from zero to 0.1, the fractal dimension decreases sharply, but for further increases in β, the fractal dimension decreases only slightly. The trend is less clear for fractal dimensions measured with the modified successive-squares method than for those measured with $C(r)$. Note that as β increases, the aspect ratio α increases, consistent with the appearances of the particles in Figure 5. The values of α for the projection are larger than for the 3d cluster because α was defined as the ratio of the principal radii of gyration. If α had been calculated from the maximum and minimum dimensions of the cluster, the 2d values would not be larger than the 3d values.

Table 5. Shape parameters for MCCA clusters generated using different mass ratios β for the colliding clusters. (See explanation for Table 4).

						Aspect ratio α		D_f Pair Corr.		D_f Succ. Squ	
β	N	R_{g3}	$\frac{R_{g2}}{R_{g3}}$	r_1	$\bar{A}$	3d	2d	3d	2d	3d	2d
0	763	20	0.91	1.17	0.53	1.31	1.36	2.31	1.81	2.46	1.85
0.1	417	21	0.85	0.89	0.63	1.62	1.94	1.85	1.61	2.09	1.78
0.2	196	14	0.85	0.92	0.70	1.81	2.11	1.86	1.57	1.99	1.75
0.3	222	14	0.85	0.86	0.70	1.92	2.15	1.76	1.52	1.96	1.78
0.5	182	14	0.86	0.82	0.71	1.92	2.16	1.70	1.47	2.05	1.69
1.0	174	14	0.82	0.76	0.71	2.16	2.30	1.60	1.41	1.93	1.77

The packing density of the clusters can be characterized by an effective primary radius r_1 based on Eq. (3),

$$r_1 = \frac{R_{g3}}{N^{1/D_f}} \quad . \tag{12}$$

Table 4 shows that r_1 decreases from 1.2 for $\beta = 0$ to 0.76 for $\beta = 1.0$. The average value for all β is 0.85, while it was found in previous simulations [9,21] that $r_1 = 0.76$ for $D_f = 1.69$ and $r_1 = 0.84$ for $D_f = 1.91$. If Eq. (3) were to hold as N approaches 1, then r_1 would be the radius of gyration of a primary particle; i.e., $r_1 = 0.77$.

Relation between 3d and 2d Measurements

Figure 8 compares the pair correlation fractal dimension of clusters (D_{f3}) and their projections (D_{f2}). As expected, the difference between D_{f2} and D_{f3} increases as the fractal dimension increases and the cluster size decreases. There is no clear difference between the results for the exact fractals and the MCCA clusters. For the large ($N > 900$) CCA clusters of Samson et al. [11], the difference between D_{f2} and D_{f3} is slightly less than for the clusters generated in this study. The data are generally consistent with the correlation between D_{f3} and D_{f2} that was obtained by Pao et al [22] for random exact clusters of the type discussed above. The transparent fractal model appears to be a lower bound on D_{f2} while the ideal fractal relations of Table 1 yield an upper bound. Using the modified successive-squares algorithm to obtain the fractal dimension, the bias from the projection was slightly reduced but the scatter was considerably increased.

The projected area fraction $\bar{A}$ is shown in Figure 9 as a function of cluster size N. If $D_{f3} < 2$, one expects $\bar{A}$ to reach a constant value for large N. The simulated results for the chains have considerable statistical error, but are consistent with theory (Table 2). For a compact spherical cluster, the area fraction $\bar{A}$ decreases continually with N at nearly the same rate as for a cube. For DLA clusters $\bar{A}$ is expected to decrease as $N^{1-1/D_f} = N^{-0.15}$, consistent with the results of Medallia [14]. The "maximum-chain" clusters [13] have lower fractal dimensions and higher values of $\bar{A}$. The data for the MCCA clusters agree well with CCA ($D_f = 1.8$) clusters [12], though there is considerable scatter in the results. Reaction-limited cluster aggregates (RCLA, $D_f \approx 2.09$) have a lower $\bar{A}$ [12], consistent with measurements by Adachi and Ooi [23] for colloidal agglomerates. The scatter in those

measurements was comparable to that observed in our simulations. The magnitude of the scatter becomes important when attempting to distinguish experimentally between DLA, CCA or RCLA type growth mechanisms.

CONCLUSIONS

Agglomerates with different morphologies were generated using a variety of algorithms. In particular, clusters were generated using a modified cluster-cluster aggregation method in which the ratio β of the masses of colliding clusters was constant. DLA clusters were obtained for β=0 while more elongated clusters with lower fractal dimensions were obtained for β=1. Intermediate values of β produced clusters with intermediate shapes, although the determination of the exact dependence on β will require simulations with larger clusters.

Comparing the morphology of 3d clusters with the shape parameters measured from 2d projections, it is possible to evaluate the usefulness of 2d projections in characterizing particle structure. The use of clusters with different morphologies gives an indication of which results can be generalized to arbitrary clusters and which parameters are strongly sensitive to the shape or measurement technique.

Fractal dimensions appear to be best estimated using the pair correlation function. The modified successive-squares algorithm gave good results for exact fractals, but appeared to overestimate the fractal dimension for smaller clusters. Both methods are sensitive to the range of lengths over which power-law behavior is assumed to apply. Fractal dimensions consistent with previous studies are obtained assuming that the upper and lower cutoff lengths are equal to the primary particle diameter and the radius of gyration respectively. For a typical agglomerate with fractal dimensions near 2.0, containing a few hundred primary particles, the fractal dimension of the projection may be 10-20% lower than the true fractal dimension. This error seems to be similar for clusters generated in a variety of ways, although it decreases as the cluster size increases.

The fraction of exposed area $\bar{A}$ is found to be a strong function of size and a weak function of fractal dimension for clusters with less than 1000 primary particles. This suggests that use of fractal relations between area and mass to determine the fractal dimension of small clusterswould be subject to error.

Acknowledgements: This work was supported by the International Fine Particle Research Institute and by the U.S. Department of Energy under grant No. DE-FG22-90PC90286.

NOTATION

$\bar{A}$	projected area fraction
A	projected area
$C(l)$	pair correlation function.
D_f	fractal dimension
D_{f3}	fractal dimension of a 3d cluster
D_{f2}	fractal dimension of a 2d projection of a cluster
D_α	fractal dimension describing mass distribution in a single cluster
D_β	fractal dimension describing mass-size scaling of many clusters
l	length scale of a measuring surface
θ_m	see Figure 2.
n	primary particle number density within a cluster
N	number of primary particles in a cluster
N_{sample}	number of sample points from which the pair correlation function is obtained
$m(r)$	mass within a sphere of radius r, normalized by cluster mass.
$M(R_g)$	mass of a cluster with radius R_g
P,Q	number P of basic units on a QxQxQ grid
r_1	effective radius of gyration of the primary particles.
R_g	radius of gyration
R_f	outer radius of a cluster
R_{g3}	radius of gyration of a 3d cluster
R_{g2}	radius of gyration of a projection
y	r / R_f .
α	aspect ratio
β	mass ratio of colliding clusters in the MCCA algorithm

REFERENCES

[1] *M. Tence, J.P. Chevalier, and R. Jullien:* On the measurement of the fractal dimension of aggregate particles by electron microscopy: experimental method, corrections and comparison with numerical models. J. Physique. *47* (1986) 1989-1998.

[2] *S.R. Forrest and T.A. Witten:* Long-range correlations in smoke-particle aggregates. J. Phys. A. Math. Gen. *12* (1979) L109.

[3] *B. Mandelbrot:* The Fractal Geometry of Nature.W.H. Freeman , New York 1983, pp. 91-92.

[4] *B.H. Kaye, G.G. Clark, J.E. Leblanc and R.A. Trottier:* Image Analysis Procedures for Characterizing the Fractal Dimension of Fineparticles. Part. Charact. *4* (1987) 63-66.

[5] *P. Meakin.:* Fractal Structures. Prog. Solid State Chem. *20* (1990) 35-233.

[6] *B.M. Smirnov*: The Properties of Fractal Clusters. Phys. Rep. *188* (1990) 1-78.

[7] *T. Cleary, R. Samson, and J.W. Gentry*: Methodology for Fractal Analysis of Combustion Aerosols and Particle Clusters. Aerosol Sci. Technol. *12* (1990) 518-525.

[8] *D. Weitz and J.S. Huang:* Self-Similar Structures and the Kinetics of Aggregation of Gold Colloids, in *F. Family, D.P. Landau* (eds.): *Kinetics of Aggregation and Gelation.* Elsevier-North Holland, Amsterdam 1984, pp. 19-28.

[9] *R.D. Mountain, G.W. Mulholland and H. Baum:* Simulation of Aerosol Agglomeration in the Free Molecular and Continuum Flow Regimes. J. Colloid Interface Sci. *114* (1986) 67-81.

[10] *A. Schmidt-Ott, U. Baltensperger, H.W. Gäggeler, and D.T. Jost:* Scaling Behavior of Physical Parameters Describing Agglomerates. J. Aerosol Sci.(1990) in press.

[11] *R.J. Samson, G.W. Mulholland, and J.W. Gentry:* Structural Analysis of Soot Agglomerates. Langmuir *3* (1987) 272-281.

[12] *P. Meakin, B. Donn, and G.W. Mulholland:* Collisions between Point Masses and Fractal Aggregates. Langmuir *5* (1989) 510-518.

[13] *D.N. Sutherland and I. Goodarz-Nia:* Floc simulation: the effect of collision sequence. Chem. Eng. Sci. *26* (1971) 2071-2085.

[14] *A. Medallia:* Morphology of Aggregates. J. Colloid Interface Sci. *24* (1967) 393-404.

[15] *R. Richter, L.M. Sander, and Z. Cheng:* Computer Simulations of Soot Aggregation. J. Colloid Interface. Sci. *100* (1984) 203-209.

[16] *M. Kolb and R. Jullien:* Chemically limited versus diffusion limited aggregation. J. Phys. *A17* (1984) L637.

[17] *R.H. Gray, G.M. Kanapilly, Y.S. Cheng, and R.K. Wolff*: Image Enhancement of Aggregate Aerosols by Stereopsis. J. Aerosol Sci. *16* (1985) 211-216.

[18] *Gentry, J.W, Mulholland, G.W., and Sullivan, F.*: The Use of Numerically Simulated Clusters to Evaluate Algorithms for Fractal Dimensionality, in *P.Wagner* (ed.): *Atmospheric Aerosols and Nucleation.* Springer-Verlag, Berlin 1988, pp. 116-119

[19] *S.N. Rogak and R.C. Flagan:* Stokes Drag on Self-Similar Clusters of Spheres. J. Colloid Interface Sci. *134* (1990) 206-218.

[20] *A.J. Hurd and W.L. Flower:* In Situ Growth and Structure of Fractal Silica Aggregates in a Flame. J. Colloid Interface Sci. *122* (1988) 178-192.

[21] *Mulholland, G.W., Samson, R.J, Mountain, R.D. and Ernst, M.H:* Cluster Size Distribution for Free Molecular Agglomeration. Energy and Fuels *2* (1988) 481-486.

[22] *J-R Pao, Y-C Chang and J.W. Gentry:* The Use of Simulated Fractals to Determine the Relation Between a Cluster and its Projection. J. Aerosol Sci. *21* (1990) s63-s66.

[23] *Y. Adachi and S. Ooi:* Geometrical Structure of a Floc. J. Colloid Interface Sci. *135* (1990) 374-384.

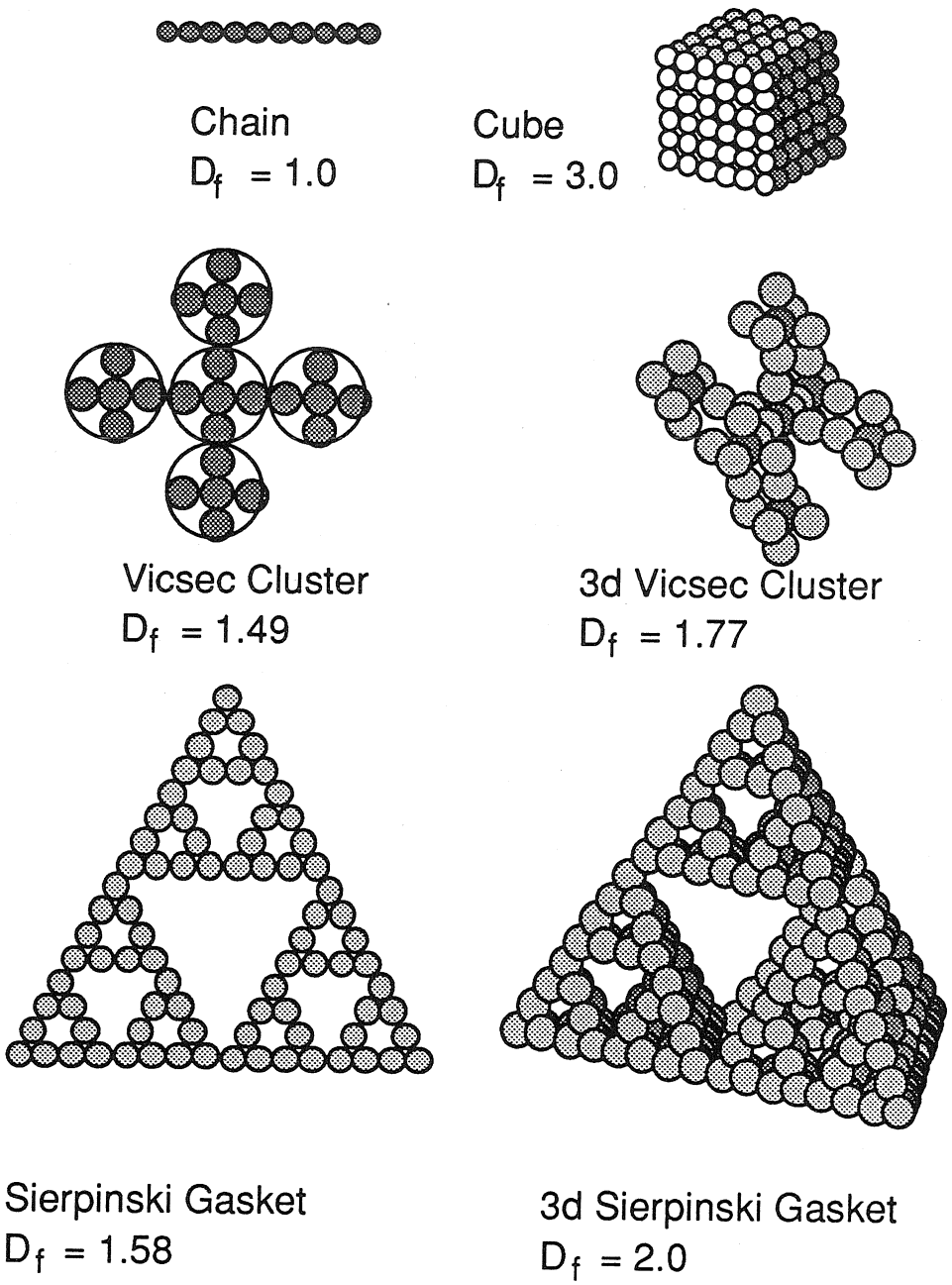

Figure 1. Clusters of spheres having exact self-similarity and known fractal dimension D_f.

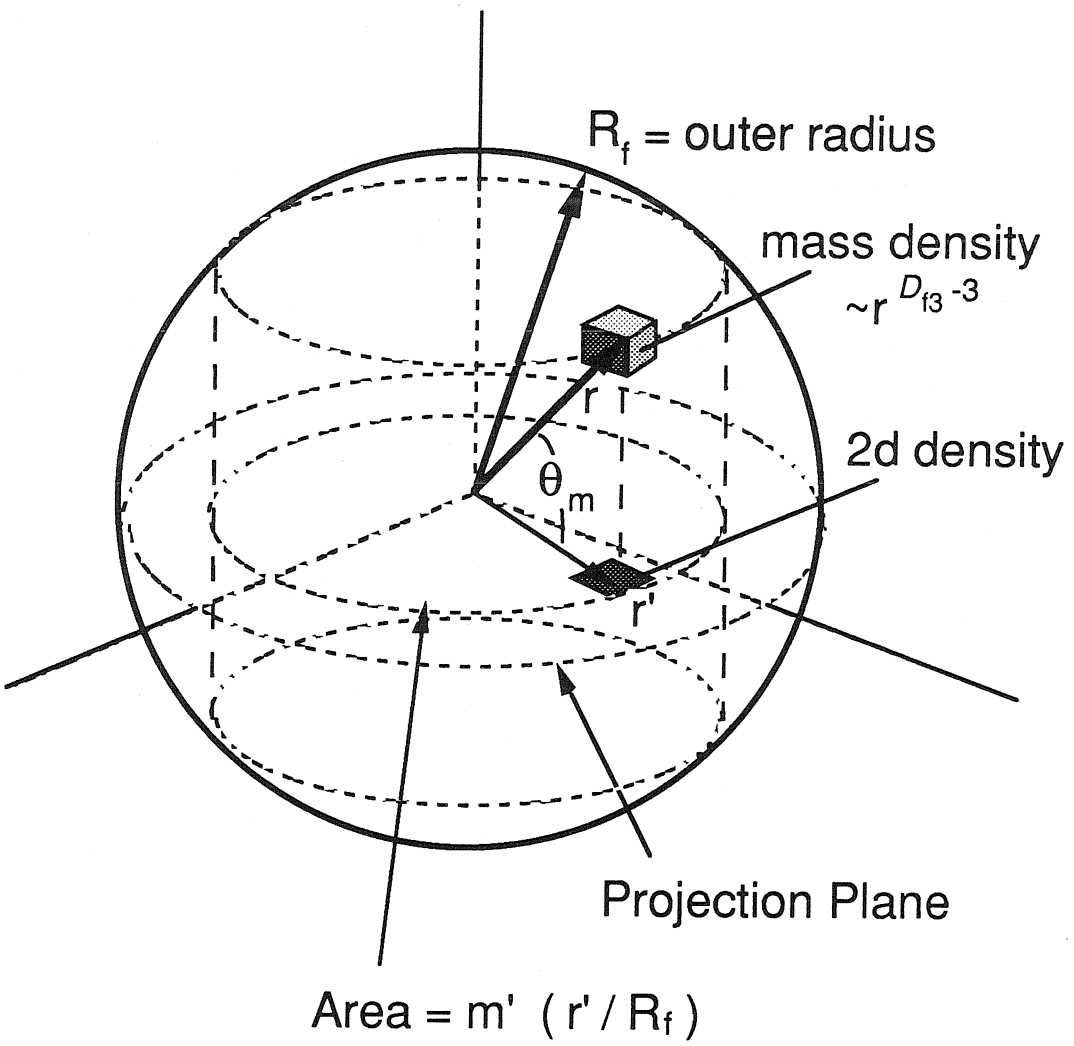

Figure 2. The projection of a transparent fractal with a spherical limiting or "cuttoff" surface onto a plane. The density of the 2d image is obtained by vertical integration of the mass density.

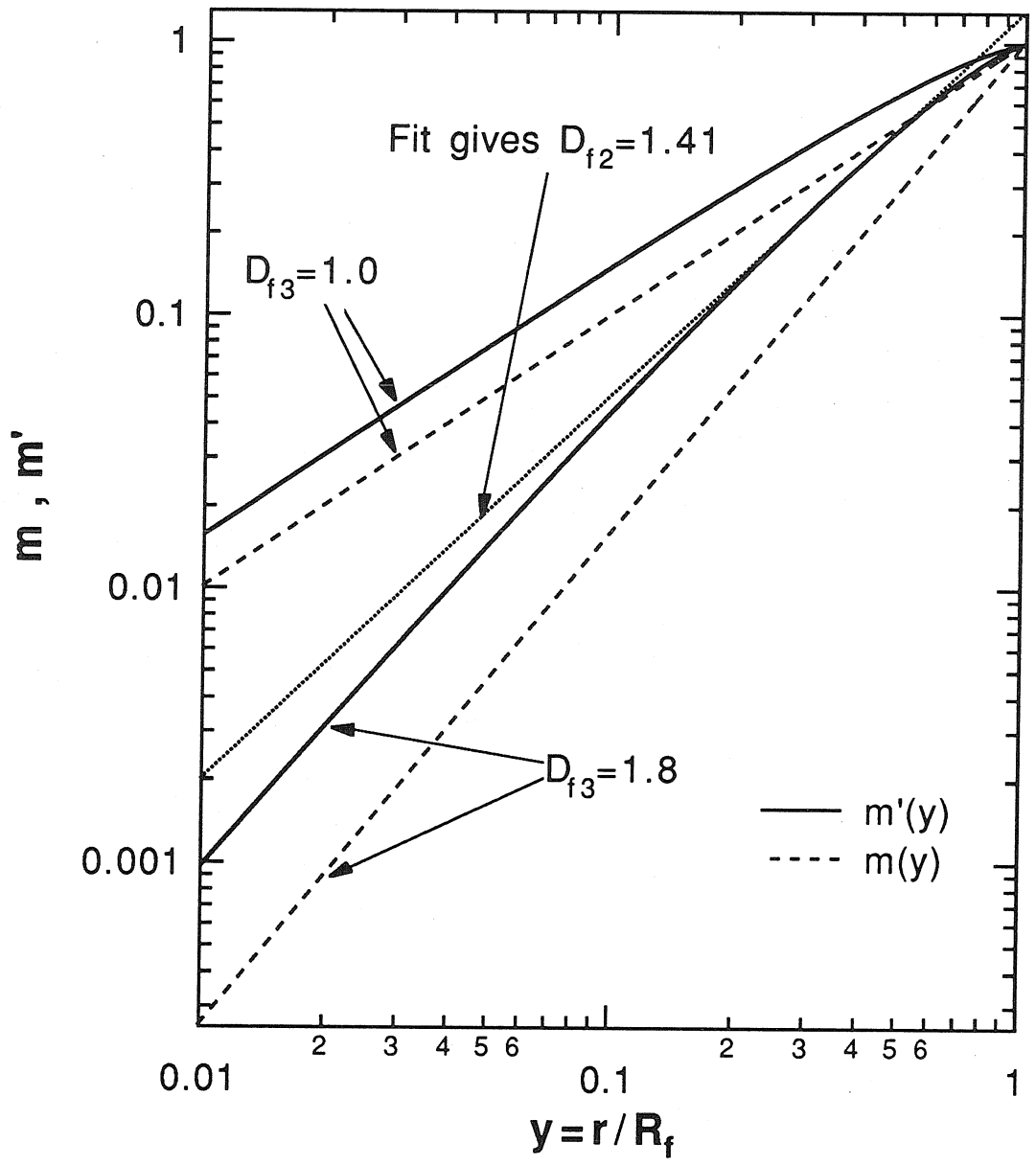

Figure 3. Mass *m(y)* contained in a measuring sphere of radius yR_f compared to the area *m'(y)* contained in a measuring circle of the same radius. These functions were obtained for the transparent fractal of Figure 2. The fractal dimension obtained from the 2d function is less than the true fractal dimension.

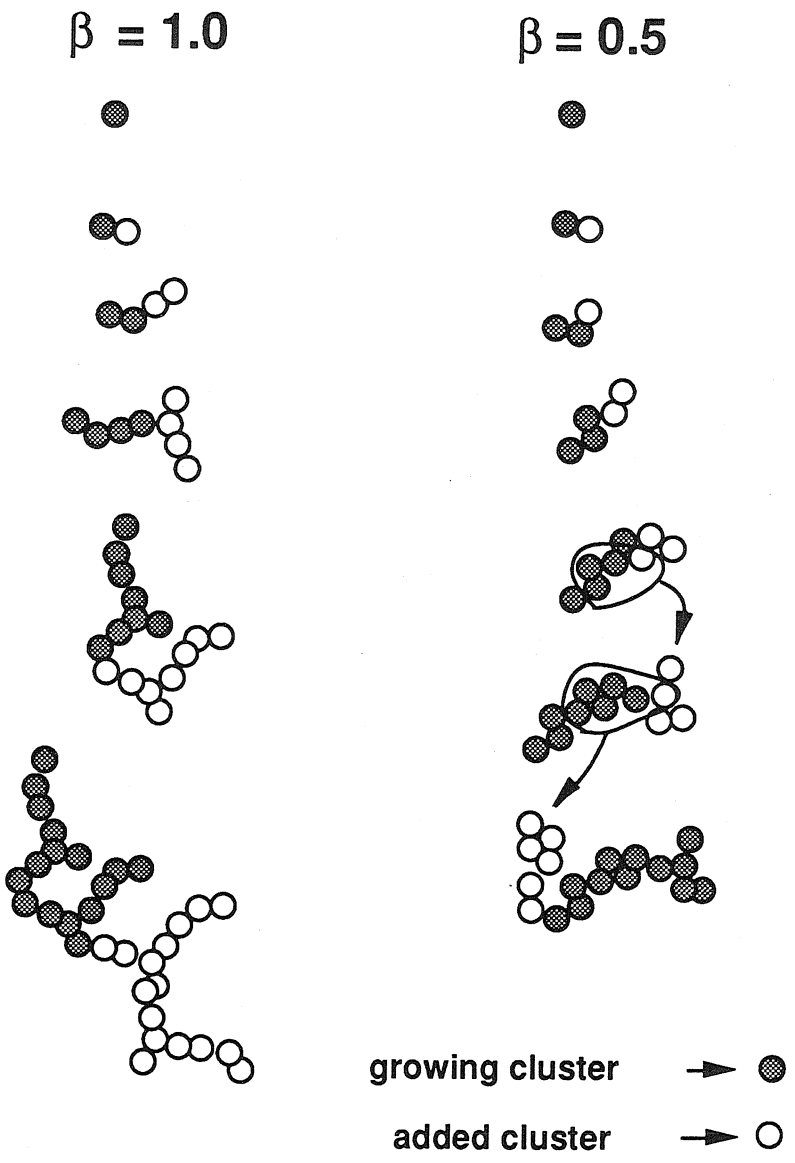

Figure 4. In the modified cluster-cluster aggregation (MCCA) algorithm, a cluster grows from a single primary particle by the addition of clusters of size $\max[1,\beta N_i]$ where N_i is the size of the growing cluster at stage i. The added clusters are obtained from part of the growing cluster.

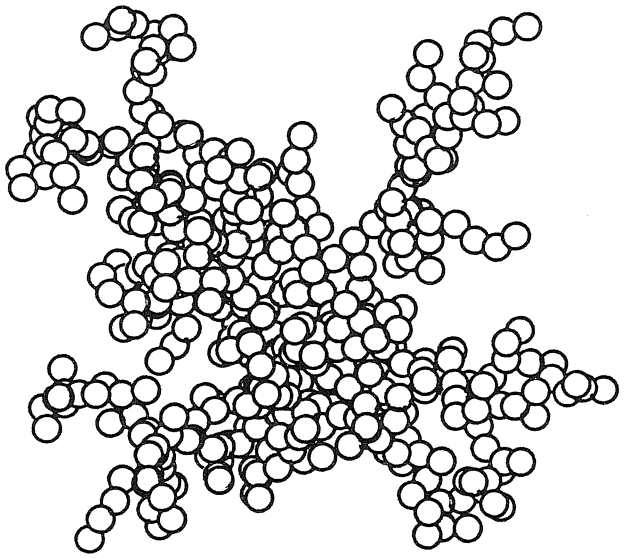

β=0

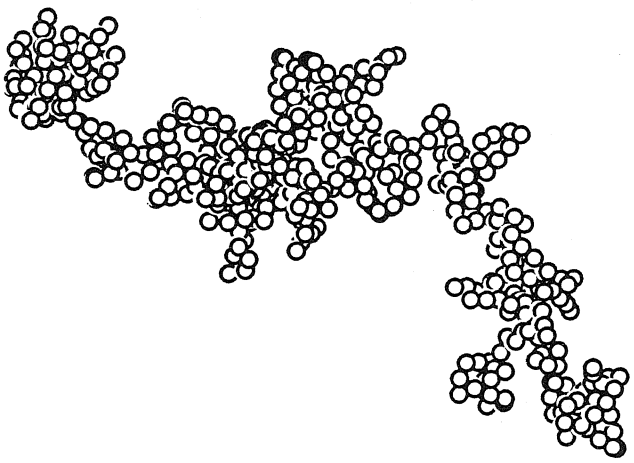

β=1

Figure 5. Agglomerates produced by Modified Cluster-Cluster Aggregation with $\beta = 0$, $N = 501$, $D_{f3} = 2.2$ (DLA) and $\beta = 1$, $N = 512$, $D_{f3} = 1.98$

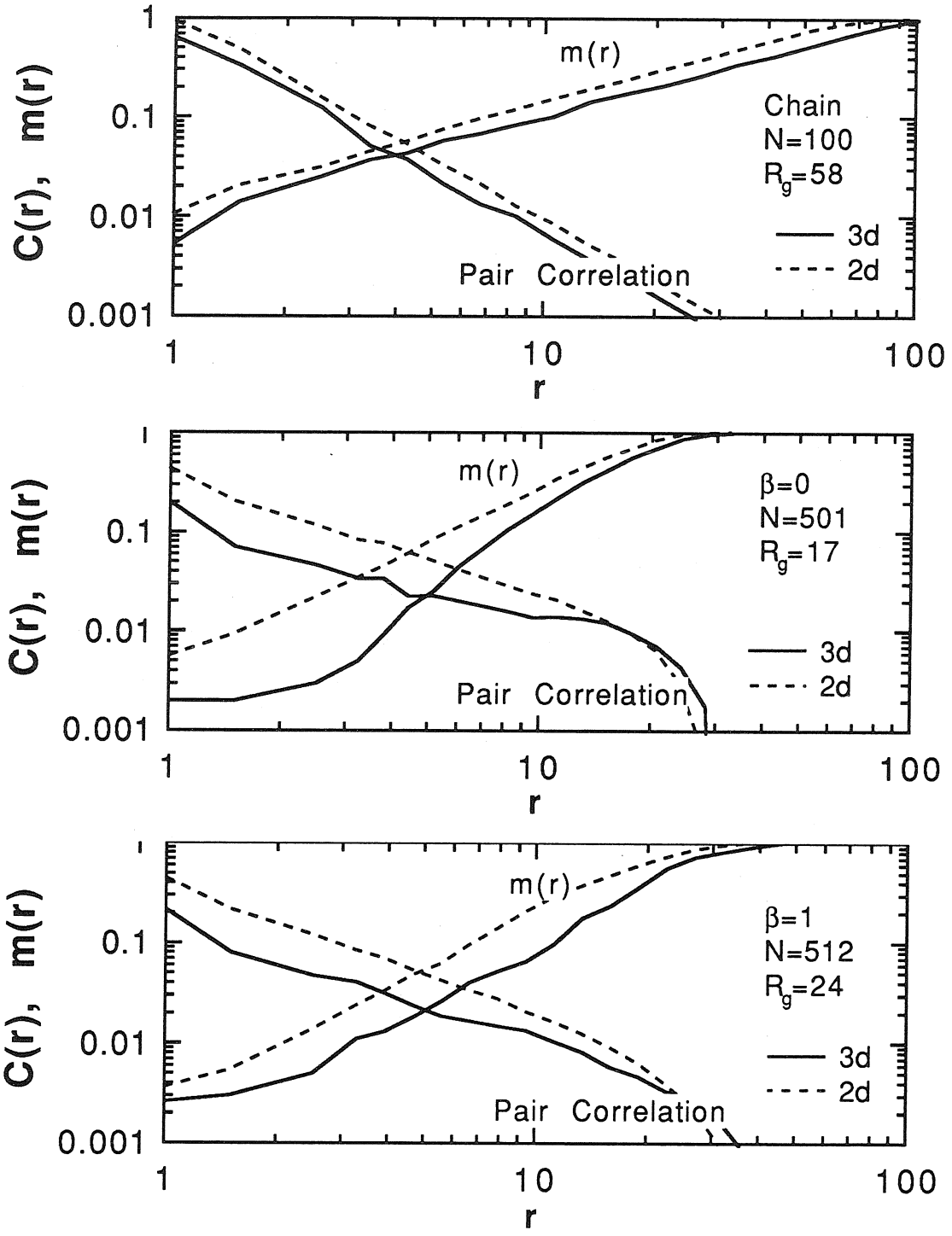

Figure 6. Pair correlation function $C(r)$ and modified successive-squares function $m(r)$ for a) a straight chain b) a DLA cluster and c) MCCA cluster, $\beta = 1.0$. The primary particle radius is 1.

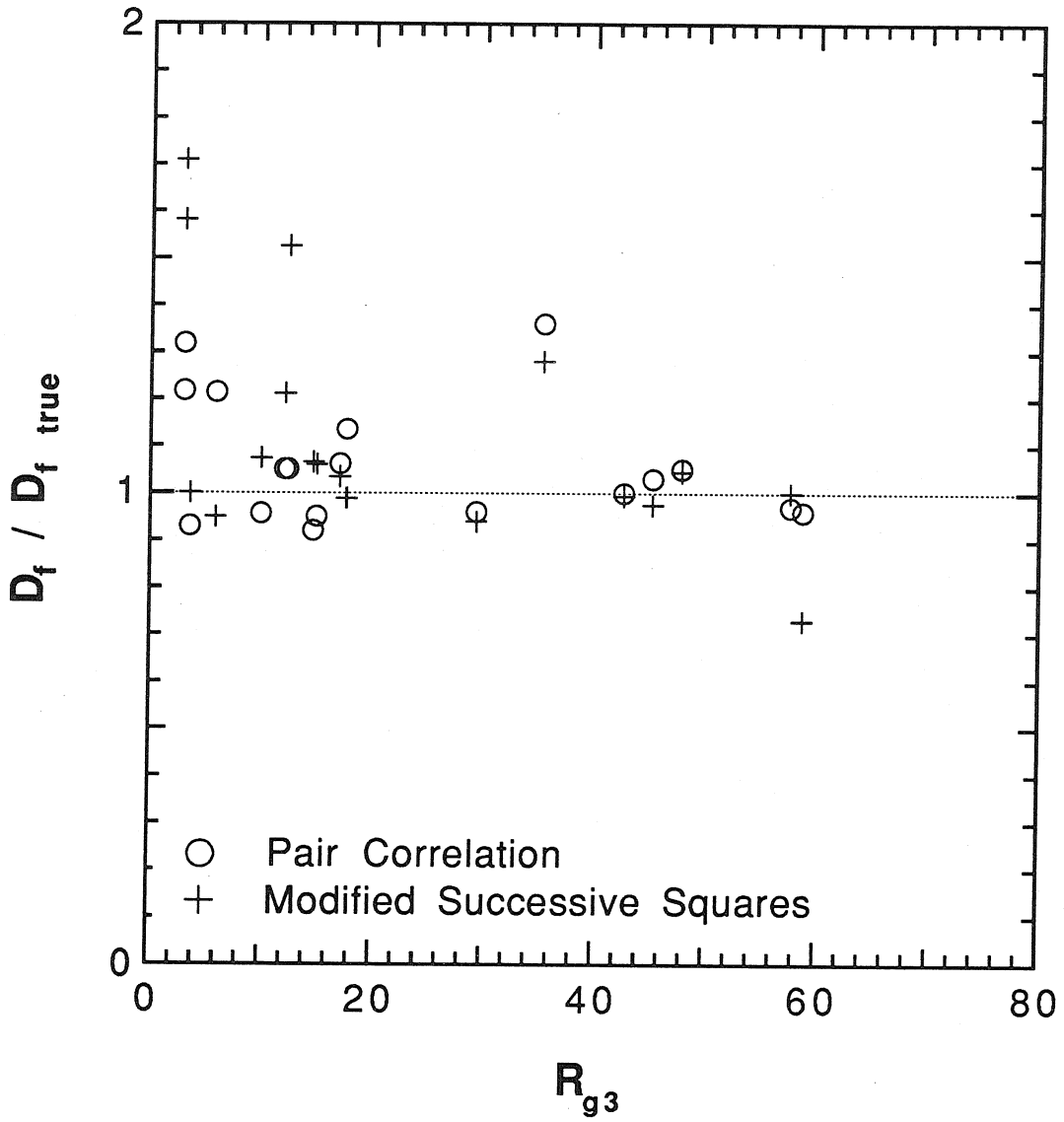

Figure 7. Performance of the pair correlation and modified successive-squares algorithms for determination of fractal dimension. As the radius of gyration R_{g3} increases, the measured fractal dimension D_f approaches the true value D_{ftrue}.

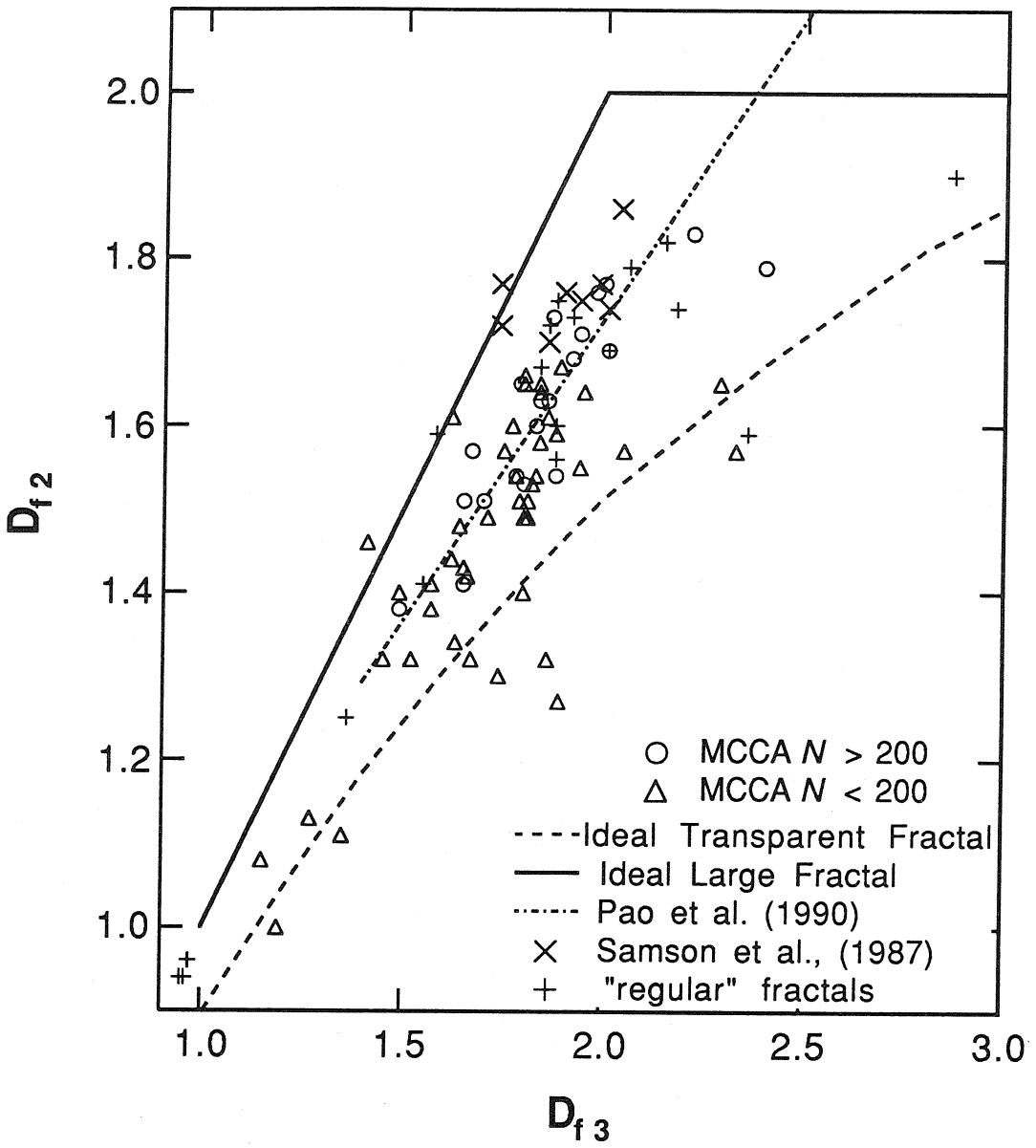

Figure 8. Fractal dimensions of clusters (D_{f3}) and their projections (D_{f2}), measured from the pair correlation function. Results for the MCCA clusters are divided into two categories based on the number of primary particles N in the cluster. The regular or exact fractals are described in Table 3 and Figure 1. CCA clusters analyzed by Samson et al. [11] contained ~1000 primaries while the correlation of Pao et al. [22] was obtained for exact fractals with 30-3000 primary particles.

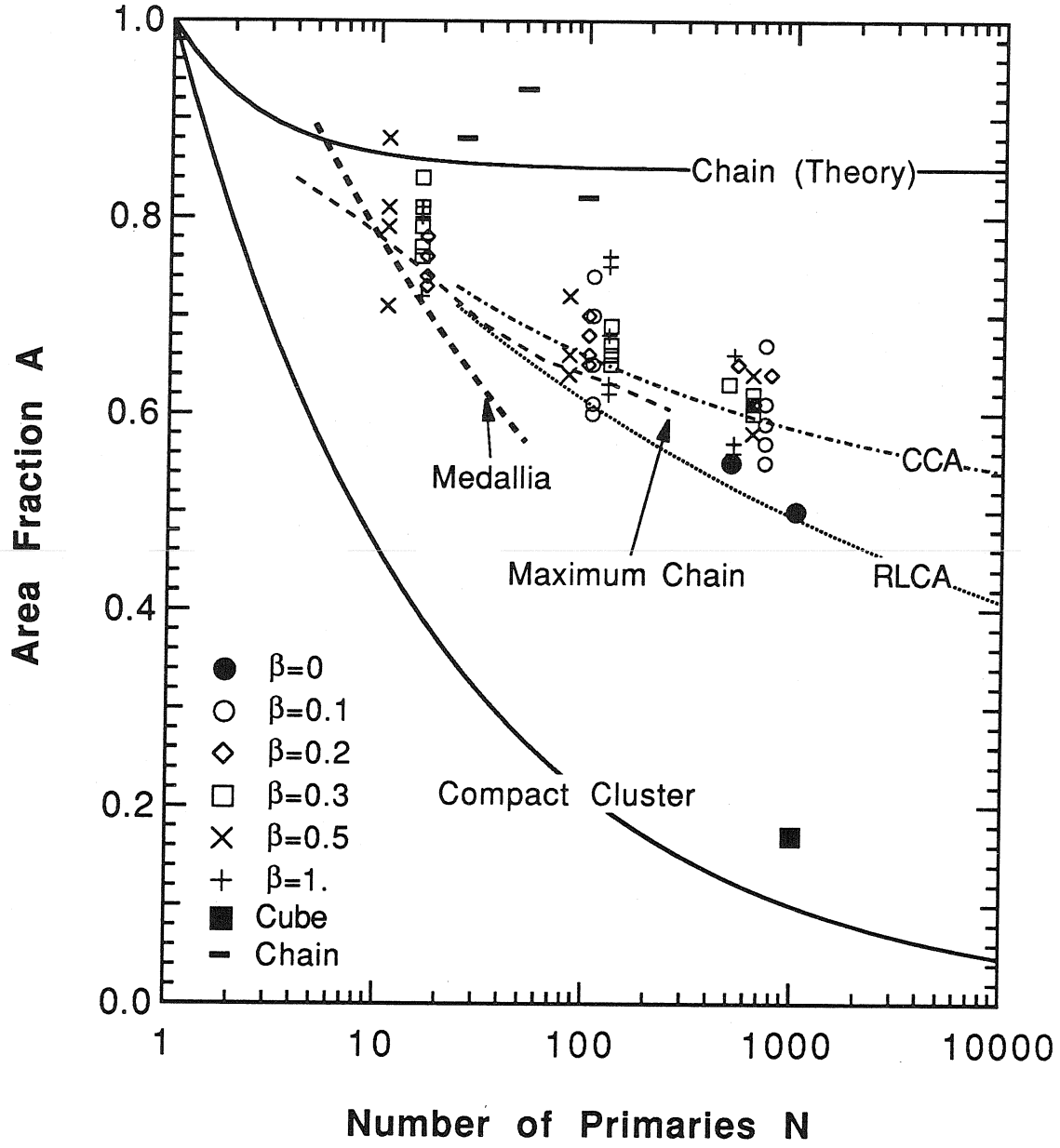

Figure 9. Projected area fraction $\bar{A} = \frac{A}{\pi N}$ as a function of the number of primary spheres N. The primary sphere has unit radius.

CHAPTER 4

Stokes Drag on Self-Similar Clusters of Spheres

STEVEN N. ROGAK AND RICHARD C. FLAGAN[1]

W. M. Keck Laboratory 138-78, California Institute of Technology, Pasadena, California 91125

Received January 13, 1989; accepted March 20, 1989

Aggregation phenomena in gas and liquid phases often produce agglomerates that appear to be fractals in the sense that the cluster mass varies with the radius of gyration to a fractional power. The creeping (Stokes) flow around the cluster may be represented by the superposition of k single-sphere velocity fields chosen to satisfy the boundary conditions at k points on the cluster. Computations can be performed for large self-similar clusters of k^n monomers by decomposing the cluster n times into smaller clusters which may be replaced by hydrodynamically equivalent spheres. The method recovers the correct results for chains, disks, and compact clusters. Computations done on random, connected clusters similar to real aggregates show that both the primary particle diameter and the cluster radius influence the drag. The influence of the primary particle size and other small-scale structure features is lost very rapidly as the fractal dimension increases above 1.3 and the number of monomers in the cluster increases above 100.

1.0 INTRODUCTION

Particles produced in gas or liquid sometimes form as aggregates of approximately equal sized, solid primary particles. Forest and Witten (1) noticed that aerosols formed in their exploding wire experiments show self-similar "fractal" structures. Since then Schmidt-Ott (2), Samson (3), and others have observed fractal agglomerates. By "fractal" we mean that the cluster mass m varies with the radius as $m\alpha R^D$. Here D is the fractal dimension and R is a characteristic cluster radius.

Computer models by Meakin (4), Mountain *et al.* (5), and others have been at least qualitatively successful in describing the formation of fractal agglomerates. These studies have shown that the fractal dimension depends on the conditions of particle formation and that D may range from less than 1.7 to 3.0.

The drag is an important characteristic of these aggregates. One must have a quantitative understanding of the drag if many of the traditional particle classifying techniques are to be applied to irregular clusters as they have been applied in the past to spherical particles. The problem of drag on nonspherical bodies has received considerable attention starting with the introduction of the "dynamic shape factor" by Fuchs (6). Work since then is discussed by Leith (7), Mountain (5), Dahneke (8, 9), Davies (10), and Schmidt-Ott (2). Meakin, *et al.* (11, 12) have computed the drag on simulated agglomerates of up to 400 spheres. Wiltzius (13) has measured the drag on high-fractal dimension colloidal aggregates. In the present work we propose a method for directly using self-similarity to aid numerical computations of drag on particles in continuum flow. This allows us to estimate the drag on clusters over a wide range of sizes and fractal dimensions. For aerosol systems, cluster radii may be comparable to the gas-mean free path. The continuum Stokes flow problem is, therefore, a limiting case for aerosols but is of direct importance to liquid phase systems.

See appendix for nomenclature.

2.0 COMPUTATION OF DRAG

Computation of the drag requires an unambiguous description of the cluster geometry.

[1] To whom all correspondence should be addressed.

0021-9797/90 $3.00

We use the radius of gyration of the cluster R_g to define an outer radius R_f and restate the scaling relation as follows.

$$R_f = \sqrt{(D+2)/D}\,R_g \qquad [1]$$

$$R_f = \frac{a}{\alpha^{1/D}}(R_v/a)^{3/D}, \qquad [2]$$

where α is a packing factor defined by [2] and R_v is the volume equivalent sphere radius (i.e., $N = (R_v/a)^3$) for the cluster of N primary particles. One obtains reasonable results for chains, disks, and spheres for $\alpha = 1$. For a chain ($D = 1$), R_f is half the chain length. For a planar arrangement of primary particles ($D = 2$), R_f is the radius of the disk with the same projected area. For $D = 3$, R_f is the radius of the volume equivalent sphere. Figure 1 shows the approximate relations of these radii as measured from the cluster centroid.

The equations of motion and incompressibility relating pressure P and velocity $\mathbf{V}$ for a Newtonian fluid at Reynolds numbers less than 1 are

$$\nabla^2\mathbf{V} = 1/\mu \text{ grad } P \qquad [3]$$

$$\nabla\cdot\mathbf{V} = 0. \qquad [4]$$

The boundary conditions for a cluster moving with velocity $\mathbf{U}$ in a quiescent fluid are that $\mathbf{V} = \mathbf{U}$ on the body and $\mathbf{V} = 0$ at large distances. The translation of a sphere of radius a (see Fig. 1) is the prototype problem in particle fluid mechanics. Stokes (14) found that

$$V_r = -\tfrac{1}{2}U\cos\theta(a/r)^2[a/r - 3r/a] \qquad [5]$$

$$V_\theta = -\tfrac{1}{4}U\sin\theta(a/r)[a/r)^2 + 3]. \qquad [6]$$

Substitution of these results into the equations of motion and integration of the shear stresses and pressure yields Stokes drag law;

$$F_{\text{total}} = 6\pi\mu Ua. \qquad [7]$$

Spheres on which the same force acts, produce the same far field velocities (14);

$$V_{r\infty} = \frac{F\cos\theta}{4\pi\mu r} \qquad [8]$$

$$V_{\theta\infty} = -\frac{F\cos\theta}{8\pi\mu r}. \qquad [9]$$

These equations must hold for bodies of arbitrary shape so we may replace an irregular cluster by a sphere of radius $R_H = F/(6\pi\mu U)$ and maintain the correct far field velocity. This fact is the basis for the numerical method used in this study.

Before discussing the numerical method we present a few simple models that qualitatively illustrate the relation between fractal dimension and drag. It is useful to present the results as a factor;

$$\beta = \frac{R_g}{R_H} = \frac{R_f}{R_H}\sqrt{\frac{D}{D+2}}. \qquad [10]$$

For clusters of spheres it is reasonable to expect β to be a function of a and N though one expects that for very large clusters the dependence on a decreases. For example, consider the case of a long straight chain where $D = 1$. Batchelor's slender body theory (15) gives, for motion parallel and perpendicular to the chain.

$$\beta_{||} = \sqrt{\frac{3}{4}}\left(\frac{\epsilon + .307\epsilon^2}{1 - \epsilon/2} + .426\epsilon^3\right)^{-1} \qquad [11]$$

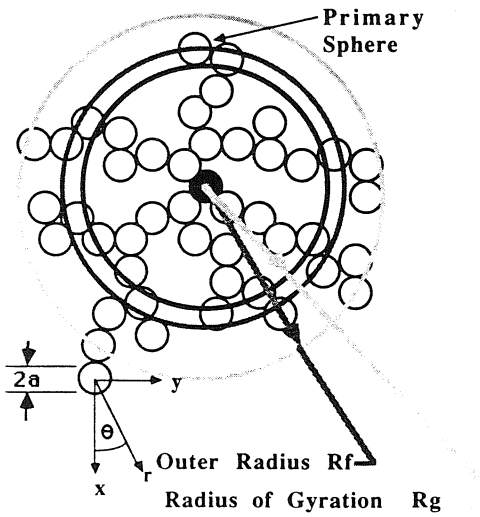

FIG. 1. Schematic of an agglomerate.

$$\beta_\perp = \sqrt{\frac{3}{16}\left(\frac{\epsilon + .307\epsilon^2}{1 + \epsilon/2} + .119\epsilon^3\right)^{-1}}, \quad [12]$$

where $\epsilon = 1/\ln 2N$. For large N, $\beta \cong \ln 2N$. This method agrees with data by Kasper (16) to within 10% with N as low as 10.

For large D we consider Mountain's (5) treatment of the cluster as a porous medium. Mountain divides the flow into three regions:

1) Flow inside the cluster satisfying Darcy's Law $\nabla P + \mu/\kappa \mathbf{V} = 0$, where κ is the hydraulic permeability.

2) External flow near the cluster where Stokes equations are valid.

3) Far field flow where the fluid inertia is considered.

Mountain matches region (2) to region (3), then calculates the force on the body by integrating the shear stress, pressure, and momentum flux over a control surface encompassing the entire cluster. Matching the radial velocity and pressure at the surface of the cluster to satisfy the internal flow, the drag is found to be

$$F = \frac{6\pi\mu RU}{1 + 3/2\ \kappa/R^2}. \quad [13]$$

Mountain used $R = R_g$ and assumed that κ/R^2 is small for large clusters. The use of R_g is incorrect for dense spheres where the drag will be underestimated by a factor $\sqrt{\frac{3}{5}}$. The assumption that κ/R^2 is small depends on the particular permeability model used. For the model discussed below, the assumption is not valid.

To be consistent with the preceding analysis, one should use the outer radius of the cluster and develop a porosity model. A simple and illustrative approach is to use the Carman–Kozeny model (17) for packed spheres.

$$\kappa = \sigma r_h^2/5.0, \quad [14]$$

where σ is the void fraction, r_h is the hydraulic radius ($=\sigma/S$), S is the surface area per unit volume, and the empirically derived factor 5.0 is strictly valid only for densely packed spheres. Applied to a cluster of N spheres of radius a with $N = \alpha(R/a)^D$,

$$\sigma = 1 - (a/R)^3 N$$

$$S = 3Na^2/R^3$$

$$r_h = \frac{1}{3}\left(\frac{R^{3-D}a^{D-2}}{\alpha} - a\right). \quad [15]$$

For $D = 3$, $r_h = \frac{1}{3}[1/\alpha - 1]$ which means that the hydraulic radius is independent of cluster size and depends only on a. For $D < 3$, r_h increases with the cluster size, which is consistent with the fractal geometry. It should be noted that this model assumes that the porosity is homogeneous throughout the cluster. For a fractal object, pores of all sizes should exist and the surface area/volume is theoretically infinite. The choice of the characteristic particle size a is important. Temporarily ignoring these objections, one can continue to find that

$$\kappa/R^2 = [1 - (a/R)^{3-D}] \times \left(\frac{(R/a)^{6-2D}}{\alpha^2} - \frac{2(R/a)^{3-D}}{\alpha} + 1\right) \times ((a/R)^2/45). \quad [16]$$

For $D < 2$, κ/R^2 goes to infinity as R increases, implying that the drag goes to 0. This happens because the characteristic pore size becomes as large as the cluster, hence Darcy's Law is no longer a reasonable model. For $D > 2$ the situation is quite different: although the pore size increases with R, κ/R^2 decreases and Darcy's Law remains a feasible model. The limitations of the slender body theory and the porous medium models motivate the use of a more general numerical method.

2.1 *Numerical Method*

We use a variation of the method of reflections of Happel and Brenner (17). The velocity field $\mathbf{V}$ is represented by the superposition of k spheres of radius a_i, each moving with virtual velocity $\mathbf{U}_i$ ($\neq \mathbf{U}$, the cluster velocity). We choose the $\mathbf{U}_i$ so that $\mathbf{V} = \mathbf{U}$ at k points on the body (the centers of the k spheres). The force on the cluster is

$$\mathbf{F} = 6\pi\mu \sum_{i}^{k} \mathbf{U}_i a_i. \qquad [17]$$

A more detailed formulation follows. The velocity at the position of particle j due to particle i is

$$\mathbf{V}_{jl} = \mathbf{T}_{ijlk}\mathbf{U}_{ik} \quad \text{for} \quad k, l = 1, 2, 3 \text{ coordinate directions.} \qquad [18]$$

$$\mathbf{U}_i = \begin{pmatrix} U_x \\ U_y \\ U_z \end{pmatrix}$$

$$\mathbf{T}_{ij} = \begin{pmatrix} x^2 f - \dfrac{y^2+z^2}{2} g & xyh & xzh \\ xyh & y^2 f - \dfrac{x^2+z^2}{2} g & yzh \\ xzh & yzh & z^2 f - \dfrac{x^2+y^2}{2} g \end{pmatrix} \qquad [19]$$

$$\begin{pmatrix} x \\ y \\ z \end{pmatrix} = \mathbf{r} = \text{difference in position of particles } i \text{ and } j$$

$$f = f(r) = -\frac{1}{2}\left(\frac{a_i^2}{r^4}\right)\left(\frac{a_i}{r} - \frac{3r}{a_i}\right) \qquad [20]$$

$$g = g(r) = -\frac{1}{2}\left(\frac{a_i}{r^3}\right)\left(\frac{a_i^2}{r^2} + 3\right) \qquad [21]$$

$$h = f + g/2$$

$$r = \text{length of } \mathbf{r}. \qquad [22]$$

The method is similar to representation of the field by Stokeslets, which was done by Kirkwood and Riseman (18), Meakin (11), Hall (19), and de la Torre and Bloomfield (20). The error associated with these methods is discussed by these authors and by Happel and Brenner (17). The error depends on the difference between the velocity field $\mathbf{V}$ averaged over the primary sphere surface and the velocity evaluated at the center of the primary sphere, which is of the order $a^2(\delta^2 V_i/\delta x_i^2)$. Since the far field velocity varies inversely with r, the error must vary as $(a/r)^3$. If we are interested in the total force rather than the force distribution, the method is more accurate than suggested above, as will be shown in the examples below. However one cannot in general expect the method to work well for compact clusters or resolve the effects of structural details such as the manner in which the primary particles are connected.

A computer code (called CLSTDR for Cluster Drag) was written to calculate the interactions of N spheres comprising a cluster. Computations on common shapes yield the following results. For a pair of spheres of radius a moving parallel to the long axis, the computed hydrodynamic radius is $1.18a$, somewhat smaller than the experimental value $1.28a$ (17). Figure 2 compares computed values of dynamic shape factor $K = R_H/R_v$ for chains of up to 50 spheres with measurements by Kasper (16). Agreement with data is closer than 6%, which is as close as computations based on prolate spheroids (8). More detailed comparisons were made for clusters of smaller numbers. Durlofsky and Brady (21) performed more precise calculations by considering point torques and lubrication forces as well as point forces. For the case of seven spheres the two methods agree to within 3% (Table I). For a close packed cluster of 13 spheres the shape factor differs by less than 1% from data by Lasso and Weidman (22), indicating that the method may provide reasonable estimates of the drag on dense clusters.

2.2 *Theory of Scaling*

The method discussed above involves inversion of an N by N matrix so that it becomes

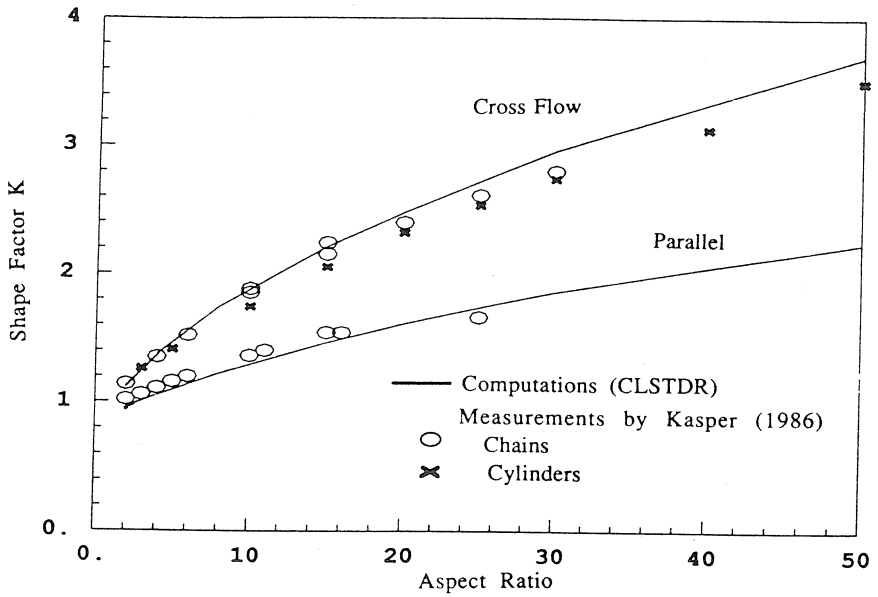

FIG. 2. Dynamic Shape factor $K = R_H/R_v$ for chains and cylinders in cross flow (upper curve) and parallel flow (lower curve). Results for chains as computed by CLSTDR are shown with solid lines —. Data from Kasper (1986) for chains ○ and cylinders × are also shown.

cumbersome for very large clusters. In this paper clusters are assumed to be self-similar in that a large cluster can be viewed as a collection of subclusters with the same general shape. It is possible to use this self-similarity to reduce the computational time. We start with the assumption that a small cluster within a large cluster may be replaced by a single sphere with the same drag. This is the same level of approximation as replacement of primary spheres by point forces. Now suppose that we know $F(k)$ = drag on a cluster of size k and that we want to know about the drag on the cluster of k^2 particles. The new cluster will be similar to the old cluster but the spatial dimensions will be stretched by $k^{1/D}$. In the large

TABLE I

Force Distributions on Chains of Seven Spheres in Cross Flow as Computed by Durlofsky and Brady (1987) (Shown in Brackets) and CLSTDR (Unbracketed)

	$\frac{F}{6\pi\mu a}$		
Sphere (from end)	$r = 2$	$r = 2.2$	$r = 2.6$
1	.616 (.515)	.627 (.530)	.651 (.575)
2	.387 (.439)	.423 (.456)	.480 (.500)
3	.389 (.421)	.415 (.440)	.461 (.478)
4	.380 (.410)	.408 (.430)	.455 (.475)
Shape factor K	1.654 (1.646)	1.745 (1.716)	1.903 (1.872)

Note. Here r is the particle center to center spacing normalized with respect to the particle radius so that $r = 2$ corresponds to a connected chain. K is the dynamic shape factor.

cluster, take groups of k particles and replace them by single spheres of the same drag. In this way the number of point forces required to represent a large cluster is reduced. At successive levels of scale, one computes the mass of the cluster, the coordinates, and the radius of the equivalent spheres and the hydrodynamic radius. We define a scale parameter p such that a cluster contains N_p particles,

$$N_p = k^{p+1} \quad p = 0 \cdots n. \qquad [23]$$

The cluster coordinates are described by N_0 vectors X_i,

$$X_{ip} = X_{i0} k^{p/D}, \qquad [24]$$

where D is the fractal dimension. The hydrodynamic radius a_p of a cluster of N_p particles is a function of the hydrodynamic radii of its constituent subclusters $a_{p-1,i}$ and their positions $X_{i,p-1}$.

$$a_p = f(a_{p-1,1} \cdots a_{p-1,k}, X_{i,p-1}), \qquad [25]$$

where the function f is evaluated by solving [17]–[22]. In [25] the size and shape of the subclusters are allowed to differ from one another.

One must consider the possibility that error is accumulated as the clusters are scaled up from k to k^n particles, as this would change the apparent scaling of drag with cluster size. The case for $k = 2$ is simple enough to analyze but should be representative of the general case. We consider two subclusters in cross flow at distances R_p and with hydrodynamic radii a_p. The hydrodynamic radius of this combination from the method of reflections is

$$a_{p+1} = a_p \frac{2}{1 + .75 a_p/R_p + .25(a_p/R_p)^3}. \qquad [26]$$

Suppose that the computed value of a_p was $a'_p = a_p(1 + \epsilon_p)$, where ϵ_p is some small error inherent in the computation of the drag on a cluster. It is a "local error" independent of our use of self-similarity. Substituting this into [26] we find after manipulation that the computed value of a_{p+1} is

$$a'_{p+1} = a_{p+1}(1 + \gamma \epsilon_p), \qquad [27]$$

where γ is a function of the cluster shape and $|\gamma| < 1$. If $\epsilon_p = \epsilon$ and γ are approximately constant at each scale (reasonable for self-similar clusters), and if $\epsilon \ll 1$ then the computed radius at level n is

$$a'_n = a_n(1 + \epsilon(1 + \gamma + \gamma^2 + \gamma^3 + \cdots)). \qquad [28]$$

Therefore, there is an accumulation of error so that the final error is, for very large n,

$$\epsilon_{\text{tot}} = \epsilon \frac{1}{1 - \gamma}.$$

It is possible to estimate γ by computing the change in the drag that occurs when the primary sphere size is changed by a known ϵ_p. This is just the difference between unity and the slope of the $a_{p+1}(a_p)$ curve obtainable from [26]. From this we found $\gamma < .6$ so $\epsilon_{\text{tot}} < 2.5\epsilon$ for a dimer. We found that CLSTDR overpredicts the drag in most test cases, so we expect that error accumulation should increase the estimated drag (or decrease β).

2.3 *Generation of Clusters*

The preceding scaling relations allow us to construct a cluster of k^n particles given a "starting cluster" of k coordinates X_{0i}. For example if X_{0i} describes $k = 8$ particles arranged as a cube, with $D = 1$, one obtains the "expanded cube" of Fig. 3. If $k = 2$, $D = 1$, and X_{0i} describe two spheres in contact, one obtains a long chain of 2^n particles after n scalings. The first example is unconnected while the second is connected. Both clusters are exactly self-similar and obey the scaling relation [2]. It is possible to convert exactly self-similar clusters into random clusters more like real aggregation products by giving the basic set of k coordinates a random rearrangement at each scale (23). The fractal dimension is unchanged on average. For this kind of cluster it is convenient to work on a lattice. In this case the fractal dimension is $\log P/\log Q$ where we have P units arranged on a cell with side length Q.

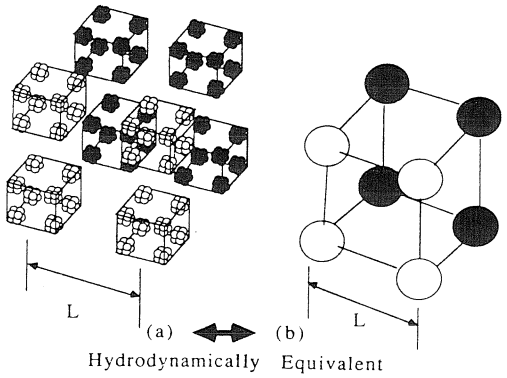

FIG. 3. (a) Fractal cluster with $D = 1$ constructed with a cube of 8 as the starting cluster. (b) The original cluster of 8^3 reduced to a cluster of 8.

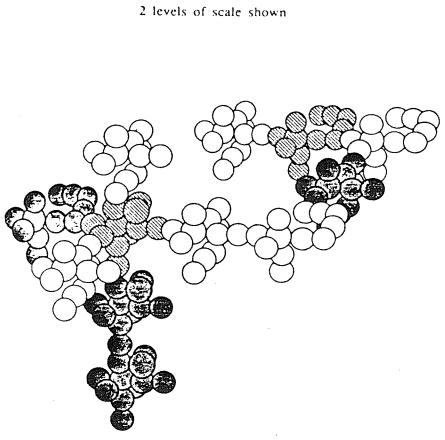

FIG. 5. Random 3-dimensional cluster with $D = \log 12/\log 4 \approx 1.79$.

At each stage one of a finite set of possible configurations is chosen at random. Typical two- and three-dimensional clusters are shown in Figs. 4 and 5. All of the random clusters used in this work except the "random dimer" are connected. The random dimer is based on two units randomly arranged on a $2 \times 2 \times 2$ lattice.

3.0 RESULTS

Computations were performed for a variety of starting clusters and fractal dimensions.

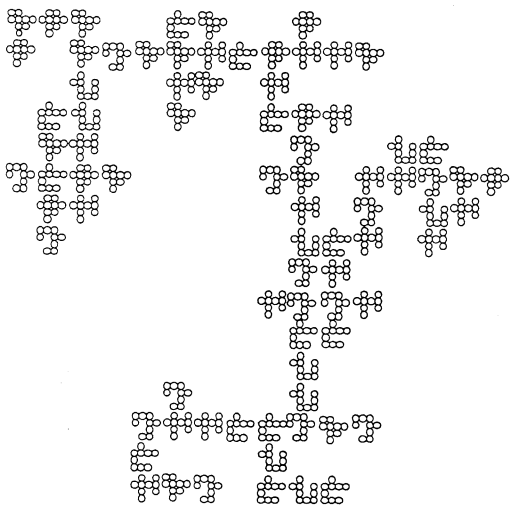

FIG. 4. Random plane cluster with D log 9/ log 4 $\approx$ 1.59 constructed by randomly choosing one of six configurations of nine units on a 4×4 lattice.

When random clusters are used the ensemble average of 10 clusters is shown as well as the curves for 4 individual clusters. This is done to qualitatively illustrate the effects of randomness.

Figure 6 shows that β varies linearly with $\log N$ if $D = 1$ regardless of the type of cluster. The plot also compares results for chains, moving parallel to their long axis, generated from starting clusters of 32 and 2. Ideally the curves for chains should be identical but there is almost a 20% difference because the dimer is such a crude representation of the chain. Results for dimer-chains in cross flow (not shown) result in β curves that are about 50% lower, as suggested by Fig. 2. The random dimer shows an average curve that is nearly the orientational average for chains. The distribution of the clusters about the ensemble mean does not grow wider as N increases, probably due to the independence of the random perturbations at each length scale.

Figure 7 ($D = 1.05$) shows a slower growing β though it does not approach a limit by $N = 10^6$. The effect of fractal dimension on the growth of β is better seen in Fig. 8, calculations for the expanded cube similar to Fig. 3. As D increases to 1.47 (Fig. 9) the variation in β is comparable to the standard deviation of the random dimer data. It appears that β increases

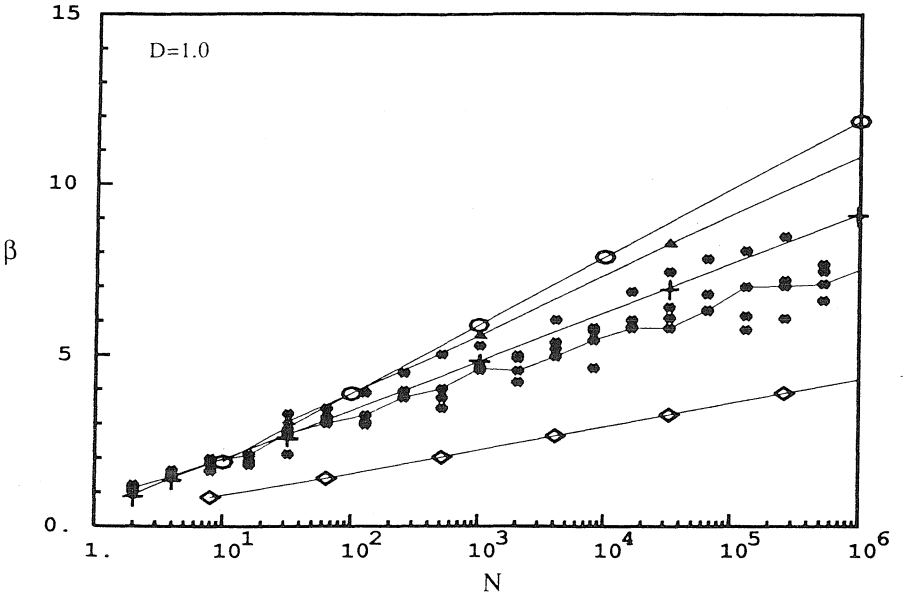

FIG. 6. $\beta = R_g/R_H$ vs number in the cluster N for $D = 1.0$. (a) ○ Slender body theory, (b) ◇ cluster based on a cube of 8, (c) ▲ cluster based on a chain of 32, (d) + a chain of 2, (3) ◆ four random dimers and their ensemble average.

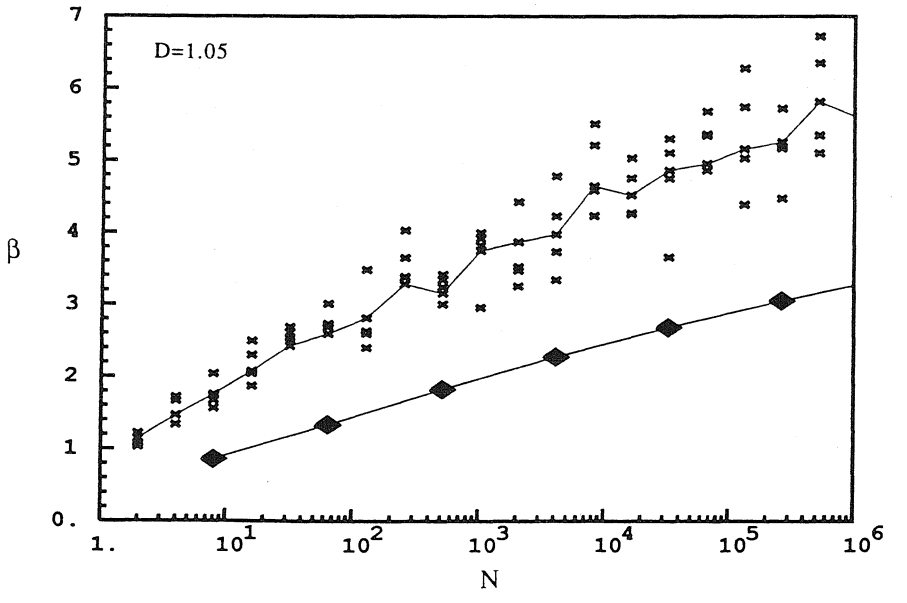

FIG. 7. β vs N for $D = 1.05$ showing that the variation of β is similar for (a) ◆ a cluster based on a cube of 8 and (b) × a random dimer.

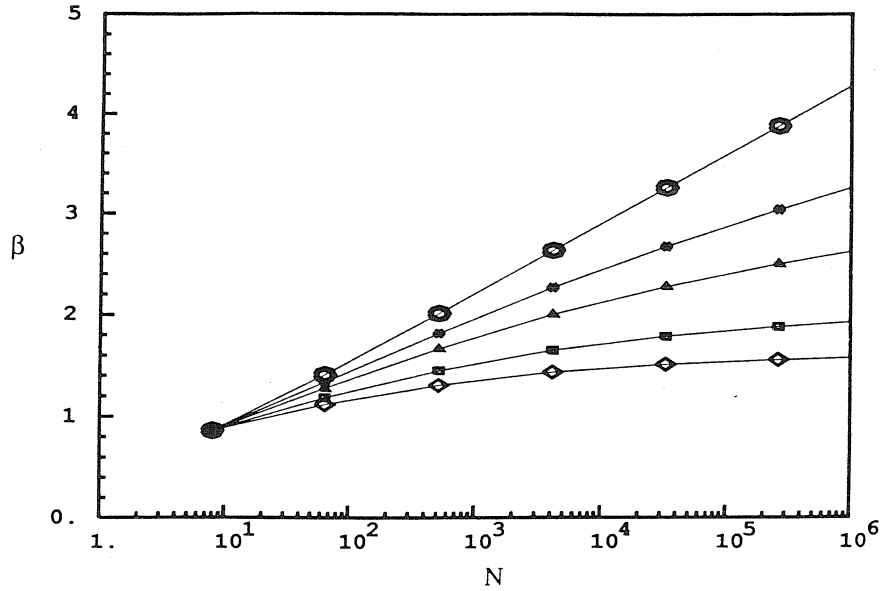

FIG. 8. β vs N for D = 1.0 ○, 1.05 ◆, 1.1 ▲, 1.2 ■, 1.3 ◇ for a cluster based on a cube of 8.

by about 40% as the cluster grows very large. The Vicsek cluster (23), based on five spheres arranged on a 3 × 3 planar lattice as a cross, has a much higher value of β. This is a result of the fact that the cluster is moving parallel to its long axis.

Figure 10 ($D \approx 1.58$) shows that the curves for a random connected cluster similar to Fig.

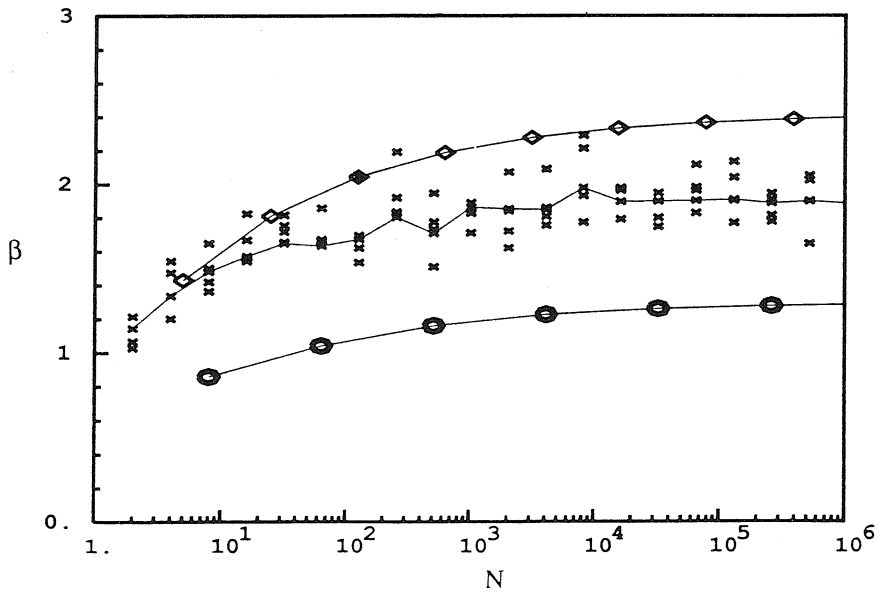

FIG. 9. β vs N for $D \approx 1.49$. The clusters are based on (a) ○ a cube of 8, (b) ◇ a Vicsek cluster (5 units on a 3 × 3 grid) and (c) × a random dimer.

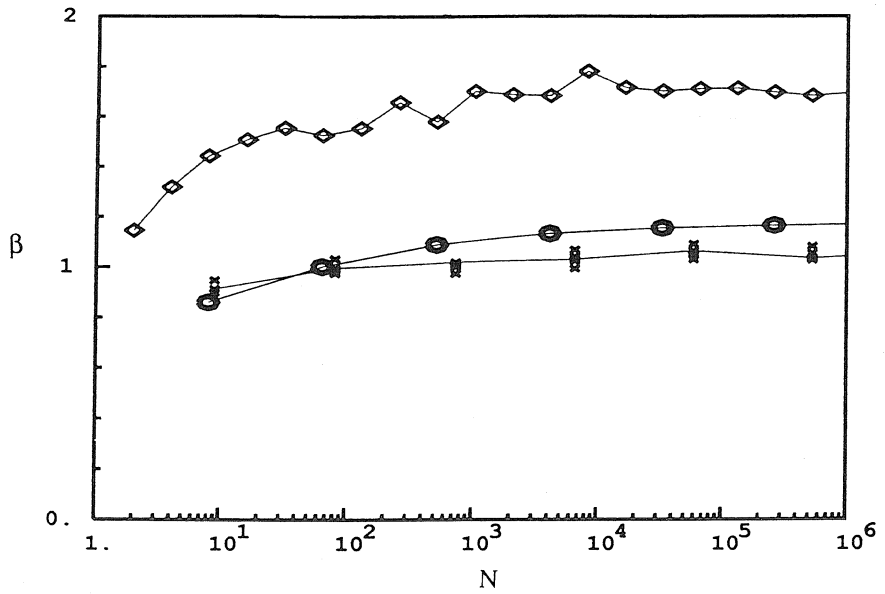

FIG. 10. β vs N for $D \approx 1.58$. Clusters are based on (a) ○ a cube of 8 (b) × 9 units randomly placed on a 4 × 4 lattice and (c) ◇ a random dimer.

4 are slightly flatter than the curves for the expanded cube or the random dimer. Figure 11 is similar but here the random connected cluster is similar to Fig. 5 and the fractal dimension is 1.79. The limiting value of β for this cluster apears to be 1.12 ($R_H/R_g = .89$).

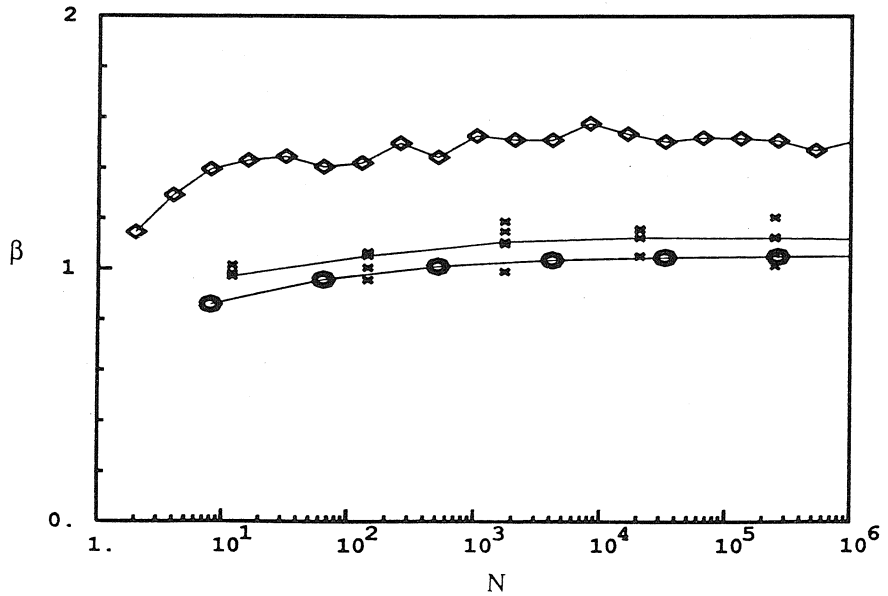

FIG. 11. β vs N for $D \approx 1.79$. Clusters are based on (a) ○ a cube of 8, (b) × 12 units placed randomly on a 4 × 4 × 4 lattice, and (c) ◇ a random dimer.

Chen and Meakin (12) found that $R_H/R_g \approx .82$ for their simulated clusters ($D = 1.78$). Because their clusters are not the same as ours, the difference may be a geometry effect rather than an indication of an error in either model.

For $D = 2$, computations for a cluster generated by seven spheres in a close packed plane may be compared to the classical result for a thin disk (14). From Fig. 12, $\beta = .83$. For a thin disk with the same projected area, $\beta = .83$ and for a thin disk with the same maximum radius, $\beta = .74$. These good results suggest that the computed trends in β are not computational artifacts.

Finally, as D increases to 2.1 (Fig. 13) the curves become very flat. In this case the curves for the random dimer decrease as N increases while no such trend is seen for the other clusters. This discrepancy is approximately as large as the expected error accumulation effects discussed earlier. The expanded cube and the cluster based on 10 units on a $3 \times 3 \times 3$ lattice behave similarly, with the latter cluster having $\beta \sim 1.0$ for large N. This is to be compared with Chen's $R_H/R_g = .97$ (12) for a simulated cluster with $D = 2.1$. Wiltzius (13) used static light scattering to measure the fractal dimension and radius of gyration of colloidal silica and compared the results with dynamic light scattering measurements of the hydrodynamic radius to conclude that $R_H/R_g = .72 \pm .02$. This measurement is coincidentally close to the value obtained for the random dimer. We suggest below that this is not an indication that Wiltzius' silica is similar to these artificial clusters.

4.0 CONCLUSIONS

We have used self-similarity to simplify the representation of fractal aggregates. This makes it convenient to examine the drag-mass scaling behavior of very large clusters although the effects of some structural details are necessarily lost. This approach differs from previous work (2, 5, 11, 13, 15) in that for a given fractal dimension it is equally valid and convenient for all cluster sizes and shapes.

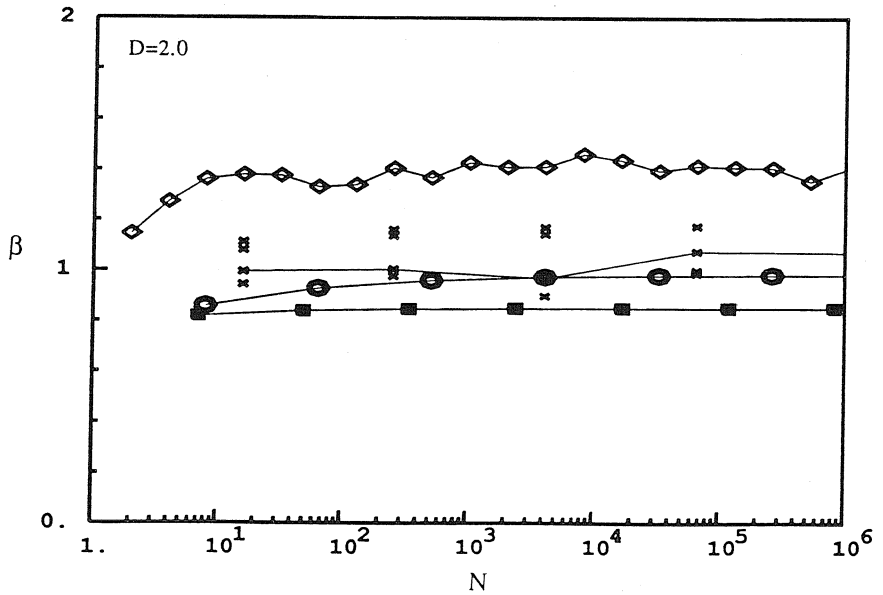

FIG. 12. β vs N for $D = 2.0$. Clusters are based on (a) ○ a cube of 8, (b) × 16 units placed randomly on a $4 \times 4 \times 4$ lattice, (c) ■ seven spheres in a close packed plane perpendicular to the flow, and (d) ◇ a random dimer.

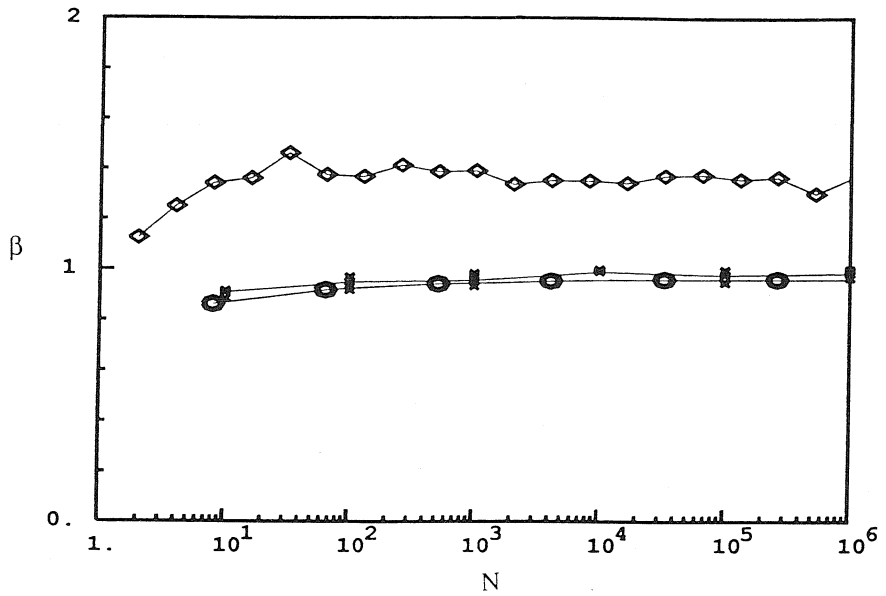

FIG. 13. β vs N for $D \approx 2.1$. Clusters are based on (a) ○ a cube of 8, (b) × 5 units placed randomly on a 2 × 2 × 2 lattice, and (c) ◇ a random dimer.

The method gives good results for known test cases so we expect it to give reasonable results for clusters with intermediate fractal dimensions. Calculations for exactly self-similar, random, connected, and unconnected clusters show that the scaling behavior is similar in all cases. We therefore believe that it is reasonable to generalize the results to real clusters.

The results are conveniently expressed as a ratio β of the radius of gyration of the cluster to the hydrodynamic radius. For $D = 1$, one finds that $\beta \cong \ln N$ while for $D > 1$, β approaches a limit as N increases. The limit is approached very rapidly for $D > 1.3$. As D increases above 2, β becomes practically independent of N. As β becomes constant, the drag is no longer affected by the fine structure details such as the primary particle size. This has important implications for the "almost fractal" objects of the real world. For example, suppose that several thousand primary particles agglomerate under conditions that result in self-similar clusters with $D = 2.1$. Suppose now that several dozen of these clusters combine under changed conditions that result in a long chain of these clusters. Since the hydrodynamics are governed by the large length scales, the new agglomerates would have a large β (Fig. 6) even though the fractal dimension over most length scales is high. Thus β may not be related to the apparent fractal dimension of "almost fractal" clusters. Even for an "exact" fractal, β can not be determined by the fractal dimension since the cluster aspect ratio is not determined by the fractal dimension alone.

This work shows some of the limits of the fractal concept when applied to aggregates and reinforces previous work in suggesting the need for detailed experiments before drag is used to measure cluster size distributions or infer structural information.

APPENDIX: NOMENCLATURE

a	primary particle radius
D	fractal dimension
F	drag force
l	coordinate direction
K	dynamic shape factor
m	mass of cluster
N	number of particles in a cluster

n	number of self-similarity scale levels for a particular cluster
P	pressure
p	scale level
R_g	radius of gyration
R_f	outer radius of the cluster
R_h	hydrodynamic radius
R_v	radius of volume equivalent sphere
R_s	radius of surface area equivalent sphere
r	radial coordinate
r_h	hydraulic radius of a porous medium
$\mathbf{U}$	velocity of a cluster
$\mathbf{V}$	virtual velocity of a particle in a cluster
x, y, z	cartesian coordinates
α	packing factor
γ	error propagation factor
β	R_f/R_h
ϵ	$1/\ln(2N)$
μ	viscosity
κ	hydraulic permeability
σ	porous medium void fraction
θ	angular coordinate

ACKNOWLEDGMENT

This work has been supported by a subcontract from Physical Sciences Inc. on the U.S. Department of Energy Contract DE-AC22-86PC90751.

REFERENCES

1. Forest, S. R., and Witten, T. A., *J. Phys. A Math. Gen.* **12,** L109 (1979).
2. Schmidt-Ott, A., *J. Aerosol Sci.* **19,** 553 (1988).
3. Samson, R. J., Mulholland, G. W., and Gentry, J. W., *Langmuir* **3,** 272 (1987).
4. Meakin, P., *Phys. Rev. A: Gen. Phys.* **29,** 997 (1984).
5. Mountain, R. D., Mulholland, G. W., and Baum, H., *J. Colloid Interface Sci.* **114,** 67 (1986).
6. Fuchs, N. A. "The Mechanics of Aerosols." Pergamon, New York, 1964.
7. Leith, D., *J. Aerosol Sci. Tech.* **6,** 153 (1987).
8. Dahneke, B., *J. Aerosol Sci.* **1,** 179 (1982).
9. Dahneke, B., *J. Aerosol Sci.* **4,** 139 (1973).
10. Davies, C. N., *J. Aerosol Sci.* **10,** 477 (1979).
11. Meakin, P., Chen, Z-Y., and Deutch, J. M., *J. Chem. Phys.* **82,** 3786 (1984).
12. Chen, Z-Y., Meakin, P., and Deutch, J. M., *Phys. Rev. Lett.* **59,** 2121 (1987).
13. Wiltzius, P., *Phys. Rev. Lett.* **58,** 710 (1987).
14. Lamb, H, "Hydrodynamics," pp. 600–607. Dover, New York, 1943.
15. Batchelor, G. K., *J. Fluid Mech.* **44,** 419 (1970).
16. Kasper, G., et al., *J. Aerosol Sci.* **16,** 535 (1985).
17. Happel, J., and Brenner, H., "Low Reynolds Number Hydrodynamics with Special Applications to Particulate Media." Nijhoff, Boston, 1963.
18. Kirkwood, J. G., and Riseman, J., *J. Chem. Phys.* **16,** 565 (1948).
19. Hall, M. S., *J. Aerosol Sci.* **19,** 317 (1988).
20. de la Torre, G. J., and Bloomfield, V. A., *Q. Rev. Biophys.* **14,** 81 (1981).
21. Durlofsky, L., and Brady, J. F., *J. Fluid Mech.* **180,** 21 (1987).
22. Lasso, I., and Weidman, P., *Phys. Fluids* **12,** 29 (1986).
23. Gentry, J. W., Mulholland, G. W., and Sullivan, F., *in* "Atmospheric Aerosols and Nucleation: Proc. of the 12th Int. Conference on Atm. Aerosols and Nucleation" (Paul E. Wagner and Gabor Vali, Eds.), pp. 116–119. Springer-Verlag, New York, 1988.

CHAPTER 5

THE MOBILITY AND STRUCTURE OF AEROSOL AGGLOMERATES

with Hung. V. Nguyen and Richard C. Flagan

submitted to Aerosol Science and Technology.

ABSTRACT

The relation between the aerosol agglomerate structure and transition regime mobility can be explained with a simple model incorporating fractal geometry and results from computer simulations. The model is consistent with previous measurements of the shape factors and allows some structural information to be inferred from these measurements. Experiments conducted here with well-characterized TiO_2 and Si agglomerates support the model's assumption that the mobility diameter of a particle in the free-molecule regime is determined solely by the projected area of the particle.

INTRODUCTION

Aerosols consisting of irregular agglomerates are found in many systems, including submicron fly-ash from pulverized coal combustion (Flagan and Friedlander,1978; Neville, et al., 1982; Quann and Sarofim, 1982), soot (Medalia and Heckman,1969; Lahaye and Prado, 1981), welding fumes (Kalliomäki et al., 1987) and synthetic fumes (Okuyama et al. 1986). All of these aerosol particles exhibit a common structure, namely, agglomerates of approximately equiaxed particles (spherules) with sizes of a few tens of nanometers. Without chemical analysis, the various particles are almost indistinguishable. This common structure has been attributed to the physical process of agglomeration without coalescence (Forrest and Witten, 1979). While the dynamics of spherical particles are relatively well understood, it is clear that a dense sphere and an irregular chain of the same mass will have very different properties. Although progress has been made in characterizing the structure of these particles (Schaefer and Hurd, 1990; Samson. et al.,

1987), the relation between the structure and the transport properties of the agglomerates remains unclear. The mobility of a particle, i.e., the speed at which it moves in response to a steady force, is one of the most fundamental of aerosol properties because it is needed to determine the particle diffusivity, coagulation kinetics, and the response of most aerosol sizing instruments. In centrifuges and impactors, the measured quantity is the drag-to-mass ratio, while in electrostatic classifiers and diffusion batteries, the mobility is measured. The mass transfer and charging properties of aerosol particles are correlated with the mobility-equivalent diameter, although these properties do not depend directly on particle drag (Rogak et al., 1991; Rogak and Flagan, 1991a). It has also been suggested that the fractal dimension of particles can be inferred from the drag-mass relationship (Schmidt-Ott, 1988; Kütz and Schmidt-Ott, 1990).

Fuchs (1964) introduced the dynamic shape factor κ defined as the ratio of the drag force acting on a non-spherical particle to that acting on a sphere of the same volume. Since then, numerous researchers have correlated measurements of drag with the particle volume (Davies, 1979; Okuyama et al., 1980). Although this relation is important, fluid mechanical and structural effects are difficult to separate. Moreover, the relationship between the shape factor and the fractal characterizations used currently is not well understood.

In the present work, drag is correlated with particle projected area and radius of gyration. This relationship is not strongly sensitive to particle structure, as is verified by measurements made here with TiO_2 and silicon agglomerates. The relation between particle volume and projected area, which is more sensitive to the particle structure, is obtained using fractal models. The model is consistent with previous measurements and also allows some structural information to be inferred from this shape factor data.

THEORETICAL CONSIDERATIONS

A Model Agglomerate

Agglomerates often exhibit self-similar or "fractal" structures over a limited range of length scales (Forrest and Witten, 1979; Smirnov, 1990; Samson et al., 1987). Although the accuracy of this fractal model is still an active area of research, the fractal concept is useful in characterizing particle structure. A collection of fractal agglomerates obeys two important scaling relationships. First, every member of the collection has a fractal structure. This is indicated by the correlation $C(r)$ between the density $\rho(r')$ at a point in the agglomerate and the neighboring densities $\rho(r'+r)$,

$$C(r) = <\rho(r'+r)\,\rho(r')> \sim r^{D\alpha-3}, \tag{1}$$

where $<>$ denote averaging over all points in the agglomerate. The scaling parameter D_α is a fractal dimension (Meakin, 1984). In addition, the entire collection satisfies a power relation between the mass M of each agglomerate and its radius of gyration R_g,

$$M \sim R_g^{D\beta}, \tag{2}$$

where D_β is another fractal dimension. In general the two fractal dimensions are not equal, but for collections of large agglomerates in which there is no rearrangement during the growth process, $D_\alpha = D_\beta$ (Meakin, 1984; Forrest and Witten, 1979). Such collections are produced in the cluster-cluster aggregation models meant to simulate agglomerate aerosol formation. These scaling relations are not sufficient for predictive modeling, so we present a simple model of an ideal fractal agglomerate for which $D_\alpha = D_\beta = D_f$. First, we relate the cluster mass to its size by

$$N = \left(\frac{d_f}{d_1}\right)^{D_f}, \tag{3}$$

where d_f is an outer diameter, d_1 is the primary particle diameter (assumed to be constant and much smaller than d_f), and N is the number of primary particles in the agglomerate. This relation is consistent with the geometry of straight chains ($D_f = 1$, d_f = length), discs

($D_f = 2$) and spheres ($D_f = 3$). By extension from these shapes, we obtain a relation between the radius of gyration and the outer diameter

$$2R_g = \int_{\text{volume}} \frac{x^2 + y^2 + z^2}{\text{volume}} \, dx \, dy \, dz = \sqrt{\frac{D_f}{D_f+2}} \; d_f \; . \tag{4}$$

The exact relation between R_g, d_f and mass can be determined only by detailed, three-dimensional structural analysis of real agglomerates. Such analyses have not yet been done, but (3) and (4) may be compared to the results from computer simulations. For simulated agglomerates with $D_f = 1.69$ (Mountain et al., 1986), R_g was 10% larger than predicted by (3) and (4).

Aerodynamic Drag or Mobility

The limiting cases where the particle is much larger (continuum regime) or much smaller (free-molecule or kinetic regime) than the gas mean free path λ are considered first since the transition regime fluid mechanics are more complex.

In the continuum regime, previous theoretical investigations (Kasper et al., 1985; Hess et al., 1986; Chen et al., 1987; Wiltzius, 1987; Rogak and Flagan, 1990) have shown that the mobility diameter of a fractal cluster scales with the radius of gyration, provided that the number of primary particles is sufficiently large and that the fractal dimension is larger than ~ 1.3 (Rogak and Flagan, 1990). The mobility diameter of the model agglomerate in the continuum regime is therefore

$$d_{mc} = 2\beta R_g = \beta d_1 \sqrt{\frac{D_f}{D_f+2}} \; N^{1/D_f} \, . \tag{5}$$

From theory and experiment, the constant of proportionality β is between 0.7 and 1.0 for clusters similar to aerosol agglomerates (Chen et al., 1987; Wiltzius, 1987). For modeling, we take $\beta = 0.9$ (Rogak and Flagan, 1990).

Chan and Dahneke (1981) performed Monte Carlo simulations to estimate the drag forces acting on straight chains of spheres in the free-molecule regime. For chains moving at random orientations, the computed mobility diameter d_{mk} was

$$d_{mk} = d_1 \sqrt{0.802(N-1)+1} . \quad (6)$$

In arriving at a factor of 0.802, it has been assumed that the fraction of molecules reflecting diffusely from the particle is 0.93, which is reasonable for most material surfaces. When d_{mk} is compared to the diameter d_A of the sphere with the same projected area as the randomly oriented chain, one finds that for $N >> 1$,

$$\frac{d_A}{d_{mk}} = 1.03 . \quad (7)$$

Meakin et al. (1989) computed the free-molecule drag on simulated agglomerates and found that $d_A = d_{mk}$ to within a few percent. The effect of the fraction of molecules undergoing diffuse reflections was small.

After relating the mobility to the projected area, one must still relate the volume to the area for a complete model. For a fractal cluster with $D_f < 2$, most of the primary spherules are exposed, so the projected area is approximately proportional to N. We assume that the projected area of an agglomerate is the same as the orientation-averaged projected area of the straight chain with the same N and d_1. Aerosol agglomerates are generally not straight chains, so not all primary particles are exposed to collisions with gas molecules. Both the average projected area and the mobility diameter are reduced. Meakin et al. (1989) found that the shielding of primary particles in agglomerates with $1.8 < D_f < 2.0$ reduces d_A by $\sim$ 10% below that for a straight chain. For $D_f > 2$, the shielding becomes increasingly important as N increases, so that d_A scales with R_g. Thus, the continuum and free-molecule regime mobility diameters are expected to be nearly the same as d_A. Tohno and Takahashi (1990) discuss the relation between agglomerate volume and area in more detail.

The transition regime mobility B is more difficult to predict, though from experiments it is well known that for a sphere of diameter d,

$$B = \frac{C_c(Kn)}{3\pi\mu d} \quad , \tag{8}$$

where μ is the gas viscosity and C_c is the Cunningham slip-correction factor,

$$C_c(Kn) = 1+Kn\,(A + B\exp(-C/Kn)) \tag{9}$$

$$Kn = 2\lambda/d$$

and A =1.257, B =0.4, C =1.1 (Seinfeld, 1986). Dahneke (1973) suggested an "adjusted sphere" generalization of this interpolation formula for non-spherical particles, in which the transition regime mobility diameter d_m satisfies

$$\frac{d_m}{C_c(Kn_m)} = \frac{d_{mc}}{C_c(Kn_{ck})} \tag{10}$$

$$Kn_m = 2\lambda/d_m \tag{11}$$

$$Kn_{ck} = \frac{2\,\lambda\,d_{mc}}{d_{mk}^2}, \tag{12}$$

where d_{mk} and d_{mc} are the kinetic and continuum regime mobility diameters. This interpolation agrees well with Pich's (1969) more rigorously derived interpolation for cylinders.

According to this model, d_m depends only on the agglomerate dimensions and λ. Thus, it is natural to normalize all lengths by λ. Predicted dimensionless agglomerate mobility and area diameters are presented in Figure 1. By assumption, $d_A = d_m$ in the free-molecule regime, but this limit is approached closely even for $d_m \sim 2\lambda$. For larger agglomerates, $d_A < d_m$ by an amount depending on D_f, d_1/λ, and the factor β used in (5). Figure 1 was computed with β=0.9. For the values of $d_m / 2\lambda$, D_f and d_1 considered in Figure 1, a 10% increase in β resulted in a decrease in d_A/d_m of less than 5%.

For an agglomerate with $D_f = 1.8$ and $d_1=0.5\lambda$, d_A and d_m are nearly equal for all agglomerate sizes. However, as D_f decreases, so does d_A/d_m. For $D_f = 1.6$, decreasing d_1 has a substantial effect on d_A/d_m (Figure 1), although the same changes in d_1 changed d_A by less than 5% for $D_f = 1.8$.

The transition between free-molecule and continuum behavior is very gradual, with the slopes of the d_A vs d_m curves changing continually as d_m increases above λ. It is therefore difficult to infer particle structure from the shape of the d_A vs d_m curves without properly considering the transition behavior. As discussed below, the aerodynamic diameter d_{ae} has often been correlated with $N^{1/6}$. The relation between d_A and d_m implied by this correlation is shown in Figure 1. Interestingly, this correlation is consistent with the present model for $1.3 < D_f < 1.6$.

So far, we have neglected the effects of particle orientation. A measure of the influence of orientation is the ratio of the minimum and maximum mobility diameters, d_{max} and d_{min},

$$\chi = \frac{d_{max}}{d_{min}} \quad . \tag{13}$$

In the free-molecule regime, χ =1.56 for long prolate spheroids, while χ = 1.31 for chains (Chan and Dahneke, 1981). This difference between long chains and spheroids disappears in the continuum regime, where the χ=1.65 for both chains and spheroids. Bends and branches in an agglomerate structure must decrease χ, as is demonstrated by the effect of a single 90° bend at the midpoint of an otherwise straight chain. If the drag force on each half of the chain is computed independently and added, one finds that χ= 1.12 in the free-molecule regime. Such a bent chain would have an aspect ratio of approximately 1.6, reasonably close to the values observed in agglomerates. For doublets of spheres (aspect ratio =2), χ= 1.12 in continuum flow. Thus, one expects χ <1.2 for typical agglomerates. Slightly greater anisotropy has been found in experiments with nearly straight chains (Wen and Kasper, 1984).

Previous Measurements of Agglomerate Mobility

The continuum regime drag has been measured for a variety of particle shapes, including small clusters of spheres (Kunkel, 1948; Kousaka et al., 1981; Kasper et al., 1985; Lee and Leith, 1989). Well-characterized fractal agglomerates have not been studied experimentally.

Data for bodies in the transition regime are more difficult to obtain. Vomela and Whitby (1967) collected aerosol agglomerates on transmission electron microscope (TEM) sample grids that were placed inside an electrical aerosol analyzer (EAA). From measurements of the number of particles and the total number of charges in the aerosol, they were able to estimate the mobility of the sampled particles as a function of the volume equivalent diameter d_v (Table 1). It should be noted that during the mobility analysis, the number of charges per particle was typically greater than 10, so it was difficult to determine the exact number of charges on a small sample of photographed particles.

Stöber and Berner (1969) used a spiral centrifuge to measure the drag on small agglomerates of latex spheres. To correlate the experimental data, they defined a shape factor

$$f_N = \frac{d_{ae}}{d_1}, \tag{14}$$

where d_{ae} was the aerodynamic diameter (diameter of the sphere having unit density and settling at the same rate as the agglomerate). Assuming that d_m was equal to the diameter of the sphere with the same surface area, it was shown that the shape factor should vary as

$$f_N \sim N^{1/4}. \tag{15}$$

This agreed to within 10% with the measurements for agglomerates with $N \leqq 11$. Non-continuum effects should have been small since d_1 was in the range 360 nm $< d_1 <$ 1300

nm. Experiments using similarly shaped agglomerates of large spheres in oil agreed with the aerosol experiments to within a few percent.

Kops et al. (1975) applied similar techniques to drag measurements on radioactively labeled Fe_2O_3 aggregates of many spherules that were generated by the exploding wire technique. The aerosol was collected for microscopy on the metal foil of a spiral centrifuge. The mass of collected aerosol could be measured from the sample radioactivity. Their data were correlated with two extensions of Stöber's model. For agglomerates with $N<10^4$,

$$d_{ae} = k N^{1/6} \sqrt{\frac{\rho}{\rho_0}}\, d_1 \exp\left(2 \ln^2 \sigma_g\right), \tag{16}$$

and for $N>10^4$,

$$d_{ae} = f N^{1/3} \sqrt{\frac{\rho}{\rho_0}}\, d_1 \exp\left(1.5 \ln^2 \sigma_g\right), \tag{17}$$

where ρ/ρ_0 is the specific gravity of the particulate material, d_1 is the median primary particle diameter and σ_g is its geometric standard deviation. Most of the measured diameters were within ±10% of the correlation (16). Similar measurements have been made on agglomerates formed from vaporized nuclear reactor fuel pellets (Allen et al., 1978), uranium oxide and copper oxide agglomerates (Van de Vate et al., 1980) and Fe_2O_3 agglomerates (Kasper, 1982; Shon, 1979). Using a Millikan electrostatic balance, Colbeck et al. (1989) found significantly higher shape factors for soot than were given in earlier studies.

Fewer shape factor measurements have been made with the differential mobility analyzer (DMA), partly because of the difficulty of accounting for multiple charging. Measurements have been made for soot agglomerates (Odumade, 1983) and Fe_2O_3 chains (Wen and Kasper, 1984).

Comparison of Model with Previous Measurements

The factor k of equation (16) was calculated using equations (3)-(12) and compared in Figure 2 with measurements by Kasper (1982) for nearly straight chains of 10 to 300 primary particles. The data appear to be consistent with $D_f \sim 1.3$ and $50 < N < 500$. Note that in previous studies it is implicitly assumed that k is independent of N. The model predictions of Figure 2 show that this assumption is not generally valid, making it difficult to interpret these data. We use the relationship between d_A and d_m as an alternate representation of the data.

The projected area was not measured in previous studies of agglomerate mobility, but it may be estimated from the published data. The number and size of the primary particles were given in most of the studies, so we assume that the agglomerates were chainlike, and we compute the average projected area using the area-mean primary particle diameter. Where possible, the volume-mean primary diameter d_{1V} and area-mean primary diameter d_{1A} were determined from measurements of the median and standard deviation of the primary particle size distribution, assuming that the primary particles were log-normally distributed. The mobility diameter can be computed from the aerodynamic diameter d_{ae} by

$$d_m = \frac{\rho\, d_v^3 C_c(d_m)}{\rho_0\, d_{ae}^2 C_c(d_{ae})} \quad . \tag{18}$$

When the volume-equivalent sphere diameter is not available, we assume that

$$d_V = N^{1/3} d_{1V} \quad . \tag{19}$$

These conversions provide an upper-bound estimate of d_A as a function of the measured mobility diameter, which is compared to the model (Equations 3-12) in Figure 3. We note that some of the data (Kops et al., 1975; Kasper, 1982) are taken from correlations based on the assumption that k is independent of N.

There are considerable differences between the various studies, although the data are generally consistent with calculations using D_f=1.6 and d_1=30 nm. For most of the data, the ratio d_A / d_m decreases steadily as the agglomerate size increases. For some of the data, with $d_m > 2000$ nm, d_A / d_m increases, which Van de Vate et al. (1980) attribute to rearrangement of the large, fragile agglomerates resulting in an increased apparent fractal dimension.

The DMA studies show substantially higher values of d_A than the centrifuge experiments, which may be due to multiple-charging or orientation effects. Depending on the size distribution of the aerosol entering the DMA, a large fraction of the mobility-classified aerosols may carry more than one elementary charge. These multiply charged particles have larger projected areas than the desired, singly-charged particles. Wen and Kasper (1984) attribute the difference between DMA and centrifuge measurements to orientation effects. Elongated particles in the centrifuge are expected to become aligned perpendicular to the settling velocity. In the DMA, elongated conducting particles are expected to become aligned parallel with the direction of motion. Since the agglomerates were not good conductors, the moments that tend to orient a particle would depend on the location of charges on the particle surface. If the charges are distributed randomly, perfect alignment in the electric field is not expected. Hence, the factor χ of (13) gives an upper limit on the difference between DMA and centrifuge measurements.

Thus, it appears to be useful to correlate d_A with d_m, although there are some anomalous variations between the studies that cannot be attributed to the method of comparison. A rigorous test of this correlation requires experiments in which d_A and d_m are measured for well-characterized agglomerates.

EXPERIMENTS

Generation and Classification of TiO_2 and Si Aerosols

Titania (TiO_2) agglomerates were produced by the thermal decomposition of the alkoxide titanium tetra-isopropoxide $Ti(OC_3H_7)_4$ as described by Rogak et al. (1991). Silicon agglomerates were produced by the thermal decomposition of dilute silane in nitrogen in the externally heated, laminar flow reactor illustrated in Figure 4. The silicon aerosol was allowed to agglomerate in long tubing coils before flowing into a "sintering" furnace. The temperature of this second furnace was varied to produce agglomerates of different structures.

The agglomerates were classified according to their electrical mobilities, using a differential mobility analyzer (DMA, Model 3071, TSI Inc., St. Paul, MN), and then collected for transmission electron microscopy (TEM) or counted with a condensation nucleus counter (CNC, Model 3760, TSI), as shown in Figure 5. In the DMA, the aerosol is passed through a bipolar neutralizer, resulting in a steady-state, bipolar charge distribution on the particles. Only a small fraction of the charged aerosol has the correct mobility-charge ratio to migrate in the classifying electrostatic field to the aerosol exit slot. In order to ensure accurate dilution ratios, the sheath gas flow across which the particles migrate was recirculated by a diaphragm pump (Figure 5). Flow resistances and 1 L tanks were needed to damp out pulsations from the pump.

The sheath gas flow rates and the analyzer voltage were found to be reproducible to within a few percent and consistent with other DMAs in the laboratory to within 3%. Calibration of the DMA was done using several sizes of polystyrene latex (PSL) particles. Micrographs of spherical silicon particles indicated that the sizing, sampling and image-processing procedures were consistent to within 5%.

Thermophoretic Sampling

Collection of aerosols for micrographic analysis using thermophoretic deposition has several advantages: (i) The thermophoretic velocity is not as size-dependent as electrostatic, diffusional or inertial deposition processes; (ii) the thermophoretic deposition process is relatively gentle, making it suitable for the collection of potentially fragile agglomerates. The sampler used consisted of an aerosol preheater, a nozzle to direct the hot aerosol over the microscope grid and a means of keeping the grid cool (Figure 6).

It was possible that the particle structure was altered by the sampling process, although inertial or fluid mechanical forces were not expected to affect the particle structure in the moderate velocity gradients present in our system (Allen et al., 1979). The thermophoretic TEM sampling method was compared with scanning electron microscopy (SEM) of samples collected on a 0.4 micron Nucleopore filter (Rogak et al., 1991). The agglomerate structure seen by TEM was similar to that from SEM, although the SEM showed larger particles, possibly because the smaller particles deposited inside the filter pores where they were invisible to the SEM.

Particle-orientation effects in the DMA and thermophoretic sampler were also considered. Dimensional analysis can be used to estimate the importance of alignment as a function of particle size. Consider a particle of characteristic diameter d having an average thermophoretic velocity V_T. One expects that the angular rate of alignment cannot exceed d / V_T because the forces causing alignment should be no larger than the forces causing the net drift. At the same time, Brownian motion tends to randomize the orientation. From dimensional considerations, the rotational diffusivity D_r is related to the ordinary diffusivity D by

$$D_r \sim \frac{D}{d^2}, \tag{20}$$

which is consistent with results obtained for elongated bodies (Eisner and Gallily, 1981; Cheng et al., 1991). The ratio of the time scales for the two competing rotational processes is

$$\frac{\tau_T}{\tau_D} = \frac{\textit{Thermophoretic time}}{\textit{Diffusional time}} = \frac{D}{d\,V_T} \cdot \qquad (21)$$

The thermophoretic velocity for spheres in the transition regime is given by Friedlander (1977). For 50 to 2000 nm spheres with unit specific gravity, (21) is evaluated for room-temperature air with a temperature gradient of 1000°C cm^{-1}, similar to the gradient in the thermophoretic sampler. These calculations show that below 100 nm the thermophoretic alignment should be destroyed by thermal motion (Table 2). Alignment may persist for particles greater than 1000 nm. Similar arguments concerning alignment in electrical fields in the DMA also suggest that alignment can be important for particles greater than 100 nm (Cheng et al., 1991). In the present study, the lengths L of 10 thermophoretically deposited agglomerates (d_m ~ 200 nm) were measured with the TEM stage tilted at 0° and 30°. It was found that $L(0°)/L(30°) = 1.08 \pm 0.15$, indicating that the thermophoretic alignment effect was probably negligible.

Image Processing

Electron Microscopy, Digitization and Structural Measurements

The TEM (Model 301, Phillips) magnifications were determined to within 5%, using a precision grating and several sizes of PSL spheres. During the microscope sessions agglomerates were selected and photographed randomly in order to minimize operator biases.

The TEM negatives were photographed with a video camera (Model WV1500x, Panasonic) and digitized (400x400 pixels with 256 gray levels) with a frame-grabber board (Quick Capture model, Data Translation Inc., Marlborough, Mass.) installed in a

microcomputer (Macintosh-II, Apple Computer Inc., Cupertino, CA). Automatic image processing of the gray-level image was impractical because of background shading and extraneous structures in the image. Instead, the boundary of the particle was located manually before it was thresholded into black and white. The area measured from the resulting binary image varied by ± 5% because of the ambiguity of the particle boundary.

In addition to the particle area, several shape parameters were measured, including the fractal dimension. Fractal dimensions are frequently measured by the "successive squares" or "boundary dilation" algorithms (Forrest and Witten, 1979; Kaye et al., 1987; Samson et al., 1987; Tohno and Kanji, 1988; Reist et al., 1989; Tohno and Takahashi, 1989); however, interpretation of the results from any single algorithm is sometimes difficult. For this reason, three techniques were used to measure the fractal dimension. These measurements, in addition to the more traditional shape parameters, were obtained using two image-processing packages (Image, National Institute of Health; TCL-Image, TNO Institute, Delft, the Netherlands), as described below.

L, W Agglomerate length, width (Figure 7).

d_{coarse} Largest primary particle visible in an agglomerate (Figure 7).

d_{fine} Smallest primary particle visible in an agglomerate. In most cases, the primary particles were partly fused, so this number was not counted (Figure 7).

R_g Polar radius of gyration of the image. The images were scaled so that the radius of gyration in pixels was approximately the same for all particles (Figure 7).

L_{co} The contour L_{co} is the set of all object pixels that are next to non-object pixels, normalized by R_g. The boundaries of holes in the object are included, but isolated object or non-object pixels are removed before measurements are made.

L_{sk} The skeleton L_{sk} is the set of all points in the image that are midway between the two nearest boundary pixels, normalized by R_g. For a rectangle, the skeleton is a line running along the long axis. For a circle, the skeleton is a single point at the center. For irregular agglomerates the skeleton is generally branched (Figure 7).

D_{sq} This fractal dimension was obtained from a modified version of the successive squares algorithm (Forrest and Witten, 1979) . In that method, the object area A enclosed in a square of side L_{sq} was measured (Figure 8). The area increases with the square size according to

$$A \sim L_{sq}^{D_{sq}} . \tag{22}$$

The structural information at small scales is determined by a relatively small fraction of the object pixels. To improve the information at small scales, we use a number of squares from which an average enclosed area is obtained. To do this, a square grid with spacing L_{sq} is placed over the object (Figure 8). If there are object pixels at the center of a square, the number of object pixels in this square is counted. The average number of object pixels in such "on" squares is determined as a function of the grid spacing L_{sq} . Note that when L_{sq} is small, a large number of squares are used, located at different points on the image. For large L_{sq}, only one square is used. The fractal dimension is determined from the slope of the log -log plot over a range of L_{sq} from $0.2R_g$ to $2R_g$. This range of L_{sq} was chosen to minimize effects from the digitizer resolution and the primary particle size.

D_{tile} To obtain this fractal dimension, the object is completely covered by N_{tile} non-overlapping squares of side L_{sq} . When L_{sq} is one pixel, $N_{tile}(L_{sq})$ is the area of the object in pixels. For a self-similar object (Samson et al., 1987) ,

$$N_{tile}(L_{sq}) \sim L_{sq}^{-D_{tile}} . \tag{23}$$

This relation was fit to the data for the range of L_{sq} discussed above.

D_{cont} This fractal dimension is measured by the contour-dilation method (Kaye et al., 1987). The boundary of the object (including the boundaries of holes) is dilated by 2 pixels (one pixel on each side) in each dilation step N_d (Figure 8). If the contour is fractal, then

$$n(N_d) \sim N_d^{-D_{tile}} \tag{24}$$

$$n = \frac{A(N_d)}{1 + 2N_d} , \tag{25}$$

where $A(N_d)$ is the area of the thickened contour after N_d dilations and $1+2N_d$ is the thickness of the contour. The fractal dimension is obtained from (24) for $N_d \leqq 40$. After 40 dilations, the contour covers most of the object.

Calibration of the Automated Image Processing

The automated procedures for measuring shape parameters were tested on twelve well-characterized images. These images included published micrographs of experimentally generated clusters as well as synthetic fractal structures such as the Sierpinski gasket, the Vicsec cluster, and clusters generated using a diffusion-limited aggregation (DLA) model. The calibrations are summarized in Table 3. The "true" fractal dimensions for the soot particles and the gold colloid are taken from the slope of a two-dimensional density-density correlation (Weitz and Huang, 1984; Samson et al., 1987). These functions were not linear, so the value of D_{true} is uncertain, as indicated.

The three fractal dimensions are not equal. For smooth plane shapes , D_{sq} and D_{tile} are approximately 2, while D_{cont} is close to 1. This is expected because the boundary of such a shape is one-dimensional over length scales that are small compared to the contour radius of curvature. For fractal objects known to be self-similar over a wide range of length scales, such as the Vicsec cluster, Sierpinski Gasket, and DLA cluster, the three fractal dimensions are nearly equal. Since the soot and gold agglomerates were self-similar only over a limited range of length scales (Samson et al., 1987; Weitz and Huang, 1984), the agreement between the different estimates of the fractal dimension is reasonable.

RESULTS

Agglomerate Structure

Detailed structural measurements were made on 137 TiO_2 and Si agglomerates with mobility diameters between 49 and 763 nm. Figures 9 to 12 show representative particles whose measurements are given in Table 4. The TiO_2 agglomerates, such as those shown

in Figures 9 and 10, are comprised of very fine, partially fused primary particles. The slender agglomerate of Figure 9 (3837a) has low D_{sq} while the more compact particle of Figure 9 (3837b) has a lower aspect ratio but higher D_{sq}. The nominal mobility diameter of the DMA size cut was 257 nm, while d_A was about 200 nm for both agglomerates. Figure 10 shows agglomerates with an 87 nm nominal mobility diameter.

Figures 11 and 12 show silicon aggregates of equal electrical mobility. Particle 3942 (Figure 11) illustrates the structure that results from coagulation at low temperature with minimal coalescence. Particle 3978 (Figure 12) would have had similar structure before processing at 1100°C. The difference in D_{sq} between the two aggregates reflects their different aspect ratios (Table 4). D_{cont} is much lower for the more sintered agglomerate because of the smoothing of the boundary that occurs during sintering. However, D_{tile} is not sensitive to the cluster aspect ratio or fine structure, so it is similar for agglomerates 3942 and 3979.

The different appearances of the particles in Figures 9 to 12 are evident in the averages of the measurements for the different TEM samples (Table 5). The TiO_2 agglomerates had primary particle diameters of 7 to 32 nm, while the silicon primaries were generally greater than 17 nm. Silicon agglomerates processed at 1430 °C consisted of 1 - 2 dense spheres. For these fully sintered particles, D_{sq} and D_{tile} are close to 2, while D_{cont} is closer to 1. The more irregular, open structures of the agglomerates produced at lower temperatures result in lower D_{sq} and D_{tile}. While D_{sq}, D_{tile} and d_1 are nearly the same for the silicon processed at 900°C and 1100°C, D_{cont} is significantly lower for the more sintered particles. Table 5 shows that there is some biasing of the fractal dimension with size. Agglomerates with few primary particles tend to have high D_{sq} and low D_{cont}.

The fractal dimension D_β, which describes the scaling of the collection of particles, may be estimated by plotting d_A against R_g (Samson et al., 1987). The scatter in the R_g measurements (for a given mobility diameter) is larger than for the d_A measurements, so it is assumed in the regression analysis that all of the error is in the R_g measurements. Figure

13 indicates that there was no clear difference in D_β for the different samples. The expected result for spheres converges with the measurements for d_A~30 nm. The average fractal dimension for the entire data set was $D_\beta = 1.64$, which is consistent with the fractal dimensions measured for individual agglomerates. The fractal dimensions obtained from the projections are expected to be 10-15% lower than the fractal dimensions of the three-dimensional agglomerates (Samson et al., 1987; Rogak and Flagan, 1991b).

Mobility and Projected Area

The projected area diameter is plotted as a function of the mobility size cut in Figure 14. The correlation appears to be poor, but there is significant grouping of the data points. The groups correspond to the different number of charges q carried by the particles as they passed through the DMA. Wen and Kasper (1984) accounted for multiple charging by plotting the number distribution obtained for each size cut. This distribution has peaks corresponding to different values of q. By taking only the first peak (q=1), the multiple charging problem was eliminated at the expense of data on the larger, more highly charged particles. Our approach is slightly different, although it also relies on the grouping of the data.

In discussions of multiple charging it is convenient to introduce the electrical mobility of a particle z_q, since it is proportional to the number of charges q carried by the particle. Note that z_1 is a known, single-valued function of d_m. We assume that the size of the agglomerate is a smooth function f of z_1,

$$d_A = f(z_1) = f(\frac{z_q}{q}) \quad . \tag{26}$$

It is difficult to determine f uniquely for $q > 4$, since the difference in mobility of a particle carrying 4 or 5 charges is comparable to the scatter in the data. In terms of Wen and Kasper's (1984) correction procedure, the high-order peaks are not well defined. The

estimated average number of charges carried by the agglomerates in the present study was only 1.55, suggesting that the correction procedure described below is reasonable.

First, a low-order polynomial in the logs of the diameters was fit to the uncorrected data, producing a first estimate of $f(z_1)$. Next, data points were assigned integer values of q more consistent with $f(z_1)$. After recalculating the mobility diameters on the basis of the new values of q, the curve was refit to the data. The procedure was iterated until the fit could not be improved by changing q. It was found that the final values of q were not sensitive to the type of curve used in the fitting process or the initial assumed values of q. Figure 15 shows the data corrected using a cubic polynomial.

Using the measured areas and radii of gyration, it is possible to compare the model of Figure 1 with the measurements. To do this it is necessary to relate R_g measured in the projection with the true R_g of the 3-dimensional agglomerate. On the basis of simulations (Rogak and Flagan, 1991b), we assume that the true radius of gyration is a factor 1.18 higher than that measured in the micrographs. Using β=0.9, the measurements of d_A are plotted against the predicted $d_m(d_A, R_g, \lambda)$ in Figure 15. The predicted mobility diameters are 5-10% higher than those determined by the DMA, using the charging correction procedure described above.

Although the charge correction procedure appears robust and there is good agreement with the theory, the TiO_2 measurements were repeated using a wider range of sizes and better control of multiple charging. In the second series of TiO_2 experiments, multiple charging was confined to fewer than 5-10 % of the particles by taking size cuts whose diameters were always greater than the peak diameter of the distribution (Rogak et al., 1991a). Figure 16 shows the data without any corrections for multiple charging. One of the smaller particles appears to have been doubly charged, and two of the larger particles seem surprisingly small (possibly because of atypical particle orientations on the TEM grid), but otherwise the data are consistent with the corrected data discussed above. Both

sets of experiments suggest that $d_m \sim d_A$ for small particles and that even for d_m as large as 1000 nm ($d_m \sim 7.2\lambda$), d_A is only 10-20% lower than d_m.

Correlations between the mobility and length scales other than d_A were investigated by considering the deviations of the data from the d_A -d_m correlation. It was found that these deviations were not correlated with aspect ratios or fractal dimensions, suggesting that a multiparameter model will not fit the data significantly better. The scatter in the data is consistent with the standard deviation expected from the width of the DMA size cut and the errors inherent in the image processing.

CONCLUSIONS

Mobility or aerodynamic diameters of agglomerate particles have been traditionally related to the particle volume, using a single empirical shape factor. This factor depends on the particle structure and Knudsen number, but the exact role of these parameters has been unclear, particularly for fractal agglomerates.

An alternative to the shape factor has been proposed to predict the drag on a fractal agglomerate of arbitrary Knudsen number. The mobility diameter d_m of an agglomerate particle in the free-molecule regime is nearly equal to the diameter d_A of a sphere with the same projected area. In the continuum regime, d_m is nearly proportional to the radius of gyration R_g. The adjusted sphere interpolation can be used to estimate d_m in the transition regime, where d_m is comparable to the gas mean free path λ. The fractal dimension D_f and primary particle diameter d_1 do not influence $d_m(d_A, R_g, \lambda)$ strongly, but are needed to relate the agglomerate volume to d_A and R_g. The model is consistent with previous shape factor measurements, though quantitative comparisons are difficult, as D_f was not measured in the earlier studies.

In the present study, TiO_2 and silicon agglomerates were characterized using traditional shape parameters and several techniques to estimate D_f. It was found that D_f could be used to characterize changes in structure that were due to sintering or material

properties. Since the particles are not true fractals, measurements of D_f are sensitive to particle size and the measurement technique used. Supporting measurements of aspect ratio, primary particle size, projected area and radius of gyration can aid the interpretation of fractal dimensions. Fractal dimensions measured by the successive-squares (D_{sq}) or "tiling" (D_{tile}) algorithms were consistent with the scaling of area with radius, characterized by D_β. For most agglomerates $D_{sq} \sim 1.5 - 1.8$, while $D_\beta = 1.64$.

For the agglomerates used in this study, $d_m \sim d_A$ if $d_m < 400$ nm. For larger agglomerates, d_m was slightly greater than d_A, consistent with model predictions using the measurements d_A and R_g. However, even for agglomerates with mobility diameters as large as 763 nm, the difference between d_m and d_A is less than 25% and barely larger than experimental uncertainty.

Although the agreement between the drag model introduced here and experimental results is encouraging, there is need for research on several related topics. Uncertainties in the continuum regime mobility diameter and the relation between agglomerate mass and area limit the precision of the model. As these relations become better understood, the drag model proposed here may be useful in the interpretation of aerosol measurements involving the mobility of agglomerates.

Acknowledgements

This research was supported by the International Fine Particle Research Institute and by the U.S. Department of Energy under grant No. DE-FG22-90PC90286.

REFERENCES

Allen, M. D., Moss, O. R. and Briant, J. K. (1978). *J. Aerosol Sci.* **10**: 43-48.

Allen, M.D., Briant, J.K and Moss, O.R. (1979). *Am. Ind. Hyg. Assoc. J.* **40**:474-481.

Chan, P. and Dahneke, B. (1981). *J. Appl. Phys.* **52**: 3106.

Chen, Z. Y., Meakin, P., and Deutsch, J. M. (1987). *Phys. Rev. Lett.* **59**: 2121.

Cheng, M.T., Xie, G.W., Yang,M., and Shaw., D.T.(1991). *Aerosol Sci. Technol.* **14**:74-81.

Colbeck, I., Eleftherjadis, K. and Simons, S. (1989). *J. Aerosol Sci.* **20**:875-878.

Dahneke, B. E. (1973). *J. Aerosol Sci.* **4**:163-170.

Davies, C.N.(1979). *J. Aerosol Sci.* **10**:477-513.

Eisner, A.D. and Gallily, I.(1981). *J. Colloid and Interface. Sci.* **81**:214-233.

Flagan, R. C., and Friedlander, S. K. (1978), in *Recent Developments in Aerosol Science* (D. T. Shaw, ed.). Wiley, New York, NY, pp. 25-29.

Forrest, S.R. and Witten , T.A. (1979). *J. Phys A.: Math. Gen.* **12**:L109-L117.

Friedlander, S. K. (1977). *Smoke, Dust, and Haze*. Wiley Interscience, New York, NY.

Fuchs, N. A. (1964). *The Mechanics of Aerosols*. Pergamon Press, New York, NY.

Gentry, J.W., Mulholland, G.W., and Sullivan, F.(1988). in *Atmospheric Aerosols and Nucleation: Proc. of the 12th Int. Conference on Atm. Aerosols and Nucleation.* (Paul E. Wagner and Gabor Vali, eds.). Springer Verlag, New York, pp.116-119.

Hess, W., Frisch, H.L., and Klein, R. (1986). *Z. Phys. B - Condensed Matter* **64**:65-67.

Kalliomäki, P.L, Grekula, A., Hagberg, J. and Sivonen, S. (1987). *J. Aerosol Sci.* **18**:781-784.

Kasper, G. (1982). *Aerosol Sci. and Technol.* **1**:201-215.

Kasper, G., Niida, T., and Yang, M. (1985). *J. Aerosol Sci.* **16**: 535-556.

Kaye, B.H., Clark, G.G., Leblanc, J.E., and Trottier, R.A. (1987). *Part. Charact.* **4**:63-66.

Kops, J., Dibbets, G., Hermans, L., and Van de Vate, J. F. (1975). *J. Aerosol Sci.* **6**: 329-333.

Kousaka,Y., Okuyama, K., and Paytakes, A.C.(1981). *J. Colloid Interface Sci.* **84**:91-99.

Kunkel, W. B. (1948). *J. Appl. Phys.* **19**:1056.

Kütz, S. and Schmidt-Ott, A. (1990). *J. Aerosol Sci.* **21**:47-50.

Lahaye, J. and Prado, G. (1981), in *Particulate Carbon* (D.C.Segla and G.W. Smith , eds.). Plenum Press, New York, pp.33-51.

Lee, C.T. and Leith, D. (1989). *J. Aerosol Sci.* **20**:503-513.

Meakin, P.(1984). *J. Colloid Interface Sci.* **102**:491-504.

Meakin, P. (1986), in *On Growth and Form* (H.E. Stanley and N. Ostrowsky, eds.). Martinus Nijhoff, Dordrecht, pp. 111-135.

Meakin, P., Donn, B., and Mulholland, G.W.(1989). *Langmuir* **5**:510-518.

Medalia, A.I. and Heckman, F.A.(1969). *Carbon* **7**:562.

Mountain, R.D., Mulholland, G.W. and Baum, H. (1986). *J. Colloid Interface Sci.* **114**:67-81.

Neville, M. , Quann, R., Haynes, B., and Sarofim, A. F. (1982), in *Nineteenth Symposium (Int.) on Combustion.* The Combustion Institute, Pittsburgh, PA, pp.1441-1449.

Odumade, O. A. (1983). Ph. D. Thesis, University of Minnesota.

Okuyama, K. , Kousaka, Y., Tohge, N., Yamamoto, S, Wu, J.J, Flagan, R.C. and Seinfeld, J.H. (1986). *AIChe. J.* **2**:2010-2019.

Okuyama, K., Kousaka, Y. and Paytakes, A.C. (1980). *J. Colloid Interface Sci.* **81**:21-31.

Pich, J. (1969). *J. Colloid Interface Sci.* **29**: 91.

Quann, R., and Sarofim, A. F. (1982), in *Nineteenth Symposium (Int.) on Combustion.* The Combustion Institute, Pittsburgh, PA, pp.1429-1440.

Reist, P.C., Hsieh, M-T. and Lawless, P.A. (1989). *Aerosol Sci. and Technol.* **11**:91-99.

Rogak, S. N., and Flagan, R. C. (1990). *J. Colloid Interface Sci.* **134**:206-208.

Rogak, S.N., Baltensperger, U. and Flagan, R.C.(1991). *Aerosol Sci. and Technol.* (in press).

Rogak, S.N and Flagan, R.C.(1991a). *J. Aerosol Sci.* (submitted).

Rogak, S.N and Flagan, R.C.(1991b). *Part. Charact. Part. Systems.* (submitted).

Samson, R.J., Mulholland, G.W., and Gentry, J.W. (1987). *Langmuir* **3**: 272-281.

Schaefer, D.W. and Hurd, A.J. (1990). *Aerosol Sci. and Technol.* **12**:876 - 890.

Schmidt-Ott, A.(1988). *Appl. Phys. Lett.* **52**:954.

Seinfeld, J. H. (1986). *Atmospheric Chemistry and Physics of Air Pollution.* John Wiley, New York, NY.

Shon, S.-N. (1979). Ph.D. Thesis, State University of New York at Buffalo.

Smirnov, B.M. (1990). *Phys. Rep.* **188**:1- 78.

Stanley, H.E. (1986), in *On Growth and Form* (H.E. Stanley and N. Ostrowsky, eds.). Martinus Nijhoff, Dordrecht, p.22.

Stöber, W., and Berner, A. (1969). *J. Colloid Interface Sci.* **29**: 710-719.

Tohno, S. and Takahashi, K. (1989). *J. Aerosol Sci.* **20**:1031-1034.

Tohno, S. and Takahashi, K. (1990). *J. Aerosol Sci.* **21**:719 - 732

Tohno, S. and Kanji, T. (1988). *Kona:Powder Science and Technology in Japan* **6**:2-14.

Van de Vate, J.F., Van Leewen, W.F., Plomp, A. and Smit, H.C.D. (1980). *J. Aerosol Sci.* **11**:67-75.

Vomela, R and Whitby, K. T. (1967). *J. Colloid Interface Sci.* **3**:331-363.

Weitz, D.A., and Huang, J.S. (1984), in *Kinetics of Aggregation and Gellation* (F.Family and D. P. Landau, eds.). Elsevier-North-Holland, Amsterdam, pp. 19-28.

Wen, H.Y and Kasper, G. (1984). *Aerosol Sci. and Technol.* **3**:397-403.

Wiltzius, P. (1987). *Phys. Rev. Lett.* **58**:710.

Table 1. Characteristics of aggregate particles studied by Vomela and Whitby (1967).

Volume Equivalent diameter d_v nm	Primary Particle diameter d_1 nm	Mobility Equivalent diameter d_m nm	material
50	32	67	soot
70	32	92	"
100	32	120	"
100	43	120	copper oxide
300	43	300	"

Table 2. Comparison of thermophoretic alignment time scale τ_T to Brownian rotation time scale τ_D.

d nm	D cm^2/s	V_T cm/s	τ_T/τ_D
50	2.4×10^{-5}	0.25	19
100	6.8×10^{-6}	0.23	3
1000	2.8×10^{-7}	0.1	0.03
2000	1.4×10^{-7}	0.09	.008

Table 3. Characteristics of images used for image-processing calibration.

Object	D_{cont}	D_{sq}	D_{tile}	D_{true}
rod (rectangle, 1:10 aspect ratio)	1.30	1.04	1.24	1
Circle	1.11	2.02	1.85	2
Square	1.10	2.06	1.85	2
Sierpinski Gasket, Stanley (1986)	1.57	1.68	1.51	1.52
Vicsec Cluster, Gentry et al. (1988)	1.49	1.55	1.48	1.46
DLA cluster, Meakin (1986)	1.67	1.82	1.65	1.67
Soot : Fig. 6a of Samson et al. (1987)	1.60	1.89	1.67	1.81-1.83
Soot : Fig. 6b of Samson et al. (1987)	1.75	2.00	1.73	1.87-1.92
Soot : Fig. 6c of Samson et al. (1987)	1.58	1.45	1.47	1.84-1.76
Soot : Fig. 6d of Samson et al. (1987)	1.58	1.69	1.53	1.77-1.80
Simulated Aggregate, Fig.13 of Samson et al. (1987)	1.64	1.89	1.67	1.70-1.89
Gold Colloid, Weitz and Huang (1986)	1.70	1.88	1.70	1.74-1.80

Table 4. Measured properties of agglomerates in Figures 9-12. Lengths are in nm.

			d_1			D_f				
Neg.	L/W	R_g	d_{fine}	d_{coarse}	d_A	D_{sq}	D_{tile}	D_{cont}	q	d_m
3837a	2.04	155	12	40	216	1.54	1.57	1.38	1	257
3837b	1.27	84	8	43	195	1.83	1.74	1.25	1	257
3850a	1.67	38	3	15	99	1.90	1.85	1.19	1	87
3850b	1.29	77	6	37	159	1.8	1.78	1.22	3	164
3850c	2.04	30	8	23	75	1.95	1.82	1.30	1	87
3850d	1.01	57	8	30	137	1.85	1.75	1.28	2	129
3979	2.28	315	13	140	357	1.34	1.60	1.27	2	341
3942	1.94	222	16	43	333	1.64	1.60	1.40	2	341

Table 5. Measurements of titania and silicon particles with 95% confidence intervals[a]. Lengths are in nm.

	T	d_m		d_1				D_f		
	°C		L/W	d_{fine}	d_{coarse}	L_{co}	L_{sk}	D_{sq}	D_{tile}	D_{cont}
			±0.4	±30%	±20%	±3	±4	±.06	±.04	±.04
TiO_2	500	87	1.74	7	25	22	20	1.83	1.76	1.30
TiO_2	500	121	1.93	9	27	27	24	1.76	1.70	1.31
TiO_2	500	257	1.94	9	32	26	19	1.74	1.67	1.36
Si	900	150	1.90	23	64	22	18	1.66	1.59	1.38
Si	900	212	1.71	24	54	20	15	1.73	1.68	1.27
Si	900	377	1.77	21	91	18	11	1.63	1.54	1.37
Si	900	411	1.82	28	81	19	12	1.59	1.58	1.37
Si	1100	68	1.43	36	86	13	15	1.96	1.82	1.23
Si	1100	212	2.03	20	107	17	14	1.64	1.65	1.27
Si	1100	377	2.03	17	151	15	12	1.67	1.64	1.24
Si	1430	377	1.56	223	322	13	7	1.95	1.86	1.18

[a] The number of images analyzed for each material and temperature was 12 ±4. Since this number varied, the confidence intervals are not the same for all averages. The value given in the table is the average confidence interval for each parameter measured, rounded upwards. It was assumed that the measurement error was normally distributed

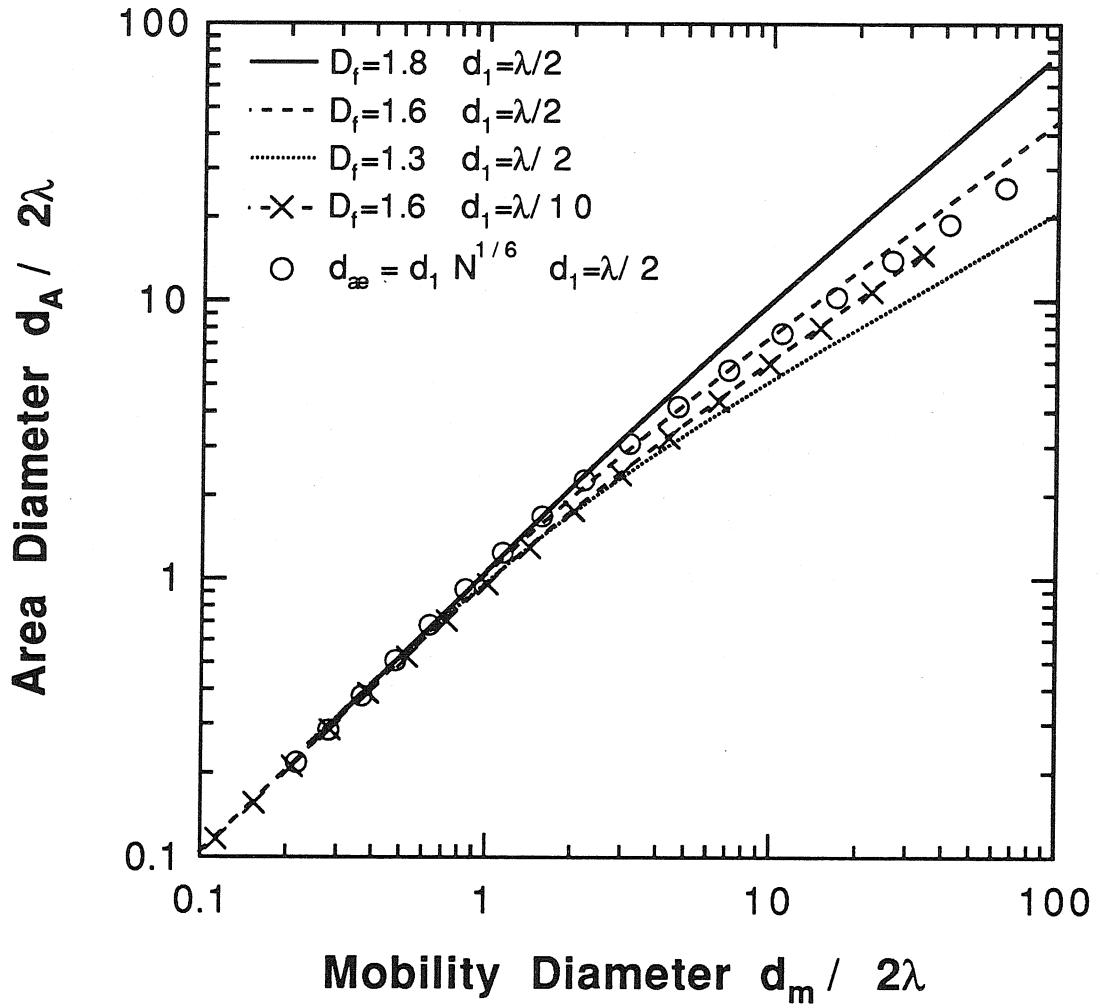

Figure 1. Area equivalent diameter d_A as a function of the transition regime mobility diameter d_m, for different fractal dimensions D_f and primary particle diameters d_1. (λ=gas mean free path) Correlations of the aerodynamic diameter with $N^{1/6}$ are nearly equivalent to the present model for $1.3 < D_f < 1.6$.

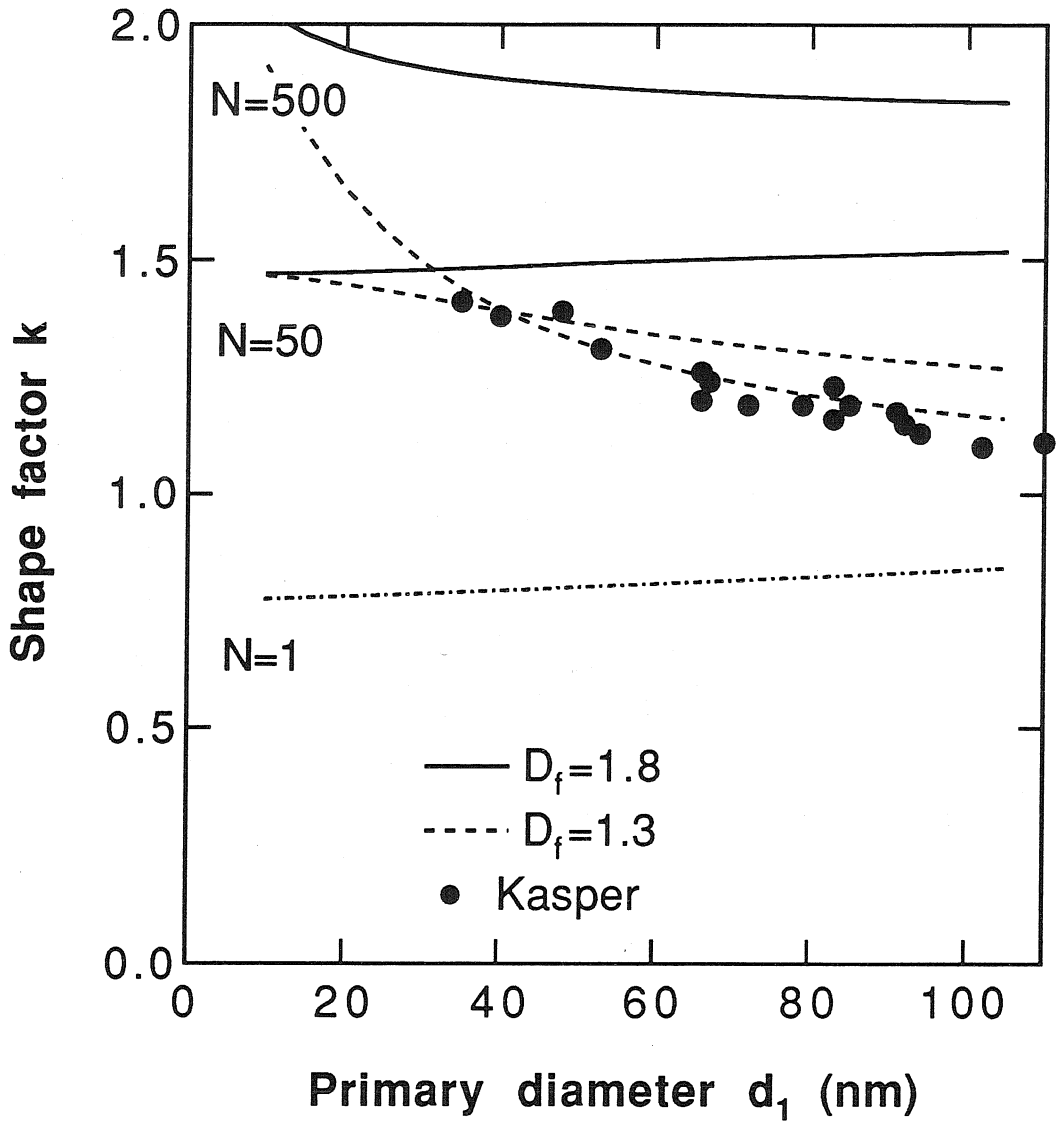

Figure 2. Shape factor k as a function of primary particle diameter d_1, fractal dimension D_f and number of primaries N. The model is compared to measurements for Fe_2O_3 chains (Kasper, 1982), assumed to have a specific gravity of 4.89.

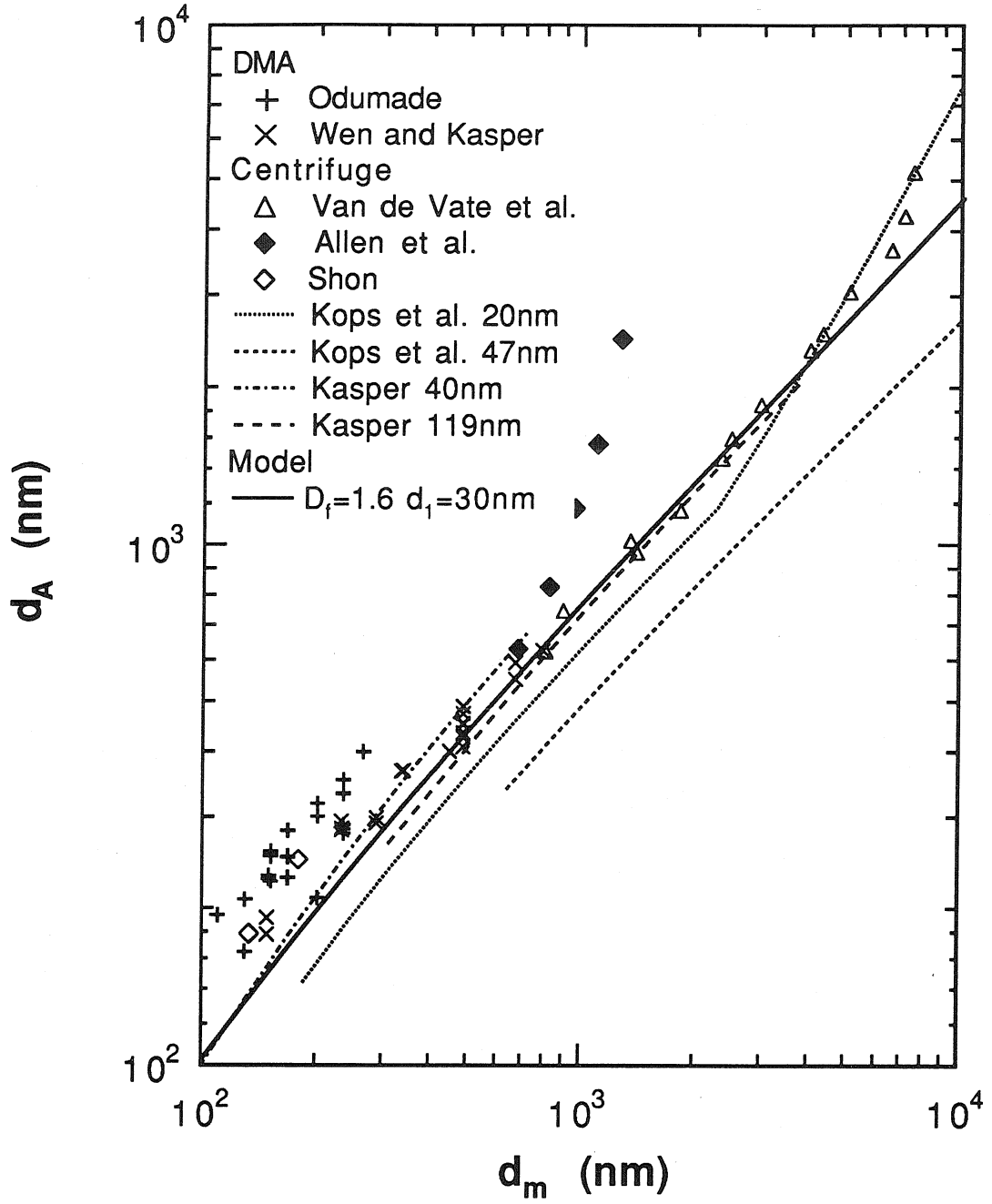

Figure 3. Projected area diameter d_A and mobility diameter d_m. Primary particle diameter d_1 ~33 nm for measurements by Odumade (1983) and 40-119 nm for measurements by Wen and Kasper (1984). For the centrifuge measurements d_1 was 25 nm (Allen et al., 1978), 33 nm (Shon, 1979), 20-26 nm (Van de Vate et al., 1980). For centrifuge measurements by Kops et al.(1975) and Kasper (1982), d_1 is indicated above. These data are compared to model predictions for D_f=1.6, d_1=30 nm, λ=69 nm.

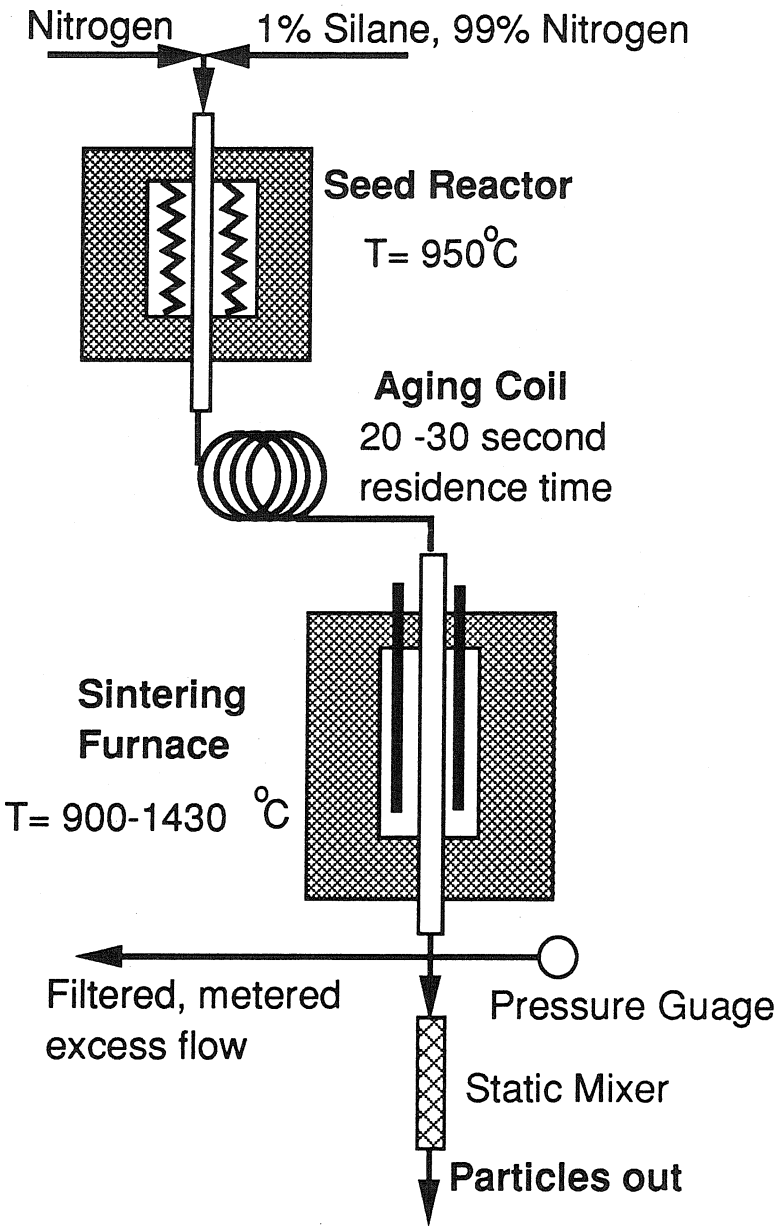

Figure 4. Silicon particles are produced in a seed reactor, allowed to coagulate in an aging coil, then processed in a sintering furnace.

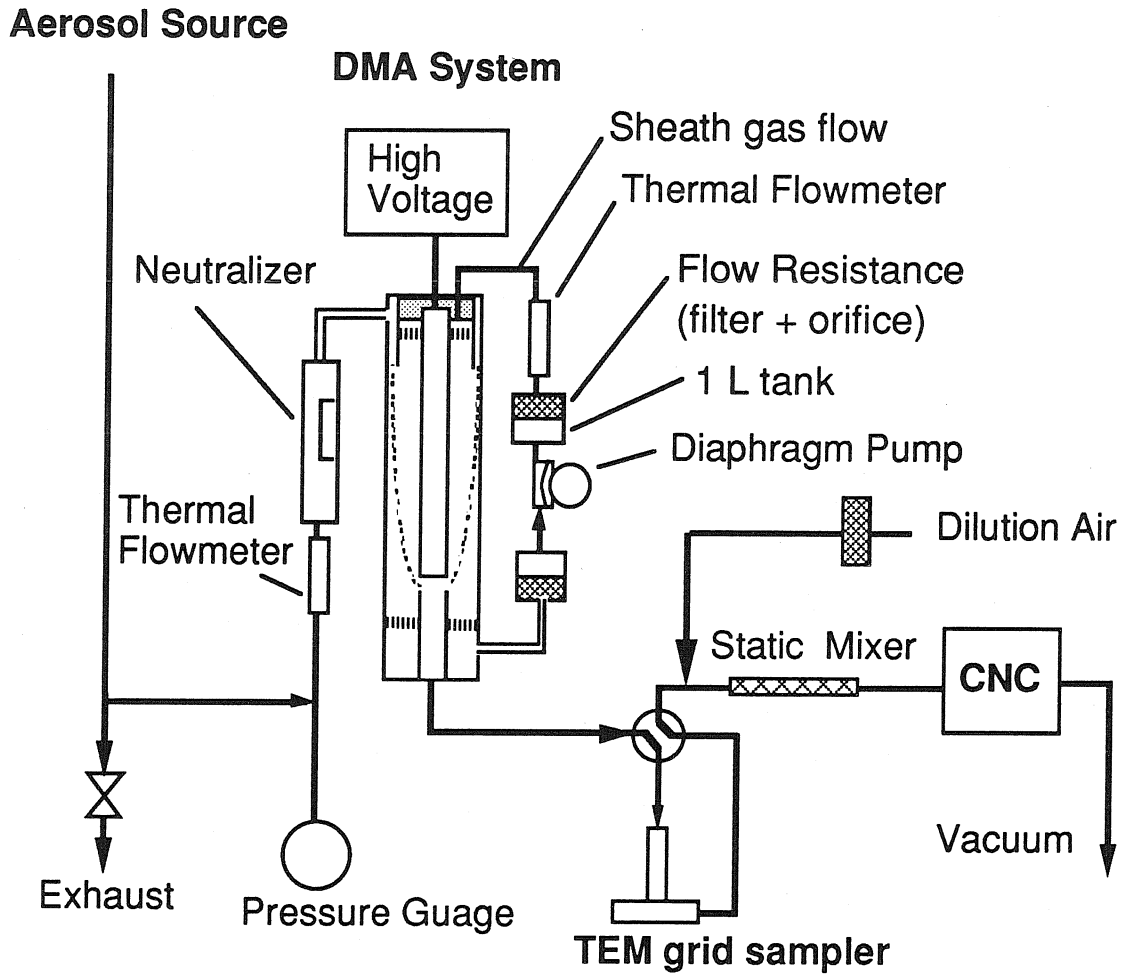

Figure 5. Mobility classification and sampling system.

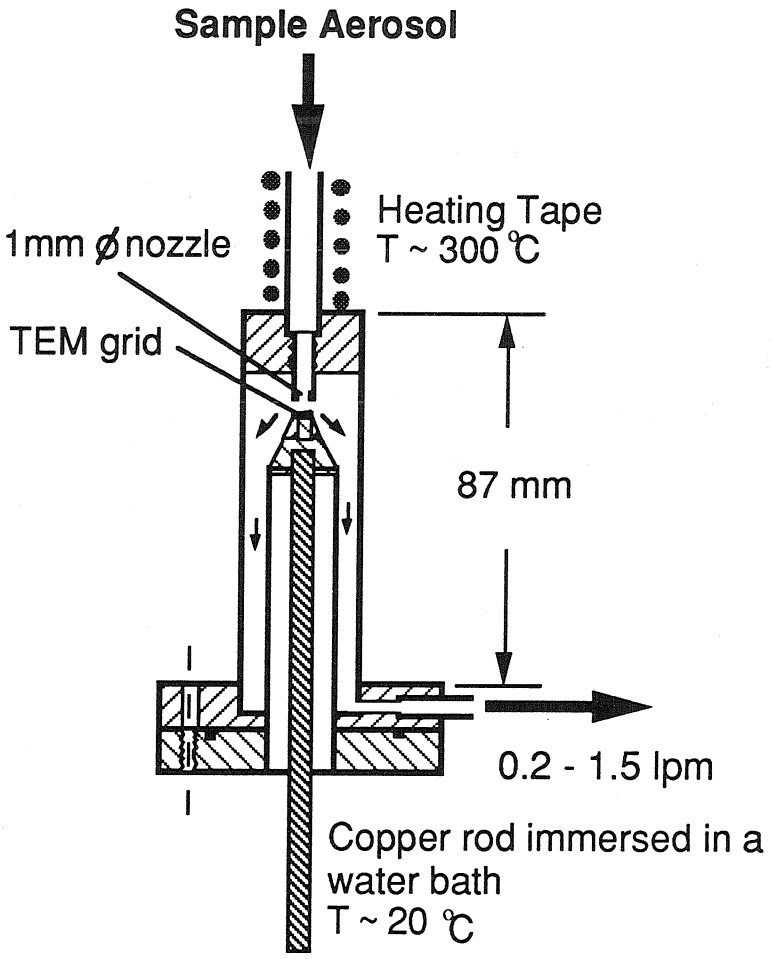

Figure 6. Thermophoretic sampler.

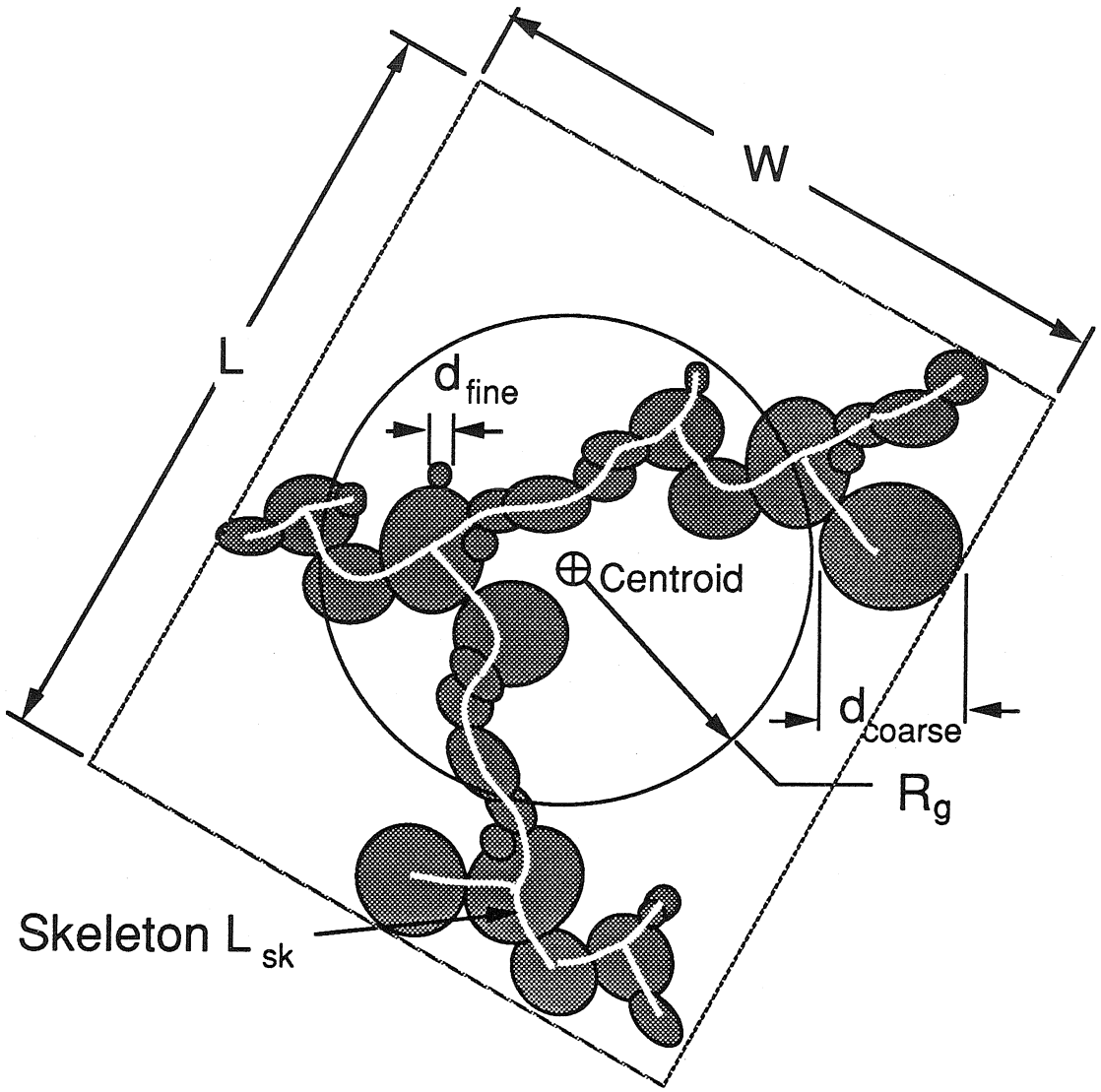

Figure 7. Traditional structural measurements made on an agglomerate.

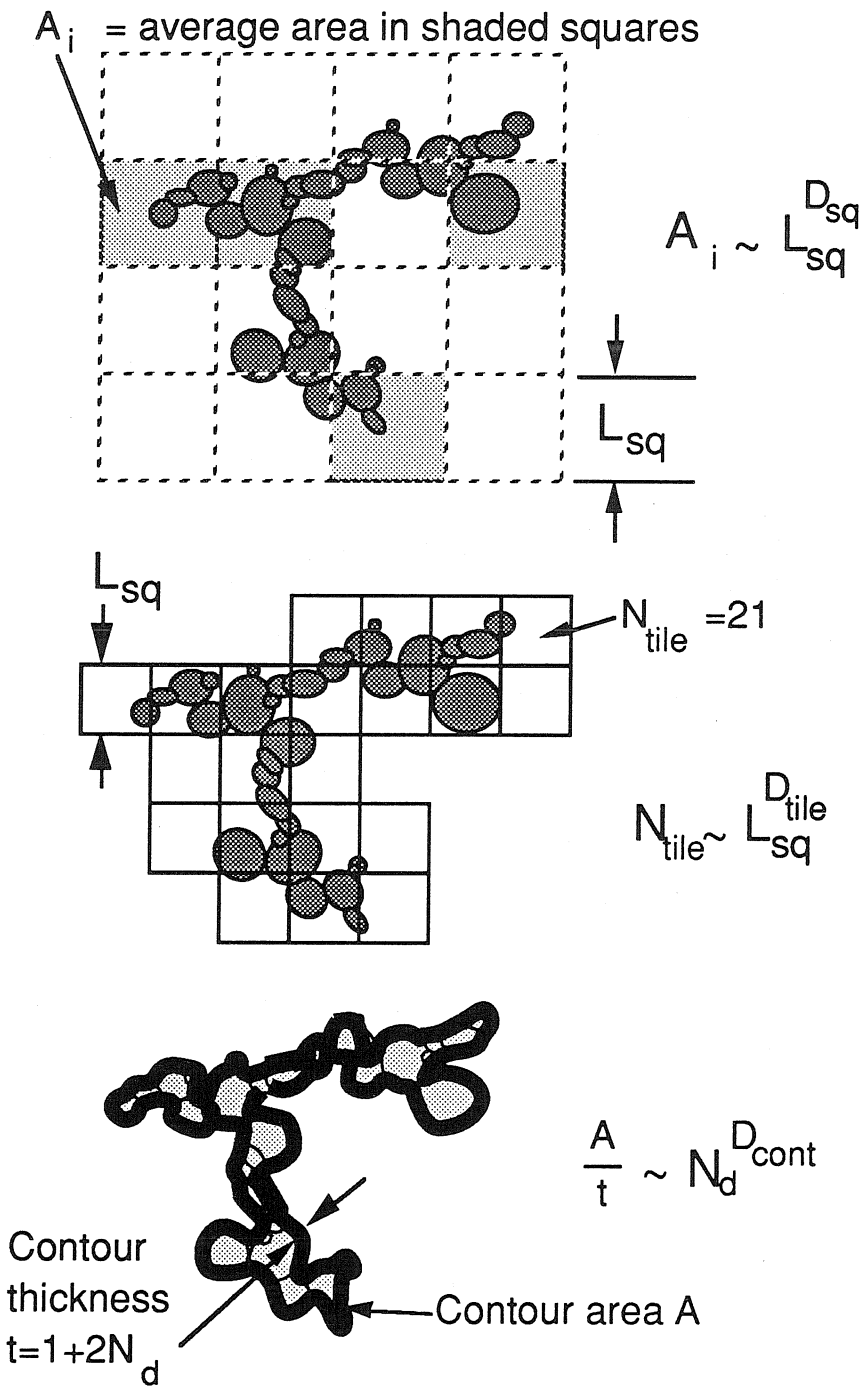

Figure 8. Algorithms used to measure fractal dimensions.

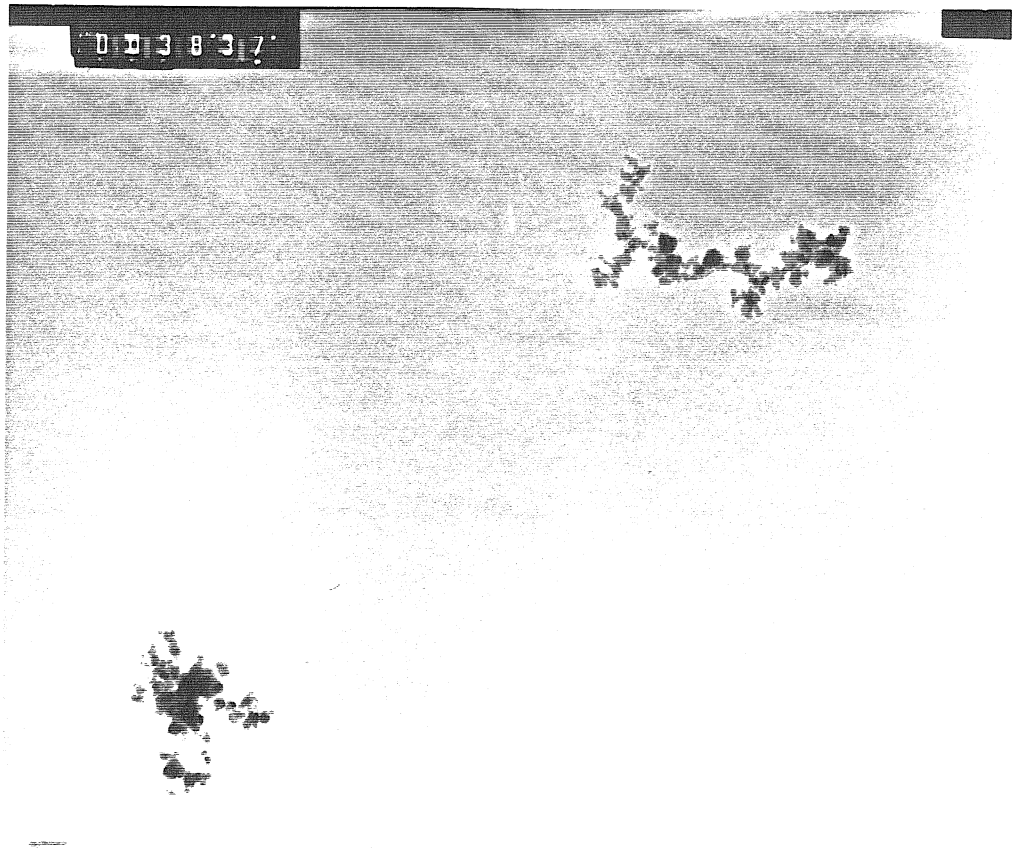

Figure 9. TiO_2 agglomerates of lengths 520 and 330 nm (Negative Nos. 3837a,b).

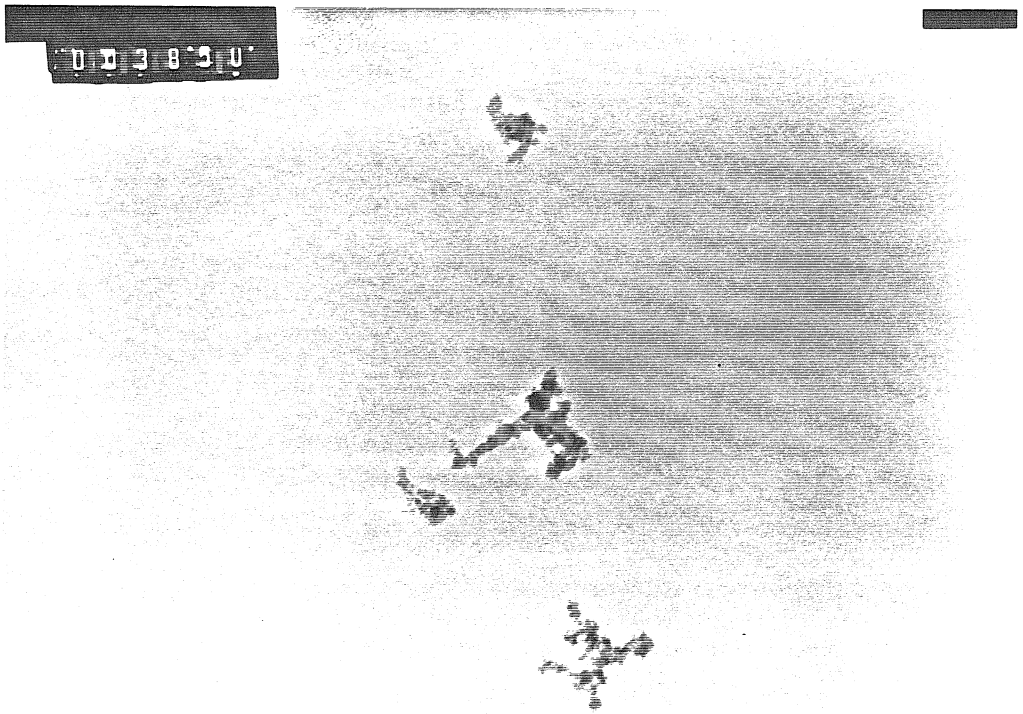

Figure 10. TiO_2 agglomerates; maximum agglomerate length is 280 nm.(Negative Nos. 3850a-d).

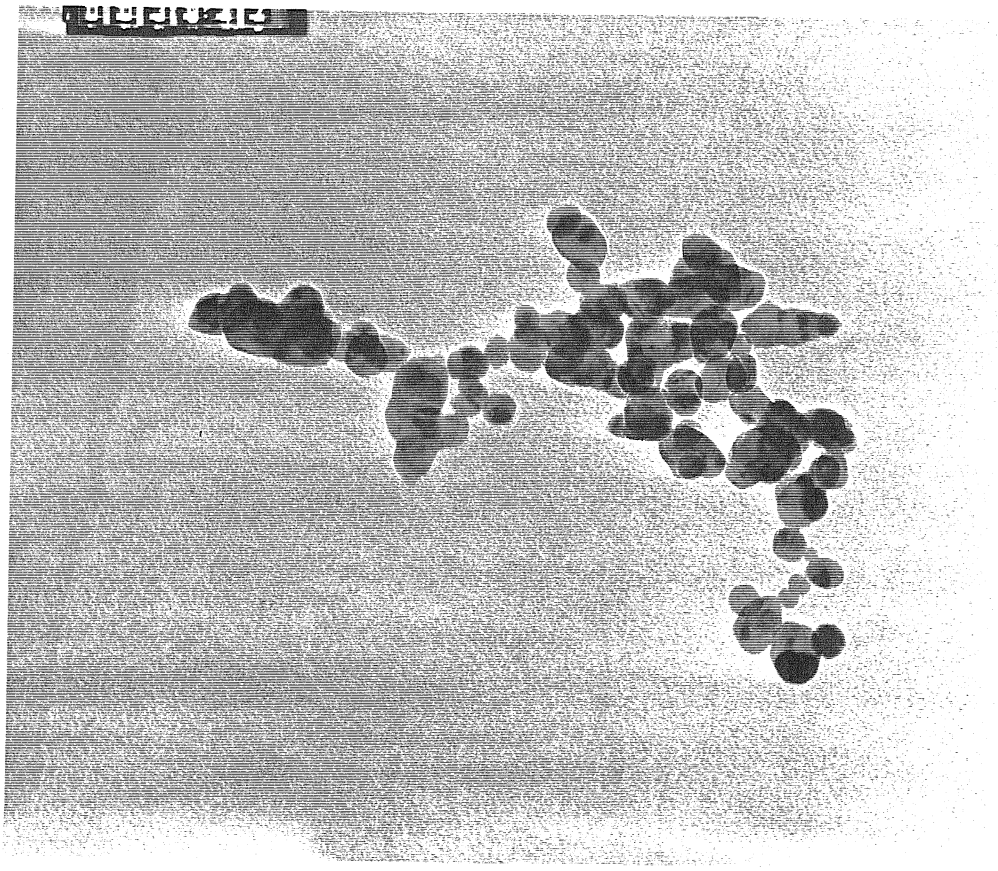

Figure 11. Silicon agglomerate with a length of 774 nm and median primary particle diameter of 37 nm. (Neg. No. 3842). Sintering furnace temperature was 900 °C.

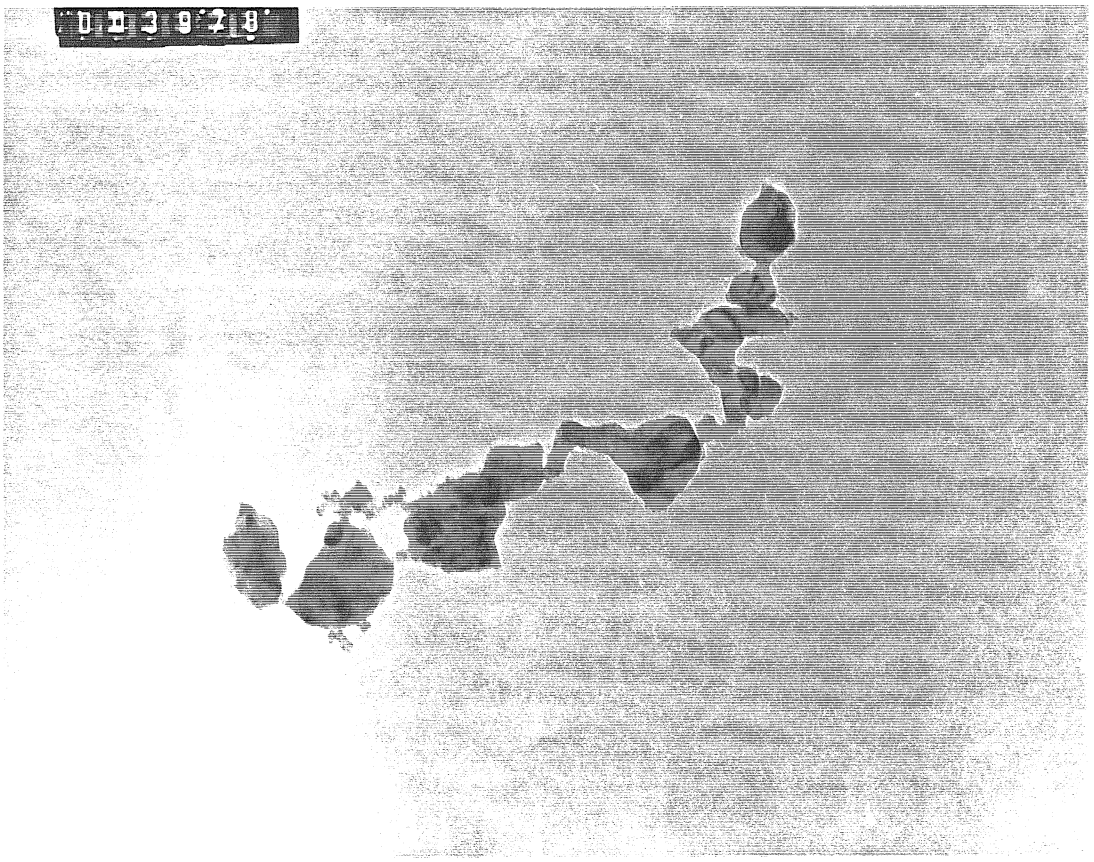

Figure 12. Silicon agglomerate with a length of 975 nm (Neg. No. 3978) Sintering furnace temperature was 1100 °C.

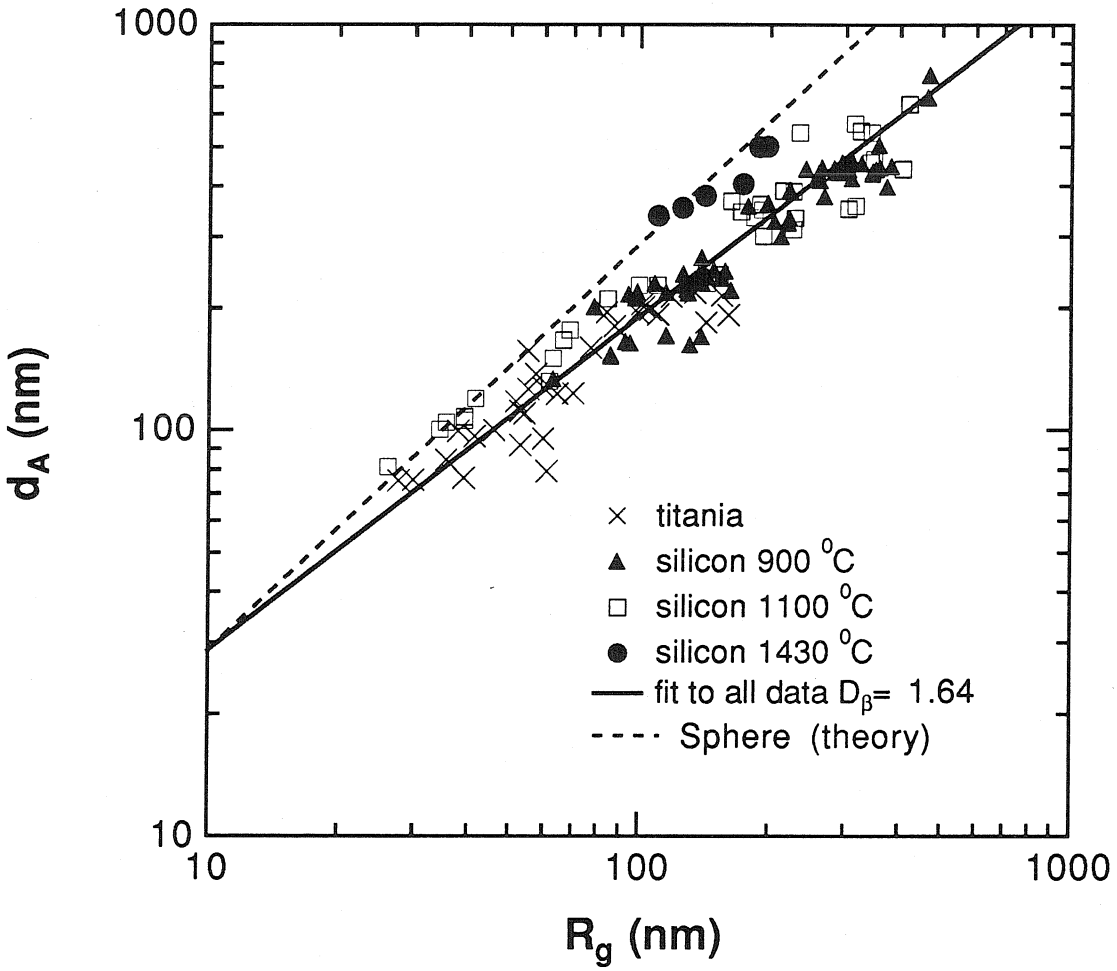

Figure 13. Area diameter d_A of agglomerates as a function of radius of gyration R_g. The slope of the data indicates that D_β = 1.64±0.04.

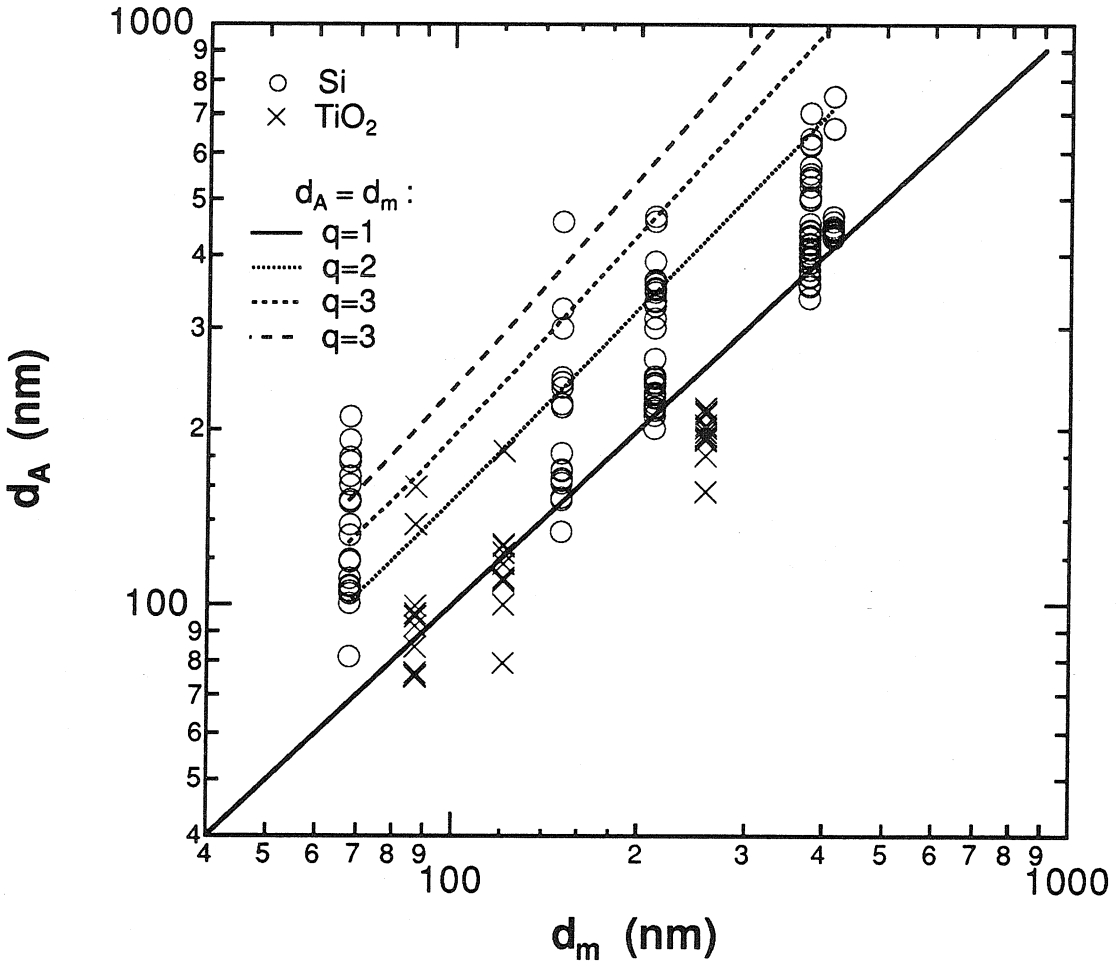

Figure 14. Projected area equivalent diameter as a function of mobility diameter, assuming single charging only. Grouping of data points indicates that multiple charging occurred. If d_A=d_m, the data would lie on the family of curves shown above for q=1-4 charges per particle.

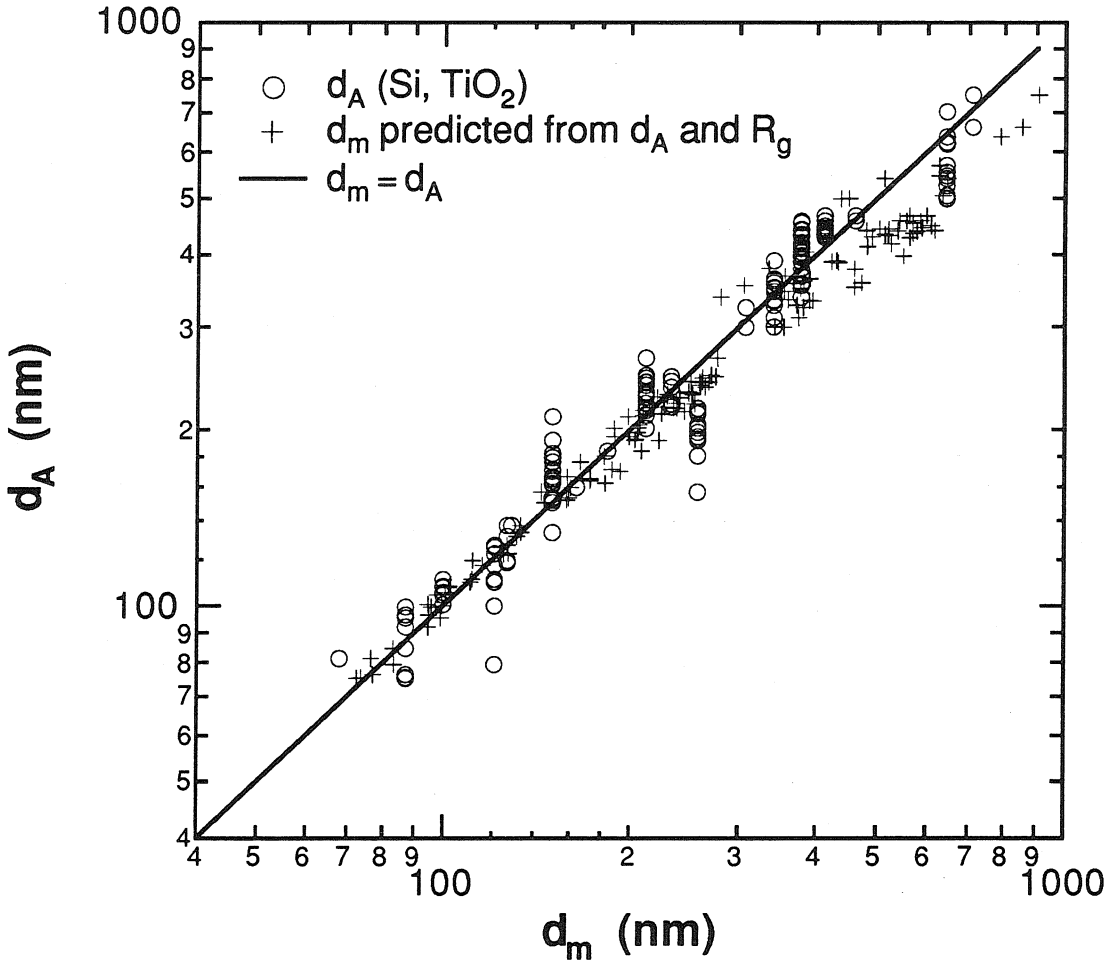

Figure 15. Projected area equivalent diameter d_A as a function of mobility diameter d_m, assuming that a cubic equation may describe $\ln(d_A)$ vs $\ln(d_m)$, and then iteratively improving the charge estimates.

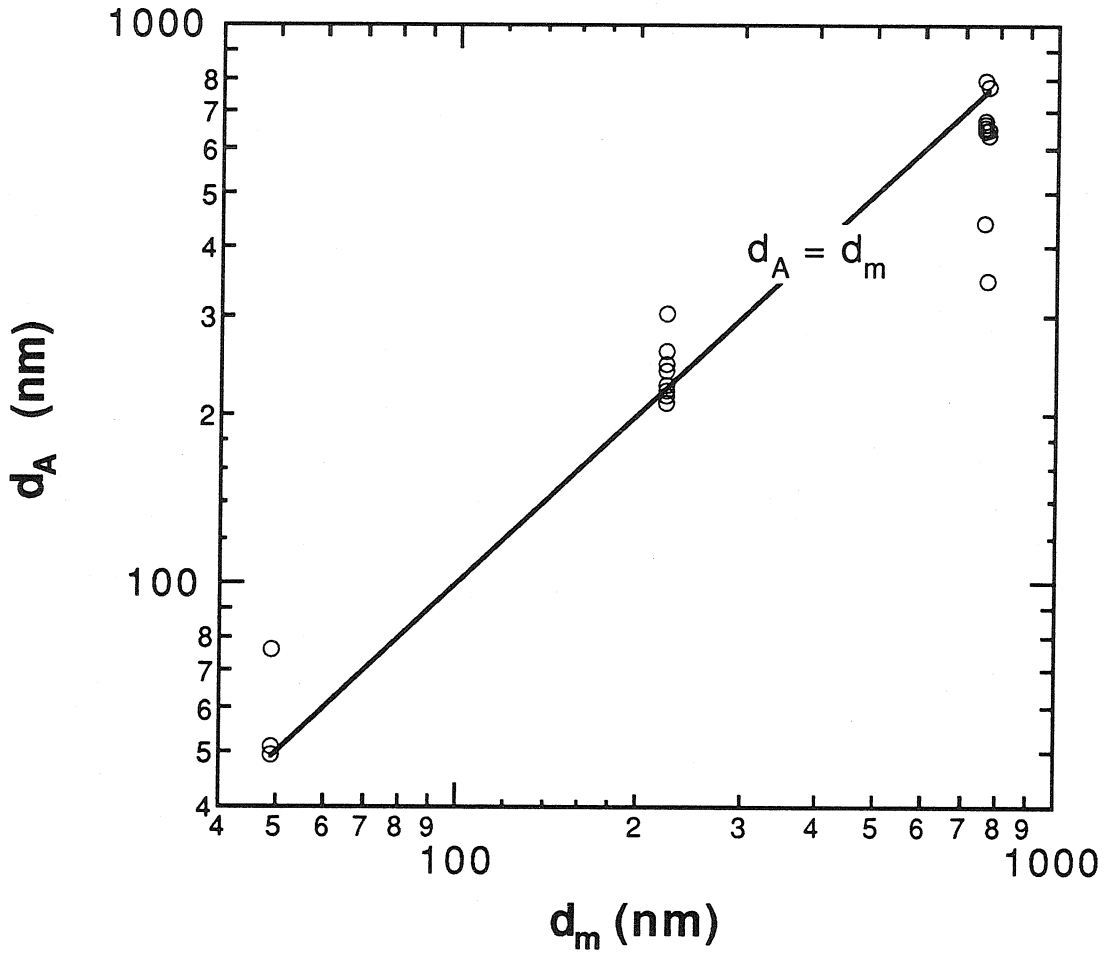

Figure 16. Projected area equivalent diameter $d_A$as a function of mobility diameter d_m for the second series of TiO_2 experiments, in which multiple charging was minimized by controlling the particle size distribution. Single charging assumed.

CHAPTER 6
MEASUREMENT OF MASS TRANSFER TO AGGLOMERATE AEROSOLS

S.N.Rogak, U. Baltensperger* and R.C.Flagan
California Institute of Technology, Pasadena CA 91125, USA

*On leave from Paul Scherrer Institute, CH-5232 Villigen PSI, Switzerland

Aerosol Science and Technology **14** in press

ABSTRACT

Mass transfer to agglomerate titanium dioxide aerosols produced in a thermal reactor was measured and compared to the mass transfer for spheres of the same mobility. The material transferred to the particles was ultrafine radioactive lead clusters produced via the decay chain of ^{227}Ac. Lead attachment rate was measured with an epiphaniometer, a device that mixes a fixed concentration of radioactive lead atoms with the sample for a period of several minutes and then measures the quantity of lead attached to the particles. In the free-molecule regime, where the particle diameter is small compared to the mean free path of the gas and the diffusing species, previous studies have shown by theory and experiment that the mass transfer to an aerosol is inversely proportional to the particle mobility. This study showed that this is also true for particles in the transition regime, where the particle diameter is comparable to the mean free path. Further, the mass-transfer rate is shown to be independent of particle shape for particles of the same mobility, at least when the mean free paths of the gas and the diffusing species are comparable.

INTRODUCTION

Mass transfer to aerosol particles is an important process in many natural and industrial systems. For example, the enrichment of atmospheric aerosols with heavy metals has been attributed to condensation of metal vapors on particle surfaces in combustion systems (Davison et al., 1974). The transport of organics to a particle is an important mechanism in soot formation (Harris and Wiener, 1983). In addition to these examples involving the transport of molecules, mass transfer of ultrafine particles plays an important role in powder synthesis (Wu and Flagan, 1987), the attachment of radon progeny to aerosols (Porstendörfer and Mercer, 1978) and in the measurement of atmospheric aerosols with the recently developed epiphaniometer (Baltensperger et al., 1990). This instrument measures the attachment rate of hydrated radioactive lead atoms to an aerosol sample. For each of these systems, it is critical to understand the relationship between the mass transfer to a particle and its physical characteristics.

Theoretical descriptions of mass transfer to particles have been based traditionally on the assumption that the particles are dense spheres. However, many combustion systems emit fumes consisting of agglomerates of tiny spherules. The structure of these agglomerates has been described as "fractal" or "self-similar" (Forrest and Witten, 1979; Meakin, 1984; Smirnov, 1990). Although the usefulness of the fractal model as a predictive tool is still an active area of research, such models are useful in characterizing the structure. A collection of fractal agglomerates obeys two important scaling relationships. First, every member of the collection has a fractal structure. This is indicated by the correlations $C(r)$ between the density $\rho(\mathbf{r}')$ at a position $\mathbf{r}'$ in the agglomerate and that at neighboring locations $\rho(\mathbf{r}'+\mathbf{r})$,

$$C(r) = <\rho(\mathbf{r}'+\mathbf{r})\rho(\mathbf{r}')> \sim r^{Da-3} \quad , \tag{1}$$

where the averaging takes place over all points in the agglomerate. The scaling parameter D_α is a fractal dimension (Meakin, 1984). The entire collection also satisfies a power relation between the mass m of each particle and its radius of gyration R_g,

$$m \sim R_g^{D\beta} \tag{2}$$

where D_β is another fractal dimension. In general the two fractal dimensions are not equal, but $D_\alpha = D_\beta$ for collections of large agglomerates in which there is no rearrangement during the growth process (Meakin, 1984). Such collections are produced in the cluster-cluster aggregation models that have been developed to simulate agglomerate aerosol formation.

Because of the complex structure of some agglomerates, many length scales may be required to describe all of the important properties of the particle. As mentioned above, the mass or volume-equivalent radius may be related to the radius of gyration through a fractal dimension. Another important length is the hydrodynamic radius R_H, the radius of the sphere that experiences the same drag as an agglomerate when both particles are moving at the same speed in the same gas. In the continuum regime, when the gas mean free path λ is smaller than R_H, R_H typically scales with R_g. In the free-molecule regime, where the particle diameter is small compared to the mean free path λ, the drag is determined by the impingement rate of gas molecules on the surface so R_H is proportional to the projected area-equivalent radius. When the fractal dimension D_β is less than two, the area-equivalent radius scales as $R_g^{D\beta/2}$ (Schmidt-Ott et al., 1990; Weitz and Huang, 1984). In this case the continuum and free-molecule hydrodynamic radii may be quite different.

The mass-transfer problem can be described by length scales analogous to those given above. Figure 1 illustrates an agglomerate and its mass-transfer-equivalent sphere (radius R_D) that are exposed to the same environment and have same surface sticking probabilities. The mean free path of the diffusing species is λ_D. The free-molecule (i.e. kinetic) regime mass transfer should be well correlated with drag because both processes

are controlled by the molecular impingement rate. Simulations by Meakin et al.(1989) have shown that the mass-transfer radius is nearly the same as the mobility-equivalent radius. These results have been corroborated experimentally by Schmidt-Ott et al. (1990). The low Reynolds number continuum regime drag is determined by the creeping flow equations. The corresponding mass transfer is described by the diffusion equation. Although not identical, the behavior is similar for both processes. For example, the mass-transfer-equivalent radius of a long slender rod (Hahne and Grigull, 1975) is only 3% larger than its orientation-averaged hydrodynamic radius (Kasper et al., 1985). In the transition regime, in general $R_H = R_H(\lambda)$ and $R_D = R_D(\lambda_D)$ so R_H and R_D will be different unless $\lambda_D \approx \lambda$.

In this paper we compare measurements of the drag and mass transfer for nearly spherical particles of ammonium sulfate, spherical polystyrene latex, and titanium dioxide agglomerates. For each aerosol, a narrow mobility range was selected with the differential mobility analyzer (DMA). This nearly monodisperse aerosol was mixed with a controlled concentration of radioactive lead atoms using the epiphaniometer (Gäggeler et al., 1989). The amount of lead attached to the particles was measured, giving an indication of the relative transfer rates of the lead to the spheres and agglomerates.

EXPERIMENTAL

The experimental system is shown in Figure 2. The main features are systems for generating spheres and agglomerates, a device for classifying the particles by mobility diameter $2R_H$ and a device for attaching and measuring the radioactive lead.

Aerosol Generation

Spherical particles were produced by the atomization of either polystyrene latex (PSL) suspensions or ammonium sulfate solutions using a constant output atomizer (Liu and Lee, 1975). Ammonium sulfate solution concentrations ranged from 0.05g/l to 80g/l

depending on the desired particle size range. PSL suspensions were formed by adding 2-5 drops of 10% solids to 100ml of water.

The agglomerates used in this study were TiO_2 particles formed by the thermal decomposition of the alkoxide titanium tetra-isopropoxide $Ti(OC_3H_7)_4$ under conditions similar to those described by Okuyama et al. (1986). The system used for this study was designed to produce a wide range of particle sizes. This was achieved by using a special alkoxide feed system and a fast-mixing furnace.

Liquid $Ti(OC_3H_7)_4$ was evaporated from a glass fiber wick in a stream of hot (120^0C) nitrogen (Figure 3). The wick was used to smooth flow fluctuations caused by the syringe pump liquid feed system. The vapor was carried through a water-jacketed line into the furnace. The water jacket was maintained at 60-80^0C in order to prevent condensation of the vapor. The alkoxide vapor was then mixed with a high-velocity jet of hot nitrogen within a MACOR™ (machinable glass) mixing chamber. The co-annular flow arrangement (Figure 2) and the use of several heating stages (Tc_1-Tc_4) made it possible to have a constant or slightly decreasing gas temperature as the aerosol flowed down to the sampling probe. The furnace temperature for all experiments was 500^0C. The sampling probe diluted and cooled the sample gas with room-temperature nitrogen blown through the walls of a porous tube. Both the titanium dioxide and atomization aerosol generators generate some water vapor. The relative humidity in the downstream instrumentation was estimated to be a few percent.

Size Classification

The aerosol was classified according to the electrical mobility of the particles using a TSI model 3071 differential mobility analyzer (DMA) set at fixed voltages and flow rates. Provided that the aerosol is singly charged, the output of the DMA is very monodisperse (Kousaka et al. 1985). For the operating conditions used in this study, the standard deviation of the mobility distribution was 6 to 10%. However, for particles with

mobility diameters larger than 100 nm, the ^{85}Kr charger used may produce large numbers of multiply-charged particles. The extent to which multiply charged particles contribute to the classified aerosol depends on the aerosol size distribution $n(D)=dN/d\log D$ and on the probability $P_i(D)$ that a particle of diameter D carries i charges. If the DMA is set for a diameter D_1, the size cut will also contain doubly-charged particles of diameter D_2. Similarly the sample includes particles with more than two charges. The ratio of the number of multiply-charged particles to singly-charged particles is

$$\psi = \frac{n(D_2)P_2(D_2)+n(D_3)P_3(D_3)+n(D_4)P_4(D_4)\ ....}{n(D_1)P_1(D_1)} \quad . \qquad (3)$$

As an example, consider the three titanium dioxide size distributions in Figure 4. The DMA data were inverted using Hoppel's method (1978) with modified Boltzman charging probabilities given by Kousaka et al. (1985), assuming that the charging probabilities for the agglomerates are the same as those for spheres with the same mobility. For a 49 nm mobility diameter size cut taken from distribution *a*, about 10% of the particles would be multiply charged. If smaller particles were taken from this size distribution, ψ would be much higher. Extracting larger particles would result in relatively fewer multiply-charged particles but the total number of particles in the sample would be greatly reduced. Therefore, the aerosol mean size was increased (distribution *b*) for measurements with the 223 nm size cut, resulting $\psi \sim 0.05$ to 0.08. Finally, much larger particles (*c*) were used for the 763 nm size cut in order to obtain a sample with the required number concentrations.

The size distribution at the entrance to the classifier was adjusted by varying the aerosol mass concentration or by electrostatic removal of charged particles after neutralization in a bipolar charger. Since the fraction of neutral particles decreases as the particle size increases, the electrostatic precipitator preferentially removes the larger particles. The precipitator was useful in adjusting aerosol distributions with small peak

diameters. As a result of these measures, the predicted fraction of multiply-charged particles was about 10% in the worst case and below 5% in most cases.

In order to extend the investigation as far as possible towards the continuum regime, very large particles were required. For this, low DMA flow rates and high voltages were needed. For these low flow rates it was necessary to calibrate the instrument using PSL particles. The analyzer voltages in this study were limited by the apparent production of particles by the DMA at potentials above 8000 volts.

It should be noted that long straight chain agglomerates may be alligned parallel to the electric field in the DMA, affecting the comparison of data obtained by different types of instruments (Wen and Kasper, 1984). For the less elongated particles seen in this study, orientation probably affects the mobility diameter by less than 10% (Rogak et al., 1991).

Mass Transfer Measurements

The epiphaniometer (Gäggeler et al., 1989) was used in conjunction with a TSI model 3065 condensation nucleus counter (CNC) to measure the average attachment rate of lead to the aerosol. Size-classified particles were diluted before the flow was split and sent to the CNC and the epiphaniometer. A static mixer was used to ensure that the number concentration was the same in both instruments.

The epiphaniometer is based on the decay chain of ^{227}Ac (Seelmann-Eggebert et al., 1981):

$^{227}Ac(T_{1/2}=21.8$ years) (β) —> $^{227}Th(T_{1/2}=18.7$ days) (α)—> $^{223}Ra(T_{1/2}=11.4$ days) (α)—> $^{219}Rn(T_{1/2}=3.96$ s) (α)—> $^{215}Po(T_{1/2}=.0018$ s) (α)—> $^{211}Pb(T_{1/2}=36.1$ min) (β)—> $^{211}Bi(T_{1/2}=2.17$ min) (α)—> $^{207}Tl(T_{1/2}=4.77$ min) (β)—> ^{207}Pb .

The half-lives of the isotopes are such that the epiphaniometer is a remarkably simple instrument. The aerosol sample is first introduced into a 2 liter exposure chamber. The actinium source at the bottom of this container provides a constant supply of ^{219}Rn gas. The radon decays with a half-life of 3.96 seconds to ^{211}Pb, which deposits on the

particles. Next, the stream of particles and unattached lead flows through a 1 m tube. The unattached lead diffuses to the walls of the tube while the aerosol continues on to a total particle filter located directly beneath an alpha detector. The attached ^{211}Pb concentration is measured via the α-decay of its daughter ^{211}Bi. The instantaneous rate of lead deposition on the filter can be deconvolved from the epiphaniometer signal using the known radioactive decay rates, as discussed in the data inversion section of this paper. This lead deposition rate is a function of the total "Fuchs surface" of the aerosol (Gäggeler et al., 1989), the lead number concentration N_{Pb} in the exposure chamber, and the residence time in the exposure chamber. The Fuchs surface is proportional to the aerosol number concentration N and the lead attachment or coagulation coefficient K . K is generally a function of particle size, shape and material as well as the lead cluster properties. Using the epiphaniometer to measure the Fuchs surface and dividing by the particle concentration we obtain a quantity proportional to K. The epiphaniometer response s is proportional to the aerosol Fuchs surface only when the lead concentration in the exposure chamber is unaffected by the aerosol. This is the case when most of the lead clusters are deposited on the walls of the instrument rather than on the particles. For large Fuchs surface, most of the lead produced in the chamber becomes attached to aerosol particles, resulting in saturation. When saturated, the detector count rate is s_{max}=330 Hz. For count rates less than 45% of this saturation activity, the epiphaniometer signal is linearly related to the Fuchs surface. The epiphaniometer response becomes significantly non-linear for higher count rates. A correction factor F was determined experimentally (Weber, 1990) as

$$F = 1 + 0.144\bar{s} - 0.0108\bar{s}^{2} - 4.88\bar{s}^{3} + 10.22\bar{s}^{4}, \qquad (4)$$

where $\bar{s} = s/s_{max}$ is the measured activity normalized by the saturation value. In order to obtain a quantity proportional to the Fuchs surface, the epiphaniometer response was multiplied by this factor. The correction was necessary for only one measurement.

Material properties of the aerosol would be expected to influence the process through a modified lead-particle sticking probability or changed electrostatic interactions. There has been much confusion about sticking coefficients of radon progeny (Ho et al., 1982); however, there is general agreement today that these sticking coefficients are equal to one (Hopke, 1990), as stated by Porstendörfer et al. (1979). Porstendörfer and Mercer (1978) and Gäggeler et al. (1989) found that the attachment of Radon daughters to particles is not greatly affected by electrostatic interactions. Therefore, the material properties are not expected to be important. This appears to be true for the present system, as discussed later. Therefore, relative differences in K for spheres and agglomerates of the same size may be attributed to particle shape.

Procedures

The first step in the experiment was the measurement and adjustment of the aerosol size distribution shape. Size distributions were measured with the DMA and CNC by stepping through 10 to 40 channels using, computer control.

Having adjusted the size distribution, the DMA was set to a fixed voltage. When the CNC readings stabilized, the aerosol was allowed to enter the epiphaniometer (Figure 2) . After 30 to 60 minutes, depending on concentrations, the flow was diverted to a thermophoretic sampler where particles were deposited on a transmission electron microscope (TEM) grid (Rogak et al. 1991) .

After measurements with a particular aerosol, the aerosol generator was changed and the tests were repeated with an aerosol of the same mobility but of different shape. Thus, the measured lead attachment rates for the spheres and the agglomerates can be directly compared.

Data Inversion

Since the ^{211}Pb atoms attaching to the aerosol have a half-life of 36.1 minutes, the ability of the epiphaniometer to detect short-term variations is limited. The system would have to operate several half-lives of ^{211}Pb in order to reach a steady state. In order to overcome this problem, an inversion algorithm was applied to the epiphaniometer data (Pandis et al., 1991). For the present data, a simplified inversion was used, as discussed below.

The epiphaniometer accumulates alpha counts for time intervals Δt , typically 5 to 30 minutes. The total number of counts in this interval Y_i depends on the amount of lead deposited during the count interval and also on previously deposited lead. After correcting for the time lag caused by the residence time in the exposure chamber and excluding the bismuth decay half-life, the average rate of deposition of lead over the count interval $i+1$ is approximately

$$f_{i+1} = \frac{Y_{i+1} - Y_i \exp(-\Delta t\, \lambda)}{1 - \exp(-\Delta t\, \lambda)} , \qquad (5)$$

where $\lambda \approx \frac{\ln 2}{36.1}$ min^{-1} is the decay constant leading to the alpha particles. A rigorous inversion giving a time resolution of several minutes includes the ^{211}Pb—> ^{211}Bi decay and the residence time distribution in the exposure chamber (Pandis et al., 1991). One can see from the simplified inversion scheme that it is difficult to measure a low concentration of aerosol immediately after accumulating a large amount of lead. For this reason, the experiments with low number concentrations and small particles were done before experiments with large particles or very high number concentrations. Also, a filter was placed upstream of the epiphaniometer whenever possible so as to reduce the amount of lead accumulating on the filter.

A few of the measurements involved particle concentrations above the linear range of the CNC , so that small corrections were required. This coincidence error, which is about 6% for the TSI model 3065 at concentrations of 10^4 cm^{-3}, has been taken into account in the data analysis.

RESULTS

Scanning electron micrographs (SEM) were taken of the epiphaniometer filters. Figures 5a-c show agglomerates with mobility-equivalent diameters of 49, 223 and 763nm. Figure 5a shows TiO_2 agglomerates of 1 to 4 primary particles. The visible particles are significantly larger than 49 nm. However, TEM samples showed particles with projected area-equivalent diameters of close to 49 nm, suggesting that the DMA was operating correctly but small particles may be deposited inside the 400 nm pores of the Nuclepore filter. Figure 5b shows TiO_2 and PSL particles of 223 nm mobility diameter. Because of the high filter loading of this sample, some of the larger agglomerates shown are probably formed on the filter. An ammonium sulfate sphere and TiO_2 agglomerate with 763 nm mobility diameters are shown in Figure 5c. The primary particle diameters for the agglomerates range from 40 to 120 nm for all size cuts. TEM analysis showed that all titanium dioxide particles were crystalline. The agglomerates are more compact than expected from cluster-cluster aggregation models (Meakin, 1984), suggesting that rearrangement had occurred before the sample was photographed. Artifacts caused by the sampling procedure are unlikely because similar structure is seen in the TEM samples in spite of very different sample handling (Figure 6). The structures of the agglomerates were characterized in terms of the projected area and an outer radius $R_{LW} = \frac{\sqrt{LW}}{2}$, where L and W are the dimensions of the smallest rectangle enclosing the agglomerate's image. It was found that the area scaled as $R_{LW}^{D_f}$ where D_f, an approximate measure of D_β (Samson et al., 1987), was between 1.3 and 1.6. On the basis of comparisons of the structure shown in each micrograph with other published pictures (Samson et al., 1987, Schmidt-Ott, 1988), the fractal dimension D_α of our agglomerates is between 1.7 and 2.1. The results of a detailed structural analysis are given in another paper (Rogak et al., 1991).

The epiphaniometer measurements are summarized in Figure 7. The measured quantity f is the rate at which the deposited lead atoms are counted by the detector (corrected for concentration effects), divided by the aerosol concentration. This can be converted to the average number of lead atoms per particle by multiplying by the epiphaniometer flow rate of 16.67 cm^3s^{-1} and using the theoretical detector efficiency of 0.2.

It can be seen that spheres and agglomerates with the same mobility have nearly the same f value. There appears to be no difference between the ammonium sulfate and PSL particles, so they are combined as "spheres" for calculation of the best-fit quadratic curve. The best-fit curves for the agglomerates and the spheres differ by less than 15 %, a difference apparently caused by a few outlying measurements. For the largest and smallest particles there is no measured difference between the spheres and agglomerates. This is expected for the smallest particles because the smallest titanium dioxide particles were nearly spherical.

We have compared the data with the coagulation theory for spheres based on the transition regime interpolation by Dahneke(1983). The coagulation frequency function K is given as a function of the radii R of the two spheres, their diffusivities D and transition regime interpolation factor β,

$$K=4\pi(R_1+R_2)(D_1+D_2)\beta \tag{6}$$

$$\beta = \frac{1+Kn_D}{1+2Kn_D(1+Kn_D)} \quad . \tag{7}$$

The Knudsen number is given by

$$Kn_D = \frac{\lambda_D}{R_1+R_2} \quad . \tag{8}$$

Here λ_D is the mean free path of the coagulation process, a function of the relative motions of the two particles.

$$\lambda_D = \frac{2(D_1+D_2)}{\sqrt{\frac{8kT}{\pi m_1}+\frac{8kT}{\pi m_2}}}, \tag{9}$$

where m is the particle mass, k the Boltzmann constant and T the temperature. The diffusivity of a sphere in a gas with viscosity μ and mean free path λ was taken as (Seinfeld, 1986)

$$D = kT\ \frac{1+\lambda/R\left(1.257+0.4\exp(-1.1R/\lambda)\right)}{6\pi\mu R}. \tag{10}$$

In previous studies, the attachment of uncharged radio-nuclides (with diffusivity D, mean free path λ and mean thermal speed $\bar{c}$) to particles of radius R has been modeled by an attachment coefficient B of the form (Porstendörfer et al., 1979; Ho et al., 1982)

$$B = \frac{4\pi DR}{\frac{4D}{\bar{c}RS}+\frac{1}{1+\lambda/R}}. \tag{11}$$

For sticking probability $S=1$, B is a simplification of the coagulation frequency function K that can be obtained by neglecting the diffusivity of the aerosol particle and the diameter of the smaller species. These are good approximations for the present conditions, since the particles studied were much larger than the lead clusters. Therefore, the coagulation coefficient estimates obtained here may be directly compared with previously reported attachment coefficients.

Comparisons of theory and experiment are difficult because the concentration and physical properties of the lead atom or cluster are not well known. The lead atom is probably surrounded by water or other molecules that lower the lead's density and diffusivity. Previous measurements suggest that the effective diameter of the lead cluster is between 0.5 nm and 3 nm (Porstendörfer et al., 1979; Strydom et al., 1990; Su et al.,1990). We have constrained the density by assuming that all molecules attached to the lead have a unit specific gravity. The concentration of the lead can be estimated

approximately from the known saturation behavior of the epiphaniometer discussed above. Given the saturation signal, the detector efficiency C=0.2 and the epiphaniometer flow rate Q=16.7 cm^3s^{-1}, the concentration of the lead in the exposure chamber is estimated to be

$$N_{Pb} \approx \frac{S_{max}}{CQ} \approx \frac{330 \text{ cps}}{0.2(16.7 \text{ cc/s})} = 100 \text{ cm}^{-3}. \qquad (12)$$

This estimate is an upper limit because it neglects the reduction in lead concentration due to wall losses in the exposure chamber. The lead deposition time scale τ depends on the lead distribution and the flow patterns in the exposure chamber. Assuming uniform plug flow, we obtain an upper limit on τ as the characteristic time $\tau=r^2/D$ for diffusion of the lead to the chamber walls. Depending on the lead cluster diffusivity D and the distance r over which it must travel, τ is between 2 and 20 minutes. This time is comparable to the 2-minute chamber residence time, so the effective lead concentration may be lower than the value given in (12). The predicted lead attachment rate is

$$f_{predicted}=CK N_{Pb} V_{ex} \quad cm^3s^{-1}. \qquad (13)$$

where K is the coagulation rate constant from equations (6)-(10), and V_{ex} is the volume of the exposure chamber. We obtain

$$f_{predicted}=4 \cdot 10^4 K \quad cm^3s^{-1}. \qquad (14)$$

This is in qualitative agreement with the data (Figure 7). The coagulation rate is plotted for lead cluster diameters of 0.6 and 1.5 nm. For a 0.6 nm lead diameter, the magnitude and shape of the coagulation curve are not consistent with the data. However, if the lead is assumed to have a 1.5 nm diameter, the shape of the coagulation curve is similar to that of the experimental data and

$$f_{measured} \sim 2 \cdot 10^4 K \quad cm^3s^{-1}, \qquad (15)$$

which is very close to the predicted epiphaniometer performance, given the uncertainty in the absolute lead concentration in the epiphaniometer. The mean free path λ_D of 1.5 nm lead-water cluster is about 69 nm, which is close to the gas mean free path of 65 nm.

The attachment coefficient of (11) is shown in Figure 7 to be nearly the same as the coagulation coefficient, provided that the same lead cluster properties are used in both models.

CONCLUSIONS

In this study we have directly compared the mass transfer to spheres and agglomerates with equal mobility. The aerosols used were titianium dioxide agglomerates, nearly spherical ammonium sulfate particles and polystryrene latex spheres. A differential mobility analyzer was used to select a narrow mobility range from each aerosol. This nearly monodisperse aerosol was mixed with a controlled concentration of radioactive lead atoms using the epiphaniometer. The amount of lead attached to the particles was measured, giving an indication of the relative transfer rates of the lead to the spheres and agglomerates.

It was found that the mass-transfer and mobility-equivalent diameters were nearly identical. This is reasonable because the mass and momentum transfer processes are analogous, at least if the mean free paths of the diffusing species and the gas molecules are similar. The predicted variation of attachment rate with particle size is identical to the data if the lead cluster is assumed to have a diameter of 1.5 nm. The mean free path of a lead cluster of this size is almost the same as the gas mean free path.

The observed equality of mass-transfer and mobility diameters may be partly due to the shape of the titanium dioxide agglomerates. If the mobility diameter is independent of the gas mean free path for an agglomerate of a certain shape, then the mass-transfer diameter for this agglomerate is expected to be independent of the diffusing species mean free path. By the same argument, if the free-molecule and continuum mobility diameters

are very different, as they would be for long chains, the mobility and mass-transfer diameters would be the same only if the relevant mean free paths were similar.

ACKNOWLEDGEMENTS

The authors gratefully acknowledge the financial support of the International Fine Particle Research Institute and the Swiss National Science Foundation. For the scanning electron microscopy we thank A. Portmann at the Institute for Inorganic Chemistry, University of Zurich, Switzerland.

REFERENCES

Baltensperger, U., Gäggeler, H.W., Jost, D.T., Emmenegger, M. and Nägeli, W. (1990). *Atmos. Environ.* **24A** (in press).

Dahneke, B. (1983), in *Theory of Dispersed Multiphase Flows* (R.E.Meyer, ed.). Academic Press, New York, pp.97-138 .

Davison, R.L., Natusch, D.F.S., Wallace, J.R and Evans, C.A. (1974). *Environ. Sci. Technol.* **8**:1107-1113.

Forrest, S.R. and Witten, T.A.(1979). *J. Phys A* **12**: L109-117.

Gäggeler, H.W., Baltensperger, U., Emmenegger, M., Jost, D.T., Schmidt-Ott, A., Haller, P. and Hofmann, M.(1989). *J. Aerosol Sci.* **20**:557-564 .

Hahne, E. and Grigull, U. (1975). *Int. J. Heat and Mass Transfer* **18**:751-767.

Harris, S.J. and Wiener, A.M.(1983). *Comb. Sci. Technol.* **31**:155-167.

Ho, W.L., Hopke, P.K and Stukel, J.J.(1982) *Atmos. Environ.* **16**:825-836.

Hoppel, W.A.(1978). *J. Aerosol Sci.* **9**:41-54.

Hopke,P.K.(1990). 3rd International Aerosol Conference, Kyoto, personal communication.

Kasper, G., Niida, T. and Shang, M.(1985). *J. Aerosol Sci.* **16**:535-556.

Kousaka,Y., Okuyama,K. and Adachi, M.(1985). *Aerosol Sci.Technol.* **4**:209-225.

Liu, B.Y. and Lee, K.W.(1975). *Am. Ind. Hyg. Assoc.* **36**:861-865.

Meakin, P.(1984). in *On Growth and Form: Fractal and Non-Fractal Patterns in Physics* (H.E. Stanley and N. Ostrowsky, eds.).Martinus Nijhoff, Hingham, MA, 111-135.

Meakin, P., Donn, B. and Mulholland, G.W.(1989). *Langmuir* **5**:510-518.

Okuyama, K., Kousaka, Y., Tohge, N., Yamamoto, S., Wu, J.J., Flagan, R.C. and Seinfeld, J.H.(1986).*AI. Che. J.* **2**:2010-2019.

Pandis, S.N., Baltensperger, U., Wolfenbarger, J.K. and Seinfeld, J.H.(1991). *J. Aerosol Sci.* (in press).

Porstendörfer, J. and Mercer, T.T.(1978). *J. Aerosol Sci.* **9**:469-474.

Porstendörfer, J., Röbig, G. and Ahmed, A.(1979).*J. Aerosol Sci.* **10**:21-28.

Rogak, S.N., Nguyen, H.V, Flagan, R.F.(1991). submitted to *J. Aerosol Sci.*

Samson R.J., Mulholland, G.W. and Gentry, J.W. (1987). *Langmuir* **3**:272-281.

Schmidt-Ott, A., Baltensperger, U., Gäggeler, H.W. and Jost, D.T.(1990).*J. Aerosol Sci.*, **21**:711-717.

Schmidt-Ott, A. (1988). *Appl. Phys. Lett.* **52**:954-956.

Seelmann-Eggebert,W., Pfennig, G., Münzel, H. and Klewe-Nebius, H.(1981). Karlsruher Nuklidkarte, 5. Auflage, Kernforschungszentrum Karlsruhe.

Seinfeld, J.H.(1986). *Atmospheric Chemistry and Physics of Air Pollution.* John Wiley, New York, p.317.

Smirnov, B.M. (1990). *Phys. Rep.* **188**:1-78.

Strydom, P., Leuschner, A.H. and Stoker, P.H.(1990) *J. Aerosol Sci.* **21**:859-873.

Su, Y.F., Cheng, Y.S., Newton, G.J. and Yeh, H.C.(1990). *J. Aerosol Sci.* **21**:785-788.

Weber, A. (1990). Paul Scherrer Institute, Villigen, Switzerland, unpublished results of Ph.D. thesis.

Weitz, D.A. and Huang, J.S. (1984). in *Kinetics of Aggregation and Gellation* (F. Family and D.P. Landau, eds.). North Holland, 19-28.

Wen, H.Y. and Kasper, G.(1984). *J. Aerosol Sci. Technol.* **3**:397-403.

Wu, J.J. and Flagan, R.C. (1987). *J. Coll. Interface Sci.* **123**:339-352.

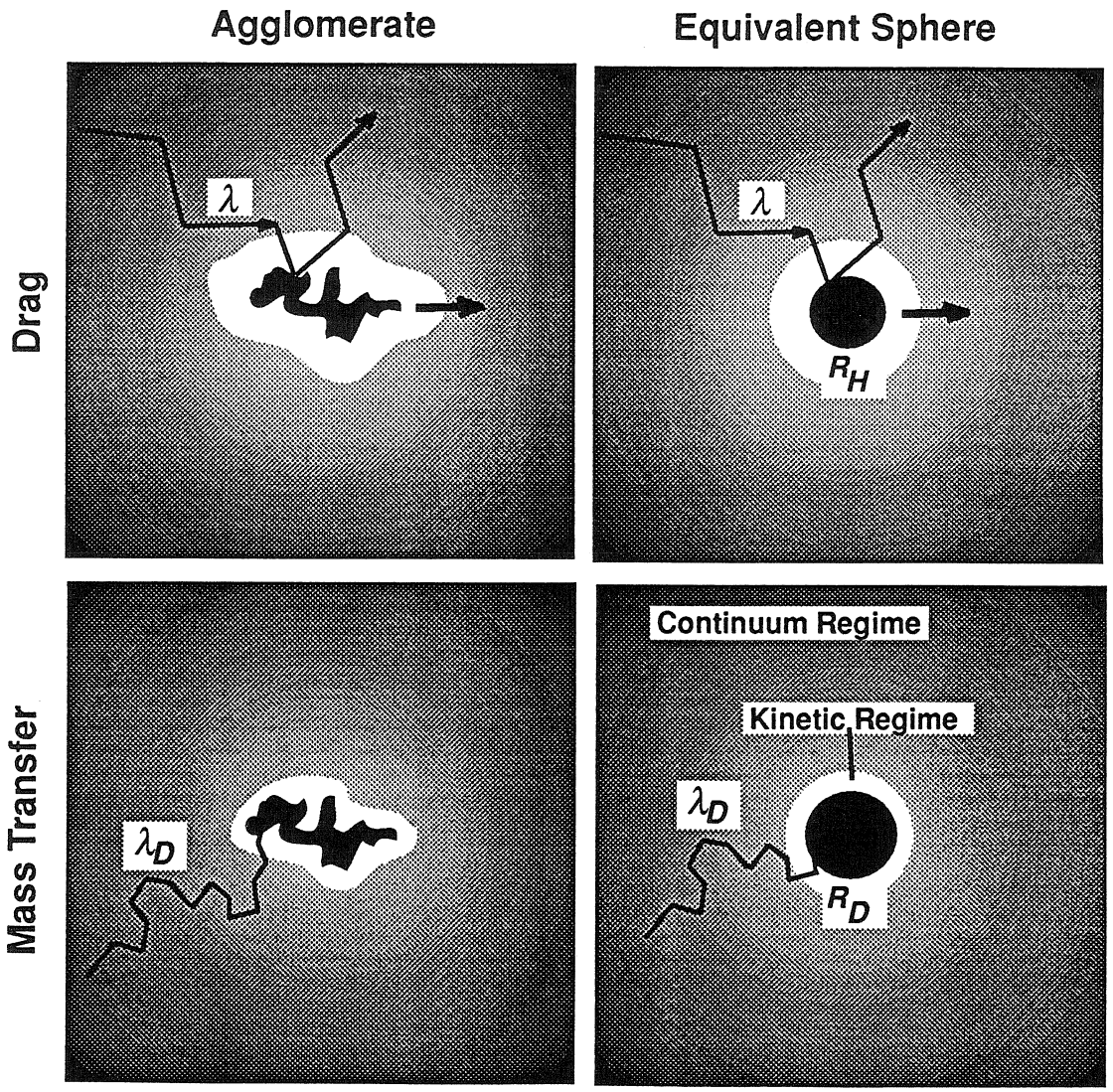

Figure 1. The orientation-averaged drag on an agglomerate can be represented by a drag-equivalent sphere of radius R_H which is in general a function of the gas mean free path as well as the geometry of the agglomerate. Mass transfer is analogous though the relevant mean free path is that of the transported species.

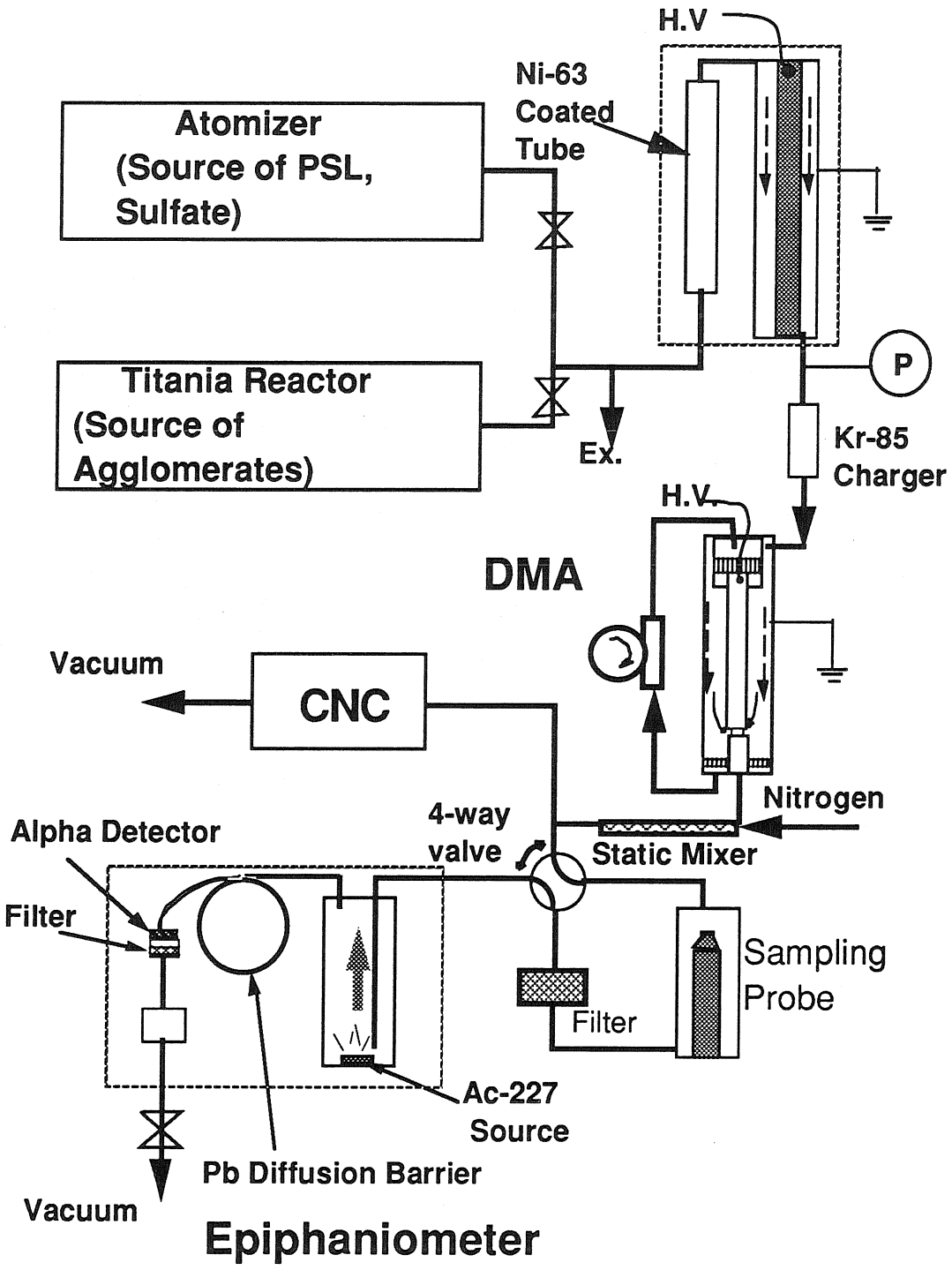

Figure 2. Apparatus for aerosol generation, size classification and measurement.

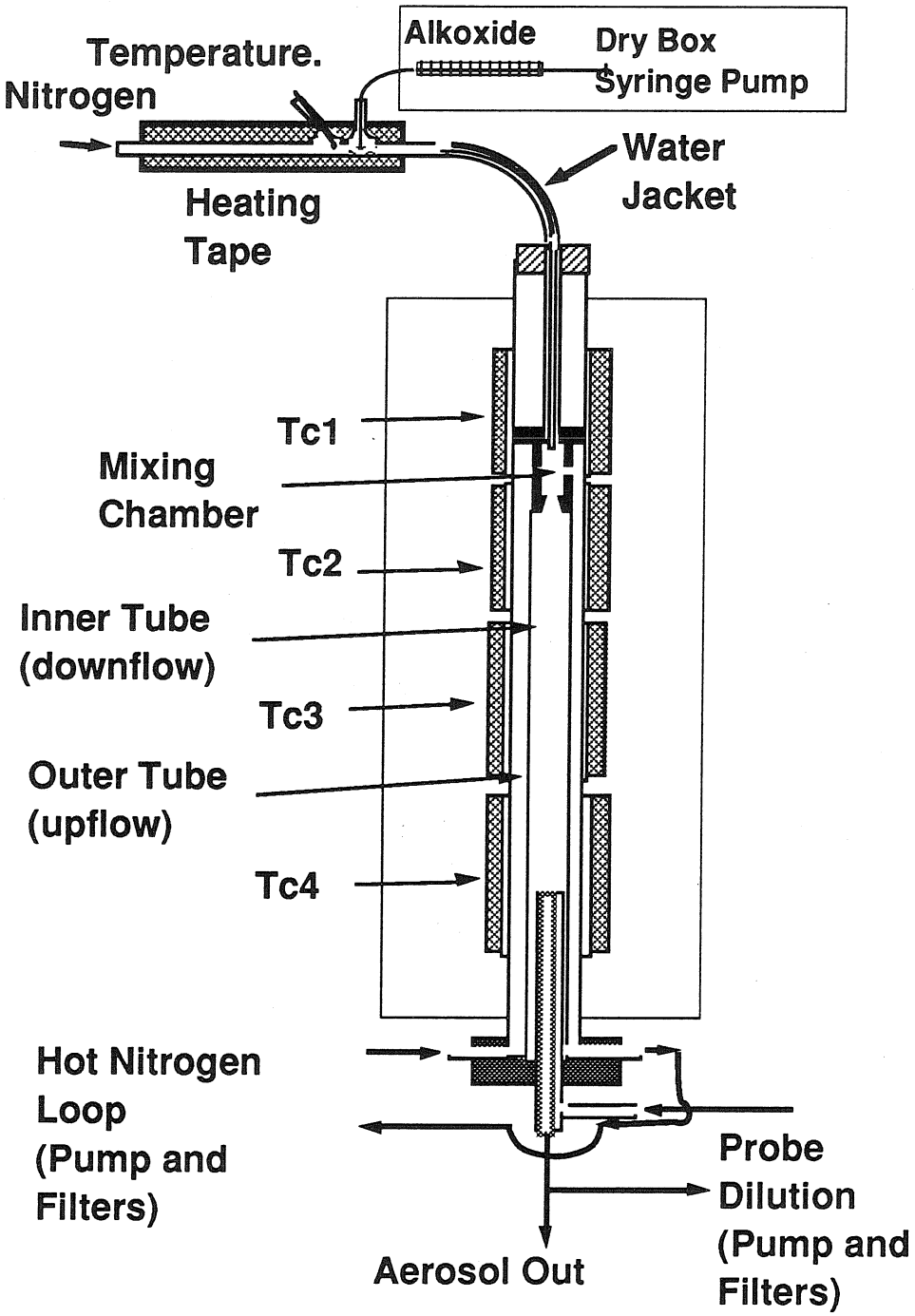

Figure 3. Titanium dioxide particle generator: alkoxide $Ti(OC_3H_7)_4$ vapor source and fast-mixing furnace.

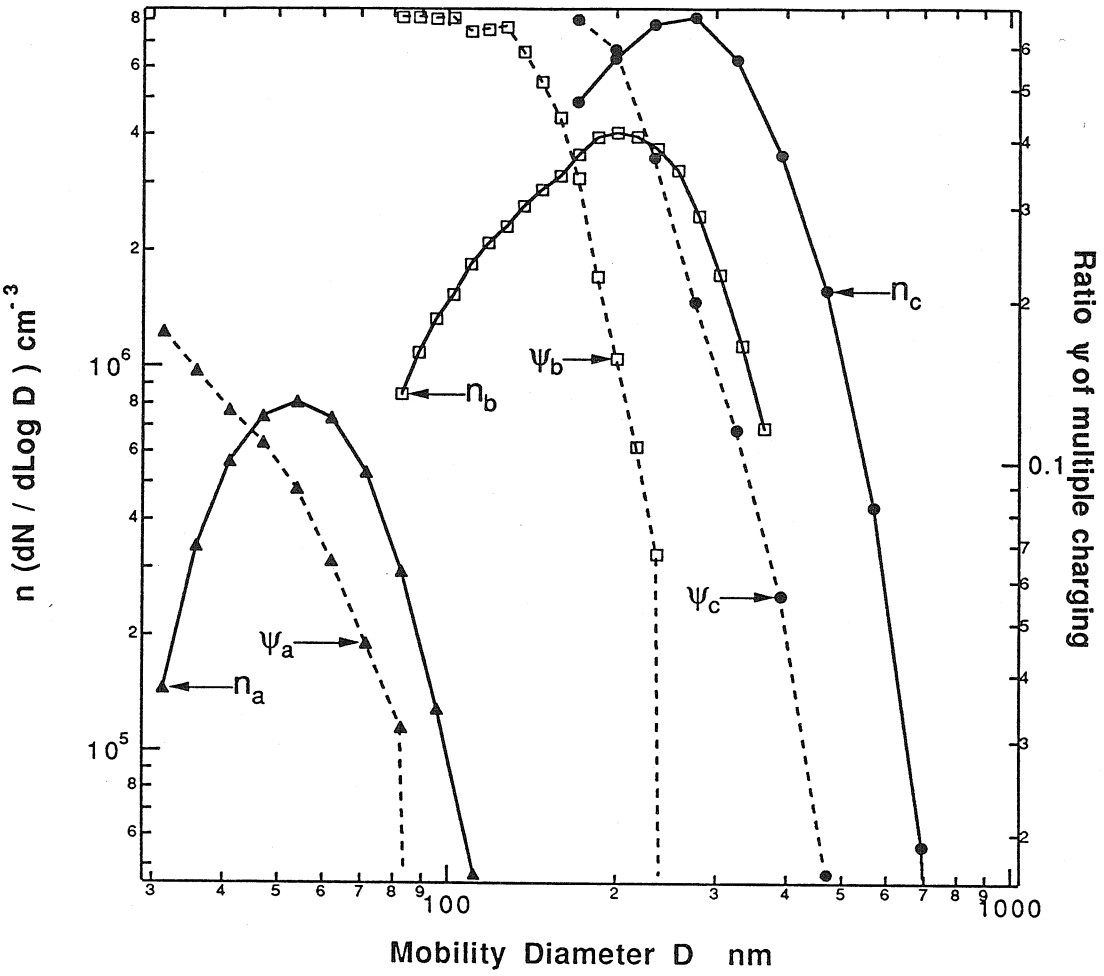

Figure 4. Ratio ψ of multiply to singly charged particles (dashed lines) for three titanium dioxide size distributions *n* (solid lines). Distributions *a-c* were used for mobility diameter size cuts of 49, 223 and 763 nm, respectively.

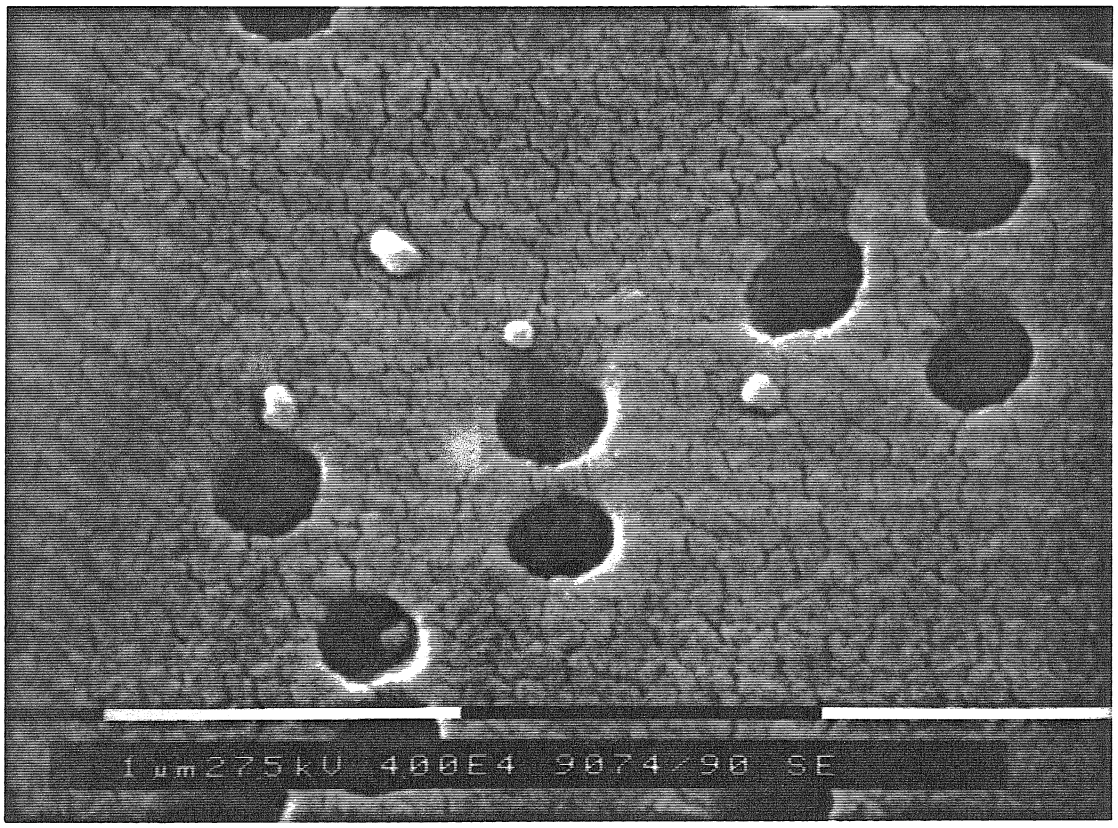

Figure 5a. Scanning electron micrographs of titanium dioxide particles from a 49 nm diameter size cut. The filter pore diameter is 400 nm (bar=1000 nm).

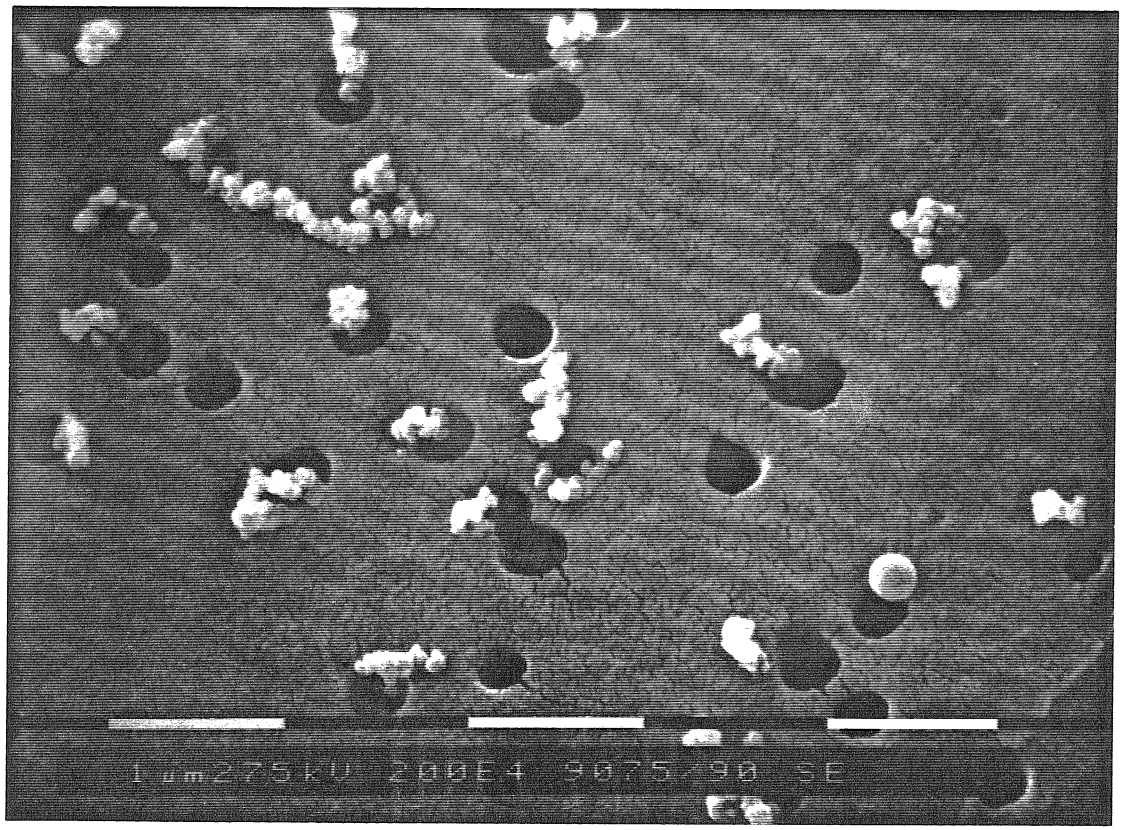

Figure 5b. Scanning electron micrographs of titanium dioxide agglomerates and a PSL sphere with 223 nm mobility diameters. The filter pore diameter is 400 nm (bar=1000 nm).

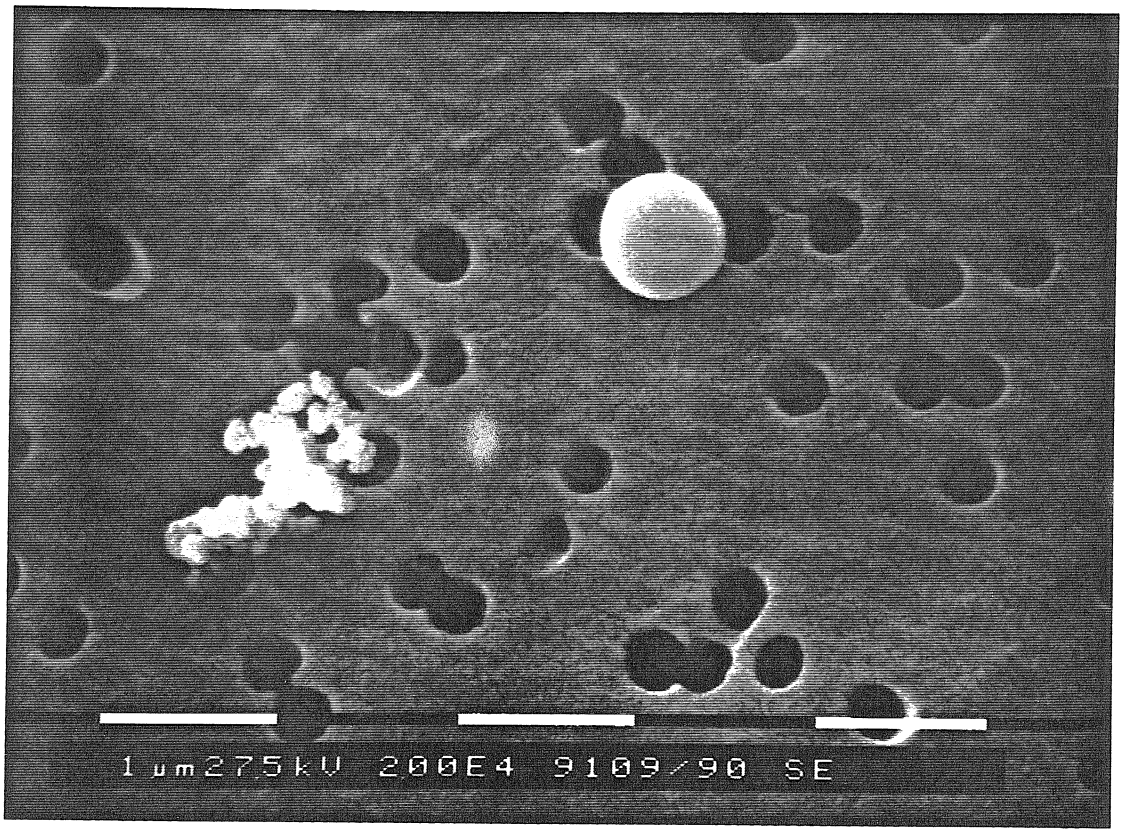

Figure 5c. Scanning electron micrographs of a titanium dioxide agglomerate and ammonium sulfate sphere with 763 nm mobility diameters. The filter pore diameter is 400 nm (bar=1000 nm).

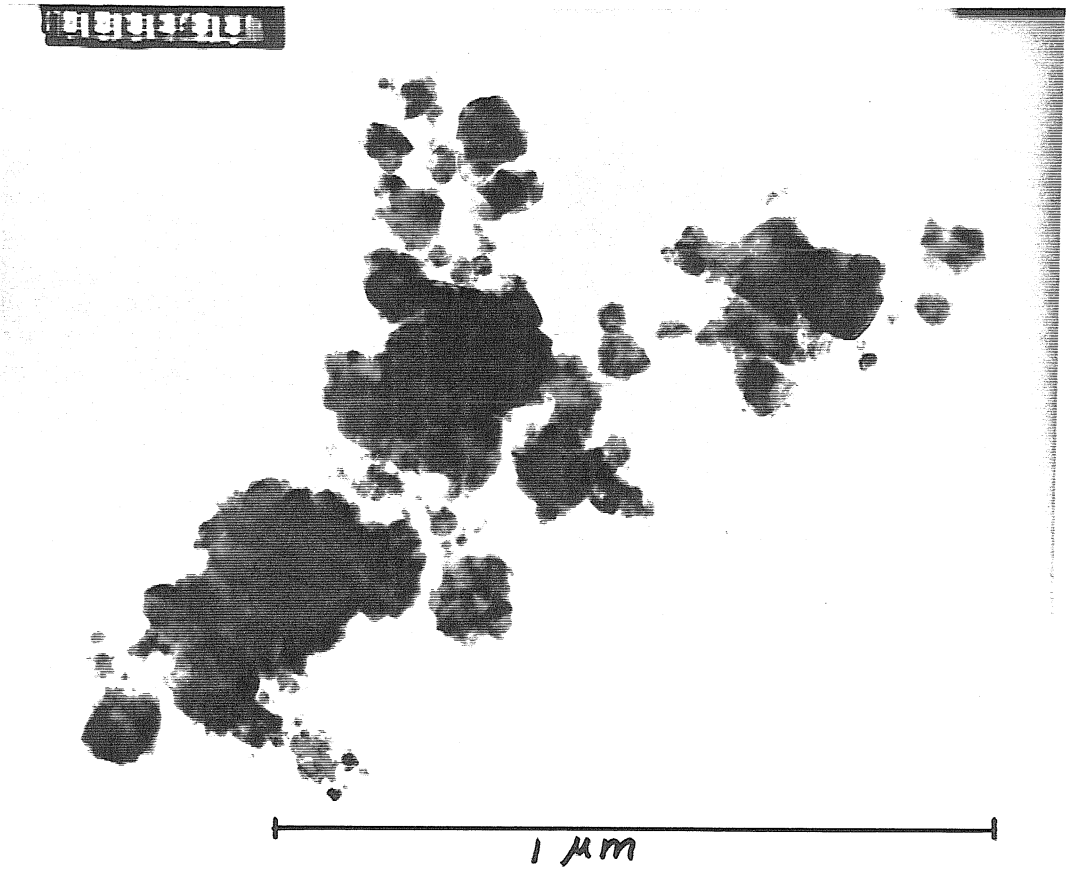

Figure 6. Transmission electron micrograph of a titanium dioxide agglomerate, 755 nm mobility diameter (bar=1000 nm).

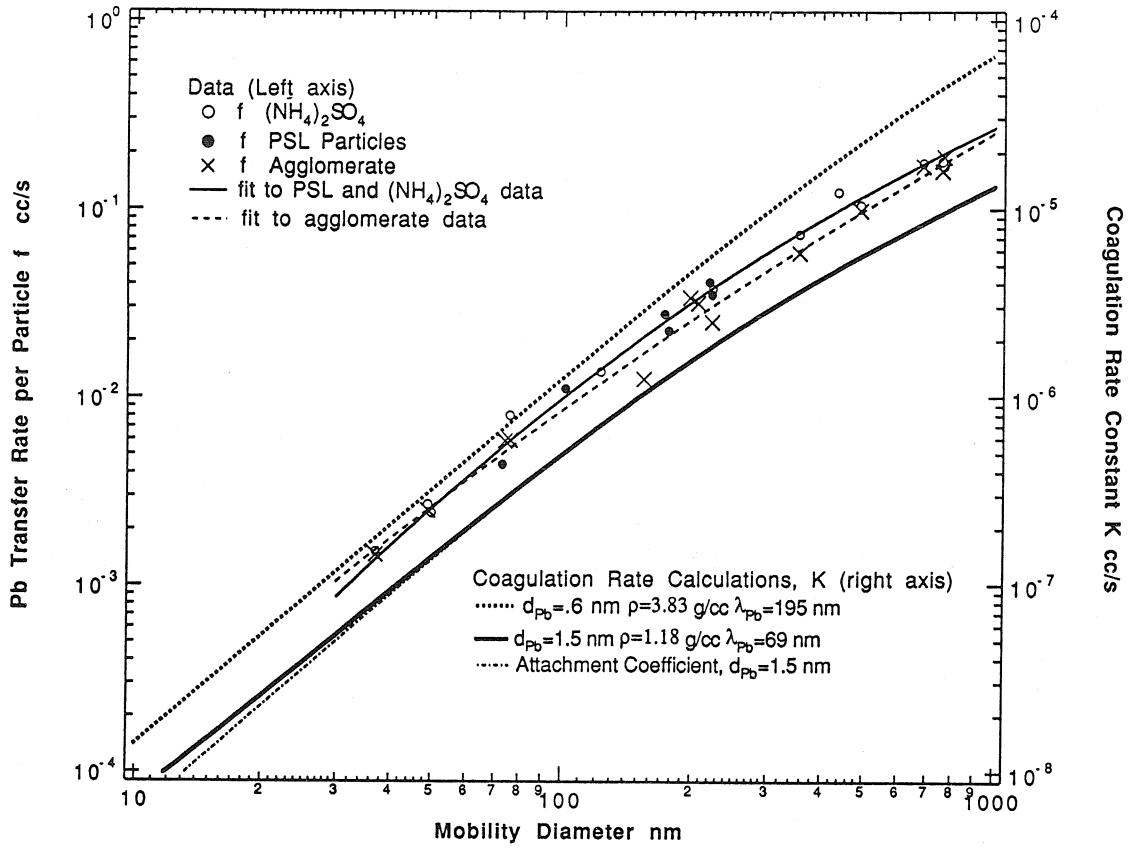

Figure 7. Lead count rate f of deposited aerosols as a function of mobility diameter, for titanium dioxide agglomerates, polystyrene latex spheres and ammonium sulfate spheres . The best-fit quadratic curve for the agglomerates is compared to the best fit to the sphere data . The transfer rate is expected to be proportional to the coagulation coefficient K, computed for lead cluster diameters of 0.6 nm and 1.5 nm . Coagulation theory is almost identical to the attachment coefficient theory of Porstendörfer et al. (1979).

CHAPTER 7
BIPOLAR DIFFUSION CHARGING OF SPHERES AND AGGLOMERATE AEROSOL PARTICLES

Steven N. Rogak and Richard C. Flagan
138-78 W.M.Keck Laboratory of Environmental Engineering Science
California Institute of Technology CA 91125

submitted to Journal of Aerosol Science

running title: Charging of Spheres and Agglomerates

ABSTRACT

The effect of particle shape on the diffusion charging of aerosols was investigated. The charging-equivalent sphere diameter d_{QE}, found previously to be much larger than the mobility diameter d_m, may be related to the uncharged fraction of particles leaving a bipolar diffusion charger. This fraction was measured for three types of particles classified by electrical mobility: polystyrene latex (PSL) spheres, ammonium sulfate spheres and TiO_2 agglomerates of 10-20 nm primary particles. The uncharged fraction was ~5% lower for the agglomerates than for spheres with the same mobility, for size range $100<d_m<800$ nm. This implies that $d_{QE}\sim 1.1 d_m$ for the agglomerates, which is a smaller difference between d_{QE} and d_m than reported by previous studies, but is consistent with the theoretical predictions (Laframboise, J.G. and Chang, J-S. (1977). *J. Aerosol Sci.* **8**:331-338).

INTRODUCTION

The attachment of gas ions to particles occurs in the atmosphere (Twomey, 1977), in flames, and in industrial systems (Burtscher *et al.*, 1986; Kruisz and Reischl, 1989). Knowledge of the ion attachment rate is important for predicting the dynamics of fine aerosols, particularly the losses of particles to surfaces, electrostatic precipitation (White, 1977) and the behavior in aerosol instrumentation (Knutson and Whitby, 1975).

The attachment of ions to spherical particles has been the subject of many theoretical studies (Keefe *et al.*, 1959; Lassen, 1961; Fuchs, 1963; Gentry, 1972; Hoppel and Frick, 1986). For particles with diameters greater than 50 nm, the Fuchs theory is widely accepted. For smaller particles, the differences between theories are generally more pronounced, but recent high-resolution experiments have been performed for particles in the 5-50 nm diameter range (Hussin *et al.*, 1983; Adachi *et al.*, 1985; Vijaykumar and Whitby, 1984). There is greater uncertainty in the charging behavior of non-spherical particles such as asbestos fibers and flame-generated particles, including soot and submicron coal ash.

Previous experiments (Vomela and Whitby, 1967; Shon, 1979; Kasper and Shaw, 1983) have suggested that long chain agglomerates may carry many more charges than those carried by a sphere of the same mobility. More recent experiments (Wen *et al.*, 1984b; Gentry *et al.*, 1990; Pao *et al.*, 1989) were consistent with several theories (Laframboise and Chang, 1977; Dua *et al.*, 1980; Cheng and Yeh, 1981) but did not verify one theory conclusively. Although Wen *et al.* (1984a) introduced the concept of a charging-equivalent diameter, none of the previous studies focuses on the relation between the mobility-equivalent diameter and the charging-equivalent diameter. Such a relationship is particularly practical since many aerosol measurements are based on mobility measurements.

We review charging theories for non-spherical particles (Laframboise and Chang, 1977; Cheng and Yeh, 1981; Wang *et al.*, 1988) and show that a single charging-equivalent diameter might describe an agglomerate adequately under certain conditions. Using differential mobility analysis methods, we relate the charging-equivalent diameter to the mobility-equivalent diameter.

THEORY

Spherical Particles

Aerosol charging is analogous to aerosol coagulation or mass transfer. All of these phenomena depend on the diffusion of an ion, particle, or chemical species to the aerosol surface. They are also influenced by the sticking probability at the aerosol surface and by forces between the particle and the diffusing species. The sticking probability of an ion at the particle surface is generally thought to be near unity (Fuchs, 1963). The rate of attachment of ions to a particle depends strongly on the ion mobility, the ion-particle coulombic force (either attractive or repulsive) and the image force (attractive). Van der Waals forces may also be important for subnanometer size particles (Huang et al., 1991). The image force depends on the dielectric properties of the aerosol, but most materials have a sufficiently low dielectric constant that the image potential is not strongly material-dependent (Davison and Gentry, 1985). For particles with diameters greater than 40 nm, the charging behavior is practically independent of the material properties, and depends only on particle size and shape.

The rate of particle charging can be characterized by the ion attachment coefficient η,

$$\eta^+(d,q) = \frac{I^+}{N_i^+} \quad ; \quad \eta^-(d,q) = \frac{I^-}{N_i^-} \quad , \tag{1}$$

where I^+ and I^- are the instantaneous fluxes of positive and negative ions to a particle of diameter d, carrying q charges, in an atmosphere where the positive and negative ion concentrations are N_i^+ and N_i^-. Fuchs (1963) included the coulomb and image potentials in his calculations of the ion attachment coefficients for spherical particles not much larger than the ion mean free path λ_{ion}. The Fuchs theory of ion attachment has since been modified to include ion trapping (gas molecule-ion collisions near the particle surface, Hoppel and Frick, 1986), but this effect is important only for particles much smaller than 10 nm. Alternative formulations have been proposed, such as the "minimum flux model"

(Gentry, 1972). The Fuchs model will be used in this study because it is consistent with available data and is widely accepted.

Ion attachment coefficients cannot be measured directly. Instead, their effect on aerosol charge distributions is obtained from a series of "birth-death" equations describing the numbers of ions and the number of particles carrying different levels of charge (Fuchs, 1963; Adachi *et al.*, 1989; Hoppel and Frick, 1990). For the special case where there is a steady source of positive and negative ions, as for example, from ionizing radiation in an aerosol neutralizer, the average number of charges carried by a particle approaches a steady-state value. The steady-state charging probabilities depend only on the ratios of the ion attachment coefficients and the relative numbers of positive and negative ions.

For large particles (d >50 nm) in an environment of identical positive and negative ions, ion attachment is a quasi-reversible process. The attachment of an ion of one sign requires the same energy as the removal of an ion of the opposite sign. If the electrostatic energy associated with such an event is smaller than the thermal energy kT, from statistical mechanics one expects the charging probability to be given approximately by a Boltzmann distribution (Keefe *et al.*, 1959),

$$P_q(d) = \sqrt{\frac{e^2}{2\pi dkT}} \exp\left(-\frac{q^2e^2}{2dkT}\right) \qquad (2)$$

where $P_q(d)$ is the probability that a particle of diameter d carries q positive or negative charges, e is the elementary charge , T is the temperature, and k is the Boltzmann constant. Although the detailed balancing assumption implicit in (2) is fundamentally wrong and results in significant errors when the ion properties are unequal (Fuchs, 1963), the fact that a purely energetic treatment gives approximately correct results suggests that the energetics is most important in determining the steady-state charge distribution on the aerosols. This observation is useful when considering the effect of particle geometry on charging.

Non-Spherical Particles

Characterization of Shape

Any single physical property of a non-spherical particle may be characterized in terms of an equivalent sphere of the size that yields the same value of that property. The volume of an agglomerate may be described by the sphere of diameter d_V having the same volume. Other useful geometric parameters include the radius of gyration R_g and the diameter d_A of the sphere having the same average projected area as the agglomerate. Mass transport, mobility and charging may also be characterized by equivalent sphere diameters but these diameters are not simply functions of the particle geometry. A parameter commonly used to characterize non-spherical particles is the dynamic shape factor κ which is defined as the ratio of the aerodynamic drag on the particle to that on the volume-equivalent sphere. Unfortunately, direct measurement of this quantity is rarely possible.

Fractal geometry has been used to describe agglomerate aerosols (Forrest and Witten, 1979; Samson et al. 1987; Meakin *et al.* 1989; Smirnov, 1990). It is particularly useful for illustrating the scaling relationships between the various equivalent diameters. A set of fractal agglomerates, each of which is composed of N primary spheres of diameter d_1, obeys the relation

$$R_g \sim d_1 N^{1/D_f}, \tag{3}$$

where D_f is the fractal dimension. From theoretical arguments (Weitz and Huang, 1986) and computer simulations (Samson *et al.*, 1987; Meakin *et al.*, 1989) it is expected, that for $D_f < 2$, the projected-area-equivalent diameter scales as

$$d_A \sim d_1 N^{1/2}. \tag{4}$$

The difference between (3) and (4) is critical for large N and low D_f, for in this case the length scales determining the dynamics of the particle diverge; d_A/R_g approaches 0 as N approaches ∞.

Mass Transfer, Mobility and Electrostatics

Consider the transport of neutral atoms or a fine aerosol to a particle surface. The transport rate will be the same to the mass-transfer-equivalent sphere of diameter d_D, given that the sphere is in the same environment and has the same sticking coefficient. When the mean free path λ_D of the transported species is large compared to the particle diameter, one expects that $d_D \sim d_A$ (Meakin *et al.*, 1989). When λ_D is relatively small, d_D is determined by the continuum diffusion equation and therefore we expect d_D to be proportional to R_g, at least for agglomerates with $D_f > 1$ (Schmidt-Ott *et al.*, 1990; Rogak *et al.*, 1991b). For long slender bodies (i.e., $D_f = 1$) of minor diameter d_1 and length Nd_1,

$$d_D \sim \frac{Nd_1}{\ln(2N)} \cdot \tag{5}$$

The mobility-equivalent sphere diameter d_m is a function of the gas mean free path λ (Dahneke, 1973c) and the particle orientation (Wen and Kasper, 1984). If the agglomerates have low aspect ratios, as in the present experiments, the diameter measured by electrostatic classification is close to the orientation-averaged mobility diameter (Rogak *et al.*, 1991a). Note that the drag on a particle is determined by the transport of momentum from the surface to the surrounding gas. This process is analogous to mass transport, so one expects $d_m \sim d_D$ if the relevant mean free paths are equal. Both d_m and d_D approach the projected area diameter d_A as the relevant mean free paths increase. The analogy was shown to be quantitative for the attachment of ^{211}Pb clusters to agglomerates (Rogak *et al.*, 1991b).

The relation between drag and charging is less obvious but worth investigation. We consider the analogy between electrostatics and diffusion, used by Fuchs (1964) to predict the coagulation rate of prolate spheroids. The electrostatic potential around a conducting particle is constant on the particle surface and obeys Laplace's equation in the surrounding space. The concentration of a species diffusing to a perfectly absorbing particle is also constant on the surface and is governed by Laplace's equation elsewhere. Therefore, the potential at an agglomerate surface will be the same as that at the surface of the mass-transfer-equivalent sphere if both particles carry the same number of charges, i.e. the potential-equivalent diameter d_ϕ is the same as the continuum mass transfer diameter d_D. From energetic considerations the charging probabilities would be given by the Boltzmann equation (2), where the appropriate diameter is d_ϕ. The continuum mobility and mass-transfer diameters are nearly equal, so that the potential, mobility and mass-transfer diameter are expected to be nearly the same, for non-spherical particles in the continuum regime. However, in the free-molecule regime one expects $d_m \sim d_A$, so that in general $d_m \neq d_\phi$.

In addition to energetics, one must consider the kinetics of the charging process. The rate of ion attachment to particles depends on the electrostatic forces (characterized by d_ϕ), image forces, and on the transport diameter d_D. Neglecting image forces (reasonable for particles larger than 40 nm diameter), the attachment of ions to uncharged particles is identical to the mass-transfer process discussed above. For the attachment of ions to charged particles, the electrostatic interactions are important so that the process is characterized by two generally unequal diameters, d_ϕ and d_D . By the previous arguments, in the continuum regime one would expect the charging to be characterized by a single, charging-equivalent sphere diameter $d_{QE} \sim d_\phi \sim d_D$. A number of models have been proposed to describe the charging of non-spherical particles in the transition regime.

Laframboise and Chang (1977) started with the small Knudsen number ($Kn_{ion} = 2\lambda_{ion} / d$) flux-matching model of Lassen (1961) that had been obtained for spheres. This

theory ignores the image-potential attraction, which makes the theory unsuitable for particles less than 40 nm. The kinetic (free-molecule) ion flux and the continuum diffusion flux are matched at the particle surface (in contrast to the Fuchs theory where the matching occurs on some "limiting sphere" that is larger than the particle). The simplicity of Lassen's result allowed it to be extended to conducting particles of arbitrary shape and size. In particular, Laframboise and Chang obtained a closed-form expression for the ion current to prolate spheroids of length L, aspect ratio N, and known surface potential. The slender-body limit has almost the same form as that for a sphere of diameter $d_{QE} = L/\ln(2N)$. Wen *et al.* (1984a) concluded that the the steady-state bipolar charging of spheroids could be obtained by using this charging-equivalent diameter in conjunction with the charging theory for spheres. They noted that the image force would be improperly calculated by such a procedure, but the error was shown to be small if the spheroid minor axis was greater than approximately 40 nm.

The image force was explicitly considered in the "minimum flux" model (Gentry, 1972), which has been extended to cylindrical particles (Wang et al., 1988). Their results compared the ion fluxes to uncharged cylinders with the fluxes to spheres of the same volume. Table 1 compares their results to those predicted by Laframboise and Chang (1977) for uncharged prolate spheroids of the same aspect ratio and minor diameter. When the minor diameter is less than 20 nm, the minimum-flux theory gives slightly lower relative ion fluxes. This difference is not unexpected since the volume-equivalent diameter of a spheroid is about 15% lower than that of the corresponding cylinder, resulting in higher normalized currents for the spheroid. For the thinnest particles, the differences are presumably caused by the image force. The minimum flux method converges surprisingly slowly to the continuum limit, so the Laframboise and Chang theory will be used as the basis for computations of the steady-state charging of elongated bodies.

Bipolar Diffusion Charging of Prolate Spheroids

The theory of Laframboise and Chang is used to obtain the ion current I_{pq} to a prolate spheroid carrying q charges. The orientation-averaged mobility diameter of the spheroid is then obtained from the classical continuum regime results (Kasper *et al.*, 1985), the kinetic regime results of Dahneke (1973a), and the adjusted sphere interpolation (Dahneke, 1973b). Lassen's result was then used to compute the ion current I_{sq} to the mobility-equivalent sphere carrying q charges. The ratio $\chi = I_{pq}/I_{sq}$ gives the shape enhancement of the ion-attachment coefficient for a spheroid, compared with a sphere of the same mobility. The mobility diameter is chosen as the basis of comparison because $\chi_q \sim 1$ in the continuum limit. Comparisons on the basis of the mass-equivalent diameter are difficult to interpret because the relation between d_{QE} and d_m is extremely sensitive to changes in the particle structure.

Using the enhancement factors χ for the ion attachment coefficients, we then use Fuchs theory to calculate the steady state charge distributions for spheroids and their mobility-equivalent spheres. This approach is not as rigorous as Fuchs theory, because of the limitations of the spheroid theory discussed above, but it is expected to be accurate for particles larger than the ion mean free path. The ion properties are taken from Kousaka *et al.* (1985), whereby the mean free paths of the positive and negative ions are 8.8 nm and 11.8 nm, respectively. In the calculations, spheroids with minor diameters d_1 of 10 and 40 nm were used, as the primary particle diameters of typical agglomerates are in this size range.

Fig. 1 shows the charging probabilities for spheres and spheroids. The minor diameter of the spheroid is fixed at 10 nm while the length and mobility diameter are changed. For d_m = 10 nm, $d_{QE} = d_m$ because the 10 nm spheroid is simply a sphere. As the mobility diameter increases beyond 30 nm ($L/d_1 \sim$ 9), the charging behavior of the spheres and spheroids begins to diverge. The neutral fraction for the spheroids is considerably lower than for the spheres of the same mobility. In general, the spheroid

curves are shifted left, implying that the charging-equivalent diameter is larger than the mobility-equivalent diameter. For example, the charging of a spheroid with a 400 nm mobility diameter (L/d_1~ 900) is similar to that of a 900 nm sphere. For comparison, the Cheng and Yeh (1981) model discussed below predicts a charging-equivalent diameter of about 9000 nm. No diameter transformation will map the spheroid charging exactly onto the sphere charging curves. The maximum probability of carrying 2 positive charges is about 0.55 for the spheroids, while the charging-equivalent sphere model would predict about 0.45. Therefore, the charging behavior cannot be described exactly by a single charging-equivalent diameter.

Fig. 2 shows that the minor diameter of the ellipsoid has a strong effect on the charging. For a 40 nm minor diameter, the charging-equivalent sphere model appears to be very good and d_{QE} is only slightly larger than the mobility diameter. The charging-equivalent sphere diameter is about 540 nm for a spheroid of 400 nm mobility diameter. If the maximum mobility diameter of the spheroid had been used (i.e. the spheroids oriented perpendicular to the motion), d_{QE} would be nearly equal to d_m.

These results can be applied qualitatively to the TiO_2 agglomerates used in the present experiments. The primary particle diameter was between 10 and 20 nm, suggesting that the results of Fig. 1 would be more applicable than those of Fig. 2. The agglomerates were not straight chains, however, but dense, branched fractal-like agglomerates with a fractal dimension much larger than 1, so d_A and R_g do not diverge as rapidly as for spheroids. Therefore, one expects the agglomerate charging to be similar to that of spheroids having minor diameters much greater than the agglomerate primary particle diameters. The charging-equivalent sphere model should be very good for such particles and d_{QE} is expected to be very close to d_m.

PREVIOUS EXPERIMENTS

Vomela and Whitby (1967) combined electron microscopy with an electrical aerosol analyzer (EAA) to relate the unipolar charging of agglomerate aerosols to mobility and particle mass. Their particles were chains of 10-300 primary spheres, where $d_1 \sim 50$ nm. The mobility-equivalent diameter was within 50% of the volume-equivalent diameter. The average charge per agglomerate was 50-70% higher than that given by the Boltzmann charge distribution for the volume-equivalent sphere.

Shon (1979) passed flame generated Fe_2O_3 through a differential mobility analyzer (DMA) with a bipolar charger. Using a centrifuge, the mobility-classified particles were sampled for microscopy according to their aerodynamic diameter. From the apparent number of multiply-charged particles in the micrographs, it was possible to compare the number of charges q on the agglomerates to the number q_m on the mobility-equivalent sphere with a Boltzmann distribution (Table 2a). The results for bipolar charging are surprising in that q/q_m increases as N decreases; the apparent charging-equivalent diameter decreases as the chain length increases. Shon also estimated the number of charges acquired by particles in the unipolar corona charger of an EAA. These results were normalized by the number of charges expected on the mobility-equivalent sphere in such a charger (Liu and Pui, 1974). The unipolar-charging results suggest that d_{QE} is slightly smaller than the chain length (Table 2b). These results were duplicated to within 20% in a similar study (Kasper and Shaw, 1983). .

Wen *et al.* (1984b) focussed on the bipolar charging of Fe_2O_3 aerosols similar to those of Shon (1979). In this study, the average number of charges on a mobility-classified particle was estimated by comparing the number concentration to Faraday cup measurements. These results were compared to model predictions using particle size distributions that were measured with a centrifuge. The average charge was higher than that predicted using a charging-equivalent diameter $d_{QE} = d_1 N / \ln(2N)$.

Yu *et al.* (1987) found that the unipolar charging rate of large fibers was 5-10% lower than predicted by Laframboise and Chang (1977). Such a small difference could be explained by uncertainties in the ion properties or concentrations. The fibers were 3 μm long by 0.3 μm, putting them well into the continuum regime where the theory is valid.

Cheng and Yeh (1981) used $d_{QE} = L$ in the Boltzmann equation, as a result of their assumption that the primary particles of a chain are electrically independent. Although this assumption is rarely valid, there is some experimental support of this model. Dua *et al.* (1980) measured the equilibrium charge distribution on singlets, doublets and triplets of 500 nm polystyrene latex spheres. The ratios of their single-sphere measurements to the probabilities predicted by the Boltzmann equation were not equal to unity, possibly because of systematic experimental errors. Their doublet and triplet data are corrected by this ratio and compared to the Boltzmann charging (Table 3). In the table, F is a comparison of the experimental data defined as follows. The measured probability of carrying q charges is P_q while P_{qV} and P_{qs} are the corresponding Boltzmann probabilities for the volume-equivalent and surface-area-equivalent spheres. P_{qmax} is the Boltzmann charging for a sphere of diameter equal to the maximum length of the doublet or triplet. For each equivalent sphere diameter,

$$F_V = \frac{\frac{P_q}{P_1}}{\frac{P_{qV}}{P_{1V}}} \quad ; \quad F_S = \frac{\frac{P_q}{P_1}}{\frac{P_{qs}}{P_{1s}}} \quad ; \quad F_{max} = \frac{\frac{P_q}{P_1}}{\frac{P_{qmax}}{P_{1max}}}, \tag{6}$$

so that F =1 for q=1. The table shows that the data are most consistent with a charging diameter equal to the maximum length of the aggregate. However, for aggregates of 2 to 3 spheres there is only a small difference between the maximum length and the mobility diameter. Recent experiments with soot agglomerates (Gentry *et al.*, 1990) are also consistent with the Cheng and Yeh model.

EXPERIMENTS

Many of the previous experiments suggest that the charging-equivalent diameter d_{QE} is even larger than that expected theoretically . Part of this discrepancy may be due to systematic experimental error, which we attempt to minimize in the present study by using spherical aerosols to calibrate the procedure. The mobility diameter d_m is used as the basis of comparison as it is expected to be much closer to d_{QE} than the volume-equivalent diameter, which has been used in previous experiments.

The model calculations show that the uncharged fraction P_0 is as sensitive to shape as the singly or doubly charged fractions. Moreover, the shape effect may be characterized well by P_0, at least to the extent that the charging-equivalent sphere model is valid. Since P_0 is easier to measure than any of the other charging probabilities, it was chosen as the focus of this study. For non-spherical particles, d_{QE} is the mobility diameter of a sphere having the same measured value of P_0.

The uncharged fraction of the aerosol was measured with the apparatus shown in Fig. 3. Spherical or agglomerate aerosols were produced by atomization or thermal reaction. The size distributions of these aerosols were then measured with a DMA (model 3071, TSI Inc., St. Paul, MN), and a condensation nucleus counter (CNC, TSI model 3760). After characterizing the size distribution, the DMA voltage was fixed and the output aerosol was diverted through a second ^{85}Kr neutralizer followed by an electrostatic precipitator. The precipitator was turned on and off periodically, resulting in periodic removal of charged particles. Fig. 4 shows a typical CNC record for a TiO_2 aerosol.

Particle Generation

Nearly spherical particles were produced by the atomization of dilute polystyrene latex (PSL) suspensions or ammonium sulfate solutions (Liu and Lee, 1975). Scanning electron microscopy (Rogak *et al.,* 1991b) verified that the resulting particles were spherical.

The agglomerate aerosol was produced by the thermal decomposition of titanium tetraisopropoxide (Okuyama et al., 1986). The alkoxide was fed by a syringe pump into a stream of warm nitrogen, where the liquid alkoxide evaporated (Fig. 5). The vapor was carried into a pyrex reactor where it was mixed with a hot stream of nitrogen. The alkoxide decomposes to form TiO_2, which nucleated to from a solid aerosol. This aerosol was then quenched with cool air in a sampling probe and carried through a static mixer into a 330 cm^3 growth chamber. The residence time in the hot (540 °C) reactor was ~0.04 second, considerably shorter than the 2 to 4 second residence time used in our earlier mobility and mass-transfer studies (Rogak *et al.*, 1991a,b). As a result, the primary particle diameter was smaller than in the earlier studies. The particles were sampled thermophoretically from the gases leaving the growth chamber. Typical samples are shown in Fig. 6. In order to produce a desirable size distribution, the alkoxide mass flow rate and the dilution downstream of the reactor were varied. This shifted the peak of the size distribution but had no apparent effect on the primary particle size.

Particle Characterization

A DMA (model 3071, TSI inc., St. Paul, MN) fitted with a TSI ^{85}Kr neutralizer was used to produce a nearly monodisperse aerosol. With a sheath gas flow of 2.6 lpm and a sample flow of 0.4 lpm, the output mobility distribution has a theoretical standard deviation of less than 10 % (Knutson and Whitby, 1975), which is sufficiently narrow for very high-resolution size distributions. Since comparative measurements for spheres and agglomerates were desired, it was critical that these flows did not change through the course of the experiments. Therefore, the pump system was run for several hours to stabilize the flows before starting the experiments. There was no detectable drift in the flows as the DMA filters became loaded. As a further precaution to avoid biasing the comparison between the spheres and agglomerates, the agglomerate measurements preceded the sphere measurements for half of the experiments, while the sphere

measurements were made first in the other experiments. Three independent runs, each including measurements of spheres and agglomerates over a wide size range, were made. Thus, the reproducibility of the measurements is reflected in the scatter of the data presented below.

Despite these precautions, there were still several potential sources of error. The mobility of an agglomerate depends on the orientation, so the effective width of the distribution may be slightly larger for the agglomerates. We have ignored this effect. More important was the problem of multiple charging. For particles with mobility diameters larger than 100 nm, the ^{85}Kr charger may produce large numbers of multiply-charged particles. The extent to which multiply-charged particles contribute to the classified aerosol depends on the aerosol size distribution $n(d_m) = dN / d(\log d_m)$ and on the charging probability $P_q(d_m)$. If the DMA is set for a diameter d_{m2}, the size cut will also contain doubly-charged particles of diameter d_{m2}. Similarly, the sample includes particles with more than two charges. The ratio of the number of multiply-charged particles to singly-charged particles is

$$\psi = \frac{n(d_{m2})\, P_2(d_{m2}) + n(d_{m3})\, P_3(d_{m3}) + n(d_{m4})\, P_4(d_{m4}) \ldots.}{n(d_{m1})\, P_1(d_{m1})} \qquad (7)$$

One method of reducing ψ is to use a low-ionization charger (Gupta and McMurry, 1989), so that $P_1 >> P_2 >> P_3 ... >> P_n$. Another approach is to sample from that portion of the particle size distribution where the concentration decreases rapidly with diameter. Fortunately, distributions resulting from coagulation or atomization of salt solutions tend to have a single peak, and low ψ can be achieved by taking a size cut diameter larger than the peak diameter. For most of the samples, the multiply-charged fraction was about 10%. This has a substantial but known effect on the data. A disadvantage of this method of reducing ψ is that it requires that the aerosol generator conditions be modified for each size studied.

The neutralizer (Fig. 7) used for the sphere-agglomerate comparison was a ^{85}Kr bipolar neutralizer (TSI model 3077) with an estimated activity of 2 mCi. An older unit of the same model was used in the DMA. In this charger, a small axial tube contains ^{85}Kr gas, a beta-particle emitter. The beta particles penetrate the containment tube and ionize the gas in the main charging volume (Liu and Pui, 1974).

Charged particles leaving the neutralizer were removed with a cylindrical precipitator with an 8000 V dc power supply (Fig. 7). This was turned off periodically, allowing the entire aerosol sample to pass through to the CNC. The neutral fraction was thus determined by the ratio of the two measurements made with a single CNC.

RESULTS

The measured uncharged fractions P_0 for TiO_2, ammonium sulfate and PSL particles are shown in Fig. 8. The difference between the spheres and the agglomerates is small, although it is statistically significant as the data were obtained from several independent experiments. Before the observed differences between the spheres and agglomerates can be attributed to shape, however, it is necessary to understand the possible differences between the agglomerate measurements and the sphere measurements. Aside from particle shape, the main differences are particle concentration, concentration fluctuations and the extent of multiple charging. We consider these factors separately below.

Experimental Biases

Particle Concentration

Non-linear instrument response to particle concentration is a potential biasing factor since the TiO_2 generator produces higher number concentrations than the atomizer. For example, particle concentrations $N_A > 10^4$ cm^{-3} would have caused large CNC coincidence errors, resulting in overestimations of P_0. However, for the values of N_A encountered in

the experiments (Table 4), corrections for coincidence error were generally much less than 1%.

Saturation of the neutralizer is a larger concern. Previous work (Porstendörfer *et al.*, 1983; Adachi *et al.*, 1989; Hoppel and Frick, 1990) has shown that the charge distribution from a neutralizer can be a function of the particle concentration and wall losses of the ions. It was of concern that losses of the ions to the particles could significantly alter the ion concentrations in the neutralizer. This is equivalent to saying that the ion-particle combination rate is comparable to the particle-independent ion sinks, i.e. wall losses and ion recombination. This is expressed by the ratio γ,

$$\gamma = \frac{\eta_A N_A}{\eta_i N_i + \frac{D_{ion}}{r^2}} , \tag{8}$$

where η_A is the ion-aerosol combination coefficient, N_A is the aerosol concentration, η_i is the ion-ion recombination coefficient, N_i is the ion concentration, D_{ion} is the ion diffusivity, and r is the typical distance over which an ion must diffuse to reach a wall. The highest aerosol concentrations were obtained for particles in the 100-200 nm range, for which a reasonable upper limit on η_A is 10^{-5} cm^3 s^{-1} (Hoppel and Frick, 1990). The ion recombination coefficient is taken as 1.6 x10^{-6} cm^3 s^{-1} (Liu and Pui, 1974) and the ion diffusivity as 4.8 x 10^{-2} cm^2/s (Adachi *et al.*, 1985). In the neutralizer, the ion-pair production rate is about 8.7 x10^6 cm^{-3}s^{-1}. This production matches the losses, which are primarily due to ion recombination when the aerosol concentration is moderate. Therefore

$$\eta_i N_i^2 \sim 8.7 \times 10^6 \text{ cm}^{-3}\text{s}^{-1} \tag{9}$$

$$N_i \sim 2.3 \times 10^6 \text{ ions cm}^{-3}$$

For $N_A \sim 10^4$ cm^{-3}, the maximum level reached in the experiment,

$$\gamma = \frac{\eta_A N_A}{\eta_i N_i} = 0.03 \tag{10}$$

At most 3% of the ions produced could be removed by the particles. Also of concern are losses in the exit tubing, in which there is no ionizing radiation. Here, the ion concentrations decline to levels where losses to walls and particles may be larger than recombination (Adachi *et al.*, 1989; Hoppel and Frick, 1990). In the worst case, the ion recombination is negligible, so that particle and wall losses compete:

$$\gamma = \frac{\eta_A N_A}{\frac{D_{ion}}{r^2}} = 0.08 , \tag{11}$$

where the diffusion distance r was taken as 0.2 cm for the exit tubing. Thus, ion losses to the particles may have a small but significant effect on the ion concentration. In order that ion recombination be much smaller than wall losses, the concentration must be less than

$$N_i << \frac{D_{ion}}{r^2 \eta_i} = 7.5 \text{ x } 10^5 \text{ cm}^{-3} \tag{12}$$

Whether or not such low ion concentrations are reached depends on the relative time scales of the ion decay and the tubing residence time. The travel time between the neutralizer to the precipitator is approximately 0.7 seconds, while the ion decay time can be found by assuming that the decay follows

$$N_i(t) = \frac{N_i(t=0)}{1+N_i(t=0)\eta_i t} \tag{13}$$

The time to reach the concentration given in (12) is approximately 0.6 seconds. Therefore, wall losses may become important within the available travel time. If losses to either walls or particles become important, the more mobile ions will be lost at a greater rate, causing the charge distribution to become symmetric (Porstendörfer *et al.*, 1983; Hoppel and Frick, 1990). This also causes the uncharged fraction to exceed that predicted by Fuchs charging with equal concentrations of positive and negative ions. Thus, ion losses may account for the difference between the experimental results and Fuchs' theory. In fact, previous experimental studies have been consistent with symmetric charging (Dua *et al.*, 1980; Kousaka *et al.*, 1981).

By the same reasoning , if the particle concentration affected the charging, one would expect the higher concentration measurements to give higher neutral fractions. The titania particles had higher concentrations but lower neutral fractions, so concentration effects cannot be responsible for the apparent difference between the spheres and agglomerates.

Particle Concentration Fluctuations

Pulses from the CNC were counted by a microcomputer for 1-second intervals. After each second, the number of counts was stored temporarily. A number of these temporary values (60 for the first few experiments, 40 for the later experiments) were averaged. This average and the standard deviation about the average were stored. The precipitator was switched on or off after one of these averaging periods, but not after every averaging period, for the reasons discussed below.

After switching the precipitator on or off, there was a substantial transient time before the CNC measurements stabilized, because of the large precipitator residence and voltage response times. The concentration rose to within 1% of the true value approximately 160 seconds after the precipitator was switched off. After switching the precipitator on, charged particles were removed from the entire precipitator volume, reducing the required waiting time to ~40 seconds (Fig. 4). The transient response of the system was characterized during experiments where N_A was particularly stable. For such experiments, the concentration change reflecting the charging probability $N_A (1-P_0)$ could be estimated by making measurements over a sufficiently long time. The measured concentration change ΔN includes transient effects;

$$\Delta N(t) = f(t)\, N_A (1-P_0) \ , \qquad (14)$$

where $f(t)$ was assumed to be a function of the precipitator. Using (14), the time response of the system was improved for better measurements during experiments with

varying input concentrations (Fig. 4). Equation (14) was also used to determine appropriate weightings for the CNC measurements.

Two procedures were used to estimate the neutral fraction from the CNC time series. In the "cell" method, time intervals before and after two changes of the precipitator voltage, e.g., times in which the precipitator was on, off and then on, were considered. The neutral fraction was estimated from the weighted averages of the concentrations for these three intervals. Thus, for the time series of Fig. 4, 11 estimates of the neutral fraction were made. From the variation in these estimates, the error σ_{cell} was computed (Table 4).

To verify that the results were not dependent on the data reduction method, a second treatment was used. First, a polynomial was fit to the CNC measurements made when the precipitator was turned off (Fig. 4). Using the fitted curve as an estimate of the total number of particles entering the precipitator, comparison with the "on" data yielded the neutral fraction P_{0fit}. It was found that P_{0fit} was insensitive to the degree of the fitting polynomial and that for both the spheres and the agglomerates, P_{0cell} and P_{0fit} are in good agreement. Exceptions are the strangely high and low neutral fractions for 98 nm agglomerates. Both σ_{cell} and $(P_{0cell} - P_{0fit})$ suggest that these anomolies were due to fluctuating aerosol concentrations. Figs. 8 and 9 display an average of these 3 data points, weighted according to σ_{cell}.

Multiple Charging

The extent of multiple charging was estimated by applying (7) to the size distribution data. The size distributions $n(\log d_m)$ were obtained from the raw data using Hoppel's algorithm in conjunction with the averaged charging probabilities (Kousaka *et al.*, 1985). Unfortunately, because of the finite voltage range of the DMA, there is no information on the concentrations of particles above 840 nm. Particles of this size carrying two charges would be included in a DMA size cut of nominal mobility diameter ~450 nm. Thus, the doubly charged fraction cannot be estimated reliably for mobility size cuts larger

than 450 nm. Crude estimates can be made by extrapolating the size distribution n. For the aerosol distributions produced by coagulation, the number distribution is generally unimodal (Friedlander, 1977). Since the peaks of the distributions were below 840 nm, a linear extrapolation of $\log(n)$ with $\log(d_m)$ must overestimate the number of particles above 840 nm, resulting in an upper bound on the multiply charged fraction for the large particles.

Once the multiply-charged fraction is known, it is possible to correct the data. We assume that ψ is equal to the fraction of doubly charged particles, which is reasonable if ψ is small. The measured uncharged fraction P_0' is then a weighted average of the true neutral fraction P_0 and the uncharged fraction for the doubly charged particles, P_{02},

$$P_0' = (1-\psi)\ P_0 + \psi P_{02}. \tag{15}$$

Fig. 9 is the result of this correction procedure. The neutral fraction for the doubly charged particles was obtained by interpolating the data with a cubic equation (the fitted curve of Fig. 9). Generally, the comparisons between the ammonium sulfate and TiO_2 are not affected by multiple charging. The fit to the agglomerate data remains ~5% lower than the ammonium sulfate data. However, the PSL data appears lower (relative to the TiO_2 and sulfate data) than in Fig. 8, particularly for the larger sizes. This is reasonable because the very monodisperse PSL aerosol was less affected by the correction procedures, which are expected to exaggerate the importance of multiple charging. It is possible that Fig. 8 is a more accurate representation of the data than Fig. 9. Nevertheless, the correction procedures do show that multiple charging affected the sulfate and TiO_2 data equally, so that multiple charging cannot explain the observed difference between the spheres and agglomerates.

CONCLUSIONS

The bipolar diffusion charging of agglomerate particles was found to be very similar to that of dense spheres of the same mobility, suggesting that DMA inversion procedures developed for spheres may be used for agglomerates as well.

The charging-equivalent diameter d_{QE} of the agglomerates was equal to the mobility diameter d_m for the smallest agglomerates (d_m~40 nm), while d_{QE}~1.1d_m for larger agglomerates (100<d_m<800 nm). Models based on long slender bodies predict a larger difference between d_m and d_{QE}. However, the difference between the length and the area-equivalent diameters is larger for slender bodies than for the agglomerates used here, which had fractal dimensions near 2. For such agglomerates, the mobility, mass-transfer and charging-equivalent diameters are expected to be similar. Taking this into consideration, the experimental results are in qualitative agreement with predictions based on the theory of Laframboise and Chang (1977). However, in interpreting the data it should be remembered that the mobility diameter measured by the differential mobility analyzer is expected to be slightly less than the orientation-averaged mobility diameter.

The measurements made here were consistent with nearly symmetrical charging. An analysis of the length and time scales of the experiment showed that the charge distribution may have been influenced by ion deposition on the tubing downstream of the neutralizer. This suggests that caution is needed in inverting DMA data, particularly when the aerosol flow rate is low and the post-charger residence time is high.

The precision of the technique used here is limited by multiple charging and fluctuations in the aerosol concentration. Even without reducing these effects, the precision is quite high and the technique could be used on fibers or long chain agglomerates to test theoretical predictions for the charging of prolate spheroids.

Acknowledgements. This research was supported by the International Fine Particle Research Institute. TEM micrographs by M. Richmond were greatly appreciated.

NOTATION

d	particle diameter
d_1	primary particle diameter
d_m	mobility diameter
d_V	volume-equivalent diameter
d_A	projected-area-equivalent diameter
d_D	mass-transfer-equivalent diameter
d_{QE}	charging-equivalent diameter
d_ϕ	potential-equivalent diameter
D_f	fractal dimension
D_{ion}	diffusion coefficient of the ion
e	elementary charge
F	charge enhancement factor
I	ion current to a particle
I_{sq}	ion current to a sphere of diameter d_m with q charges
I_{pq}	ion current to a prolate spheroid with q charges
k	Boltzmann constant
Kn_{ion}	$2\,\lambda_{ion}\,/\,d$
N_A	aerosol concentration
N_i	ion concentration
N	number of primary particles in and agglomerate
$n(d)$	aerosol size distribution
$P_q\,(d)$	probability of a particle of diameter 2 carrying q charges
P_0	uncharged fraction.
q	number of charges on a particle
q_m	number of charges expected on sphere dm
T	absolute temperature
R_g	radius of gyration
r	characteristic radius of plumbing
L	length of a slender body
χ	I_{pq}/I_{sq} shape induced ion flux enhancement factor
γ	fraction of ions lost to particles
η	ion attachment coefficient
η_A	ion-aerosol attachment coefficient
η_i	ion-ion recombination coefficient
κ	dynamic shape factor
λ_D	mean free path of a diffusing species
λ	gas mean free path
λ_{ion}	ion mean free path
σ_{cell}	estimate of the standard deviation from the "cell" data inversion
ψ	ratio of multiply charged particles to singly charged particles

REFERENCES

Adachi, M., Kousaka, Y., Okuyama, K. (1985), *J. Aerosol Sci.* **16**,109-123.

Adachi, M., Okuyama, K., Kousaka, Y., Kozuru, H. and Pui, D.Y.H.(1989), *Aerosol Sci. Technol.* **11**,144-156.

Burtscher, H., Reis, A. and Schmidt-Ott, A.(1986), *J. Aerosol Sci.* **17**,47-51.

Cheng, Y-S and Yeh, H-C. (1981), *J. Colloid Interface Sci.* **84**,444-450.

Cheng, Y-S and Yeh, H-C.(1983), *J. Aerosol Sci.* **20**,1095-1098.

Dahneke, B.(1973a), *J. Aerosol Sci.* **16**,147-161.

Dahneke, B.(1973b), *J. Aerosol Sci.* **16**,535-556.

Dahneke, B. (1973c), *J. Aerosol Sci.* **4**,163-170

Davison, S.W. and Gentry, J.W.(1985), *Aerosol Sci. Technol.* **4**,157-163.

Dua, S.K., Mayya, Y.S. and Kotrappa, P.(1980), *J. Aerosol Sci.* **11**,415-419.

Forrest, S.R. and Witten, T.A.(1979), *J. Phys A, Math Gen.* **12**,L109-117.

Friedlander, S.K.(1977), *Smoke, Dust and Haze* Wiley-Interscience, New York, pp.194-202.

Fuchs, N.A.(1963), *Geofis. Pura. Appl.* **56**,185-193.

Fuchs, N.A. (1964), *The Mechanics of Aerosols* Pergammon Press, New York, NY.

Gentry, J.W., Spurny,K., Hochrainer, D., Schoermann, J., Althaus, W., Han, R-J., Wang, G., Fletcher,R., and Steele, E.(1990), in *Aerosols,Science, Industry, Health and Environment.* vol. 1 (S. Masuda and K. Takahashi, eds.) Pergamon 435-438.

Gentry, J.W.(1972), *J. Aerosol Sci.* **3**,65-76.

Gupta, A. and McMurry, P.H.(1989), *Aerosol Sci. Technol.* **10**,451-462.

Hoppel, W.A. and Frick, G.M.(1986), *Aerosol Sci. Technol.* **5**,1-21.

Hoppel, W.A. and Frick, G.M.(1990), *Aerosol Sci. Technol.* **12**,471-496.

Huang, D.D., Seinfeld, J.H., and Okuyama, K.(1991), *J. Colloid Interface Sci.* **141**,191-198.

Hussin, A., Scheibel, H.G., Becker, K.H and Porstendörfer, J. (1983), *J. Aerosol Sci.* **14**,671-677.

Kasper, G. and Shaw, D.T.(1983), *Aerosol Sci. Technol.* **2**,369-381.

Kasper, G., Niida, T. and Yang, M.(1985). *J. Aerosol Sci.* **16**,535-556.

Keefe, D., Nolan, P.J and Rich, T.A.(1959) *Proc. R Ir. Acad.* 60A, 27.

Knutson, E.O. and Whitby, K.(1975), *J. Aerosol Sci.* **6**,443.

Kousaka, Y., Okuyama, K. and Endo, Y. (1981), *J. Aerosol Sci.* **12**,339-348.

Kousaka, Y., Okuyama, K. and Adachi, M. (1985), *Aerosol Sci. Technol.* **4**,209-225.

Kruisz, C. and Reischl, G.P.(1989), *J. Aerosol Sci.* **20**,1381-1384.

Laframboise, J.G. and Chang, J-S.(1977), *J.Aerosol Sci.* **8**,331-338.

Lassen, L. (1961), *Z. Phys.* **163**,339.

Liu, B.Y. and Lee, K.W.(1975), *Am. Ind. Hyg. Assoc.* **36**,861-865.

Liu, B.Y.H and Pui, D.Y.H.(1974), *J. Aerosol Sci.* **5**,465-472.

Meakin, P., Donn, B. and Mulholland, G.W.(1989), *Langmuir* **5**,510-518.

Okuyama, K., Kousaka, Y., Tohge, N., Yamamoto, S., Wu, J.J., Flagan, R.C. and Seinfeld, J.H.(1986), *AI. Che. J.* **2**,2010-2019.

Pao, J-R., Wang, C.C., Cleary, T.G. and Gentry, J.W.(1989), *J. Aerosol Sci.* **20**,1095-1098.

Porstendörfer, J., Hussin, A., Scheibel, H.G., and Becker, K.H (1983), *J. Aerosol Sci.* **15**,4756.

Rogak, S.N., Flagan, R.C. and Hguyen, H.V. (1991a), submitted to *J. Aerosol Sci.*

Rogak, S.N., Baltensperger, U. and Flagan, R.C. (1991b), *Aerosol Sci. Technol.*,(in press).

Samson R.J., Mulholland, G.W. and Gentry, J.W. (1987), *Langmuir* **3**,272-281.

Schmidt-Ott, A., Baltensperger, U., Gäggeler, H.W., and Jost, D.T.(1990). *J. Aerosol Sci.* **21**:711-717.

Shon, S-N.(1979), Ph.D. thesis, University of Buffalo.

Smirnov, B.M. (1990), *Phys. Rep.* **188**,1-78.

Twomey, S. (1977), *Atmospheric Aerosols*, New York, Elsevier North Holland, pp. 247-270.

Vijaykumar, R. and Whitby, K.T.(1984), *Aerosol Sci. Technol.* **3**,25-30.

Vomela, R. and Whitby, K.(1967), *J.Colloid Interface Sci.* **25**,568-576.

Wang, C.C., Pao, J-R and Gentry, J.W.(1988), *J. Aerosol Sci.* **19**,805-808.

Weitz, D.A. and Huang, J.S. (1986), in *Kinetics of Aggregation and Gellation* (F. Family and D.P. Landau, Eds.). North Holland, 19-28.

Wen, H.Y. and Kasper, G.(1984), *Aerosol Sci. Technol.* **3**,397-403.

Wen, H.Y., Reischl, G.P. and Kasper, G. (1984a), *J. Aerosol Sci.* **15**,89-101.

Wen, H.Y., Reischl, G.P. and Kasper, G. (1984b), *J. Aerosol Sci.* **15**,103-122.

White, H.J. (1977), *J. Air Pollut. Control Assoc.*, **27** Nos. 1,2,3,4.

Yu, P.Y. , Wang, C.C. and Gentry, J.W. (1987), *J. Aerosol Sci.* **18**,73-85.

Table 1. Ion flux ratios normalized by the fluxes to the volume-equivalent sphere, from Wang *et al.*, (1988, no parenthesis) and Laframboise and Chang (1977, in parenthesis).

Aspect Ratio	Minor Diameter d_1 (nm)			
	0.02	20	2000	infinity
1	1	1	1	1
10	0.74 (1.70)	1.4 (1.57)	1.72 (1.54)	1.64 (1.54)
100	1.8 (3.65)	3.50 (3.84)	3.80 (4.06)	3.54 (4.06)

Table 2. Data by Shon (1979) for the charging of chain agglomerates in a) a bipolar charger and b) a unipolar polar charger.

(a)

No. Primaries N	Length L (nm)	Mobility Dia. d_m (nm)	charge q/q_m	Charging Dia. d_{QE} (nm)
9	297	140	4.09	2044
13	429	170	2.57	1020
20	660	230	2.46	1300
24	792	260	2.16	1130
33	1089	310	2.08	1270
35	1155	330	1.85	1080
41	1353	360	1.71	1020
49	1617	410	1.6	1020

(b)

No. Primaries N	Length L (nm)	Mobility Dia. d_m (nm)	charge q/q_m	Charging Dia. d_{QE} (nm)
12	396	170	1.8	310
22	726	290	2.5	740
43	1420	380	3.3	1270
47	1550	400	3.4	1380
47	1550	400	3.5	1420
59	1950	450	3.8	1730
59	1950	450	4.0	1830
62	2046	470	3.6	1720
80	2640	550	4.0	2230

Table 3. Comparison of charging data for doublets and triplets of 500 nm diameter (Dua *et al.*, 1980) with the Boltzmann distribution. F is the ratio of multiply charged particles to singly charged particles, normalized by the predicted ratio from Boltzmann charging. Volume, surface and length-equivalent spheres were used for the comparison (subscripts v, s and max, respectively).

	Doublets			Triplets		
q	F_v	F_s	F_{max}	F_v	F_s	F_{max}
1	1.00	1.00	1.00	1.00	1.00	1.00
2	1.45	1.42	1.32	1.14	1.10	1.02
3	1.21	1.13	0.93	1.33	1.22	0.98
4	-	-	-	-	-	-
5	1.55	1.35	1.18	-	-	-

Table 4. Summary of Experimental Results.

	DMA Setting					Uncharged Fraction		
Material	Voltage V	d_m (nm)	N_A (cm^{-3})	σ_{cell}	ψ	P_{0cell}	P_{0fit}	P_{0fit} [a]
TiO_2	80	40.2	6000	0.015	0.09	0.659	0.653	0.663
	100	45.3	6000	0.019	0.12	0.651	0.643	0.660
	400	98	400	0.018	0.05	0.379	0.385	0.388
	400	98	800	0.019	0.05	0.410	0.420	0.424
	400	98	7000	0.067	0.05	0.438	0.470	0.477
	500	111	1800	0.007	0.13	0.382	0.382	0.392
	800	148	1000		0.10	0.329	0.321	0.328
	1504	222	500	0.005	0.07	0.260	0.257	0.261
	2000	270	9000	0.003	0.27	0.227	0.224	0.241
	4000	450	2000	0.002	0.09	0.172	0.170	0.174
	4819	522	2300	0.005	0.20	0.153	0.151	0.161
	7189	725	2300	0.010	0.40	0.121	0.125	0.149
	8000	794	1500	0.001	0.30	0.111	0.111	0.123
	8000	794	120	0.001	0.045	0.119	0.119	0.121
PSL	233	72	1600	0.004	0.06	0.484	0.485	0.490
	233	72	1500	0.006	0.06	0.520	0.520	0.528
	1138	185	300	0.004	0.025	0.306	0.308	0.310
	4819	522	8.2	0.001	0.01	0.162	0.161	0.162
	4819	522	8.5	0.003	0.01	0.164	0.165	0.166
	7189	725	6.0	0.02	0	0.123	0.124	0.124
Sulfate	80	40.2	3600	0.004	0.10	0.0682	0.676	0.689
	100	45.3	4100	0.005	0.11	0.644	0.642	0.657
	500	111	1100	0.002	0.23	0.399	.395	0.420
	800	148	200	0.012	0.24	0.342	0.334	0.357
	1504	222	140	0.002	0.13	0.268	0.267	0.277
	2000	270	700	0.003	0.22	0.241	0.239	0.256
	4000	450	60	0.003	0.085	0.181	0.181	0.186
	8000	794	3.50	0.002	0.027	0.129	0.127	0.128
	8000	794	2.2	0.001	0.06	0.124	0.124	0.127
	8000	794	2.2	0.004	0.06	0.130	0.128	0.131

[a] Corrected for multiple charging.

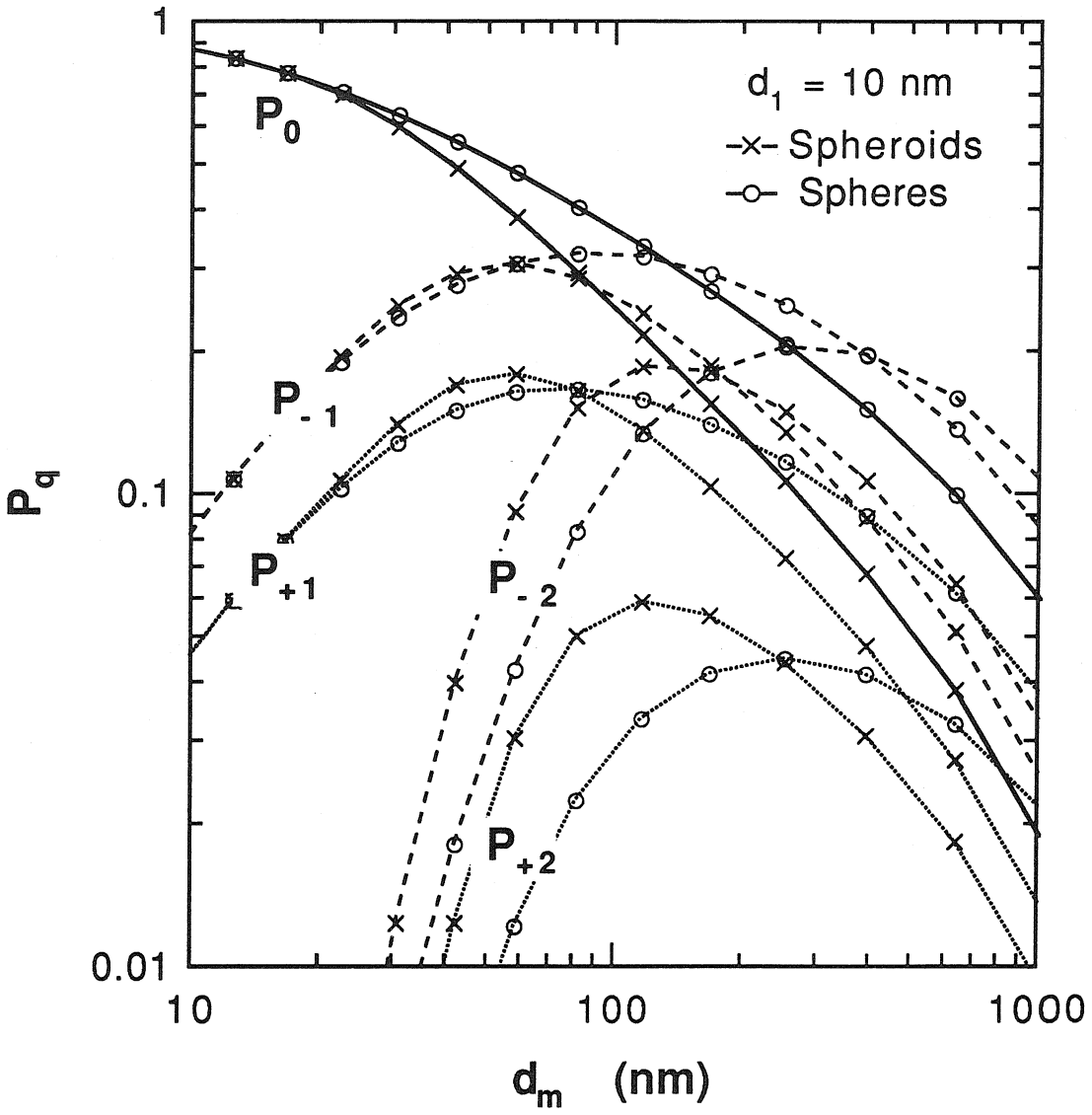

Fig. 1. Steady-state charge distribution for spheres and prolate spheroids (Laframboise and Chang, 1977). $P_q(d_m)$ is the probability that a particle with mobility diameter d_m carries $\pm q$ charges. The minor diameter of the prolate spheroids is d_1=10 nm.

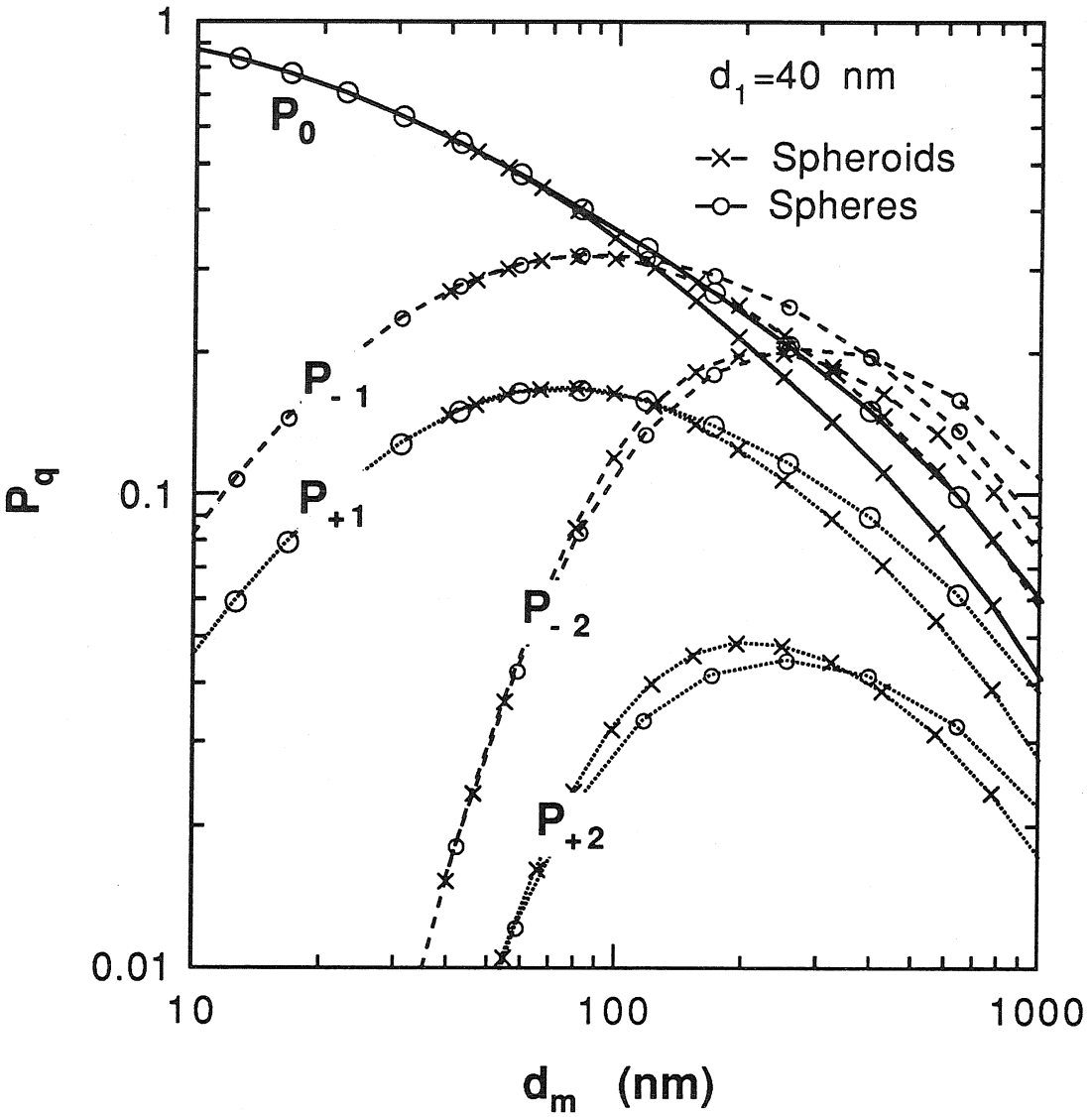

Fig. 2. Steady-state charge distribution for spheres and prolate spheroids (Laframboise and Chang, 1977). $P_q(d_m)$ is the probability that a particle with mobility diameter d_m carries $\pm q$ charges. The minor diameter of the prolate spheroids is d_1=40 nm.

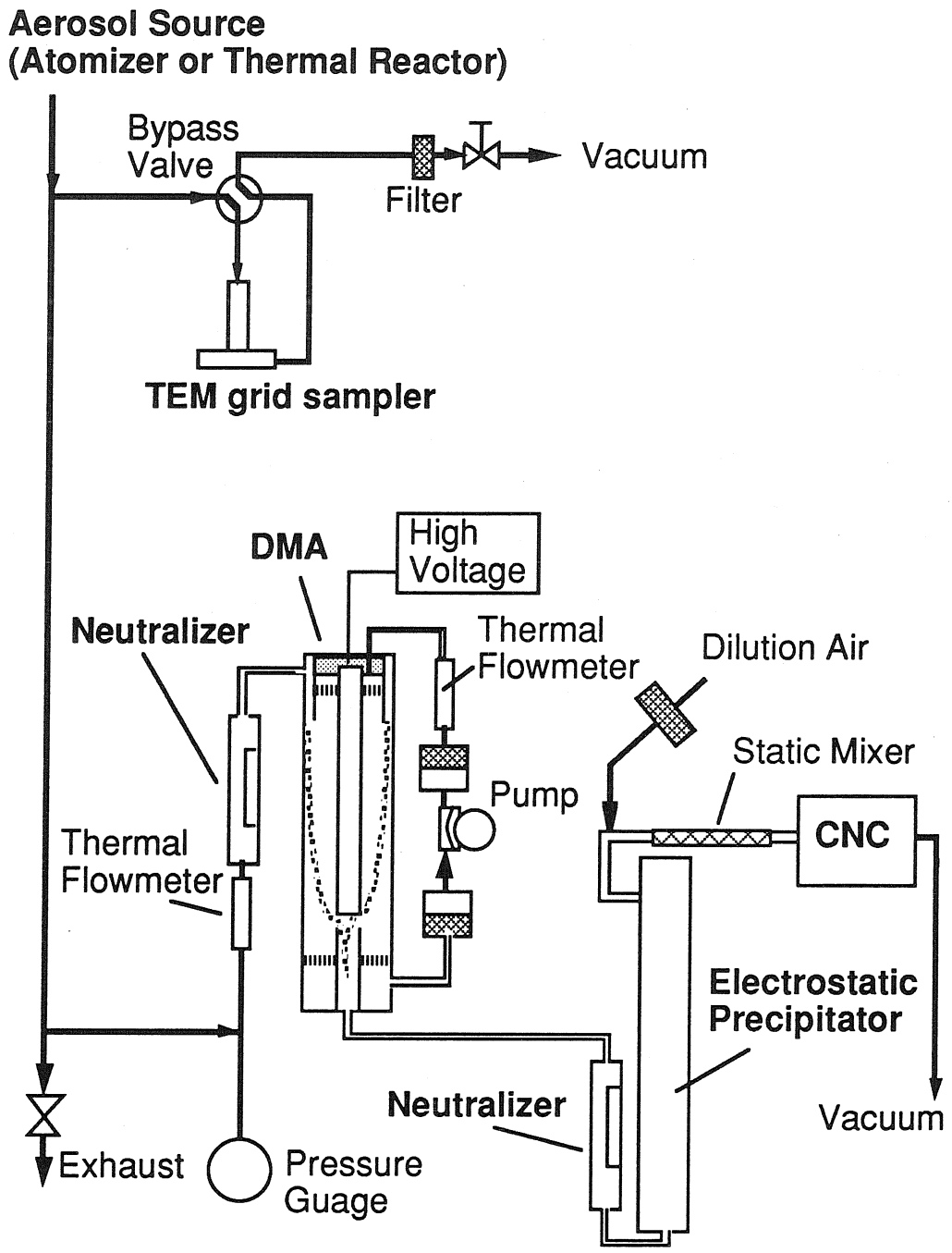

Fig. 3. Schematic of the apparatus used to classify, neutralize and count aerosol particles. Turning the precipitator on and off allows counting of the uncharged and charged fractions of the aerosol.

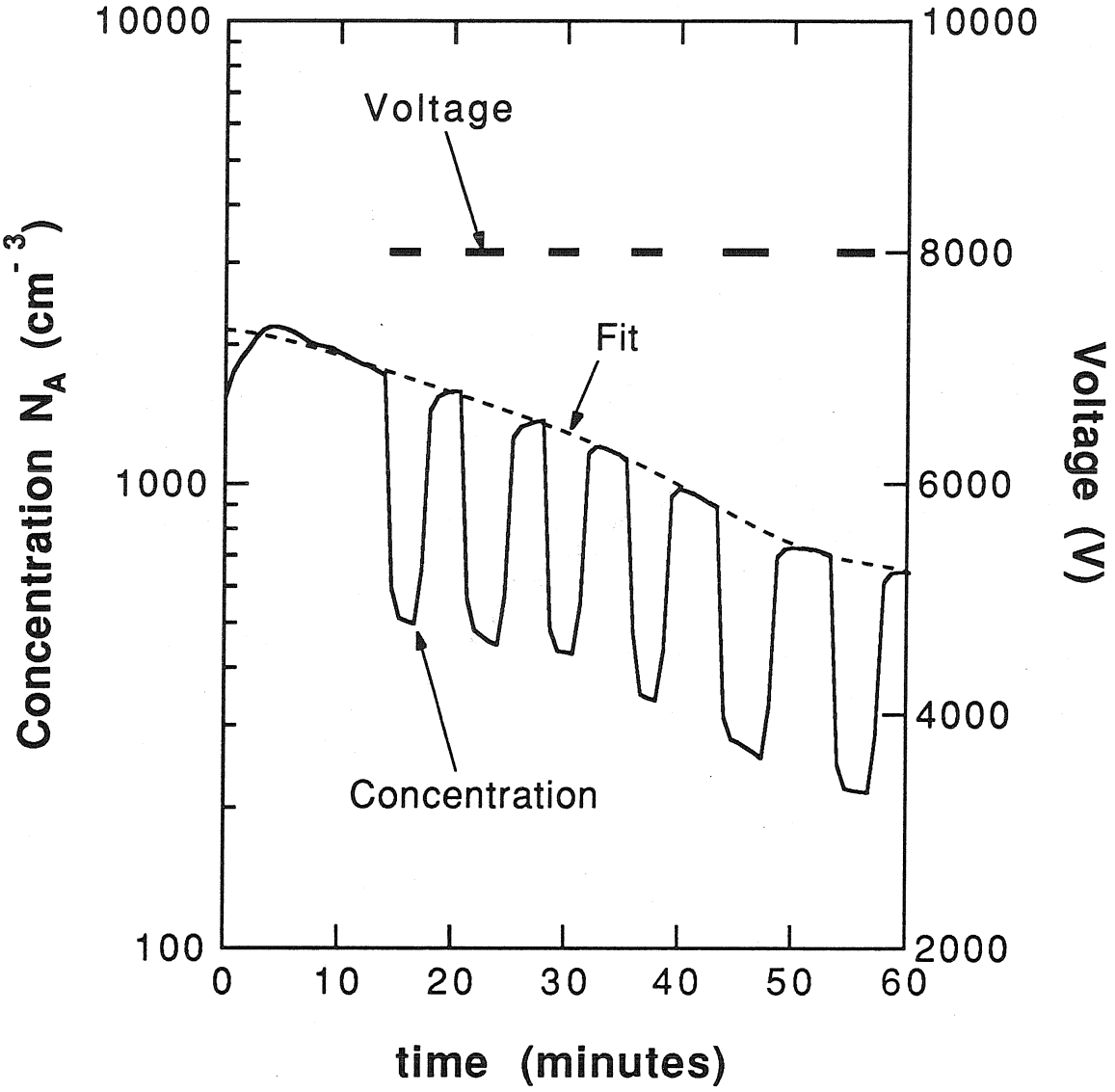

Fig. 4. Concentration time histories for titania leaving the precipitator (solid line) and the estimated concentration entering the precipitator, obtained by interpolating measurements taken with the precipitator voltage = 0.

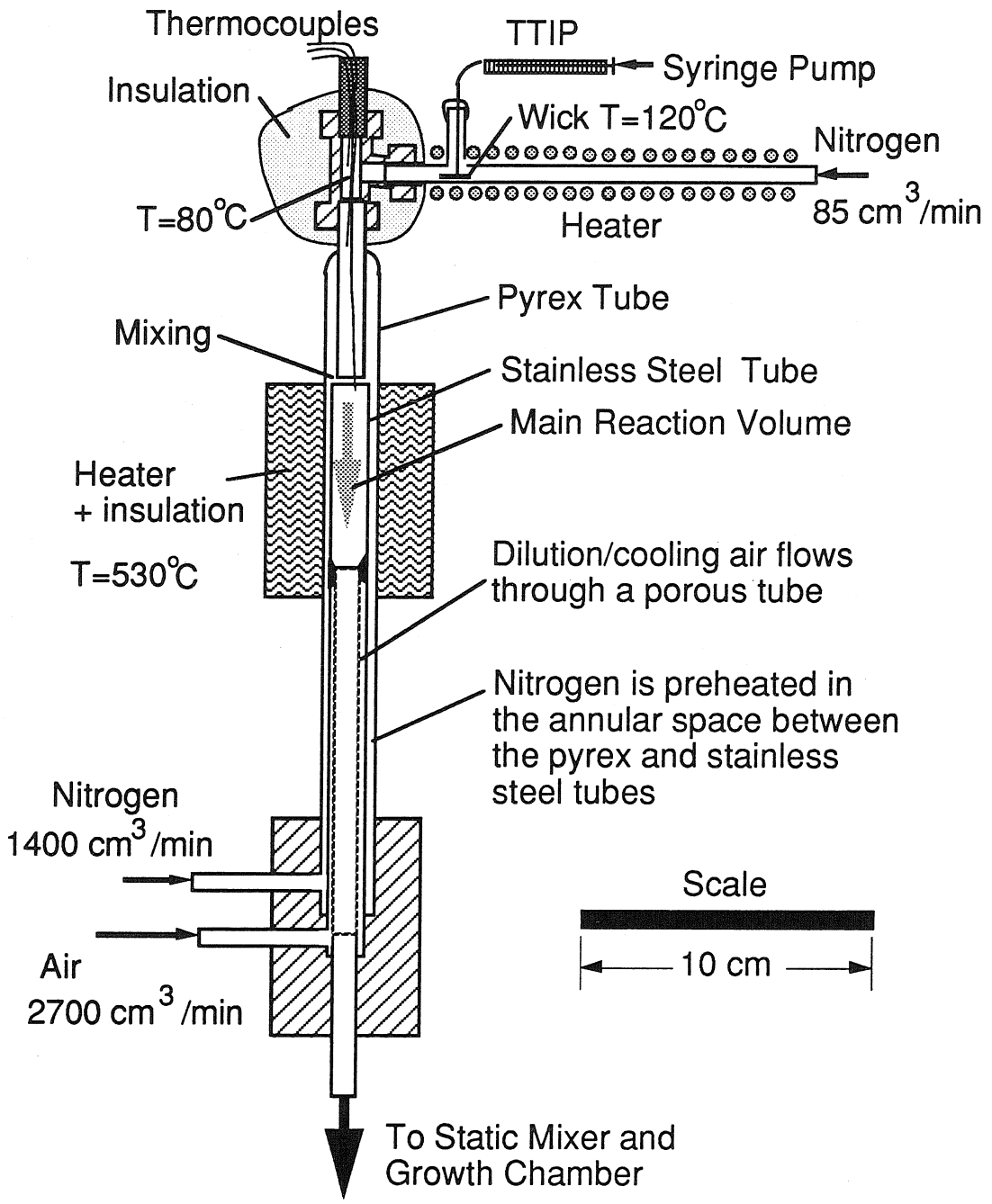

Fig. 5. TiO_2 aerosol generator. Warm nitrogen carries titanium tetraisopropoxide vapor (TTIP) into a pyrex reactor where it mixes with preheated nitrogen, decomposes and forms TiO_2 agglomerates.

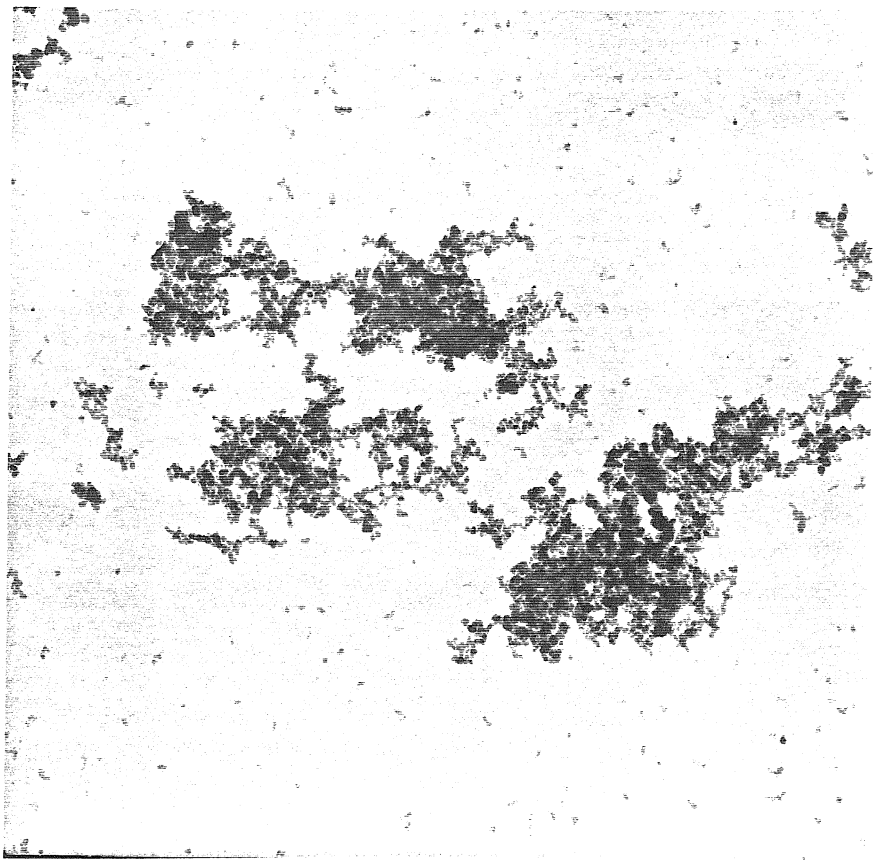

1000 nm

Fig. 6a. TiO_2 agglomerate produced in the thermal reactor from alkoxide decomposition.

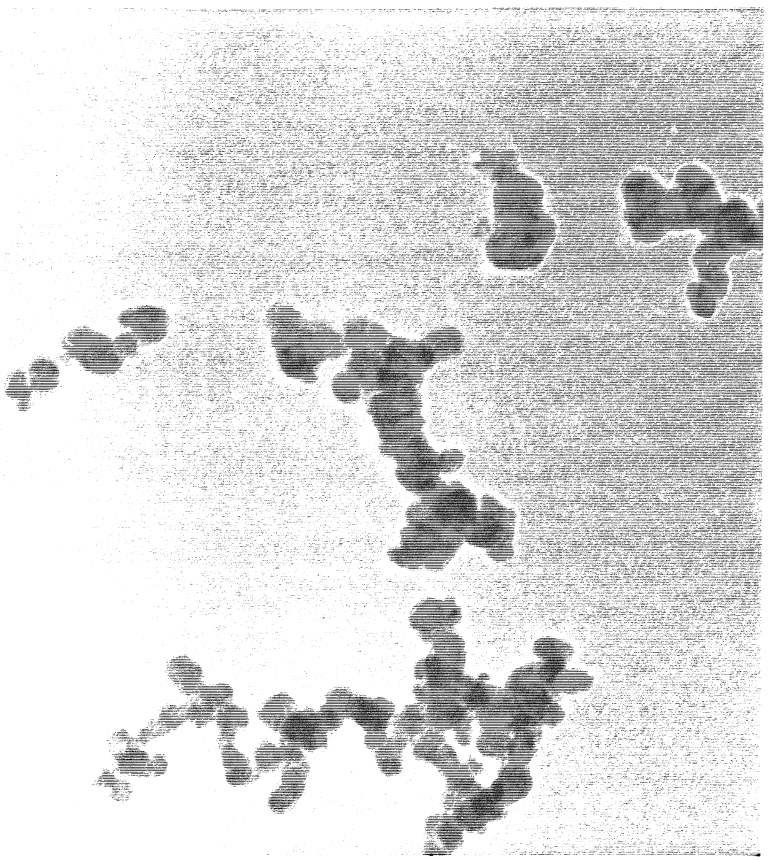

100 nm

Fig. 6b. TiO_2 agglomerate produced in the thermal reactor from alkoxide decomposition.

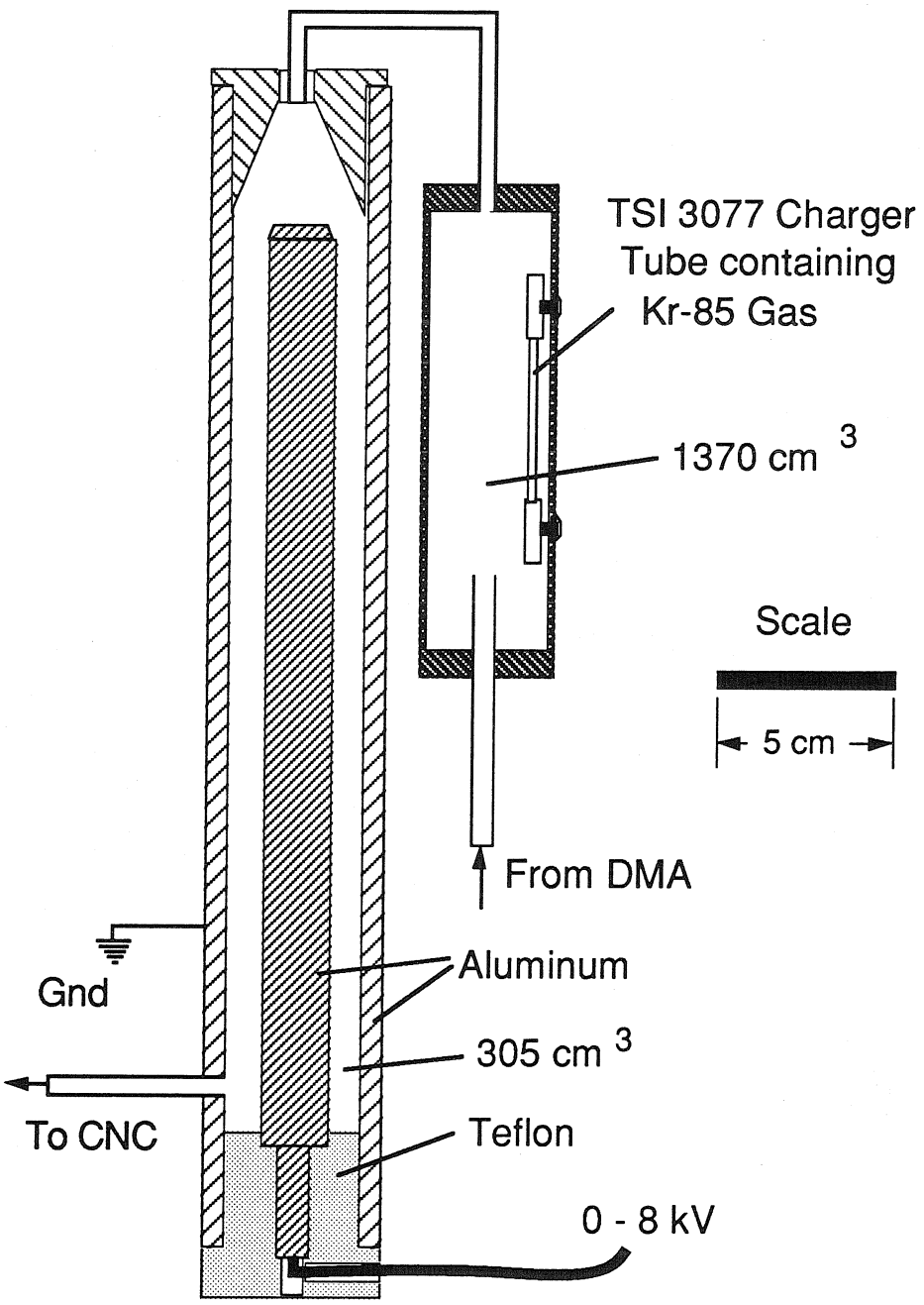

Fig. 7. Electrostatic Precipitator and Neutralizer

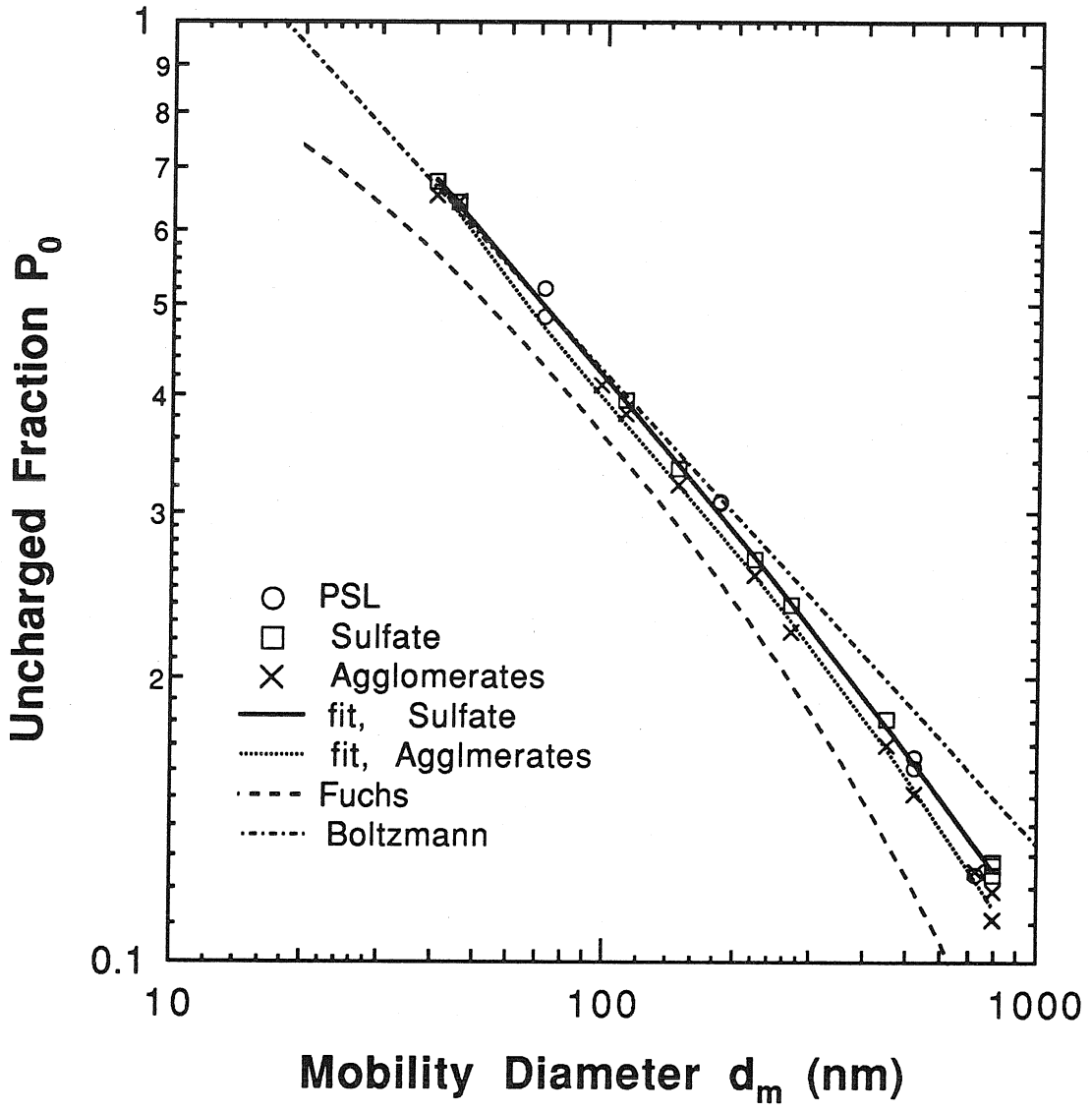

Fig. 8. Neutral fraction P_0 vs mobility diameter d_m for spheres (ammonium sulfate and polystyrene latex) and agglomerates (TiO_2). The neutral fraction was higher than that predicted by Fuchs theory, due to ion losses, and agrees better with symmetric charging (Boltzmann distribution). No corrections for multiple charging.

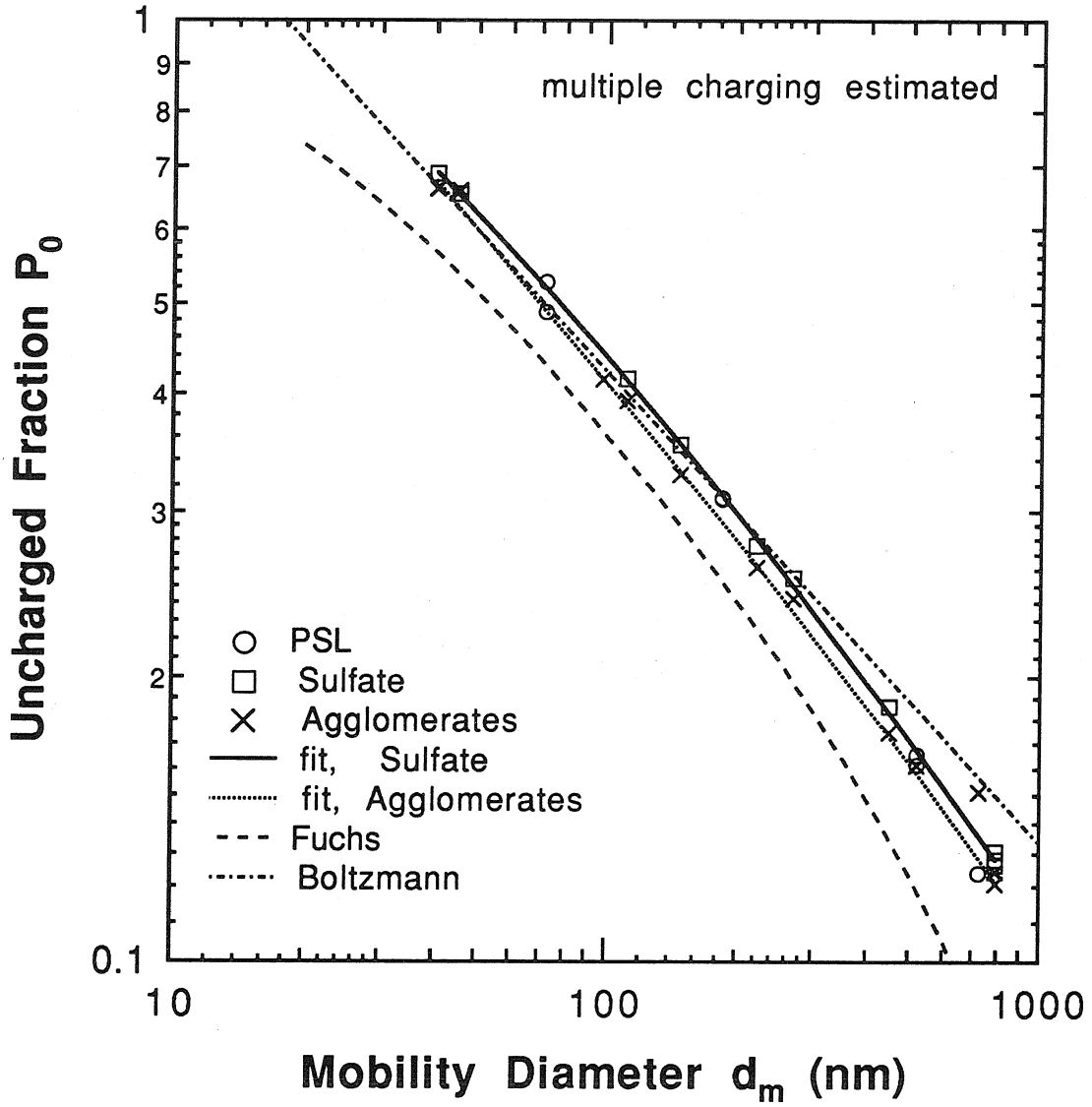

Fig. 9. Neutral fraction P_0 vs mobility diameter d_m after approximate corrections for multiple charging.

CHAPTER 8
COAGULATION OF AEROSOL AGGLOMERATES IN THE TRANSITION REGIME

Steven N. Rogak and Richard C. Flagan

California Institute of Technology 138-78

Pasadena, CA 91125

submitted to Journal of Colloid and Interface Science

ABSTRACT

Aerosol agglomerates are produced by homogeneous nucleation and Brownian coagulation. Coagulation models developed previously for spheres may be applicable to the initial stages of growth in which the colliding particles coalesce rapidly. Particles larger than a critical size d_1 are not expected to coalesce, leading to the formation of fractal-like agglomerates of dense primary particles. To describe coagulation in such systems, it is necessary to predict the mobilities, collision diameters and mean free paths of agglomerate particles having sizes comparable to the gas mean free path λ. Using existing data on particle mobility and structure, these quantities are obtained for model agglomerates with fractal dimensions D_f in the range $1< D_f <3$. For $D_f \sim 1.8$, the resulting coagulation frequency function K is found to be significantly higher than for spheres with the same mobility and material density ρ, in part because of the low effective density of the agglomerates. Numerical solutions of the coagulation equation show that as the aerosol grows from coalescing particles past the critical primary particle size d_1, both the width, σ_g, of the size distribution and the coagulation rate increase. For aerosols where the average particle is much larger than d_1, both σ_g and the coagulation rate are reduced. Although the growth is affected by D_f, d_1, λ and ρ, results for large agglomerates are consistent with

similarity solutions using a simplified collision frequency function. For the simplified coagulation frequency function it is assumed that the agglomerates are smaller than λ but much larger than the agglomerate mean free paths.

INTRODUCTION

Coagulation is the process by which particles suspended in a gas or liquid agglomerate because of Brownian motion, turbulent diffusion, interparticle forces or gravitational settling (1,2,3). In some cases the process may be reversible or limited by surface reactions, especially for agglomerate formation in colloidal systems (4). In this paper we focus on the process most relevant to aerosol particles in the 10-1000 nm diameter range, namely, Brownian coagulation in which every particle collision is successful and irreversible. Such Brownian coagulation is well understood for liquid particles, where the coalescing particles maintain a spherical shape (2,3,5). The coagulation of solid, non-spherical particles is less well understood, particularly for aerosol particles in the transition regime, where the particle dimensions are comparable to the gas mean free path.

Aerosol agglomerates generally result from systems that undergo homogeneous nucleation and Brownian coagulation at temperatures well below the melting point of the product material. For sufficiently small particles, which densify rapidly because of their large surface free energy (6), the coalescing coagulation model may be applicable. However, larger particles do not coalesce on experimental time scales, and so growth leads to low-density agglomerates of fully densified primary particles. It should be noted that although there is substantial evidence that sintering rates may control the primary particle size (7,8,9), in some systems it may be influenced by the formation rate of the nucleating species and temperature variations (10,11). Even in these complex systems, there is a well-defined primary particle size.

Examples of aerosol agglomerates are soot, coal ash, and synthetic fumes (TiO_2, SiO_2, etc.), for which the primary particle diameters are in the range $6<d_1<100$ nm (9,12,13,14,15,16). Without chemical analysis, the various particles are often indistinguishable. Forest and Witten (14) observed that metal oxide aggregates produced in their experiment exhibited power-law scaling of the density correlation function. Thus, a square with sides L placed over an image of an aggregate covered an area $m(L)$, for which

$$m(L) \sim L^{D\alpha} , \qquad [1]$$

where D_α, which has been called the *fractal dimension,* generally has a value below the Euclidean dimension of 3. In addition to Eq. [1], the masses M of agglomerates are expected to scale with the radius of gyration R_g,

$$M(R_g) \sim R_g^{D\beta} , \qquad [2]$$

where $D_\beta \sim D_\alpha$ for large fractal agglomerates (17). In this paper we assume that $D_\beta = D_\alpha = D_f$. Real agglomerates typically have fractal dimensions in the range $1.6< D_f<1.9$ (16,17,18). However, rearrangement can produce denser structures (19) with higher fractal dimensions while nearly straight chains ($D_f \sim 1$) are produced in systems where strong interparticle forces influence the agglomeration (20).

Computer simulations of the coagulation of hard spheres yield fractal-like structures and can provide insights into the formation mechanisms (21,22,23). For example, relatively dense particles ($D_f \sim 2.4$) are produced when individual spheres diffuse to the surface of the growing aggregate (diffusion-limited aggregation or DLA), while low-density aggregates ($D_f \sim 1.8$) result from coagulation of like-sized aggregates (cluster-cluster aggregation or CCA).

While simulations reveal important features about the structure of aggregate particles, the computational demands are great. Efforts to predict particle formation and growth in aerosol systems require an alternate approach that retains the essential physics

while reducing the magnitude of the computations. Coagulation of rapidly coalescing particles is usually described by extensions of the theory originally proposed by Smoluchowski (24) in which the evolution of the particle size distribution is described by population balance equations (5,13,25). Solution procedures range from solving ordinary differential equations to follow moments of the particle size distribution or concentrations of the discrete particle sizes (monomer, dimer, trimer ... n-mer), to solving an integro-differential equation for a continuous particle size distribution function. This approach can be applied to aerosols consisting of agglomerate particles by replacing the collision frequency function in the coagulation equation with a function that is appropriate for the agglomerate particles. Mountain et al. (22), Mulholland et al. (26) and Kaplan and Gentry (27) have applied this method to the dynamics of agglomerate particles in the free-molecule regime, while continuum regime agglomeration calculations have been performed for Brownian coagulation (22,28,29,30) and differential sedimentation (31). However, the collision frequency functions for agglomerates in the transition regime have not been developed.

This paper develops a method to describe the dynamics of agglomerate particles as they grow from the free-molecule regime through the transition regime and into the continuum regime. Brownian coagulation theory for spheres in the transition regime is reviewed briefly and found to be applicable to non-spherical particles if the collision, mobility and volume-equivalent diameters of the particles are known. Fractal scaling can be used to estimate these diameters, resulting in a simplified coagulation equation for which similarity solutions exist. More accurate predictions of agglomerate growth require detailed models of the particle structure, mobility and collision properties. Incorporating these elements into a sectional representation of the coagulation equation, the evolution of an aerosol can be followed numerically. As a first attempt to incorporate partial coalescence into the dynamics, it is assumed that particles below the primary particle size are dense spheres, while larger particles have a low-density, fractal structure.

EVOLUTION OF AN AEROSOL BY BROWNIAN COAGULATION

The Coagulation Equation

Brownian coagulation is a stochastic process depending not only on the average concentrations of the relevant particles but also on the concentration fluctuations. The full coagulation equation involves the correlation of these fluctuations (1,32) but for systems with many particles, the simpler Smoluchowski equation may be used (5,13). The evolution of a non-reacting or non-reforming aerosol population of the type considered here is thus governed by

$$\frac{dn_j}{dt} = \frac{1}{2}\sum_{i=1}^{j-1} K_{i\,j-i} n_i n_{j-i} \; - \; n_j \sum_{i=1}^{\infty} K_{i\,j}\, n_i \;, \qquad [3]$$

where n_j is the number concentration of particles containing j molecules and $K_{ij}n_in_j$ is the collision frequency of particles of size i with particles of size j.

In Eq. [3], there is no explicit dependence on particle structure. However, the form of the collision frequency function, or coagulation kernel, K_{ij}, varies with particle structure and background gas properties.

The Transition Regime Brownian Coagulation Kernel

The coagulation of non-spherical particles is characterized by a number of equivalent diameters, which have been summarized in Table I. The role of these diameters in the coagulation process can be understood by reviewing the approach taken to derive the collision frequency function for spheres, for which all of the equivalent diameters are the same. The collision rate for spheres of volume-equivalent diameters d_{c1} and d_{c2} may be found by calculating the diffusion rate of a point particle to an "absorbing sphere" (5,13). The point particle has diffusivity D_1+D_2, and the absorbing sphere has diameter $d_{abs}=d_{c1}+d_{c2}$. The absorbing surface is generated by the position of the center of one

sphere relative to the other sphere after all possible collisions. By analogy, the absorbing sphere diameter d_{abs} for non-spherical particles may be defined as the sum of the collision-equivalent diameters d_{c1} and d_{c2}. The transition regime kernel function is thus

$$K = 2\pi (d_{c1} + d_{c2}) (D_1 + D_2) \beta , \qquad [4]$$

where the factor β accounts for the finite mean free paths of the diffusing particles. The particle diffusivities are given by the generalized Stokes-Einstein relation between the particle mobility diameter d_m and the diffusivity,

$$D = \frac{kT\, C_c(Kn)}{3\pi\mu d_m} , \qquad [5]$$

where k is the Boltzmann constant, T is the absolute temperature, μ is the gas viscosity and C_c is the Cunningham slip correction factor,

$$C_c(Kn) = 1 + Kn\, (A + B \exp(C/Kn)) \qquad [6]$$

$$Kn = \frac{2\lambda}{d_m} , \qquad [7]$$

where A= 1.257, B = 0.4 and C = -1.1 are empirically determined (5).

The transition regime correction factor β may be obtained from the widely accepted flux-matching model of Fuchs (13). However, a simpler approximation due to Dahneke (33) differs from the Fuchs theory by less than 4%, and is the model used here. The Dahneke expression is

$$\beta = \frac{1+Kn_D}{1+2Kn_D(1+Kn_D)} . \qquad [8]$$

The diffusion Knudsen number Kn_D characterizes the transition between continuum and free-molecule diffusion. This transition occurs at a distance on the order of λ_{12} from the surface of the absorbing sphere, where λ_{12} is the diffusion mean free path. The diffusion Knudsen number is given by

$$Kn_D = \frac{2\lambda_{12}}{d_{c1} + d_{c2}} . \qquad [9]$$

The diffusion mean free path λ_{12} is comparable to the particle mean free paths and depends on the particle masses, which are characterized by the volume-equivalent sphere diameters d_{vi}, and on the particle diffusivities:

$$\lambda_{12} = \frac{2(D_1+D_2)}{\sqrt{\frac{12kT}{\pi^2\rho}\left(d_{v1}^{-3} + d_{v2}^{-3}\right)}} , \qquad [10]$$

where ρ is the particle density. Thus, the coagulation kernel for non-spherical particles depends on d_v, d_c, and d_m in addition to the background gas properties. As illustrated in Figure 1, relations between these equivalent diameters will be developed and incorporated into the sectional model of the aerosol equation of Wu (9) and Gelbard et al. (34). However, a qualitative understanding of the coagulation process may be gained by non-dimensionalizing the equations and then considering similarity solutions to the coagulation equation.

Non-Dimensionalization

Aerosol coagulation is characterized by numerous parameters, resulting in many valid ways to normalize the equations. Since this paper focuses on the transition regime coagulation, it is natural to choose characteristic scales based on the background gas properties. Using the normalization procedure described below, the normalized particle sizes and concentrations are of order unity for normalized times near unity.

The characteristic length is taken as 2λ, so normalized volume-equivalent particle diameters are, for example,

$$\tilde{d}_v = \frac{d_v}{d_0} \quad ; \quad d_0 = 2\lambda . \qquad [11]$$

For spheres of equal size in the continuum regime, the coagulation kernel (Eq.[4]) is independent of the particle size and may be taken as the characteristic coagulation rate K_0 of the system. The non-dimensional kernel function is therefore

$$\tilde{K} = \frac{K}{K_0} \quad ; \quad K_0 = \frac{8kT}{3\mu} . \qquad [12]$$

For a given aerosol volume fraction ϕ, the characteristic number concentration n_0 is obtained by using the volume of a sphere of diameter d_0. The particle size distributions are therefore normalized by n_0 with

$$\tilde{n} = \frac{n}{n_0} \quad ; \quad n_0 = \frac{6\phi}{\pi\, d_0^3} . \qquad [13]$$

The normalization of the time t follows naturally as

$$\tilde{t} = \frac{t}{t_0} \quad ; \quad t_0 = \frac{1}{K_0 n_0} . \qquad [14]$$

The background gas provides a characteristic density ρ_0 by which the particle density ρ may be normalized,

$$\tilde{\rho} = \frac{\rho}{\rho_0} \quad ; \quad \rho_0 = \frac{72\, d_0 \mu}{K_0} . \qquad [15]$$

Substituting these non-dimensional quantities into Eqs.[4]-[10], the coagulation kernel takes the form

$$\tilde{K} = \frac{(\tilde{d}_{c1} + \tilde{d}_{c2})}{4} \left(\frac{C_c(Kn_1)}{\tilde{d}_{m1}} + \frac{C_c(Kn_2)}{\tilde{d}_{m2}} \right) \beta(Kn_D) . \qquad [16]$$

The diffusion Knudsen number Kn_D can be related to the non-dimensionalized diameters and particle density,

$$Kn_D = \sqrt{\tilde{\rho}}\, \frac{\dfrac{C_c(Kn_1)}{\tilde{d}_{m1}} + \dfrac{C_c(Kn_2)}{\tilde{d}_{m2}}}{(\tilde{d}_{c1} + \tilde{d}_{c2}) \sqrt{\tilde{d}_{v1}^{-3} + \tilde{d}_{v2}^{-3}}} . \qquad [17]$$

Figure 2 shows the coagulation kernel $\tilde{K}$ for spherical particles (d_c=d_m=d_v), plotted for two values of $\tilde{\rho}$. A non-dimensional density of $\tilde{\rho}$=0.02 corresponds approximately to iron oxide in air at 298 K and 1 atm, while $\tilde{\rho}$=0.001 corresponds to soot at 1500 K and 1 atm. Since the coagulation kernel is symmetric in $\tilde{d}_{v1}$ and $\tilde{d}_{v2}$, Figure 2 shows only values of $\tilde{K}$ where $\tilde{d}_{v2} \geq \tilde{d}_{v1}$. For equal-sized particles in the free-molecule regime, the coagulation kernel $\tilde{K}$ increases with size to a maximum at $Kn_D \sim 1$. The free-molecule behavior of $\tilde{K}$ ends near $\tilde{d}_{v1} \sim 0.1$ for $\tilde{\rho}$=.001 and near $\tilde{d}_{v1} \sim 0.4$ for $\tilde{\rho}$=0.02. In the transition regime $\tilde{K}$ decreases with particle size, while in the continuum regime $\tilde{K}$ approaches a constant value. The continuum behavior starts for $\tilde{d}_{v1} \sim 3$, regardless of the particle density.

Similarity Solutions

Under certain conditions the Brownian coagulation kernel may be simplified to a homogeneous form, for which similarity solutions to the coagulation equation can be found [3]. The particle volumes v are first normalized by the mean particle volume $\bar{v}$ of the size distribution. If a coagulation kernel for particles of volumes $\bar{v}\,\eta_1$ and $\bar{v}\,\eta_2$ can be written as

$$K(\bar{v}\eta_1, \bar{v}\eta_2) = \bar{v}^{\gamma} K(\eta_1, \eta_2), \qquad [18]$$

the kernel is said to be homogeneous of degree γ and the coagulation equation may be solved using similarity techniques (35,36).

To obtain the similarity solution, it is assumed that the size distribution $n(v,t)$ is proportional to a time-invariant, or self-preserving, distribution $\psi(\eta)$ according to

$$n(v,t) = \frac{n_T^2(t)\,\psi(\eta)}{\phi} \qquad [19]$$

$$\eta = \frac{v}{\bar{v}} \qquad [20]$$

$$\bar{v}\,(t) = \frac{\phi}{n_T}\,, \qquad [21]$$

where n_T is the total number of particles in the system and ϕ is the aerosol volume fraction. Substituting these variables into the coagulation equation and integrating over all particle sizes (36), the rate of change of the total number of particles is

$$\frac{dn_T}{dt} = -\frac{1}{2}\,\kappa\left(\frac{\phi}{n_T}\right)^{\gamma} n_T^2\,, \qquad [22]$$

where

$$\kappa = \int_0^{\infty}\int_0^{\infty} K(\eta_1,\eta_2)\,\psi(\eta_1)\,\psi(\eta_2)\,d\eta_1 d\eta_2\ . \qquad [23]$$

Since κ and ψ are independent of time, Eq. [22] can be solved. For $\gamma < 1$ (37),

$$n_T(t) = \left[n_T^{\gamma-1}(0) + \frac{(1-\gamma)}{2}\,\phi^{\gamma}\,\kappa\,t\right]^{\frac{1}{\gamma-1}}\ . \qquad [24]$$

For large t, when n_T is much smaller than the initial number concentration $n_T(0)$, the time-dependent behavior of n_T reduces to

$$n_T \sim t^{-z}\,, \qquad [25]$$

where z, the dynamic exponent, is related to the degree of homogeneity by

$$z = \frac{1}{1-\gamma}\ . \qquad [26]$$

Since particle mass is conserved during coagulation, the mass-averaged diameter evolves according to

$$d_v(t) = \bar{v}^{1/3} \sim t^{z/3} . \qquad [27]$$

Thus, the dynamic behavior of a coagulating system is expected to depend in a well-defined manner on the degree of homogeneity of the kernel function. We next consider homogeneous kernels that have been proposed to describe the coagulation of fractal agglomerates in the continuum, free-molecule and transition regimes.

In the continuum regime, it has been assumed that both mobility and collision diameters are proportional to the radius of gyration R_g (22,27). Therefore, from the fractal scaling of R_g with the number of primary particles N in an agglomerate (Eq. [2]),

$$K \sim \left(N_1^{1/D_f} + N_2^{1/D_f}\right)\left(N_1^{-1/D_f} + N_2^{-1/D_f}\right) . \qquad [28]$$

Mulholland et al. (26) obtained a free-molecule regime (Kn>>1 and Kn_D >>1) kernel function, for which they assumed that the drag on an agglomerate is proportional to its projected area and that the collision diameter scales with R_g. Further, they assumed that the projected area is proportional to N for $D_f < 2$, and to R_g^2 for $D_f > 2$. Using fractal scaling as above, this gives

$$K \sim \left(N_1^{1/D_f} + N_2^{1/D_f}\right)^{D_f}\left(N_1^{-1} + N_2^{-1}\right)^{1/2} \qquad (D_f < 2) \qquad [29]$$

$$K \sim \left(N_1^{1/D_f} + N_2^{1/D_f}\right)^{2}\left(N_1^{-1} + N_2^{-1}\right)^{1/2} \qquad (D_f > 2) . \qquad [30]$$

We introduce a new kernel function for agglomerates in the transition regime (Kn>1>Kn_D). In this regime it is reasonable to assume that the drag is determined by free-molecule physics, but that particle diffusion is governed by the continuum equations (β=1 in Eq. [4]). Assuming that the collision diameter is proportional to R_g, we obtain

$$K \sim \left(N_1^{1/D_f} + N_2^{1/D_f}\right)^{D_f} \left(N_1^{-1} + N_2^{-1}\right) \qquad (D_f < 2) \qquad [31]$$

$$K \sim \left(N_1^{1/D_f} + N_2^{1/D_f}\right)\left(N_1^{-2/D_f} + N_2^{-2/D_f}\right) \qquad (D_f > 2)\,, \qquad [32]$$

where the dynamic exponent z was obtained for these kernel functions using Eqs. [18] and [26]. Figure 3 shows that z, and hence the dynamic behavior, is a strong function of the fractal dimension D_f in the free-molecule regime. For agglomerates with fractal dimensions less than 2, one expects z to first decrease from 2 to about 0.7, then to increase to 1.0 as the particles grow out of the free-molecule regime through the transition regime and finally into the continuum regime.

These similarity solutions are based on simplistic kernel functions and furthermore assume that the particle size distribution maintains a self-preserving form. It will be demonstrated that these assumptions may be valid for particles with large N, but for accurate predictions of particle coagulation, it is generally necessary to consider the mobility and collision diameters in more detail and to solve the coagulation equation numerically.

GEOMETRY OF THE AGGLOMERATES

Fractal scaling relations do not define the particle structure completely; two agglomerates with the same measured fractal dimension may have different structures (38). We assume that the fractal dimension D_f, the primary particle diameter d_1, and the number of primary particles N completely determine the structure. Although the anisotropy, or aspect ratio, of a cluster is not explicitly considered, we have developed models that are consistent with real systems. For example, when D_f=3, the clusters are assumed to be spheres, with aspect ratios of 1. When D_f=1.6 to 1.8, we attempt to match the model to experimental data for aerosol fumes that have aspect ratios of 1 to 3, and when D_f=1, the

cluster is modeled as a straight chain. Another assumption made is that all of the primary spherules have the same diameter, while the primary particles in real agglomerates are approximately log-normally distributed with a geometric standard deviation of 1.1 to 2 (20, 39, 40). Because the primary particles vary in size, the particle structure should vary smoothly as the mass increases past the average mass of the primary particle. In the present model, all clusters have the same fractal dimension D_f if they are larger than the primary spherule mass, while smaller particles are assumed to be dense spheres (D_f=3).

The critical structural parameters determining the particle dynamics are the outer diameter, radius of gyration and projected area. The outer diameter of the model agglomerate is defined as

$$d_f = d_1 N^{1/D_f}. \qquad [33]$$

This definition is consistent with the geometry of straight chains (D_f=1, d_f = length), discs (D_f=2) and spheres (D_f=3). By comparison, the volume-equivalent diameter $d_v = d_1 N^{1/3}$ is frequently much smaller. Consider a fractal object obeying [33], whose density decreases as r^{D_f-3} at distances r from its center. One can then show that the radius of gyration is related to the outer diameter by

$$2R_g = \sqrt{\frac{D_f}{D_f+2}}\ d_f\ . \qquad [34]$$

The exact relation between R_g, d_f, and N can be determined only by detailed structural analysis of real agglomerates. Such experimental data are not available, so we can only compare [35] and [36] to the results of computer simulations. For simulated agglomerates with $D_f = 1.69$, the relation between mass and size was found (22) to follow

$$2R_g = 0.76\ d_1 N^{1/1.69}, \qquad [35]$$

while Eqs. [33] and [34] give a value of R_g that is 11% lower. For computer-generated agglomerates with D_f=1.91, Eqs. [33] and [34] underestimate R_g by 20% (26).

There is no rigorously derived relation between projected area A of an irregular agglomerate and its mass, but an estimate can be made by considering several limiting cases. An upper limit on A is the projected area of a straight chain of N spheres, viewed at random orientations,

$$A = \frac{\pi {d_1}^2}{4}\left(1 + \alpha(N\text{-}1)\right) \quad , \quad \alpha \sim 0.85 \, . \qquad [36]$$

We can assume that this relation may be extended to agglomerates having low fractal dimension if α is modified appropriately. For large clusters with fractal dimensions greater than 2, the area is proportional to d_f^2 (41). In order to obtain a function continuous in D_f that gives the correct result for $D_f = 3$, we choose $\alpha = 0.67$ and interpolate between $D_f = 2$ and $D_f = 3$. Noting also that the projected area-equivalent diameter d_A cannot be larger than the volume-equivalent diameter d_v, these limiting cases are combined to give

$$\left(\frac{d_A}{d_1}\right)^2 = \frac{4A}{\pi d_1^2} =$$

$$\max\left[N^{2/3} \; ; \; \min\left[1 + \alpha(N\text{-}1) \; ; \; \frac{D_f}{3} N^{2/D_f} \right]\right] . \qquad [37]$$

This expression gives reasonable results for a variety of shapes. For example, $d_A = 0.64 d_f$ for a disc ($D_f = 2$), while Eqs. [33] and [37] give $d_A = 0.67 d_f$. For $D_f < 2$, the model predicts that 33% of the particles are hidden from view. This agrees well with the analysis of stereo images of soot particles, in which Gray et al. (42) found that 36% $\pm$ 5% of the particles were hidden. Simulated clusters (41) exhibited less shielding than predicted by Eq.[37], but Figure 4 shows that the agreement is reasonable for $N > 10$.

MOBILITY DIAMETER

The mobility diameter d_m of a non-spherical particle is the diameter of a sphere moving at the same speed as the agglomerate and experiencing the same drag force. We neglect the dependence of d_m on particle orientation and assume that a single value of d_m may be used to characterize the agglomerate for a particular gas mean free path λ. Estimates of the transition regime (Kn~1) mobility diameter are obtained after considering the free-molecule (Kn>>1) and continuum (Kn<<1) cases.

Free-Molecule Regime

In the free-molecule or kinetic regime, mobility diameter d_{mk} is expected to be proportional to the projected area equivalent diameter d_A (18,43). Simulations have shown that the momentum transferred by each collision of a gas molecule with an agglomerate depends on the cluster size and the particle surface properties (40,42). With D_f in the range $1.8 < D_f < 2.09$ and N~1000, the simulations showed that $d_{mk} \sim 1.05\, d_A$ when the gas molecules undergo specular reflections at the particle surface and that $d_{mk} \sim 0.97 d_A$ when the molecules reflect diffusely. Thus we assume that $d_{mk}=d_A$.

Continuum Regime

In the continuum regime, for sufficiently high fractal dimension ($D_f > 1.3$) and large cluster size, the continuum mobility diameter d_{mc} is proportional to R_g (44,45). Experiments and numerical models have shown that $1.4R_g < d_{mc} < 2R_g$ for typical agglomerates with fractal dimensions slightly less than 2 (44,45,46). Hess et al. (47) obtained an analytical expression for d_{mc} using the method of superposition of point-force singularities or Stokeslets. Their results are much higher than the experimental results for spheres and agglomerates, so we use a simple interpolation that is consistent with the experimental and numerical results,

$$d_{mc} = \left(\frac{D_f - 1}{2}\right)^{0.7} d_f . \qquad [38]$$

For very low D_f, the mobility diameter is not proportional to the radius of gyration and must be corrected by a logarithmic factor, as predicted by slender-body theory (48,49). The correct expression in this case is

$$d_{mc} = \frac{d_f}{\ln(2\frac{d_f}{d_1}) + 1 - \ln 2} . \qquad [39]$$

This expression gives the correct scaling for chains and recovers the correct limit for the degenerate case where there is only one primary particle ($d_f = d_1$). For long spheroids at random orientations, it underestimates the mobility diameter by about 10%. Both Eqs. [38] and [39] are expected to be valid for only certain ranges of fractal dimension. When applied to agglomerates with fractal dimensions outside these ranges, d_{mc} is underestimated. Therefore, these equations represent lower bounds on d_{mc}. An additional lower bound on d_{mc} for typical aerosol agglomerates is the projected area diameter, d_A (18). Hence, the continuum mobility diameter for arbitrary fractal dimension is taken as

$$d_{mc} = \max\left[\frac{d_f}{\ln(2\frac{d_f}{d_1}) + 1 - \ln 2} \; ; \; \left(\frac{D_f - 1}{2}\right)^{0.7} d_f \; ; \; d_A \right] . \qquad [40]$$

Transition Regime

The transition regime mobility diameter d_m is bracketed by the free-molecule and continuum limits calculated above. Dahneke's adjusted sphere interpolation (50) gives good results for cylinders and converges to the correct result for spheres. According to this interpolation, d_m must satisfy

$$\frac{d_m}{C_c(Kn)} = \frac{d_{mc}}{C_c(Kn_a)} , \qquad [41]$$

where the adjusted sphere Knudsen number is

$$Kn_a = \frac{2\lambda\, d_{mk}}{d_{mc}^{\,2}} \quad . \qquad [42]$$

Although the mobility model contains many components, reviewing Eqs.[37]-[42] shows that the mobility diameter is a function of only five quantities, d_1, d_f, d_A, D_f, and λ:

$$d_m = d_m(d_{mc}, d_A, \lambda) \quad ; \quad d_{mc} = d_{mc}(d_1, d_f, D_f) \, . \qquad [43]$$

This conceptual organization of the model is useful later when the absorbing cluster is discussed. It is important to note that D_f and d_1 are critical in relating agglomerate mass to the projected area and outer diameter, but that once these quantities are determined, the models introduced above are fairly insensitive to the fractal dimension (18).

The mobility diameters, calculated assuming that $D_f = 1.8$, are compared with available measurements (39,40,51-53) in Figure 5. Since the fractal dimension was not measured for the particles used in the earlier studies, an exact comparison is not possible. Nonetheless, the differences between theory and experiment are small and could be due to variations in D_f and d_1.

THE COLLISION DIAMETER AND ABSORBING CLUSTER

General Considerations

Consider the collision of a small particle with a large cluster (Figure 6a). The collision diameter d_{c2} of the small particle is twice the average separation between its centroid and the surface of the large agglomerate. If the smaller particle is a single sphere, d_{c2} is equal to the diameter of the sphere. The collision diameter of the large agglomerate is also defined as twice the separation of its centroid and the surface of the other particle. Depending on the particle mean free paths and interparticle forces, the small particle may attach near the extremities of the agglomerate, or closer to its centroid. If the agglomerate is rotating rapidly, the collision diameter is increased (13,56). The collision diameter also

depends on the relative sizes of the particles because a small particle may penetrate the agglomerate, while a larger particle will generally contact the agglomerate near the outside.

Relations developed previously for the mobility diameters of agglomerates may be exploited by noting that mass transfer and momentum transfer to agglomerates are analogous processes. For example, the attachment rate of nanometer-sized clusters to agglomerates was found to be nearly the same as to spheres with the same mobility diameters (57) . In general, when the mean free path of the gas molecules and the diffusing species are the same, a single, characteristic collision diameter should apply to the transfer of both momentum and mass.

We next consider the collision diameter of non-spherical particles in special situations in order to arrive at reasonable upper and lower bounds on the collision diameter and to develop a more general model for agglomerates with arbitrary fractal dimension and Knudsen number.

Upper Limit

From previous considerations, the collision diameter cannot be larger than the maximum dimensions of the agglomerate. The outer diameter d_f defined earlier is equivalent to the maximum diameter for certain particle geometries. It is assumed that it will also represent the maximum diameter for agglomerates, and thus the upper limit is given by

$$d_{abs} \equiv d_{c1} + d_{c2} \leqq d_{f1} + d_{f2} \quad . \qquad [44]$$

Lower Limit

The drag models described earlier indicate that the mobility diameter of an agglomerate decreases as the gas mean free path increases, until the free-molecule limit is

reached ($d_m = d_A$). This is consistent with computer simulations showing that small particles with infinite mean free paths penetrate an agglomerate more deeply than those undergoing Brownian motion (23). Different trends have been reported for clusters with D_f~2.4 (58); however, we assume that for agglomerates with lower fractal dimensions, the minimum collision diameter is obtained for collisions with point masses travelling in straight lines. Since the mean free path of the gas molecules is typically much larger than the particle mean free paths, the mobility diameter is a reasonable lower bound on the collision diameter, and

$$d_{abs} \geqq d_{m1} + d_{m2} . \qquad [45]$$

This approach has been proposed to model the collision diameters of both colloidal agglomerates (28) and aerosol agglomerates (3).

Arbitrary Fractal Dimension and Knudsen Number

A better estimate of the agglomerate collision diameter can be obtained by extending the absorbing surface concept introduced by Fuchs to predict the coagulation rate of prolate spheroids (13). The collision between two agglomerates is transformed into the collision between an absorbing cluster and a point particle (Figure 6b), where the point particle has diffusivity D_{12} and mean free path λ_{12}, while the absorbing cluster is stationary. The collision frequency is the same in the original and transformed situations (Figures 6a,b) provided that the absorbing cluster is correctly defined. Once the absorbing cluster is defined, the absorbing sphere diameter d_{abs} is the collision diameter of the absorbing cluster.

The absorbing cluster is a conceptual device representing all possible collision configurations. Nevertheless, we assume that the diffusion of point particles to the absorbing cluster is described qualitatively by the drag-mass transfer analogy. Thus, the collision diameter is the mobility-equivalent sphere of the absorbing cluster, using a mean

free path λ_{12}. In order to use the drag model given above [43], the structural parameters required by the model must be defined for the absorbing cluster. These are the fractal dimension D_{f12}, projected area diameter d_{A12}, outer diameter d_{f12}, and fine-scale dimension d_{112} (Figure 6b).

The outer diameter is expected to be slightly less than the sum of the outer diameters of the colliding agglomerates, because of inter-penetration, but lacking a quantitative model for this effect, we assume that

$$d_{f12} = d_{f1} + d_{f2} \,. \qquad [46]$$

The fractal dimension D_{f12} and fine-scale dimension d_{112} are generally difficult to determine, but are easily found for the collision of nearly straight chains with much smaller particles (Figure 6a,b; Ref.(13)). In this case the absorbing cluster is a thickened chain, and we assume that the fractal dimension of the absorbing cluster is the same as that of the larger chain,

$$D_{f12} = D_f \,. \qquad [47]$$

Assuming that the collision diameter of the smaller cluster may be approximated by its outer diameter, the thickness of the absorbing cluster is (Figure 6b)

$$d_{112} = d_1 + d_{f2} \,. \qquad [48]$$

For the special case that the absorbing cluster is a thickened chain, its projected area can be obtained directly from its length and width given in Eqs. [46] and [48]. However, this model of the absorbing cluster is not applicable to all situations, so two additional limiting cases are considered. A lower limit on the projected area diameter d_{A12} is $d_{A1}+d_{A2}$, obtained by noting that

i) From the definition of the absorbing sphere diameter d_{abs}, d_{abs} can be no smaller than the sum of the minimum collision diameters.

ii) The minimum collision diameter of an agglomerate is the projected area diameter d_A, obtained for collisions of the agglomerate with a point mass having an infinite mean free path, i.e., $d_c \geqq d_A$

iii) By analogy with (ii), if $\lambda_{12} >> d_{abs}$, then $d_{abs} = d_{A12}$.

Finally, we note that the projected area diameter must be smaller than the outer diameter. Thus, d_{A12} can be computed in a manner analogous to that used for d_A (Eq. [37]):

$$d_{A12} = \max\left[d_{A1}+d_{A2} \; ; \min\left[\sqrt{(d_1 + d_{f1})^2 + 2/3\,(N-1)(d_1 + d_{f1})\,d_1} \; ; \; \sqrt{\frac{D_f}{3}}\, d_{f12} \right] \right] . \qquad [49]$$

Having determined the relevant dimensions of the absorbing cluster, the absorbing sphere diameter is determined from the mobility model (Eq. [43]),

$$d_{abs} = d_m(d_{mc}, d_{A12}, \lambda_{12}) \quad ; \quad d_{mc} = d_{mc}(d_{112}, d_{f12}, D_{f12}) . \qquad [50]$$

Comparison of Collision Diameter Models

Figure 7 compares free-molecule regime, absorbing sphere diameters d_{abs} with the model of Mulholland et al.(26), which was used in Eq. [29]. For D_f=1.91, the three absorbing sphere models developed above differ by at most 30%, and the collision diameter used by Mulholland et al. is close to our lower limiting model. We also note that models equivalent to our upper limiting model have been used by Kaplan and Gentry (27) as well as by Matsoukas and Friedlander (37).

In general, the collision diameters can be expected to vary with the diffusion Knudsen number Kn_D. However, Figure 8 shows that for collisions of equal-sized clusters or high fractal dimension (D_f>1,8), d_{abs} is almost independent of Kn_D. For low

fractal dimension (D_f=1.0-1.3) and larger particle size ratio (N_1/N_2=1000), d_{abs} decreases significantly as Kn_D number increases.

Our continuum regime results for D_f=1.0 may be compared with the model developed by Fuchs (13) for prolate spheroids. For collisions of spheres of diameter d_1 with prolate spheroids of length $1000d_1$ and thickness d_1, the Fuchs model predicts that d_{abs}=13.1(d_{v1}+d_{v2}), while the absorbing cluster model gives d_{abs}=12.6 (d_{v1}+d_{v2}). For chains of equal length, Fuchs used Müller's model (59) and estimated an upper limit of d_{abs} = 0.66 (d_{f1}+d_{f2}), while our absorbing cluster model predicts that d_{abs} = 0.3 (d_{f1}+d_{f2}).

RESULTS

Collision Frequency Function

The collision frequency of agglomerate particles can be related to the structures of the colliding agglomerates in an approximate but physically consistent manner through the entire range of particle Knudsen numbers, using the mobility and collision diameter estimates derived above. For spheres, the non-dimensional collision frequency $\tilde{K}$ is a function only of the Knudsen numbers of the spheres, ie. $\tilde{d}_m^{-1}$, and the non-dimensional particle density $\tilde{\rho}$. For fractal agglomerates, $\tilde{K}$ also depends on the primary particle diameter $\tilde{d}_1$ and the fractal dimension D_f.

The collision frequency function $\tilde{K}$ has been calculated for conditions typical of some TiO_2 fume synthesis experiments (15,57), i.e., particles in air at atmospheric pressure and 873 K. The primary particle diameter ranges from 6 nm to over 27 nm; i.e., $\tilde{d}_1$ = 0.013-0.057. For this background gas and using a particle density of 3.9 g cm^{-3}, $\tilde{\rho}$ =0.00025, a value bracketed by the two densities assumed in Figure 2. Figure 9 shows the collision frequency function for agglomerates of mobility diameters d_{m1} and d_{m2} as a function of d_{m1}. The primary particle diameters were chosen to bracket those expected in the TiO_2 system, and the assumed fractal dimension D_f =1.8 is the most commonly quoted

value for vapor-phase aggregates. The "mid" or absorbing cluster model was used to compute the collision radius. Note that the variations in primary particle size appear to have a similar effect to that produced by density variations (Figure 2). This not unexpected, since an effective density based on the cluster mass and the mobility diameter is much lower than the density of TiO_2. For a fractal, this effective density decreases as the primary particle diameter decreases or the mobility diameter increases.

The effect of varying the fractal dimension is shown in Figure 10, using the three collision diameter models developed here. For these comparisons, the agglomerate was assumed to have 1000 primary particles of primary diameter $\tilde{d}_1$=0.1 and density $\tilde{\rho}$=0.0025. For $D_f = 3$, all three models converge to the traditional, coalescing sphere model. As the fractal dimension decreases, the predicted coagulation rate may increase or decrease depending on the particle size ratio and the model used. First note that for $D_f > 2$, the three models differ only slightly. For chainlike agglomerates with fractal dimensions less than 2, the choice of model is important. When the colliding agglomerates have very different sizes, the "min" model is close to our absorbing cluster model ("mid" model). In this case, penetration of small particles into a large agglomerate cannot be neglected. Thus, the upper limiting model is inappropriate. On the other hand, when the colliding clusters have nearly the same size, the collision diameters may be substantially larger than the mobility diameters, so the "min" model is inappropriate here. The absorbing cluster model is expected to give the correct behavior for any size ratio.

The models may be compared to Shon's (52) measurements of the coagulation rate of magnetic Fe_2O_3 agglomerates (Figure 11). The fractal dimension was not measured in the study, but the agglomerates were nearly straight chains, so we assume that $1.0 < D_f < 1.2$. The absorbing cluster model predicts coagulation rates that are lower than the data by a factor of 2 to 3; results from the model of Lee and Shaw (56) were too low by the same amount. The disagreement may be due to magnetic dipole moments, which tend to align the particles so that collisions tend to occur at the ends of the chains (56). Zebel (60) has

developed a theory for dipole-enhanced coagulation, but given the lack of data on the magnetic properties of fine Fe_2O_3 particles, it is difficult to apply this theory in the present case.

Magnetic alignment of Fe_2O_3 particles is probably responsible for the low fractal dimensions of this system The observed magnetic effect raises an important but subtle issue in the modeling of agglomerate coagulation. The force-free agglomeration of straight chains is expected to give rise to clusters of higher fractal dimensions ($D_f \sim 1.8$) after a long time, since the fractal dimension found in cluster-cluster aggregation simulations is independent of the fine-scale details. When fine clusters deposit on a large agglomerate, the fractal dimension is expected to approach a higher value, on the basis of diffusion-limited aggregation models. Thus, the fractal dimension is directly related to the conditions of particle growth, and the present model must be applied with caution, with the fractal dimension being selected to reflect the appropriate physics.

Size Distribution Evolution

Coagulation rates are generally inferred from measured size distributions rather than from experiments designed to measure K directly. The practical implications of the preceding models are demonstrated by calculating the evolution of size distributions. The coagulation equation [3] was solved using the Discrete-Sectional (DISC) code (9,61). In these calculations, the particle size distribution is represented by 25 size classes, geometrically spaced over the range of particle masses considered. The volume-equivalent diameter $\tilde{d}_v$ ranged from 0.00244 to 3.61 . The models developed here were used to calculate the coagulation kernel K as a function of the particle mass; the simulated conditions corresponded to the synthesis of TiO_2 fumes discussed above. It was assumed that the chemical reactions forming the nucleating phase are very rapid compared to the time required to form the primary particles. In this case, the initial condition is a high concentration of particles in the smallest size classification.

Shape of the Size Distributions

Figure 12 compares the calculated mobility diameter distributions with a TiO_2 distribution measured by Okuyama et al. (15). The experiments are best modeled by using D_f=1.8 and $\tilde{d}_1$=0.057 (d_1=27 nm). For these conditions, the computed size distribution is shown at $\tilde{t}$= 0.00013, 0.0013 and 0.013. The measurements were made at $\tilde{t}$ = 0.0013 (t ~ 1.8 s), and the computed distributions using different fractal dimensions and primary particle sizes are shown for this time as well. The measured size distribution is broad, consistent with the fractal models, although there are substantial differences between the measured and predicted particle concentrations and sizes. Quantitative comparisons of these quantities depend on accurate knowledge of the mass concentration and particle loss rates. However, the shape of the size distribution is expected to be less sensitive to these factors.

Initially, most of the particles are smaller than the primary particle d_1, so the computed distribution is identical to that expected for spheres, with the exception of a slight increase in the number of large particles. At $\tilde{t}$= 0.0013, most particles are larger than the primary sphere, and therefore have an agglomerate structure. The smallest particles appear to lag behind the growth of the main part of the distribution, resulting in a broad distribution. This trend is even more pronounced for a lower fractal dimension or smaller primary diameter, while the expected distribution for coalescing spheres is much narrower. Later, all particles are larger than the primary sphere and the distribution becomes narrower. It appears that the mobility size distribution does not approach a self-preserving form, nor can the distributions be described exactly by a log-normal distribution. However, in order to represent the dynamics more compactly, it is convenient to assume that the distributions are log-normal and to present only the median and geometric standard deviation of the distributions.

Figure 13 shows the medians and standard deviations for distributions, based on both the volume and mobility diameters. Predicted time evolutions of these quantities using the "min", "max" and "mid" models are compared to the results from the rapid coalescence model. The conditions are the same as in Figure 12. It is important to note that the three models developed here give qualitatively similar results, and they would in fact be difficult to distinguish experimentally. Therefore, only the absorbing cluster model is used in the remaining computations. Changing the number of computational sections has little effect on the results; using 30 sections instead of 25 resulted in number concentrations decreased by 1.5% and σ_g values decreased by < 1%.

The size distribution width increases significantly as the median diameter grows from the primary particle size to 3 to 4 times this value. Figure 14 shows that this trend is also apparent in the measurements of Al_2O_3, SiO_2 and TiO_2 particle size distributions (15). The TiO_2 and SiO_2 data show a single trend, regardless of the material, temperature or concentration. The primary particle diameter used to normalize the data (d_1=27 nm) was taken from micrographs of TiO_2 ; thus, disagreement with the model may be partly due to variations in the primary particle diameter. Interpretation of the measurements is complicated further by variations in the precursor formation kinetics and measurement biases. Low counting efficiencies and high loss rates for particles less than 5 nm may have reduced the width of the size distributions for the smallest median diameters.

Growth Rates

Although mobility diameters are measured more frequently than volume-equivalent diameters, the general behavior of the coagulating system is best represented in terms of the volume-equivalent diameters, since mass is conserved during coagulation. The total number concentration is directly related to the average volume-equivalent diameter, while the relation between mobility diameter and number concentration is sensitive to the particle structure.

Figures 15 and 16 show the evolution of the median and geometric standard deviation of the computed volume-equivalent diameter distributions, for $\tilde{\rho}$=0.0025. For comparison, the growth rate predicted by the similarity solutions (Eqs. [27] to [32]; D_f=3.0) for spheres in the free-molecule, transition and continuum regimes are plotted above the numerically computed results.

First consider the evolution of coalescing spheres. Initially ($\tilde{t} < 10^{-3}$), the particles are much smaller than either the mean free path of the gas or the particle mean free paths, i.e., the free-molecular coagulation kernel is applicable, and the growth rate agrees very well with the similarity solution result. As the median diameter grows to 0.1, the transport Knudsen number Kn_D is no longer large, and the slope of the curve approaches that predicted by the transition regime similarity solution. If the calculations were carried out for a sufficiently long time, the behavior would approach that predicted by the continuum similarity solution. At the same time, the geometric standard deviation σ_g decreases from slightly under 1.5 in the free-molecule regime to slightly under 1.4 in the continuum regime (Figure 16).

The coagulating agglomerates show distinctly different behavior. In the free-molecule regime, the low density clusters coagulate much faster than spheres of the same mass. However, when Kn_D is small, the growth trends are similar for all fractal dimensions and primary particle size. Decreasing either the fractal dimension or the primary particle diameter decreases the effective density of the agglomerate, so that the transition regime behavior starts earlier than for dense spheres.

CONCLUSIONS

Agglomerates typically form under conditions where they are much larger than their mean free paths, although they may be smaller than the gas mean free path λ. For this transition regime, similarity solutions using simplified coagulation kernels suggest that the

behavior is quite different from that expected in either the free-molecule regime or the continuum regime.

Agglomerate formation cannot be described accurately by similarity solutions, however, since both λ and the primary particle dimension influence the coagulation rate. Noting that the primary particle size is typically uniform and related to the sintering kinetics of the material, particles below the primary particle diameter d_1 are assumed to be dense spheres, while larger particles have a fractal-like structure. Combining this hybrid structural model with estimates of the coagulation rates for agglomerates, the dynamics of agglomerate aerosols over the range of fractal dimensions $1< D_f <3$, growing from particles smaller than d_1, were examined. This model may be viewed as a first step toward the development of an aerosol dynamics model that treats both agglomeration and coalescence.

The coagulation rate for agglomerate particles depends on the particle mobility and the effective collision diameter. Published measurements of the aerodynamic drag on agglomerate particles and fractal structure models provide a firm basis for estimating the mobilities of agglomerates. The collision diameters are less well understood. Previous studies have assumed that the collision diameter of an agglomerate is equal to either the mobility diameter or the outer diameter. These models may be satisfactory for agglomerates with high fractal dimensions ($D_f >1.8$), but they are inadequate for more chainlike particles with lower fractal dimensions. Better estimates of the collision diameters require consideration of the relative sizes of the colliding particles, their mean free paths and their fractal dimensions. To this end, the absorbing surface concept was extended for fractal agglomerates.

The resulting coagulation frequency kernels differ substantially from those expected for dense spheres with the same mobility diameters. These differences are due in part to the decreased effective density of the agglomerates, resulting in very small particle mean free paths. Because of this, the coagulation rate is enhanced for agglomerates with sizes comparable to the gas mean free path.

Differences in the coagulation kernel functions result in different aerosol growth rates and size distributions. In particular, the width σ_g of the distribution increases dramatically as an aerosol grows past the primary particle size. At the same time, there is a short acceleration of the growth rate. This is particularly noticeable for size distributions based on the mobility diameter, but may also be seen in the distributions based on the volume-equivalent diameter. These effects have not been observed in previous simulations where the aerosol was assumed to grow from a monodisperse collection of primary particles. Such size distribution broadening near the primary particle diameter is consistent with size distribution measurements made in oxide particle synthesis experiments.

For agglomerates much larger than d_1 but comparable in size to λ, the growth rate of the volume-equivalent diameter (or the decay of the particle number concentration) is insensitive to d_1 and increases only slightly as D_f decreases. Since the mobility diameter of an agglomerate is generally much larger than the volume-equivalent diameter, the growth rate of the mobility diameter is substantially increased as D_f or d_1 decreases. Similarly, the width of the volume-equivalent diameter distribution is not affected noticeably by either D_f or d_1, though σ_g of the mobility-equivalent diameter distributions increases greatly as D_f decreases.

Although the present calculation employs a number of simplistic models, the results clearly show that the kinetics of agglomerate formation are strongly influenced by the gas mean free path and by the transition between rapid coalescence and agglomeration without coalescence. Experiments and detailed simulations will address these questions more fully in the future.

Acknowledgments: This research was supported by the International Fine Particle Research Institute and by the U.S. Department of Energy under grant No. DE-FG22-90PC90286. Comments made by B. Dominik and B. Wyslouzil during the preparation of this work are greatly appreciated.

REFERENCES

1. Drake, R.L., *in* "Topics in Current Aerosol Research Part 2." (G.M. Hidy and J.R. Brock, eds.), pp.208-237, Pergamon, New York, NY, 1972.
2. Mercer, T.T., *in* "Fundamentals of Aerosol Science." (D.T.Shaw, Ed.), pp. 85-134 John Wiley, New York, 1976.
3. Bunz, H., *J. Aerosol Sci.* **21,** 139-153 (1990).
4. Weitz, D.A., Huang, J.S., Lin, M.Y.,and Sung, J., *Phys. Rev. Lett.* **54,** 1416 (1985).
5. Seinfeld, J. H., "Atmospheric Chemistry and Physics of Air Pollution." John Wiley, New York, NY, 1986.
6. Herring, C., *J. Appl. Phys.* **21,** 301-303 (1950).
7. Helble, J.J. and Sarofim, A.E., *Colloid Interface Sci.* **128,** 348-362 (1989).
8. Wu, J.J. and Flagan, R.C., *J. Appl. Phys.* **61,** 1365 (1987).
9. Wu, J.J., Ph.D. Thesis, California Institute of Technology (1986).
10. Kasper, G., Shon, S-N., and Shaw, D.T., *Am. Ind. Hyg. Assoc. J.* **41,** 288-296 (1980).
11. Schaefer, D.W. and Hurd, A.J., *Aerosol Sci. Technol.* **12,** 876-890 (1990).
12. Kuhn, W.E., "Ultrafine Particles." John Wiley, New York, 1963.
13. Fuchs, N. A., "The Mechanics of Aerosols." Pergamon Press, New York, NY, 1964.
14. Forest, S.R. and Witten , T.A., *J. Phys A.: Math. Gen.*, **12,** L109-L117 (1979).
15. Okuyama, K., Kousaka, Y., Tohge, N., Satoru, Y., Wu, J.J., Flagan, R.C. and Seinfeld, J.H., *AIChe. J.* **2,** 2010-2019 (1986).
16. Samson, R.J., Mulholland, G.W., and Gentry, J.W., *Langmuir* **3,** 272-281 (1987).
17. Meakin, P., *Prog. Solid State Chem.* **20,** 35-233 (1990).
18. Rogak, S.N, Flagan, R.C. and Nguyen H.V., *J. Aerosol Sci.* submitted (1991a).
19. Schmidt-Ott, A, *Appl. Phys. Lett.* **52,** 954-956 (1988).
20. Kasper,G, *Aerosol Sci. Technol.* **1,** 201-215 (1982).

21. Meakin, P., *in* "On Growth and Form." (H. Stanley and N. Ostrowsky, eds.), pp. 111-135, Martinus Nijhoff, Boston, 1986.

22. Mountain, R.D., Mulholland, G.W. and Baum, H., *Colloid Interface Sci.* **114,** 67-81(1986).

23. Meakin, P. *Adv. Coll. Int. Sci.* **28,** 249-331(1988).

24. Smoluchowski, M.V., *Z. Phys. Chem.* **92,** 129-168 (1917).

25. Friedlander, S. K. , "Smoke, Dust, and Haze." p.195, Wiley-Interscience, New York, NY, (1977).

26. Mulholland, G.W., Samson, R.J., Mountain, R.D. and Ernst, M.H., *Energy and Fuels* **2**,481-486 (1988).

27. Kaplan, C.R. and Gentry, J.W., *Aerosol Sci. Technol.* **8,** 11-28 (1988).

28. Okuyama, K. , Kousaka, Y. and Paytakes, A.C., *Colloid Interface Sci.* **81,** 21-31 (1980).

29. Leyvraz, R. *in* "On Growth and Form." (H.E. Stanley and N. Ostrowski eds.), p. 111, Martinus Nijhoff, Boston, 1986.

30. Williams, M.M.R., *Ann. Nucl. Energy* **17,** 161-167 (1990).

31. Simons, S. and Simpson, D.R., *Ann. Nuclear Energy* **16,** 353-359 (1989).

32. Balusubramanian, T. and Murthy, K.P.N., *Colloid Interface Sci.* **119,** 294-295 (1987).

33. Dahneke, B.E., *in* "Theory of Dispersed Multiphase Flow." (R.E. Meyer, ed.), pp.97-138, Academic Press, New York, (1983).

34. Gelbard, F., Tambour, Y., and Seinfeld, J.H., *Colloid Interface Sci.* **76,** 541 (1980).

35. Friedlander, S.K. and Wang, C.S., *Colloid Interface. Sci.* **22,** 126 (1966).

36. Lai, F.S, Friedlander, S.K., Pich, J., and Hidy, G.M., *Colloid Interface Sci.* **39,** 395 (1972).

37. Matsoukas, T. and Friedlander, S.K., *Colloid Interface Sci.* (in press) (1991).

38. Mandelbrot, B.B., "The Fractal Geometry of Nature." p.333, W.H. Freeman, New York, 1983.

39. Kops, J., Dibbets, G., Hermans, L., and Van de Vate, J. F., *J. Aerosol Sci.* **6,** 329-333 (1975).

40. Van de Vate, J.F., Van Leewen, W.F., Plomp, A. and Smit, H.C.D., *J. Aerosol Sci.* **11,** 67-75 (1980).

41. Meakin, P., Donn, B., Mulholland, G.W., *Langmuir* **5,** 510-518 (1989).

42. Gray, R.H., Kanapilly, Cheng, Y.S. and Wolff, R.K., *J. Aerosol Sci.* **3,** 211-216 (1985).

43. Chan, P. and Dahneke, B., *J. Appl. Phys.* **52,** 3106 (1981).

44. Chen, Z. Y., Meakin, P., and Deutsch, J. M., *Phys. Rev. Lett.* **59,** 2121 (1987).

45. Rogak, S. N., and Flagan, R. C., *Colloid Interface Sci.* **134,** 206-218 (1990).

46. Wiltzius, P., *Phys. Rev. Lett.* **58,** 710 (1987).

47. Hess, W., Frisch, H.L. and Klein, R., *Z. Phys. B. Condens. Matter* **64**,65-67 (1986).

48. Batchelor, G. K., *J. Fluid Mech.* **44**, 419 (1970).

49. Kasper, G., Niida, T., and Yang, M., *J. Aerosol Sci.* **16,** 535-556 (1985)

50. Dahneke, B. E., *J. Aerosol Sci.* **4**, 163-170 (1973).

51. Allen, M. D., Moss, O. R., and Brian, J. K., *J. Aerosol Sci.* **10,** 43-48 (1978).

52. Shon, S.-N., Ph.D. Thesis, State University of New York at Buffalo (1979).

53. Kasper, G., *Aerosol Sci. Technol.* **1,** 201-215 (1982).

54. Odumade, O. A., Ph. D. Thesis, University of Minnesota (1983).

55. Zeller, W., *Aerosol Sci. Technol.* **4,** 45-63 (1985).

56. Lee P.S. and Shaw, D.T., *Aerosol Sci. Technol.* **3,** 9-16 (1984).

57. Rogak, S.N., Baltensperger, U. and Flagan, R.C., *Aerosol Sci. Technol.* (in press) (1991b).

58. Hagenloch, R. and Friedlander, S.K., *Colloid Interface Sci.* **133,**185-191 (1989).

59. Müller, H., *Kolloidchem Beih.* **27**, 223 part 3 (1928).

60. Zebel, G., *Staub* **19**, 381-387 (1959).

61. Wu, J.J., Flagan, R.C. and Seinfeld, J.H., *Colloid Interface Sci.* **123**, 339-352 (1988).

Table I. Length scales used to characterize the coagulation of agglomerate aerosols. The quantity's symbol is followed by its description, functional dependencies in the model and references to figures or equations if appropriate.

Characteristics of a single agglomerate of N primary particles, fractal dimension D_f.			
d_1	primary particle diameter	assumed constant	
d_v	volume-equivalent diameter	$d_1 N^{1/3}$	
d_f	outer diameter	$d_1 N^{1/Df}$	
R_g	radius of gyration	$2R_g = \sqrt{\frac{D_f}{D_f+2}}\, d_f$	
d_c	collision diameter	d_c (particle mean free paths, shape,size)	Figure 6a
d_A	projected area diameter	$d_A(d_1, N, D_f)$	Eq. [37]
d_{mk}	kinetic regime mobility diameter	$d_{mk}=d_A$	
d_{mc}	continuum regime mobility diameter	$d_{mc}(d_1,d_f,,D_f)$	Eq. [40]
d_m	transition regime mobility diameter	$d_m(d_{mc}, d_A, \lambda)$, $2\lambda/d_m=Kn$	Eqs. [37]-[42]

Characteristics of a pair of colliding agglomerates.			
d_{abs}	diameter of the absorbing sphere	$d_{abs}= d_{c1}+d_{c2} =2\lambda_{12}/Kn_D$	Figure 6c
d_{f12}	outer diameter of absorbing cluster	$d_{f12} = d_{f1}+d_{f2}$	Eq. [46]
d_{112}	smallest dimension of the absorbing cluster	d_1+d_{f2} , $d_{f1} > d_{f2}$	Figure 6b Eq. [48]
d_{A12}	area diameter of absorbing cluster	$d_{A12} = d_{f1}+d_{f2}$	Eqs. [49]
λ_{12}	mean free path of relative motion of 2 agglomerates		Eqs. [10]

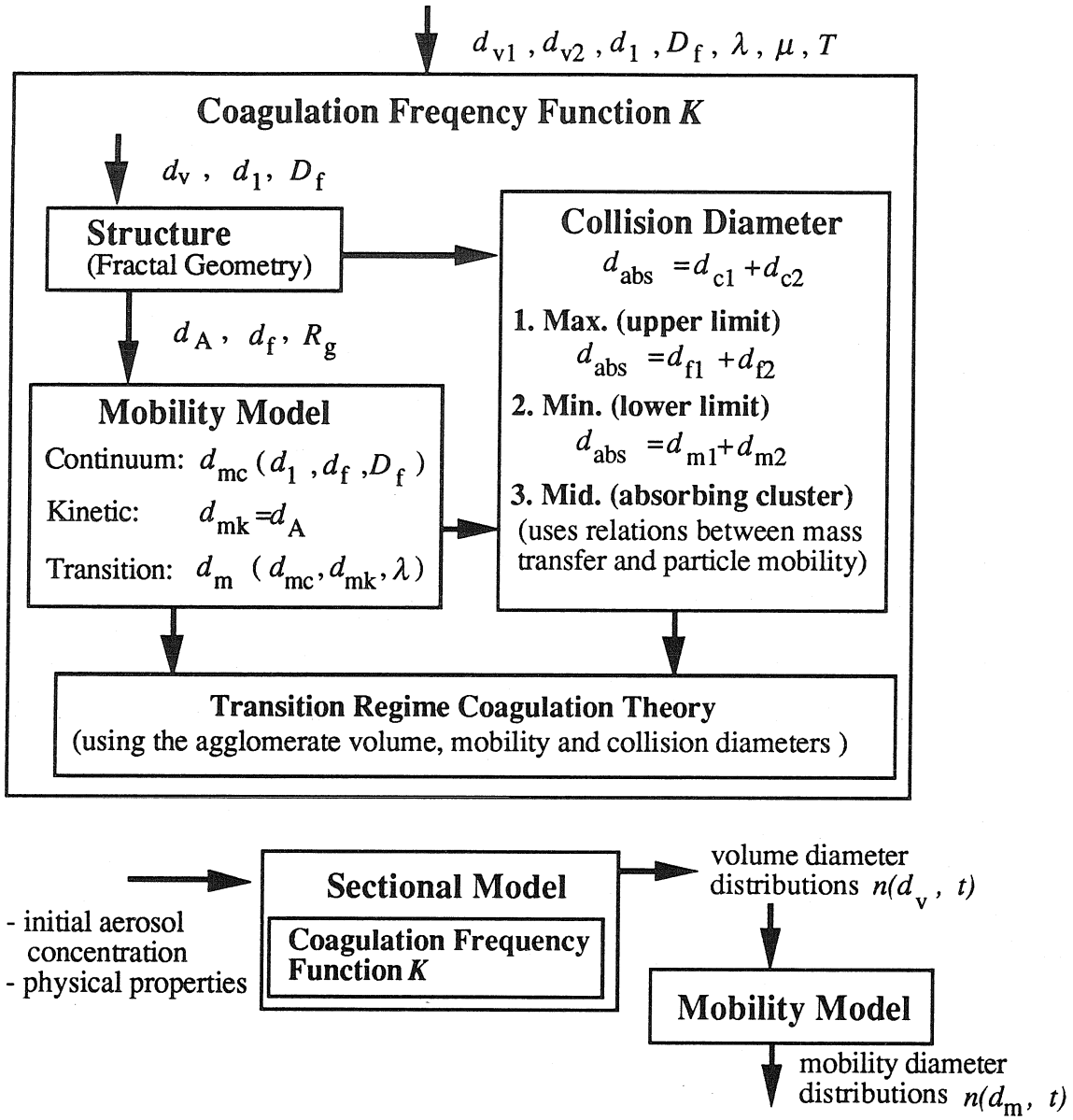

Figure 1. Conceptual organization of structure, mobility and collision models used to estimate the coagulation frequency function. The coagulation frequency function is then incorporated into the sectional aerosol model.

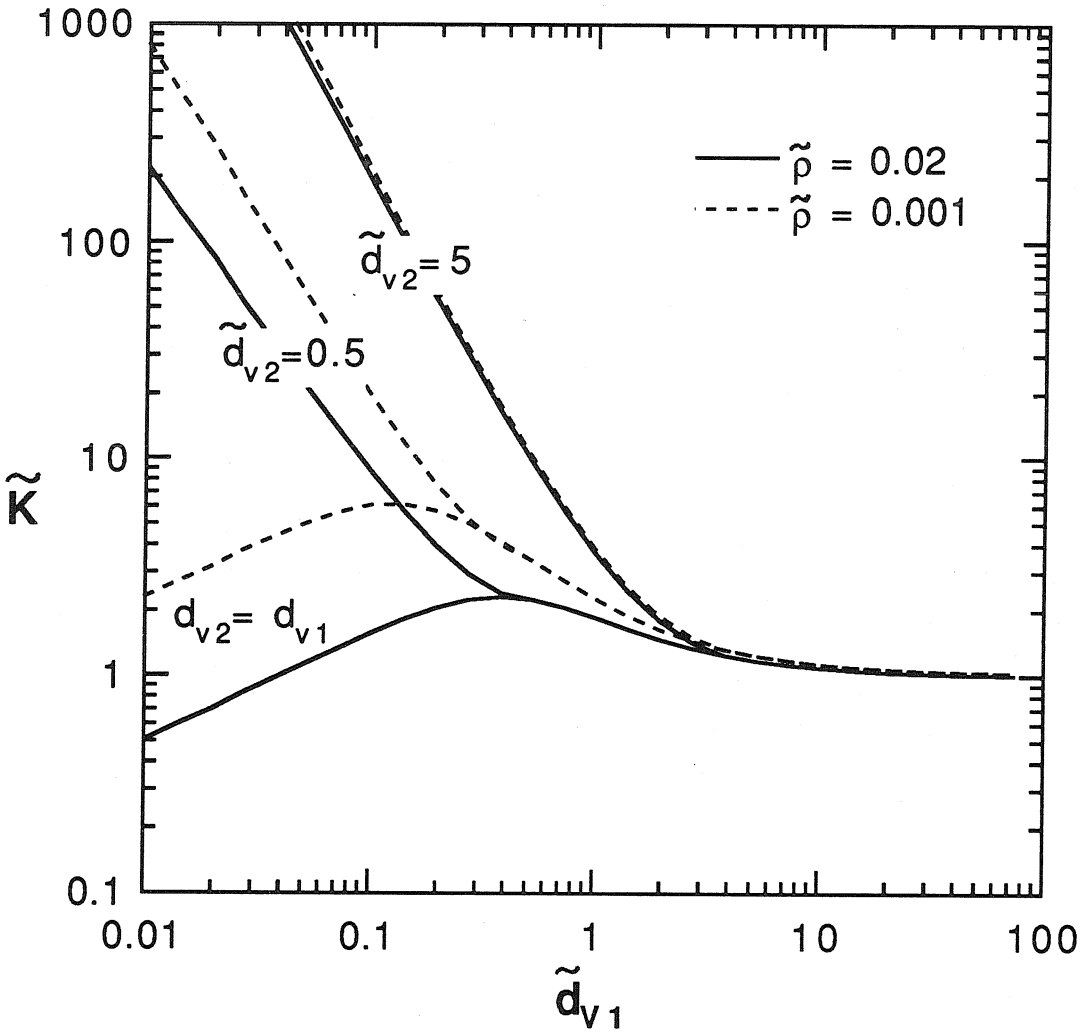

Figure 2. Coagulation kernel $\tilde{K}$ for spheres of diameter $\tilde{d}_{v1}$ and $\tilde{d}_{v2}$, and having material density $\tilde{\rho}$. Quantities are non-dimensionalized using the characteristic scales of the background gas.

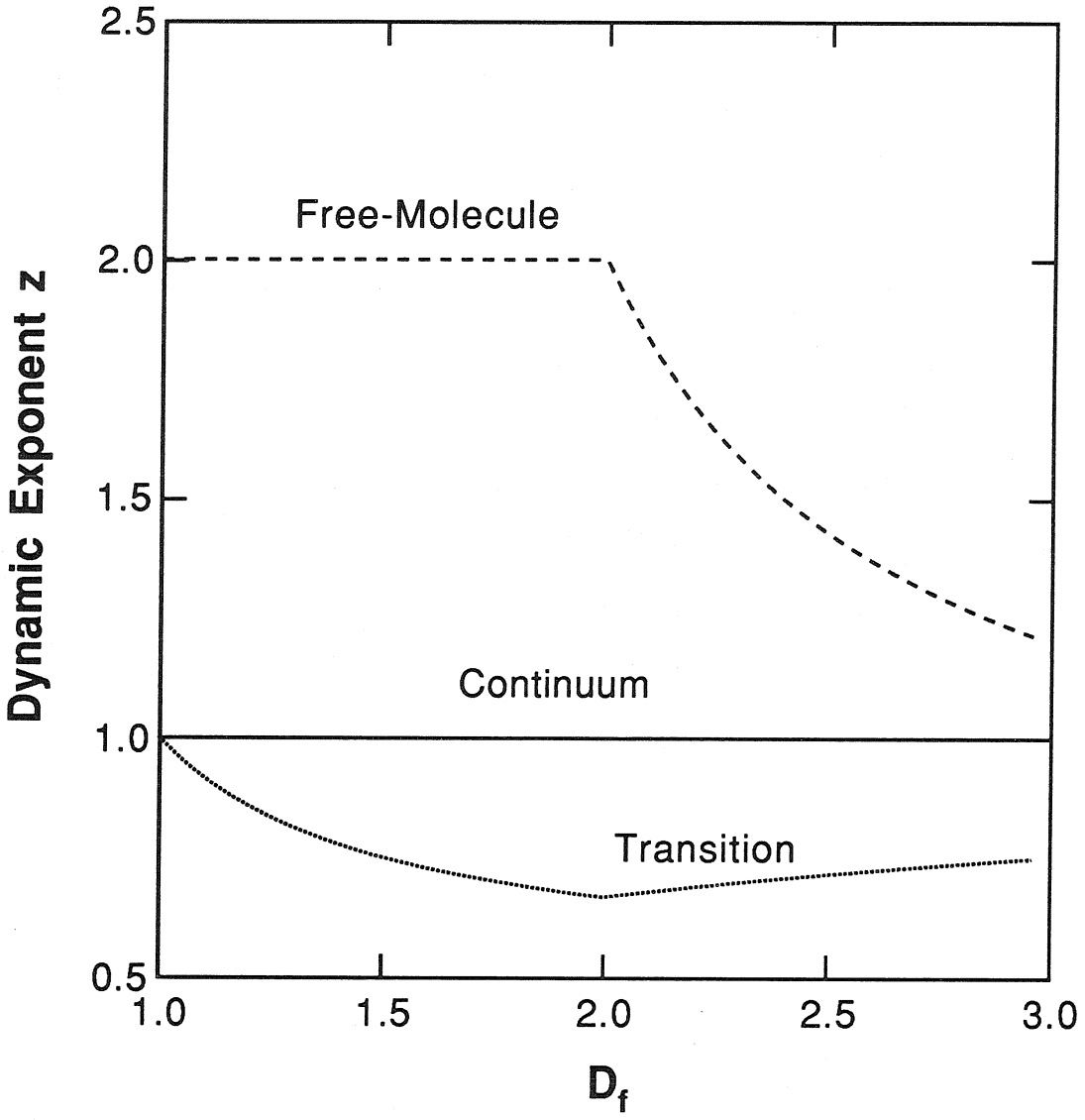

Figure 3. Dynamic exponent z as a function of fractal dimension D_f for the different transport regimes. Similarity solutions of the coagulation equation predict that the particle number concentration decays with time t as t^{-z}

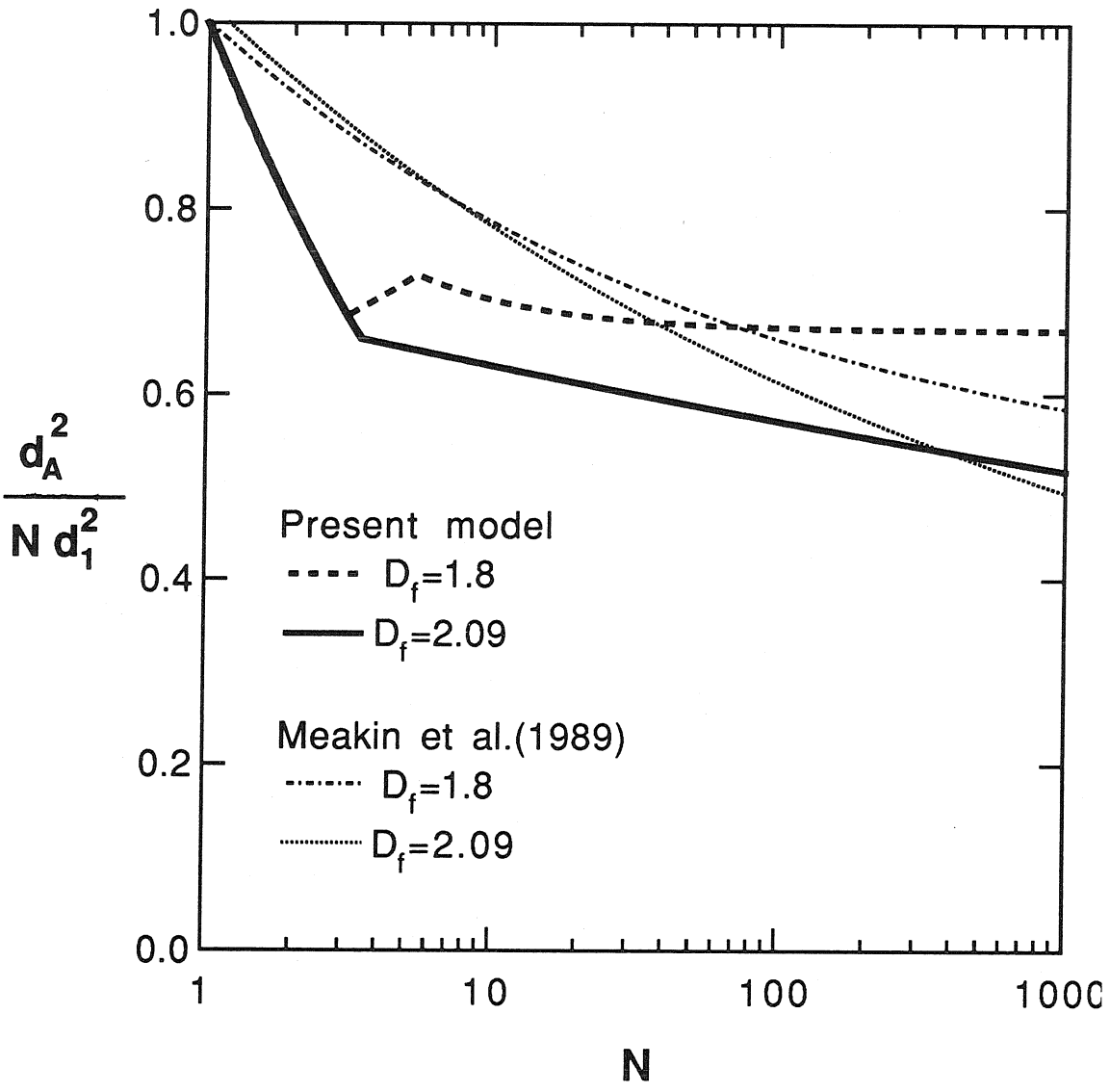

Figure 4 . Relation between the number of primary particles N of diameter d_1 in a cluster and the projected area diameter d_A. The model used in this study is compared with correlations determined from simulations by Meakin et al. (40) for two values of D_f.

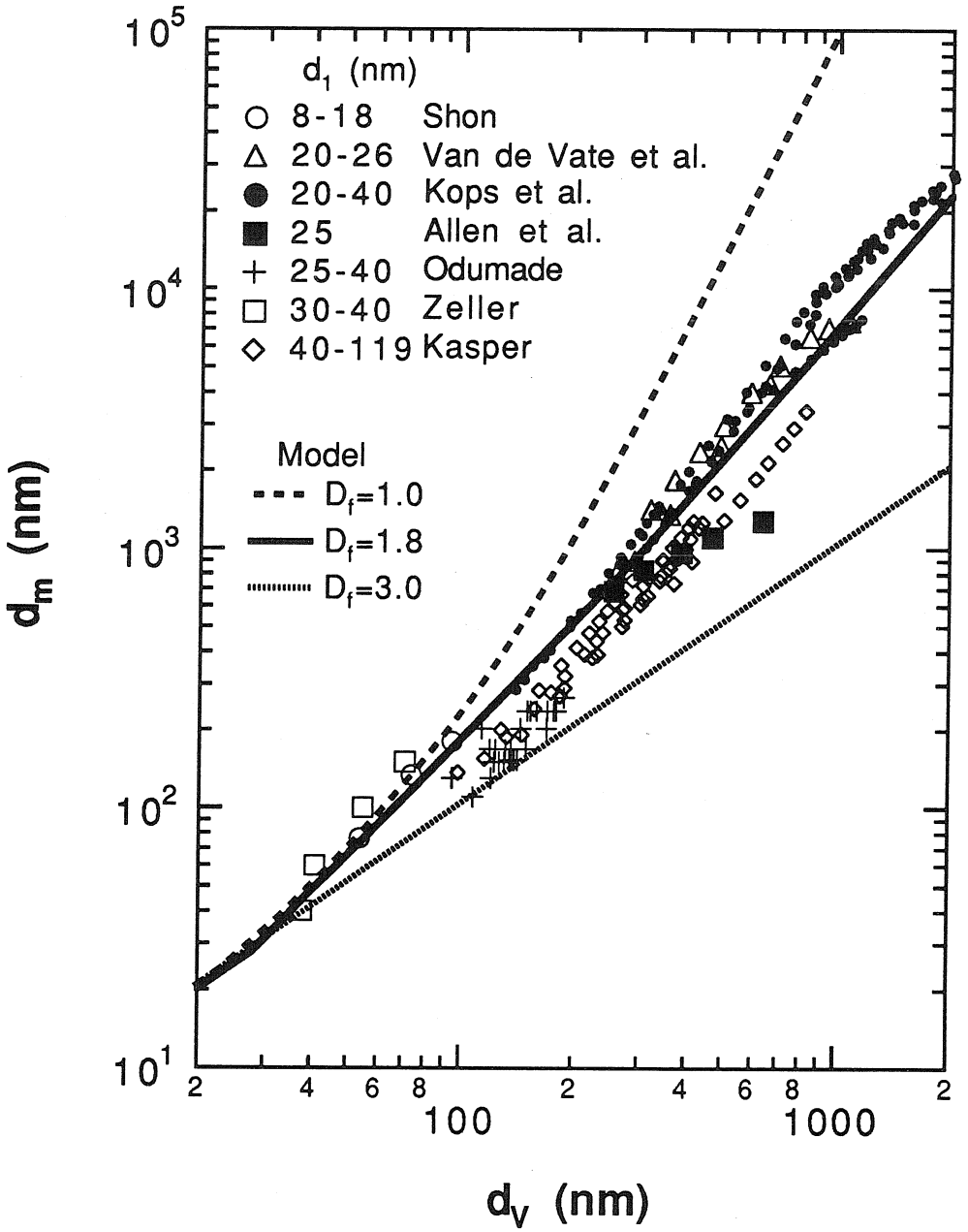

Figure 5. Mobility diameter d_m and volume-equivalent diameter d_v for agglomerates as measured by Kops et al.(39), Allen et al., (51), Shon (52), Van de Vate et al. (40), Kasper (53), Odumade (54) and Zeller (55). The data are compared with model calculations done for d_1 =20 nm, λ = 69 nm.

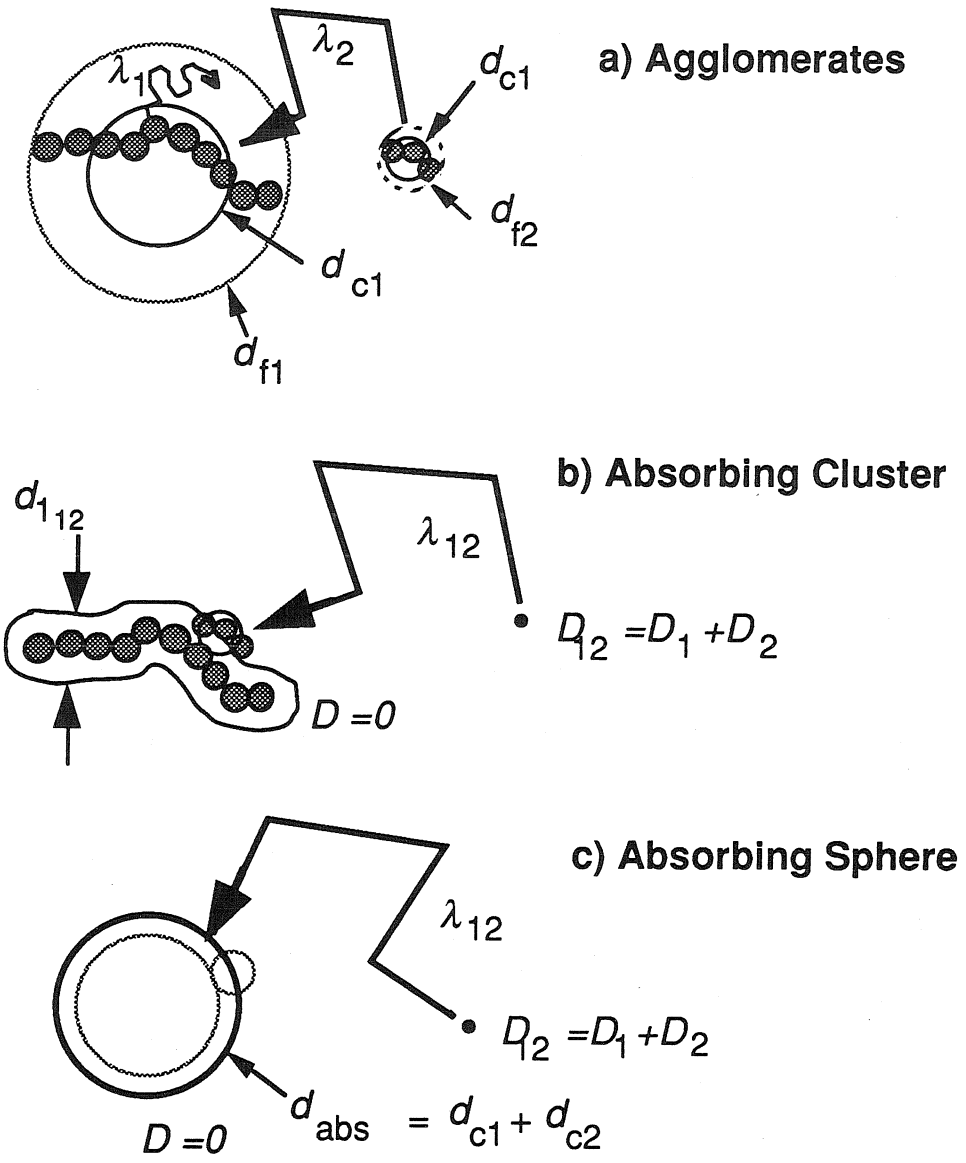

Figure 6. a) The collisions of agglomerates are characterized by the particle mean free paths λ_1 and λ_2, diffusivities D_1 and D_2, and the collision diameters d_{c1} and d_{c2}. b) This problem is equivalent to a point particle with diffusivity D_{12} colliding with a stationary absorbing cluster. c) The absorbing cluster may be transformed into an absorbing sphere of diameter d_{abs}.

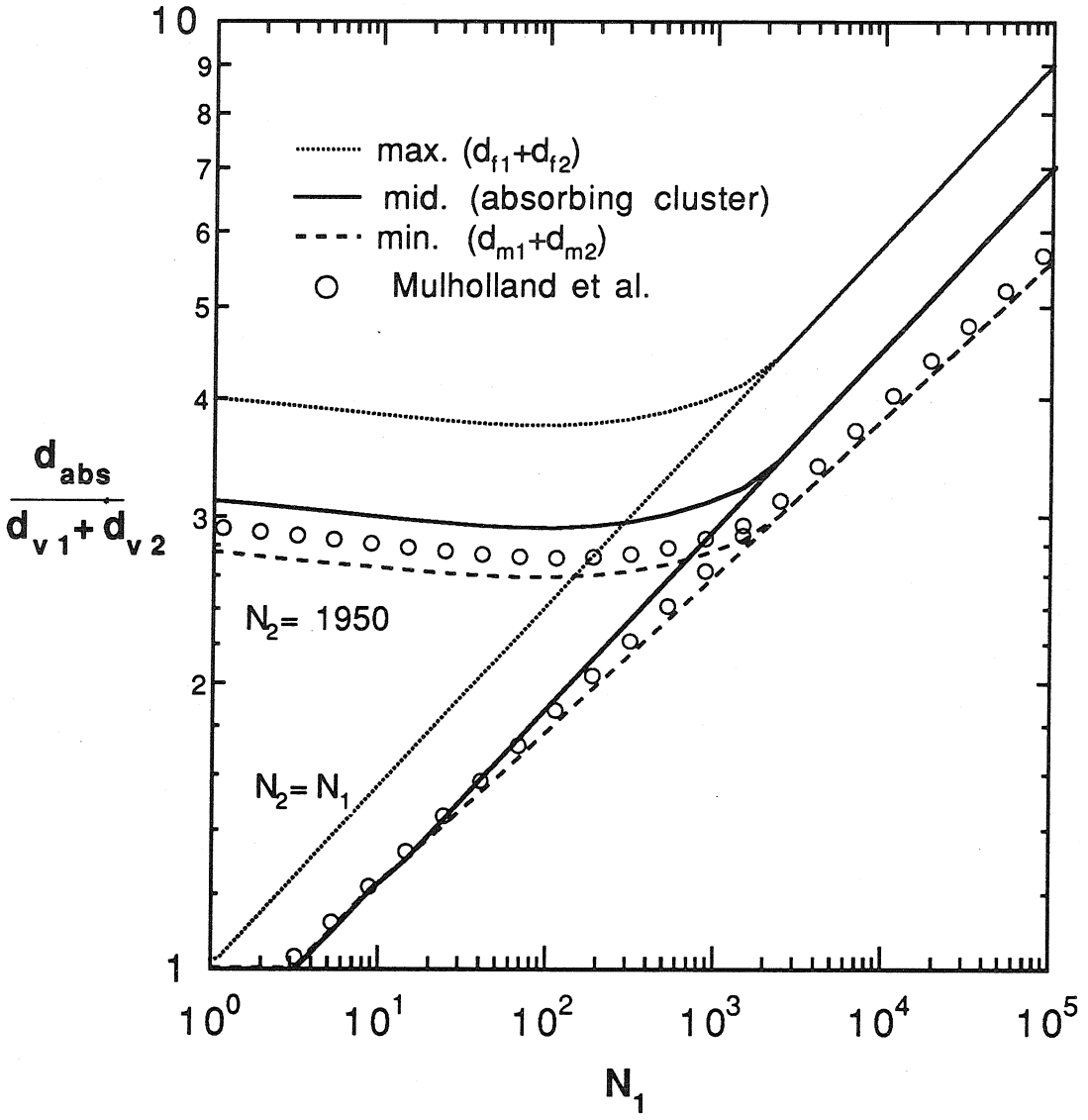

Figure 7. The absorbing sphere diameter d_{abs} for fractal agglomerates in the free-molecule regime, with D_f=1.91. As the number of primaries N in the agglomerates increases, d_{abs} increases with respect to the result for spheres, d_{v1}+d_{v2}. The three models used in the present study are compared with the work of Mulholland et al. (26).

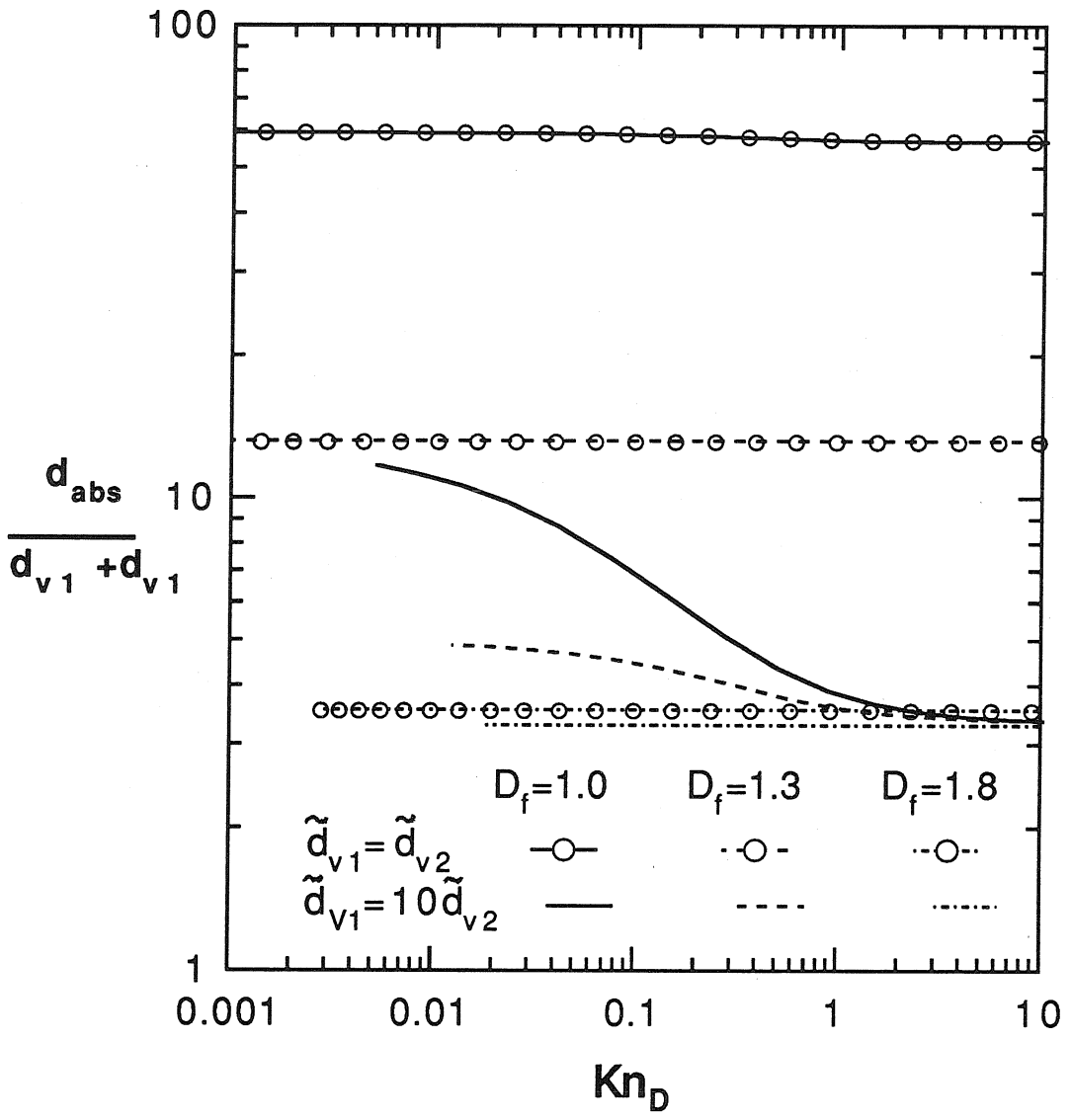

Figure 8. The absorbing sphere diameter d_{abs} for fractal agglomerates decreases as the diffusion Knudsen number Kn_D increases. Depending on the particle size ratio $\tilde{d}_{v1}/\tilde{d}_{v2}$ and the fractal dimension D_f, the variations may be slight. ($\tilde{d}_{v1}/\tilde{d}_{v2} = 10$)

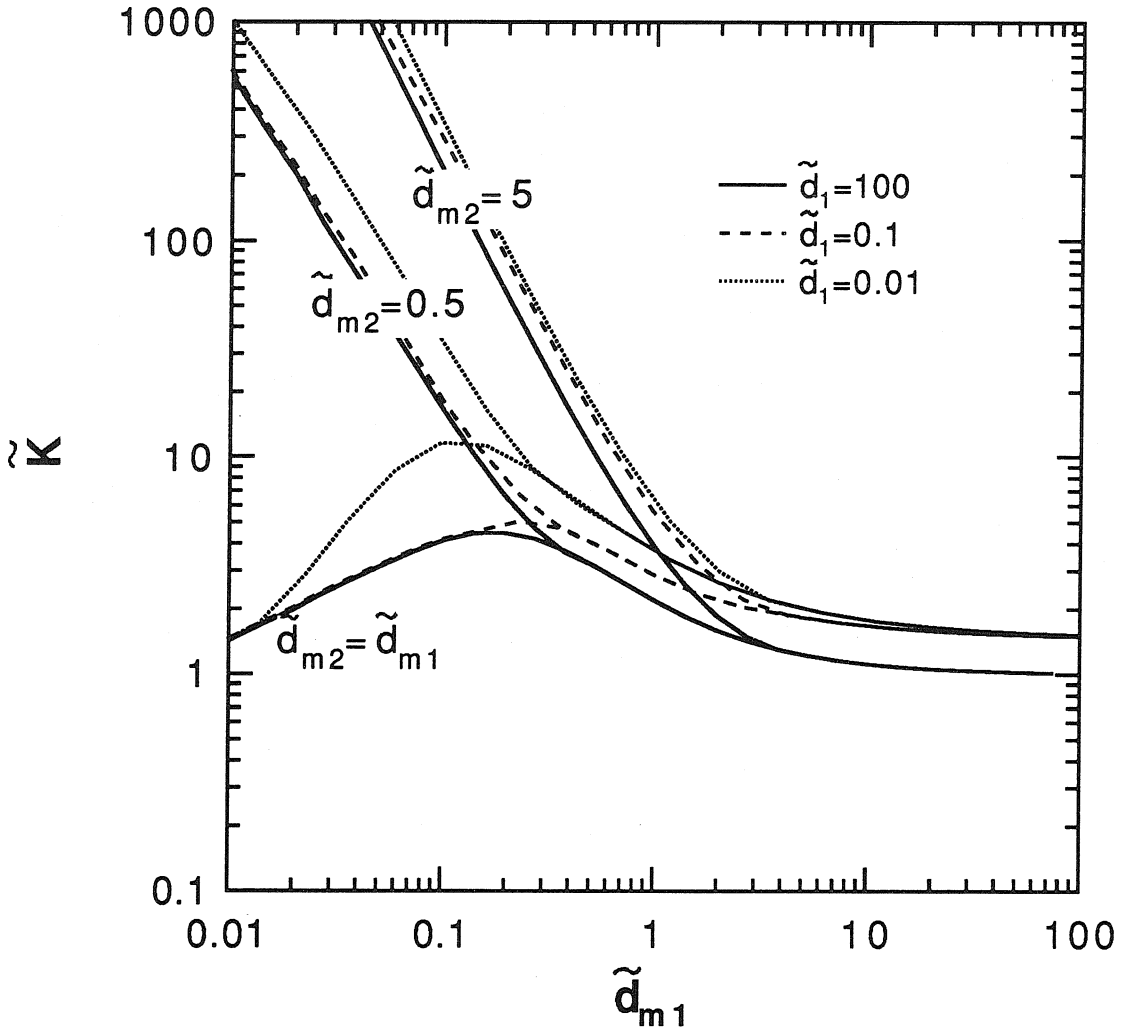

Figure 9. Coagulation kernel $\tilde{K}$ for agglomerates with mobility diameters $\tilde{d}_{m1}$ and $\tilde{d}_{m2}$, (D_f=1.8, $\tilde{\rho}$.=0.0025). For primary particle diameter $\tilde{d}_1$ = 100, the model is equivalent to the traditional model of rapidly coalescing spheres.

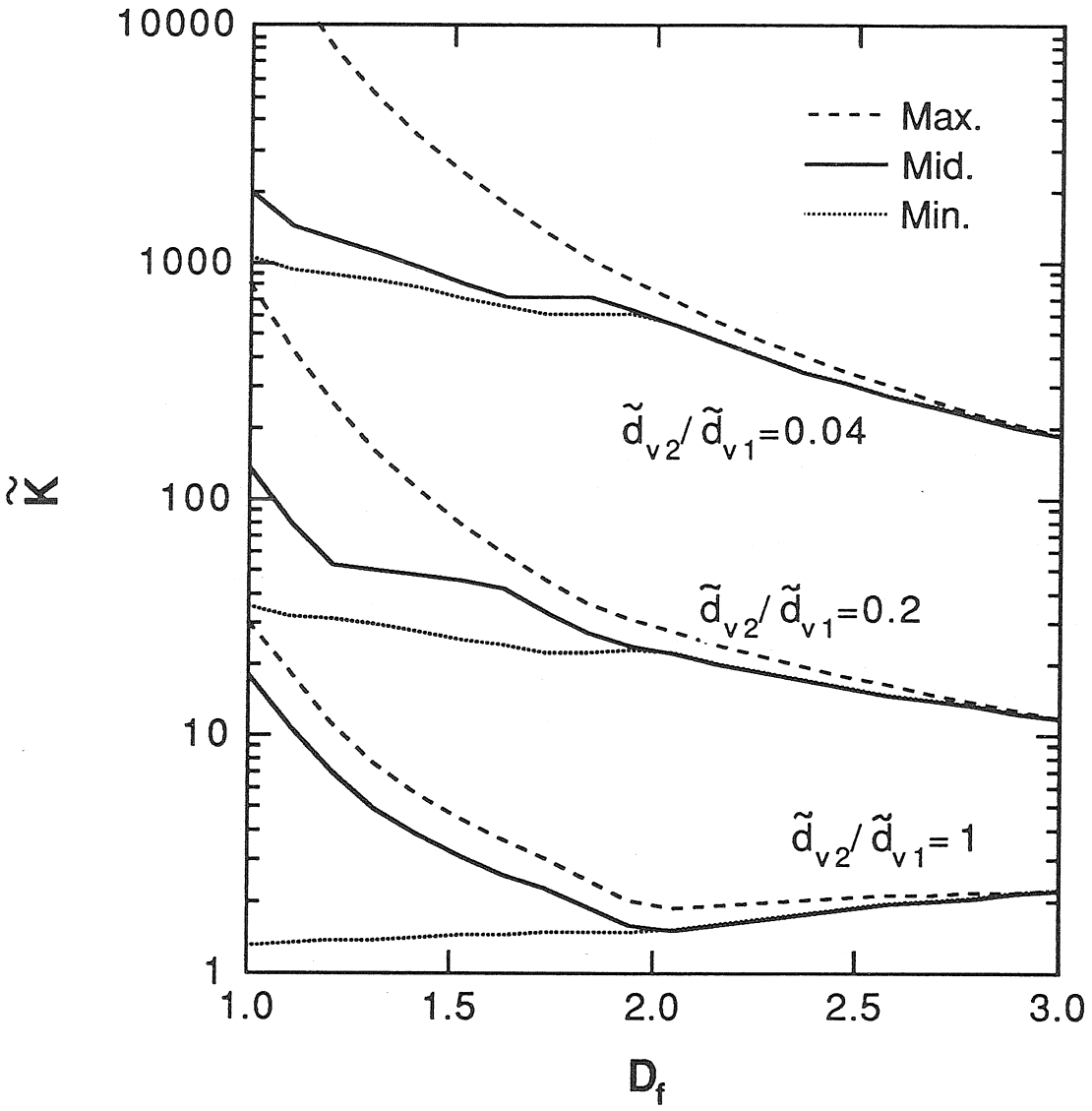

Figure 10. Coagulation kernel $\tilde{K}(\tilde{d}_{v1}, \tilde{d}_{v2})$ for agglomerates as a function of fractal dimension D_f. The absorbing cluster model ("mid") is bracketed by models using the outer diameters ("max") and mobility diameters ("min") as collision diameters ($\tilde{d}_{v1}$=1.0, $\tilde{d}_1$=0.1, $\tilde{\rho}$=0.0025).

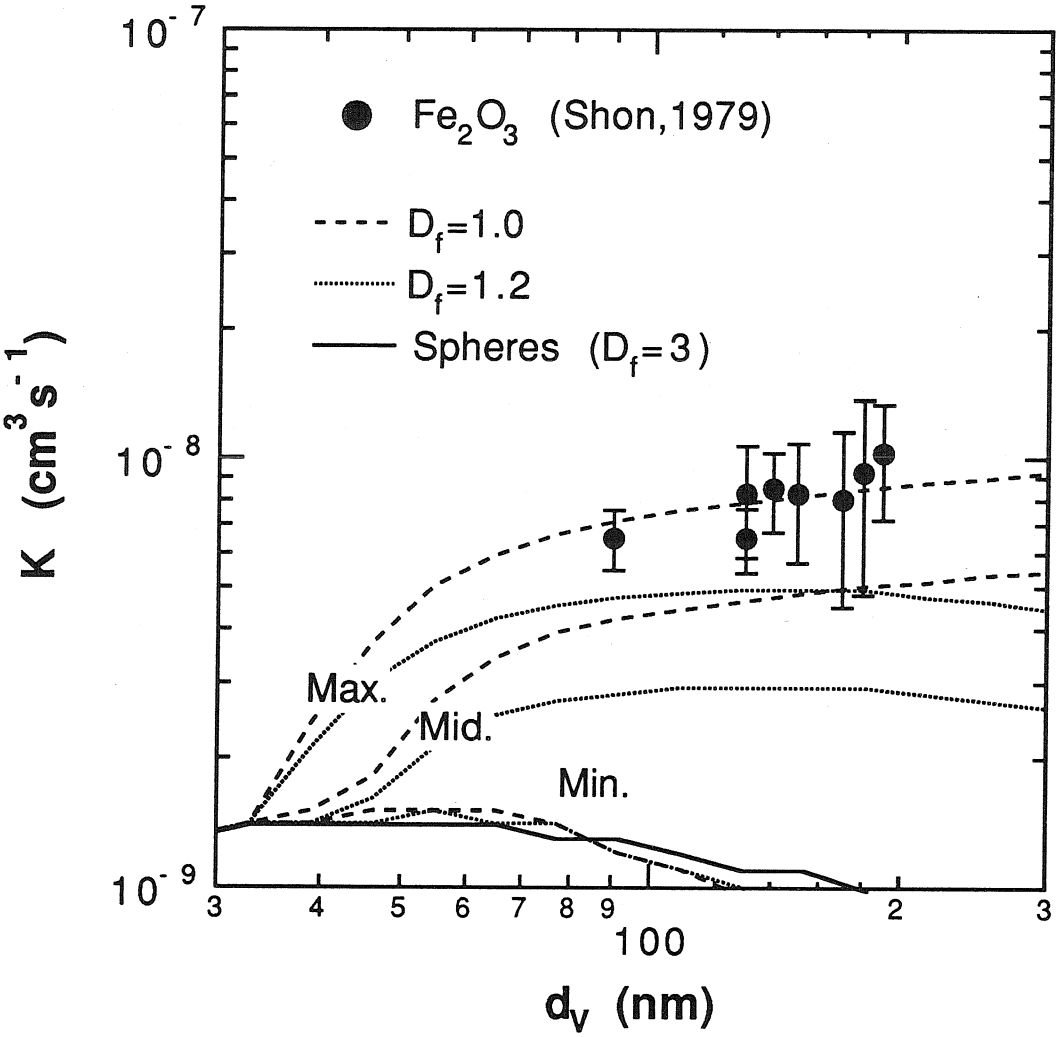

Figure 11. Comparison of data by Shon (52) for the coagulation of Fe_2O_3 chains with the present models, assuming fractal dimensions of 1.0, 1.2 and 3.0 (spheres). Calculations assume air at atmospheric pressure, T=298 K, d_1=33 nm.

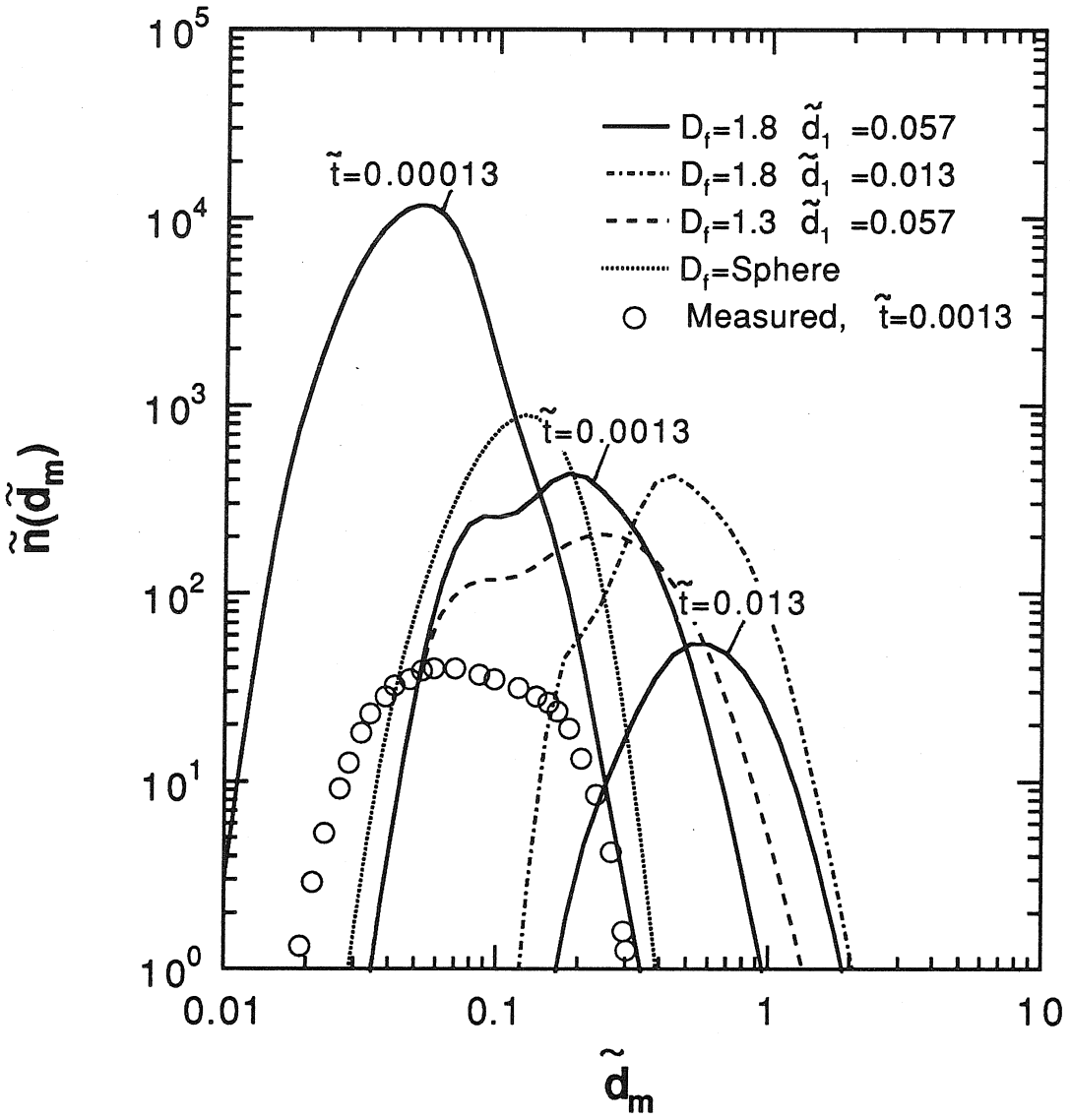

Figure 12. Mobility distribution $\tilde{n}(\tilde{d}_m)$ evolution for agglomerates. For fractal dimension D_f=1.8, $\tilde{d}_1$=0.057, distributions are shown for $\tilde{t}$=0.00013, 0.0013 and 0.013. Other distributions, including measurements by Okuyama et al. (15), are for $\tilde{t}$=0.0013. Conditions correspond to TiO_2 formation in nitrogen at 873 K.

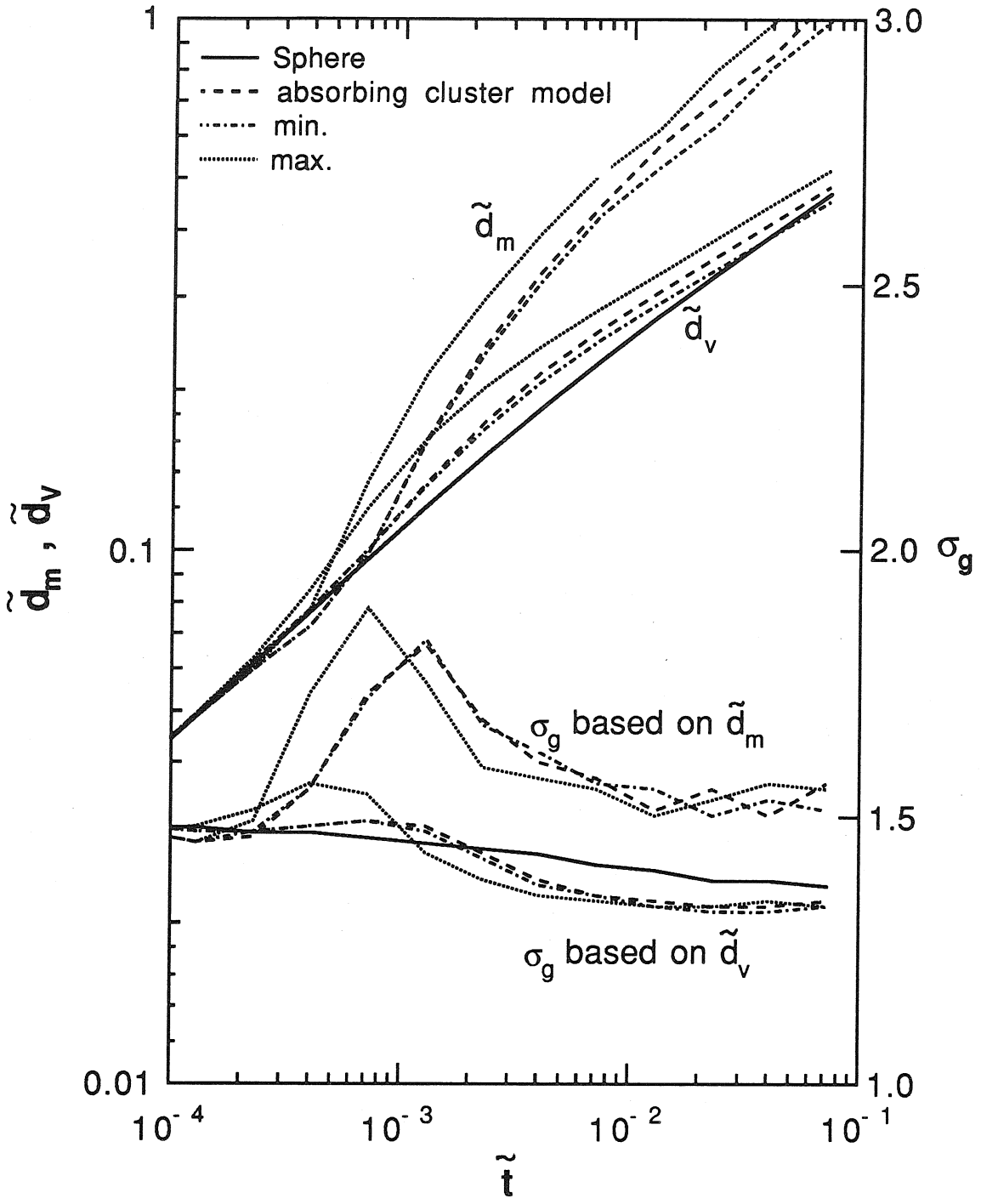

Figure 13. Growth of the median mobility- and volume-equivalent diameters $\tilde{d}_m$ and $\tilde{d}_v$ as a function of the non-dimensional time $\tilde{t}$ ($\tilde{d}_1$=0.0057, $\tilde{\rho}$.=0.0025, D_f=1.8). The geometric standard deviations σ_g are based on the mobility- and volume-equivalent distributions.

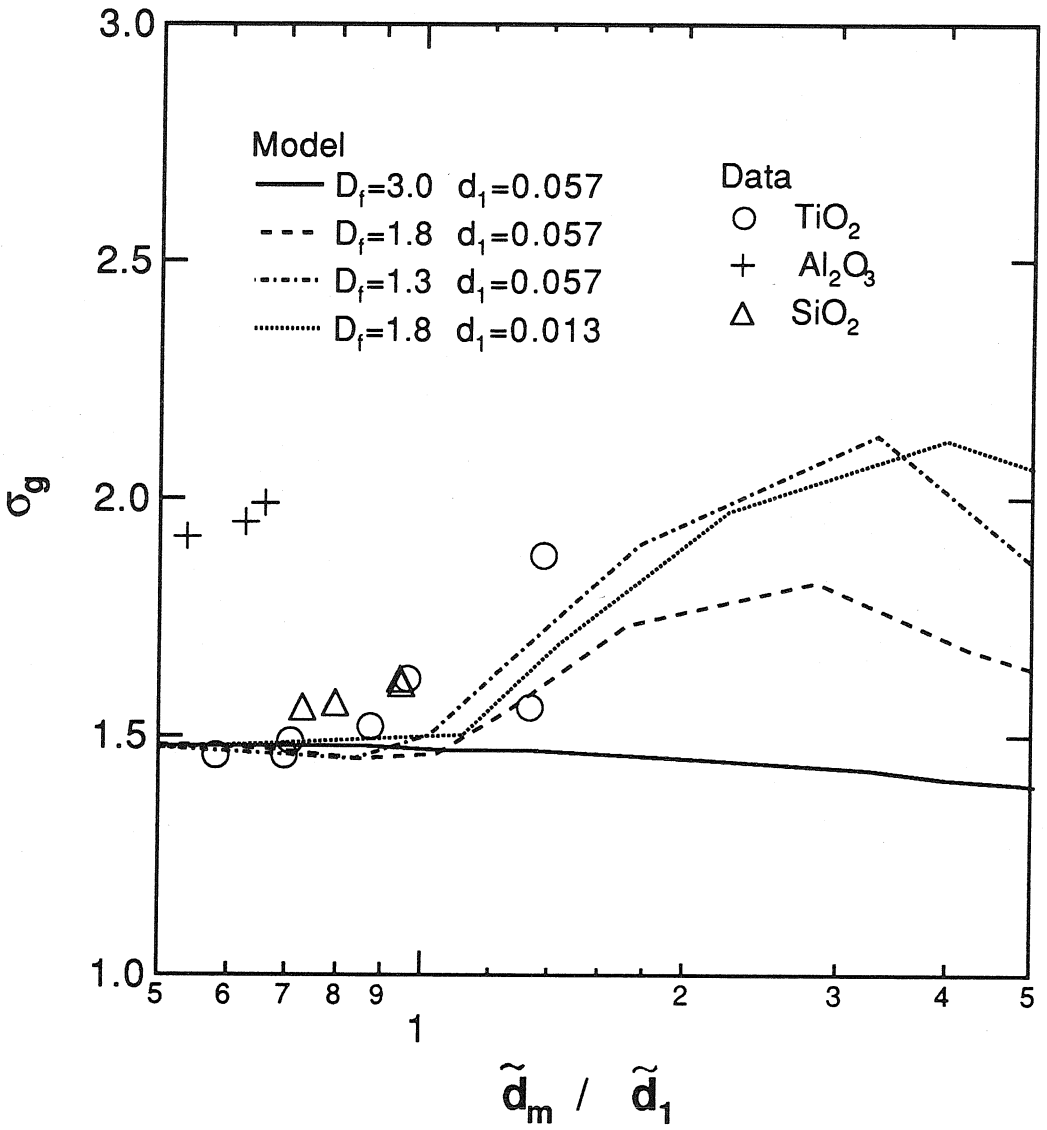

Figure 14. Measured geometric standard deviations σ_g, based on the mobility diameter distributions, as a function of the median mobility diameters of the distributions (15). Calculations assume that T=873 K, ρ=3900 kg m^{-3}. To normalize the data, the primary particle diameter was assumed to be d_1=27 nm.

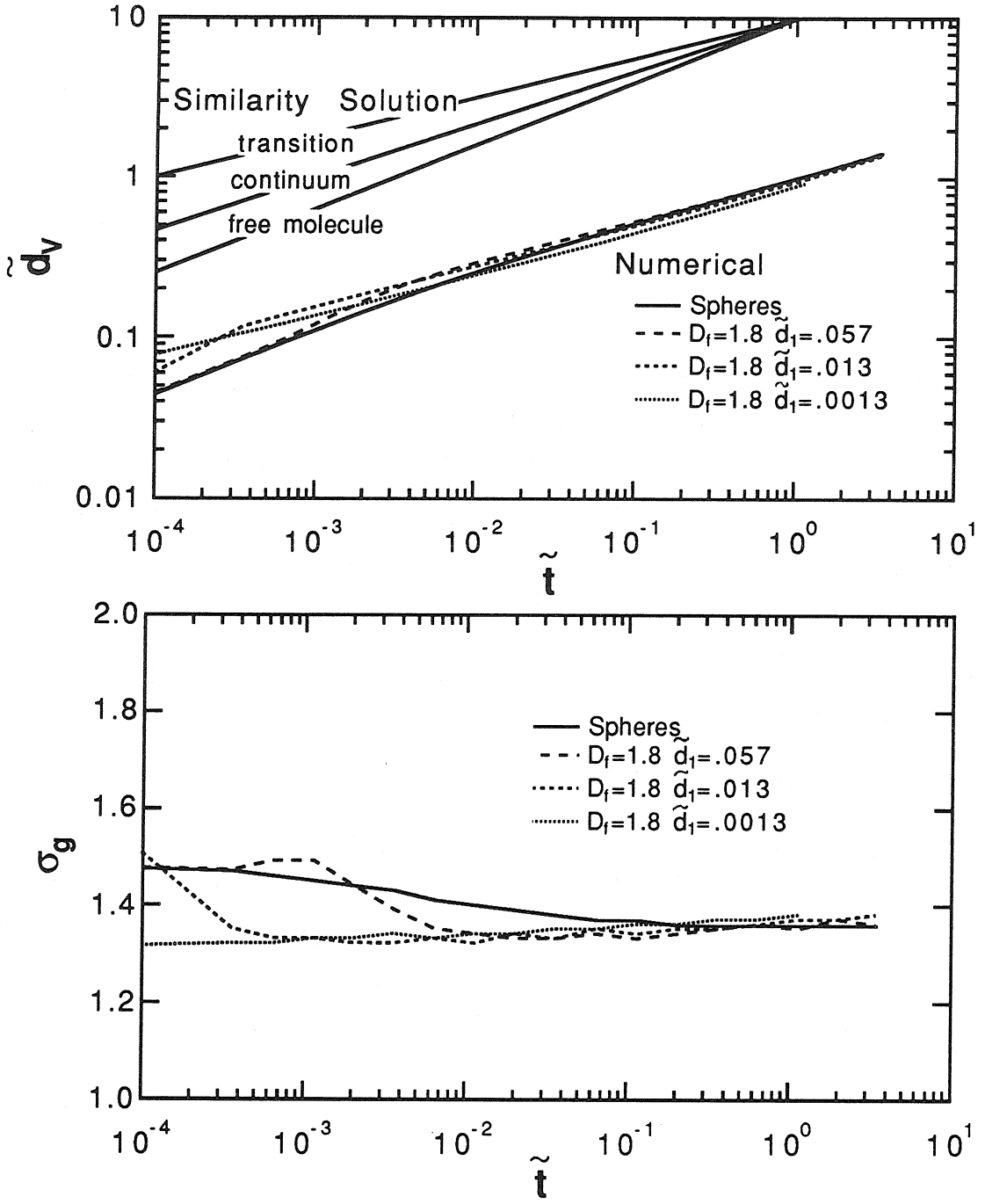

Figure 15. Evolution of the median volume-equivalent diameter $\tilde{d}_v$ for $D_f = 1.8$, compared to similarity solutions for spheres in the free-molecule, continuum and transition regimes (top 3 curves of the upper graph; arbitrary scale). The evolution of the geometric standard deviation σ_g is shown in the lower graph, for the same conditions.

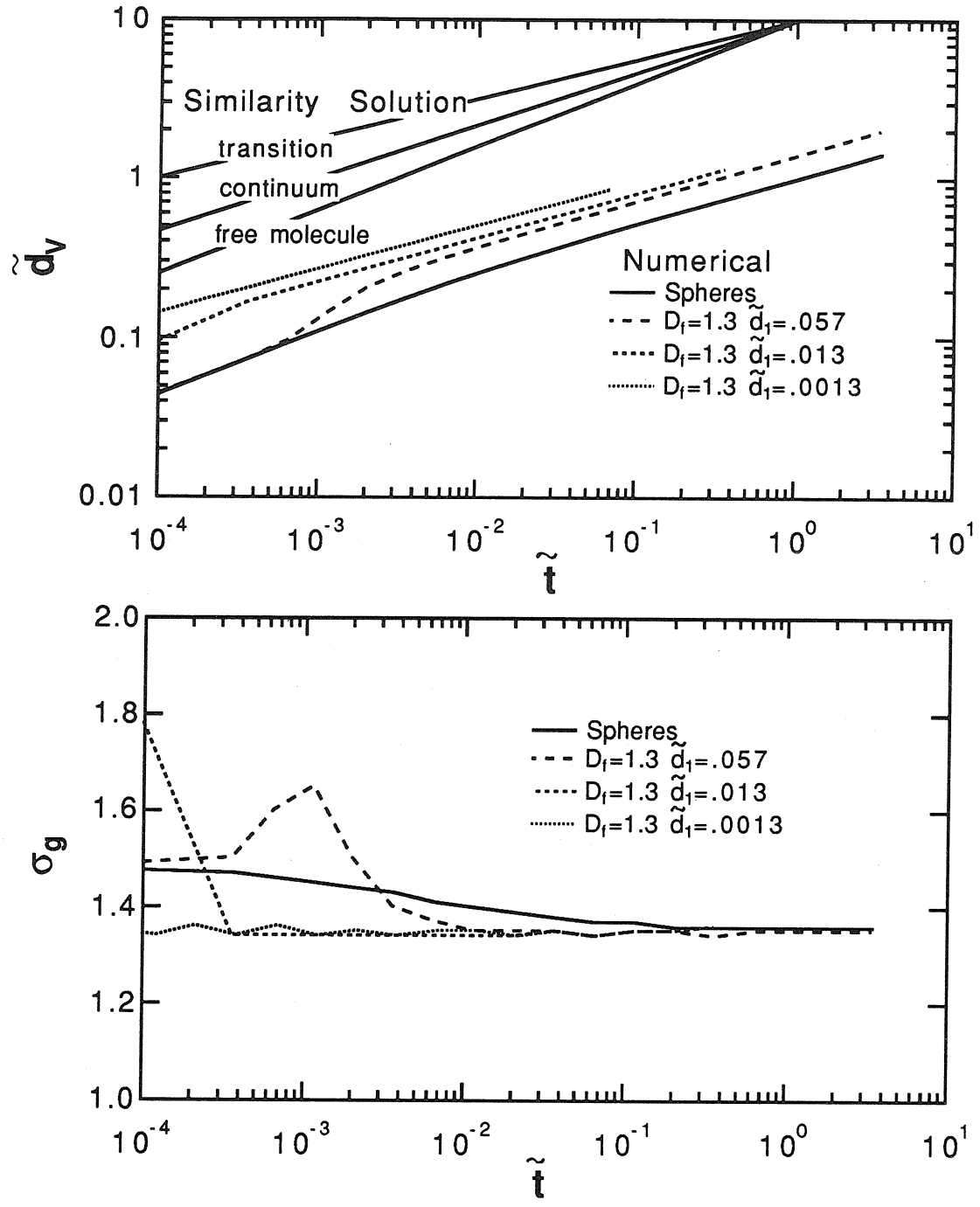

Figure 16. Evolution of the median volume-equivalent diameter $\tilde{d}_V$ and geometric standard deviation σ_g for fractal dimension D_f = 1.3. The growth of $\tilde{d}_v$ is compared to that expected from similarity solutions for spheres in the three transport regimes (upper curves, arbitrary scale).

CHAPTER 9

CONCLUSIONS AND RECOMMENDATIONS

The formation of aerosol agglomerates depends on both aerosol dynamics and material properties, although particles with similar structures are produced in a variety of systems. This suggests that the results obtained in this study using a few model systems may be applicable to a broad range of particle systems.

The structure and dynamics of agglomerate aerosol particles have been studied for several decades, but early studies neglected important scaling properties of the particle structure that have been recently ncharacterized by fractal geometry. Investigations employing fractal models have rarely considered the effect of finite particle size and finite gas mean free path. Consideration of these finite size effects is critical to the correct interpretation of aerosol measurements, particularly for agglomerates with fewer than 1000 primary particles.

Agglomerate fractal dimensions measured from micrographs are subject to substantial error, even for agglomerates whose fractal dimensions are less than 2, and are generally not sufficiently accurate to verify the results of computer simulations using specific growth mechanisms. Measurement of fractal dimensions, however, may be valuable in characterizing changes in particle structure.

Inferences of the fractal dimension from the scaling of particle mobility with mass may be performed *in situ*, but require a detailed understanding of the agglomerate aerodynamics. The finite cluster size and gas mean free path cannot be neglected. For example, the assumption that the mobility diameter of a fractal agglomerate in Stokes flow is proportional to the radius of gyration is valid only for clusters of several hundred primary particles, for fractal dimension greater than about 1.3. In the transition regime, the mobility diameter is nearly equal to the projected area diameter, but simulations show that for clusters with less than 1000 primaries, the projected area is not strongly sensitive to the fractal dimension. Thus, it is difficult to determine fractal dimensions from mobility data.

Measurements of mass transfer and charging of agglomerates show a strong correlation between these phenomena and aerodynamic drag. Although the equivalent diameters vary depending on the phenomenon considered, the collision of particles or ions with agglomerates can generally be described as a function of two length scales, namely, the projected area equivalent diameter and the radius of gyration. The relative importance of these two length scales is determined by the relevant length scale of the transport process being considered. Thus, if the relevant mean free paths involved in two processes are equal, both processes are characterized by the same equivalent sphere.

The analogy between drag and mass transfer was used to predict the coagulation rates of agglomerate particles in the transition regime. The calculations show an interesting acceleration of the agglomeration kinetics as the particles grow from rapidly coalescing particles to agglomerate-forming solid particles.

A number of important, unresolved problems in agglomerate dynamics are suitable for theoretical investigation. Monte-Carlo simulations have been useful in investigating the effect of structure on dynamics but the effects of finite mean free path, sintering kinetics and reaction kinetics have not been considered. A logical extension of previous work is the simulation of the attachment of ions to agglomerates. Aggregation simulations including sintering are more difficult but also follow from simulations of rearranging clusters. For aerosol reactor research, the numerical models developed here may be used directly, or extended to consider sintering in more detail. An outline of such a model is given in Appendix F.

Experimental verification of the aerosol dynamics models developed here remains extremely challenging. The results of this thesis may best be applied to experimental studies of particle formation. For example, static and dynamic light scattering might be used to follow the evolution of the particle structure and of the size distribution, yielding important information on the sintering and reaction chemistry.

APPENDIX A
GENERATION AND CHARACTERIZATION OF SIMULATED AGGLOMERATES

c Projections of Chains with
c log-nornally distributed primary particles

PROGRAM LOGCHAIN

```
C - computes the average projected area of straight chains
c  of primary particles that have lognormally distributed diameters.
c Based on the program LOGNOR.BAS
     REAL  d(500),cl(2,500),cl0(2,500)
     REAL D1, SIGG, XMEAN, XSIG, MEANL, MEANA, L, A, A0,length
     INTEGER N, NK, K,ISIG
     open(UNIT=4, FILE= 'lognor.out',STATUS='NEW')
     N=500
     D1=2.
     NK=20
     DO 300 ISIG=1,2
      sigg=1.0+(ISIG-1)*0.2
      write(4,*) ' N, d1, sig',N, D1, SIGG
      meana=0
      meanl=0
     xmean=log(d1)
      xsig=log(sigg)
      write(4, 55)
55    FORMAT('   Length      Area      Area(0)      Area/Area(0)')
      DO 200 K=1,nk
       length=0
       dmax=0
       DO 100 i=1,n
        call normal(x,xmean,xsig)
        d(i)=exp(x)
       if (d(i).GT.dmax) dmax=d(i)
        length=length+d(i)
        cl0(2,i)=50
        if (i.EQ.1) cl0(1,i)=d(1)/2.
       if (i.GT.1) cl0(1,i)=cl0(1,i-1)+(d(i-1)+d(i))/2.
        cl(1,i)=cl0(1,i)
        cl(2,i)=cl0(2,i)
100    CONTINUE
       xmin=0
       xmax=length
       call mcint(CL0,d,xmin,xmax,dmax,a0,n)
       a0=a0/n/3.14159*4./d1**2.
      area=0
      DO 150 nrotate=1,100
        call rotate(CL,CL0,D,n,xmin,xmax)
        call mcint(CL,d,xmin,xmax,dmax,atht,n)
        atht=atht/n/3.14159*4./d1**2.
c         write(4,*) 'A(tht)', atht
       area=area+atht/100.
```

```
 150    CONTINUE
        meana=meana+area
        meanl=meanl+length/n/d1
        write(4,60) length/n/d1, area,a0,area/a0
 60      FORMAT(4F12.4)
 200    CONTINUE
       write(4,*) 'mean L,area=', meanl/nk,meana/nk
 300  CONTINUE
     close(4)
      STOP
      end
      SUBROUTINE normal(x,xmean,xsig)
 c    Gaussian deviates
      REAL X, XMEAN, XSIG,X1,X2,R,FAC
      INTEGER IDUM
      IDUM=1
 1     x1=2.*RAN1(IDUM)-1.0
      x2=2.*RAN1(IDUM)-1.0
      r=x1*x1+x2*x2
       if(r.GT.1.OR.r.EQ.0) goto 1
      fac=SQRT(-2.*log(r)/r)
      x=x2*fac*xsig+xmean
     RETURN
     END
     SUBROUTINE mcint(CL,d,xmin,xmax,dmax,area,n)
 c    Monte Carlo integration to determine the projected area of the chain.
     REAL CL(2,500),d(500),XMIN,XMAX,DMAX,AREA,XR,YR
     INTEGER N,NR,IR,I,IDUM
     IDUM=1
    area=0
    nr=1000
    DO 100  IR=1, nr
     xr=RAN1(IDUM)*(xmax-xmin)+xmin
     yr=50+(RAN1(IDUM)-.5)*dmax
      DO 50 i=1,n
       X=cl(1,i)
       Y=cl(2,i)
      DIST=SQRT((xr-X)**2+(yr-Y)**2)
          IF(DIST.LE.d(i)/2.) THEN
             area=area+1
              goto 100
           endif
50     CONTINUE
100   CONTINUE
    area=(xmax-xmin)*dmax*area/nr
     RETURN
     END
     SUBROUTINE rotate(CL,CL0,D,n,xmin,xmax)
     REAL CL(2,500),CL0(2,500),D(500),XMIN,XMAX,DZ,C
     INTEGER IDUM
     IDUM=1
    dz=2.*RAN1(IDUM)-1.
    c=SQRT(1.-dz*dz)
     xmin=9999999.
     xmax=-9999999.
     DO 100 i=1,n
      cl(1,i)=150.+c*(cl0(1,i)-150.)
      if ((cl(1,i)-d(i)/2.).LT.xmin) xmin=cl(1,i)-d(i)/2.
```

```
      if ((cl(1,i)+d(i)/2.).GT.xmax) xmax=cl(1,i)+d(i)/2.
100   CONTINUE
      RETURN
      END
```

FUNCTION RAN1(IDUM) returns a random number between 0 and 1.
(see Numerical Recipes by Press et al.)

```
' 3-D CLUSTER GROWTH BY THE ADDITION OF CLUSTERS MCCA
'  july 31,1987
' Jan 1991 fix routine that calculates DMAX
' Revised March 1989 so that a modified hierarchical scheme is used.
' At each stage we make the addition cluster from the primary cluster.
' This is done by selecting GA=GC*BETA connected particles from the cluster
' CLUSTER.
'           S.Rogak
OPTION BASE 1
DEFINT E-P
DIM SHARED ADD(3,512),CLUSTER(3,1024),ACTIVE(1024)
CLS
SCREEN 9
PALETTE 0, 1
COLOR 14
WINDOW (0,0)-(300,200)

INPUT "Input batch data file",INAMES$
OPEN INAMES$ FOR INPUT AS #5
INPUT #5,NFILES ' number of clusters produced in this batch
FOR IFILE=1 TO NFILES
   INPUT #5,CNAME$
   RANDOMIZE(CVI(CNAME$)) 'output name for cluster
   INPUT #5,LNAME$                    'log file name
   INPUT #5,KFIN                     ' number of additions
   INPUT #5,BETA                     ' ratio of cluster sizes
   DP=40.                           ' primary particle diameter
   GC=1                             ' start with a single particle
   OPEN LNAME$ FOR OUTPUT AS #3
   SCALE=10
   X0=150*SCALE:Y0=100*SCALE:Z0=100*SCALE 'position of screen center
   CLUSTER(1,1)=X0:CLUSTER(2,1)=Y0:CLUSTER(3,1)=Z0
   MINA=1:MINC=1 ' initial (dummy) locations of the two closest particles
   CALL MOVECG(GC,DP,X0,Y0,Z0,DMAX,RGYR) 'calc. init. max. radius
' - MAIN GROWTH ALGORITHM ------
   CALL CLSGRPH(GC,DP,SCALE)
  FOR KK=1 TO KFIN' number of clusters to be added to the observed cluster
     DS=2*DP+2*DMAX:CIRCLE (150,100),DS/SCALE
'     radius of the starting cluster.
350   CALL MAKEADD(GC,GA,DP,BETA,scale)
360   CALL ROTADD(GA)
'    give the cluster a random initial rotation
     CALL RNDDIR(NX!,NY!,NZ!)
     TX=-ADD(1,1)+DS*NX!+X0
     TY=-ADD(2,1)+DS*NY!+Y0
     TZ=-ADD(3,1)+DS*NZ!+Z0
     CALL MOVEADD(GA,TX,TY,TZ) 'translate
     PSET(ADD(1,1)/SCALE,ADD(2,1)/SCALE)
```

```
420   CALL MINDIST(GC,GA,X0,Y0,Z0,DP,DMAX,DMIN,WALK,MINC,MINA)
       IF DMIN>DS*2! THEN
        GOTO 360
       END IF
       IF (DMIN-DP)>DP*0.1 THEN
        CALL WALKER(GA,WALK)
        PSET(ADD(1,1)/SCALE,ADD(2,1)/SCALE)
        GOTO 420
       ELSE
'           If the separating distance is > than some small value
'           (2 is used since integer math is used) then walk to
'           a new circle with max. radius=smallest separating dist.
'     Otherwise, begin process of joining ADD to CLUSTER
       IF(ABS(DMIN-DP)>.001*DP) THEN
        TX=(CLUSTER(1,MINC)-ADD(1,MINA))/DMIN*(DMIN-DP)
        TY=(CLUSTER(2,MINC)-ADD(2,MINA))/DMIN*(DMIN-DP)
        TZ=(CLUSTER(3,MINC)-ADD(3,MINA))/DMIN*(DMIN-DP)
        CALL MOVEADD(GA,TX,TY,TZ)
       END IF
       CALL ADDER(GC,GA)  ' add the new cluster to "CLUSTER"
       CALL MOVECG(GC,DP,X0,Y0,Z0,DMAX,RGYR) ' Movethe cluster to the origin
       CLS
       PRINT GC,CNAME$
       CALL CLSGRPH(GC,DP,SCALE)
       CALL FILER(CNAME$,GC)
     END IF
   NEXT KK
   CLOSE #3
NEXT IFILE
CLOSE #5
END

      SUB FILER(CNAME$,GC) STATIC
      BIG=9.E9
      OPEN CNAME$ FOR OUTPUT AS #2
      FOR G=1 TO GC
       WRITE #2,CLUSTER(1,G),CLUSTER(2,G),CLUSTER(3,G)
      NEXT G
      write #2, BIG,BIG,BIG
      CLOSE #2
    END SUB
   SUB MAKEADD(GC,GA,DP,BETA,scale) STATIC
      J=GC/2.0+.4
      ADD(1,1)=CLUSTER(1,J)
      ADD(2,1)=CLUSTER(2,J)
      ADD(3,1)=CLUSTER(3,J)
      GA=BETA*GC
      IF(GA<=1) THEN
       GA=1
       GOTO 901
      END IF
      FOR I=1 TO GC
       ACTIVE(I)=1
      NEXT I
      NCOUNT=1
      OLDN=1
      TOL=.01*DP
      ACTIVE(J)=0
```

```
890    FOR JJ=1 TO GA
         FOR J=1 TO GC
          IF(ACTIVE(J)>0) THEN
           FOR K=1 TO OLDN
           DXS!=( CLUSTER(1,J)-ADD(1,K) )^2
           DYS!=( CLUSTER(2,J)-ADD(2,K) )^2
           DZS!=( CLUSTER(3,J)-ADD(3,K) )^2
           D=SQR(DXS!+DYS!+DZS!)
           IF((D-DP)<TOL) THEN
            NCOUNT=NCOUNT+1
            ACTIVE(J)=0
            ADD(1,NCOUNT)=CLUSTER(1,J)
            ADD(2,NCOUNT)=CLUSTER(2,J)
            ADD(3,NCOUNT)=CLUSTER(3,J)
            PSET(ADD(1,NCOUNT)/SCALE,ADD(2,NCOUNT)/SCALE),1
            IF(NCOUNT>=GA) THEN GOTO 901
            GOTO 900 ' next J
           END IF
          NEXT K
         END IF
900       CIRCLE (CLUSTER(1,J)/SCALE,CLUSTER(2,J)/SCALE),1,2
        NEXT J
       OLDN=NCOUNT
      NEXT JJ
      TOL=1.5*TOL
      WRITE #3,"error in finding ADD: NCOUNT,GC,GA,TOL :" ,NCOUNT,GC,GA,TOL
      GOTO 890
901  print "finished Making ADD"
   END SUB
   SUB ADDER(GC,GA) STATIC
       FOR J=GC+1 TO GC+GA
        CLUSTER(1,J)=ADD(1,J-GC)
        CLUSTER(2,J)=ADD(2,J-GC)
        CLUSTER(3,J)=ADD(3,J-GC)
       NEXT J
       GC=GC+GA
   END SUB
   SUB clsgrph(gc,DP,scale) static
   FOR J=1 TO GC
'    graph CLUSTER as a series of circles
      RADIUS=DP/2/SCALE
      IF (RADIUS<2) THEN
       PSET(CLUSTER(1,J)/SCALE,CLUSTER(2,J)/SCALE),2
      ELSE
       CIRCLE(CLUSTER(1,J)/SCALE,CLUSTER(2,J)/SCALE),RADIUS,2
      END IF
   NEXT J
   END SUB
   SUB MINDIST(GC,GA,X0,Y0,Z0,DP,DMAX,DMIN,WALK,MINC,MINA) STATIC
1230  DMIN=9999
   D0=SQR( (ADD(1,1)-X0)^2 +(ADD(2,1)-Y0)^2 +(ADD(3,1)-Z0)^2 )
    IF D0> 3*DMAX THEN
      DMIN=D0
      WALK=DMIN-2*DMAX
      GOTO 1250
    END IF
    FOR J=1 TO GA
      AX=ADD(1,J):AY=ADD(2,J):AZ=ADD(3,J)
```

```
        D0=SQR((AX-X0)^2+(AY-Y0)^2+(AZ-Z0)^2)
        IF D0<1.3*DMAX THEN 1240 ' we have little choice but to check all points
        IF D0<DMIN THEN DMIN=D0
      next j
     WALK=DMIN-DMAX
     GOTO 1250
1240  FOR J=1 TO GC
        CX=CLUSTER(1,J)
        CY=CLUSTER(2,J)
        CZ=CLUSTER(3,J)
        FOR K=1 TO GA
         D=SQR((CX-ADD(1,K))^2+(CY-ADD(2,K))^2+(CZ-ADD(3,K))^2)
         IF D<DMIN THEN
          DMIN=D
          MINC=J
          MINA=K
'       the locations of the closest points are stored
         END IF
        NEXT K
      NEXT J
     WALK=DMIN-DP
1250  DUMMY=0
    END SUB
    SUB MOVEADD(GA,TX,TY,TZ) STATIC
       FOR J=1 TO GA
         ADD(1,J)=ADD(1,J)+TX
         ADD(2,J)=ADD(2,J)+TY
         ADD(3,J)=ADD(3,J)+TZ
       NEXT J
    END SUB
    SUB RNDDIR(X,Y,Z) STATIC
       Z=2*RND-1!
       THT!=2*3.14159*RND
       X=COS(THT!)*SQR(1-Z^2)
       Y=SIN(THT!)*SQR(1-Z^2)
    END SUB
   SUB WALKER(GA,WALK) STATIC
    CALL RNDDIR(NX!,NY!,NZ!)
    TX=NX!*WALK
    TY=NY!*WALK
    TZ=NZ!*WALK
    CALL MOVEADD(GA,TX,TY,TZ)
   END SUB
   SUB ROTADD(GA) STATIC
   ROT!=6.28318*RND
   FOR J=1 TO GA
'  rotate about the first particle, about z axis
   X=ADD(1,J)-ADD(1,1)
   Y=ADD(2,J)-ADD(2,1)
   ADD(1,J)=ADD(1,1) + X*COS(ROT!) - Y*SIN(ROT!)
   ADD(2,J)=ADD(2,1) + X*SIN(ROT!) + Y*COS(ROT!)
   NEXT J
   ROT!=6.28318*RND
   FOR J=1 TO GA
'  rotate about the first particle, about x axis
   Y=ADD(2,J)-ADD(2,1)
   Z=ADD(3,J)-ADD(3,1)
   ADD(2,J)=ADD(2,1) + Y*COS(ROT!) - Z*SIN(ROT!)
```

```
      ADD(3,J)=ADD(3,1) + Y*SIN(ROT!) + Z*COS(ROT!)
     NEXT J
     END SUB
          SUB RETRIEVE(GC,INAME$,X0,Y0,Z0) STATIC
          PRINT "RETRIEVEING CLUSTER":OPEN INAME$ FOR INPUT AS #4
          FOR J=1 TO GC
            INPUT #4,CLUSTER(1,J),CLUSTER(2,J),CLUSTER(3,J)
          NEXT J
          CLOSE #4
' cluster is retrieved but may be in the wrong place
          TX=X0-CLUSTER(1,1)
          TY=Y0-CLUSTER(2,1)
          TZ=Z0-CLUSTER(3,1)
          FOR J= 1 TO GC
           CLUSTER(1,J)=CLUSTER(1,J)+TX
           CLUSTER(2,J)=CLUSTER(2,J)+TY
           CLUSTER(3,J)=CLUSTER(3,J)+TZ
          NEXT J
          PRINT "CLUSTER RETREIVED"
         END SUB
         SUB MOVECG(GC,DP,X0,Y0,Z0,DMAX,RGYR) STATIC
         XG=0:YG=0:ZG=0
         FOR I=1 TO GC
          XG=XG+CLUSTER(1,I)/GC
          YG=YG+CLUSTER(2,I)/GC
          ZG=ZG+CLUSTER(3,I)/GC
         NEXT I
         INERTIA!=0:DMAX=0
         FOR I=1 TO GC
          DX=CLUSTER(1,I)-XG
          DY=CLUSTER(2,I)-YG
          DZ=CLUSTER(3,I)-YG
          DS=DX*DX/DP/DP+DY*DY/DP/DP+DZ*DZ/DP/DP
          INERTIA!=INERTIA!+DS+3./20.
          IF(SQR(DS)+1>DMAX) THEN DMAX=SQR(DS)+1.
          CLUSTER(1,I)=DX+X0
          CLUSTER(2,I)=DY+Y0
          CLUSTER(3,I)=DZ+Z0
         NEXT I
         RGYR=SQR(INERTIA!/GC)
         write #3,GC,RGYR,DMAX
         DMAX=DMAX*DP
     END SUB

' PROGRAM  FRACTAL.BAS
' VERSION 52.0 JAN 17 1991
' Program to measure the fractal dimension of a set of coordinates in
' 3-D and from the 2-D projection as displayed on the screen.
' March 16, 1989
' Reworked Nov. 30, 1990 by S. Rogak.
' Modified Dec 13, 1990 so that the radius spacing of the correlation points
'   give more useful information at the small length scales.
' Jan 8 1991 add pair correlation function measurement for 2-d images.
'   Fractal dimensions are calculated from each projection, then averaged
'   over the nrot projections. The aspect ratios are calculated from the estimated
'   maximum and minimum radii of gyration
' Jan 17 91 the properties of the 3-d cluster and its projection are calculated from
'   a random sample of points within the solid object or the projected region.
```

```
 CLEAR
 OPTION BASE 1
 DEFINT G-Q
 DIM cl(4500,3),rncl(1000,3)' THE DESIRED CLUSTER COORDINATES
 DIM dm(30),dm2(30),adm2(30) ' The accumulating variable for the density-density
 DIM rL(30),rrL(30),cen(30)
 DIM area(10),rg(10),Dcorr(10),Dcum(10),asp2(10)
 DIM x(30),cm3(30),cm2(30),acm2(30) ' cumulative mass-radius curves,
' d1  primary particle diameter
' gc is the number of particles in the cluster
 nclass=20 ' total number of radius classes
 nsample=1000
 unit=1
 zero=0
bname$=FILES$(1,"TEXT")
OPEN bname$ FOR INPUT AS #2
batout$=bname$+".out"
OPEN batout$ FOR OUTPUT AS #6
WRITE #6, bname$,DATE$
WRITE #6, "      file                gc   rg3/d1 rg2/Rg3  area  coord# aspect3 aspect2 DfC3  DfC2  Dfm3
Dfm2"
RANDOMIZE
INPUT " hardcopy output? (1=yes)",iprint
INPUT #2, nfiles
FOR ifile=1 TO nfiles
  CLS
  INPUT #2,iname$
  INPUT #2,oname$
  OPEN iname$ FOR INPUT AS #3
  OPEN oname$ FOR OUTPUT AS #4
  PRINT #4,iname$
  INPUT #2 , gc,d1,scale, NDIM
 igc=gc
  FOR i=1 TO gc
  IF(NDIM=3) THEN
    INPUT #3, cl(i,1),cl(i,2),cl(i,3)
   ELSE
    INPUT #3, cl(i,1),cl(i,2)
    cl(i,3)=0
  END IF
  IF cl(i,1)>100000! THEN
    igc=i-1
    PRINT " end of data has been reached, set gc=",igc
     GOTO 1
   END IF
 NEXT i
1 gc=igc
  CLOSE #3
 d1=d1*scale
  FOR i=1 TO gc
   cl(i,1)=cl(i,1)*scale
   cl(i,2)=cl(i,2)*scale
   cl(i,3)=cl(i,3)*scale
  NEXT i
 rg2=9999!
 xh=250
 yh=200 ' pixel coordinates of particle ig3
 CALL coornum(cl(),gc,d1,coordn,d1calc)
```

```
   CALL center(cl(),ig3,rg3,gc,R3max,d1,asp3) ' get ig3 the number of the particle closest to centroid,and
RG3
   CALL clusgrph(cl(),gc,d1,ig3,xh,yh,pix) ' plot the cluster coordinates
   CALL rclasses(rL(),rrL(),d1,rg3,nclass)
   CALL sample3d(cl(),rncl(),gc,d1,nsample)
   CALL center(rncl(),ig,rgg,nsample,Rmax,zero,asp3)
   CALL clusgrph(rncl(),nsample,unit,ig,xh,yh,pix)
   CALL corr(rncl(),nsample,rL(),dm(),cen(),Rmax,ig,nclass,d1)
   CALL massR(rncl(),nsample,rrL(),cm3(),ig,nclass)
   xmin=d1/2!
   xmax=rg3
   CALL logfit(rrL(),dm(), b,Dcorr3,xmin,xmax,nclass)
   Dcorr3=3!+Dcorr3
   CALL logfit(rrL(),cm3(), b,Dcum3,xmin,xmax,nclass)
   PRINT #4,"      gc      2Rg3/d1      Dcorr 3-d      Dcum 3-d      Aspect coord#   d1calc/d1 "
   PRINT #4,USING "######.###"; gc,2*rg3/d1,Dcorr3,Dcum3,asp3,coordn,d1calc/d1

' Start Analyzing the projected images
   PRINT #4,"      Dcum2      Dcorr2      area2          rg2          asp2 "
   FOR L=1 TO nclass
      acm2(L)=0
      adm2(L)=0
   NEXT L
   IF(NDIM=2) THEN
     nrot=1
    ELSE
     nrot=4
   END IF
  CALL countpix(rpix,d1) ' measure number of pixels per primary particle
  FOR irot=1 TO nrot
   IF NDIM=3 THEN
    CALL rotate(cl(),gc)
   END IF
   CALL clusgrph(cl(),gc,d1,ig3,xh,yh,pix)
   CALL sample2d(rncl(),nsample,xh,yh,R3max)
    CLS
   FOR iii=1 TO nsample
     PSET(rncl(iii,1),rncl(iii,2))
   NEXT iii
   CALL center(rncl(),ig2,rg2,nsample,R2max,unit,asp)
  area(irot)=pix*1!/gc/rpix
  rg(irot)=rg2/rg3
  asp2(irot)=SQR(asp^2-1)
  CALL corr(rncl(),nsample,rL(),dm2(),cen(),R2max,ig2,nclass,d1)
  CALL massR(rncl(),nsample,rrL(),cm2(),ig2,nclass)
  xmin=d1/2!   ' fit range for finding fractal dimensions
  xmax=rg2
  CALL logfit(rrL(),dm2(), b,Df,xmin,xmax,nclass)
  Dcorr(irot)=Df+3!
  PRINT"Dfcorr2=",Df+3!
  CALL logfit(rrL(),cm2(), b,Df,xmin,xmax,nclass)
  Dcum(irot)=Df
  PRINT"Dcum2=",Df
  PRINT #4,USING "####.###";Dcum(irot),Dcorr(irot),area(irot),rg(irot),asp2(irot)
  FOR L=1 TO nclass
    acm2(L)=acm2(L)+cm2(L)/nrot
    adm2(L)=adm2(L)+dm2(L)/nrot
  NEXT L
```

```
 NEXT irot
 CALL med(Dcorr(),nrot,Dcorrm,scorr)
 CALL med(Dcum(),nrot,Dcumm,scum)
 CALL med(rg(),nrot,rgm,srg)
 CALL mean(area(),nrot,aream,sarea)
 CALL mean(asp2(),nrot,aspm,sasp)
 PRINT #4," median values, sigs:"
 PRINT #4,USING "####.###";Dcumm,Dcorrm,aream,rgm,aspm
 PRINT #4,USING "####.###";scum,scorr,sarea,srg,sasp
 PRINT #4, "  2r/d1   Corr3(2r/d1)   Corr2(2r/d1)   m3(2r/d1)      m2(2r/d1)  "
 FOR L=1 TO nclass-1
  rrL(L)=2*rrL(L)/d1  ' rescale the radius classes with primary radius d1/2
  PRINT #4,USING "#####.#####"; rrL(L),dm(L),adm2(L),cm3(L),acm2(L)
 NEXT L
CLOSE #4

PICTURE ON
LOCATE 1,10
Tx$= DATE$
DrawText Tx$
LOCATE 2,10
Tx$="input file:  " +iname$
DrawText Tx$
LOCATE 3,10
Tx$="output file:  " +oname$
DrawText Tx$
LOCATE 4,10
Tx$="N="+STR$( gc)+"  Rg3/(d1/2)= "+STR$(2*rg3/d1)
Tx$=Tx$+"  Rg2/Rg3= "+STR$(rgm)
Tx$=Tx$+"   d1= "+STR$(d1)+" pixels"
DrawText Tx$
LOCATE 5,10
Tx$="3-d aspect ratio="+STR$(asp3)+"    2-d ratio="+STR$(aspm)
DrawText Tx$
LOCATE 6,10
Tx$="# rotations="+STR$(nrot)
Tx$=Tx$+"  exp. area="+STR$(aream)+" coord. #="+STR$(coordn)
DrawText Tx$
LOCATE 7,10
Tx$="H-B dimen.s based on  d1/2< r< Rg3 (3-d)  and d1/2< r< Rg2 (2-d)"
DrawText Tx$
 LOCATE 8,10
Tx$= "shape function f(r'): C(r')       C2(r')       m3(r')      m2(r') :"
DrawText Tx$
LOCATE 9,10
Tx$= "fractal dimension : "+ STR$(Dcorr3)+STR$(Dcorrm)+STR$(Dcum3)+STR$(Dcumm)
DrawText Tx$
LOCATE 10,10
Tx$="            symbol:"
DrawText Tx$
CIRCLE(210,150),1 :CIRCLE(280,150),2:CIRCLE(340,150),3:CIRCLE(410,150),4
PICTURE OFF
head$=PICTURE$

PICTURE ON
LOCATE 4,11
x0=1
y0=.001
```

```
 xmax=60
 ymax=1
 xlab$="r'=2r/d1"
 ylab$="f(r')"
 CALL logaxes(x0,y0,xmax,ymax,xlab$,ylab$)
  isym=1
 CALL logplot(rrL(),dm(),x0,y0,xmax,ymax,isym)
  isym=2
 CALL logplot(rrL(),dm2(),x0,y0,xmax,ymax,isym)
  isym=3
 CALL logplot(rrL(),cm3(),x0,y0,xmax,ymax,isym)
 isym=4
 CALL logplot(rrL(),acm2(),x0,y0,xmax,ymax,isym)
 PICTURE OFF
 graf$=PICTURE$
 PICTURE ,graf$
 IF iprint=1 THEN
   OPEN "LPT1:" FOR OUTPUT AS #5
   WINDOW OUTPUT #5
   PICTURE (0,80),head$
   PICTURE (0,240), graf$
   CLOSE #5
 END IF
 PICTURE ON:PICTURE OFF

 PRINT #6, USING"\                    \"; iname$;
 PRINT #6, USING "#####.#"; gc,2*rg3/d1;
 PRINT #6, USING "####.##";rgm,aream,coordn,asp3,aspm,Dcorr3,Dcorrm,Dcum3,Dcumm
NEXT ifile
CLOSE #2
CLOSE #6
END

SUB coornum(cl(),gc,d1,coordn,dcalc) STATIC
' Calculate the average coordination number and the
' average distance to the nearest neighbor (should be d1)
  n=0
  ntry=0
  try=100!/gc
  rsHigh=(1.01*d1)^2
  FOR i=1 TO gc
   IF RND<try THEN
     x=cl(i,1)
     y=cl(i,2)
     z=cl(i,3)
     ntry=ntry+1
    dcalc=9000000!
     FOR j=1 TO gc
      rsij=(x-cl(j,1))^2 + (y-cl(j,2))^2 + (z-cl(j,3))^2
      IF i<>j AND rsij<dcalc THEN dcalc=rsij
       IF rsij<rsHigh THEN
          n=n+1
       END IF
     NEXT j
    END IF
 NEXT i
coordn=n*1!/(ntry*1!)-1!
dcalc=SQR(dcalc)
```

```
  PRINT "coordination number=",coordn,"   calc. d /d1=",dcalc/d1
 END SUB

 SUB corr(cl(),npoints,rL(),dm(),cen(),Rmax,ig,nclass,d1) STATIC
 PRINT " getting  DENSITY DENSITY correlations "
 xcen=cl(ig,1) : ycen=cl(ig,2) : zcen=cl(ig,3)
 FOR L=1 TO nclass-1
     dm(L)=0
     cen(L)=0
  NEXT L
  FOR i=1 TO 200
   xi=cl(i,1)
   yi=cl(i,2)
   zi=cl(i,3)
   Redge=Rmax-SQR((xi-xcen)^2+(yi-ycen)^2+(zi-zcen)^2)
   ni=ni+1
   FOR L=1 TO nclass-1
     rHigh=rL(L+1)
     rLow=rL(L)
     IF Redge>rLow THEN
       cen(L)=cen(L)+1
        FOR j=1 TO 200
         rij=SQR( (xi-cl(j,1))^2+(yi-cl(j,2))^2+(zi-cl(j,3))^2 )
         IF (rLow=<rij) AND (rij<rHigh) THEN dm(L)=dm(L)+1
        NEXT j
     END IF
   NEXT L
  NEXT i
  FOR L=1 TO nclass-1
      IF cen(L)>0 THEN
       dm(L)=dm(L)*(d1/2!)^3!/cen(L)/  (rL(L+1)^3!-rL(L)^3!)
       END IF
      PRINT rL(L),cen(L),dm(L)
 NEXT L
 END SUB

 SUB massR(cl(),gc,rrL(),cm3(),ig,nclass) STATIC
 PRINT " getting mass in each sphere radius class"
 xcen=cl(ig,1)
 ycen=cl(ig,2)
 zcen=cl(ig,3)
  FOR L=1 TO nclass-1
     cm3(L)=0
     FOR j=1 TO gc
      rij=SQR( (xcen-cl(j,1))^2+(ycen-cl(j,2))^2+(zcen-cl(j,3))^2 )
      IF  (rij=<rrL(L)) THEN cm3(L)=cm3(L)+1
     NEXT j
    cm3(L)=cm3(L)/gc
 NEXT L
 END SUB


 SUB sample2d(rncl(),npoints,xh,yh,Rmax) STATIC
 FOR i=1 TO npoints
 10 x=xh+Rmax*(2*RND-1!)
    y=yh+Rmax*(2*RND-1!)
    IF(POINT(x,y)=30) THEN GOTO 10
       rncl(i,1)=x
```

```
        rncl(i,2)=y
        rncl(i,3)=0
        PSET(x1,1)
        PSET(1,y1)
  NEXT i
  END SUB

  SUB countpix(rpix,a) STATIC
  ' -- generate a test pattern of 36 random circles to calibrate the  ---
  ' -- projected area measurments                                      ---
     CLS
     rpix=0
     FOR i=1 TO 6
      x=i*2*a+RND*a+10+a
      FOR ii=1 TO 6
       y=ii*2*a+RND*a+5+a
       FOR j=x-a/2-1 TO x+a/2+1
           FOR jj=y-a/2-1 TO y+a/2+1
            DIST=SQR((j-x)^2+(jj-y)^2)
             IF(DIST<a/2!) THEN
               PSET(j,jj)
               rpix=rpix +1
             END IF
           NEXT jj
       NEXT j
      NEXT ii
    NEXT i
   rpix=rpix/36!
   PRINT rpix
 END SUB


 SUB clusgrph(cl(),gc,a,ig3,xh,yh,pix) STATIC
     CLS
    xcen=cl(ig3,1)-xh
    ycen=cl(ig3,2)-yh
    pix=0
    FOR i=1 TO gc
     xii=cl(i,1)-xcen
     yii=cl(i,2)-ycen
     FOR j=xii-a/2-1 TO xii+a/2+1
       FOR jj=yii-a/2-1 TO yii+a/2+1
        DIST=SQR((j-xii)^2+(jj-yii)^2)
         IF(DIST<a/2!) THEN
          IF(POINT(j,jj)=30) THEN
            PSET(j,jj)
            pix=pix+1
          END IF
        END IF
       NEXT jj
    NEXT j
   NEXT i
END SUB

SUB rotate(cl(),gc) STATIC
PRINT " ROTATION ABOUT THE Z, X, Y AXIS"
'          (corresponds to 3, 1, 2 axis)
   thtx=RND*6.28318
```

```
    thty=RND*6.28318
    thtz=RND*6.28318
    FOR i= 1 TO gc
    x=cl(i,1)*COS(thtz)-cl(i,2)*SIN(thtz)
    y=cl(i,1)*SIN(thtz)+cl(i,2)*COS(thtz)
    cl(i,1)=x
    cl(i,2)=y
    NEXT i
    FOR i= 1 TO gc
    y=cl(i,2)*COS(thtx)-cl(i,3)*SIN(thtx)
    z=cl(i,2)*SIN(thtx)+cl(i,3)*COS(thtx)
    cl(i,2)=y
    cl(i,3)=z
    NEXT i
    FOR i= 1 TO gc
    z=cl(i,3)*COS(thty)-cl(i,1)*SIN(thty)
    x=cl(i,3)*SIN(thty)+cl(i,1)*COS(thty)
    cl(i,3)=z
    cl(i,1)=x
    NEXT i
END SUB

SUB center(cl(),ig,rg,gc,Rmax,d1,aspect) STATIC
PRINT " getting  center particle, IG3"
    xm=0 :  ym=0 :  zm=0
    sx=0  :  sy=0  :  sz=0
    xy=0  :  xz=0  :  yz=0
    s1=d1*d1/20! ' half of the Inertia of a single primary
    FOR i= 1 TO gc
      xm=xm+cl(i,1)
      ym=ym+cl(i,2)
      zm=zm+cl(i,3)
    NEXT i
    xm=xm/gc : ym=ym/gc : zm=zm/gc
    rm=10^8
    Rmax=0
    FOR i= 1 TO gc
      x=cl(i,1)-xm
      y=cl(i,2)-ym
      z=cl(i,3)-zm
      sx=sx+x*x+s1   :   sy=sy+y*y+s1  : sz=sz+z*z+s1
      xy=xy+x*y   :   xz=xz+x*z  : yz=yz+y*z
      rrr=SQR(x*x+y*y+z*z)
      IF(rrr<rm) THEN
         rm=rrr
         ig=i
      END IF
     IF(rrr+d1/2!>Rmax) THEN Rmax=rrr+d1/2!
    NEXT i
    xx=sy+sz
    yy=sx+sz
    zz=sx+sy
    CALL cubic(xx,yy,zz,xy,xz,yz,smax,smid,smin)
    stot=(smax+smid+smin)/2!
    Rgmin=SQR(smin/gc)
    Rgmax=SQR(smax/gc)
    aspect=Rgmax/Rgmin
    rg=SQR(stot/gc)
```

```
      PRINT sx,sy,sz
      PRINT xy,xz,yz
      PRINT "  Rgmax     Rgmin          aspect          rg          rmax "
      PRINT USING "#####.###";Rgmax,Rgmin,aspect,rg,Rmax
      IF Rmax>215 THEN WRITE #4, "scale too large"
  END SUB

  SUB logfit(x(),y(),a,b,xmin,xmax,nclass) STATIC
  PRINT " getting fit to data"
  ' Fit yfit=a*x^b, IGNORE NEGATIVE DATA, OR DATA SMALLER THAN 1e-10
      sumx=0
      sumy=0
      sumxx=0
      sumxy=0
      npts=0
      FOR L=1 TO nclass-1
        IF(x(L)>xmin) THEN
         IF(x(L)<xmax) THEN
          IF(y(L)>1E-10) THEN
            sumx=sumx+LOG(x(L))
           sumxx=sumxx+( LOG(x(L)) )^2!
            sumy =sumy +LOG(y(L))
           sumxy=sumxy+LOG(y(L))*LOG(x(L))
            npts=npts+1
           END IF
          END IF
        END  IF
      NEXT L
      IF npts>1 THEN
      b=(npts*sumxy-sumx*sumy)/(npts*sumxx-sumx^2!)
      ELSE
      b=100!
      END IF
  END SUB

  SUB logplot(x(),y(),x0,y0,xmax,ymax,isym)  STATIC
  ' all x axis points are divied by xb
  DEFINT G-Q
  i0=60
  imax=500
  j0=340
  jmax=40
  xs=(imax-i0)/(LOG(xmax)-LOG(x0))
  ys=(jmax-j0)/(LOG(ymax)-LOG(y0))
  lineflag=0
  FOR i = 1 TO 30
    ix=xs*(LOG(x(i)+1E-20)-LOG(x0))+i0
    iy=ys*(LOG(y(i)+1E-20)-LOG(y0))+j0
    IF ix>=i0 AND ix=<imax AND iy>=jmax AND iy=<j0 THEN
       lineflag=lineflag+1
      IF lineflag >1 THEN LINE -(ix,iy)
      CIRCLE(ix,iy),isym,33
    END IF
  NEXT i
  END SUB


  SUB logaxes(x0,y0,xmax,ymax,xlab$,ylab$) STATIC
```

```
' coordinates of graph box on screen:
DEFINT G-Q
' scaling of axis
i0=60
imax=500
j0=340
jmax=40
xs=(imax-i0)/(LOG(xmax)-LOG(x0))
ys=(jmax-j0)/(LOG(ymax)-LOG(y0))
LINE (i0,j0)-(i0,jmax)
LINE (i0,jmax)-(imax,jmax)
LINE (imax,jmax)-(imax,j0)
LINE (imax,j0)-(i0,j0)
' tick marks ticks per decade
'first find the lowest decade,put in 10 ticks
lowdec= INT(LOG(x0)/LOG(10#))
maxdex=INT(LOG(xmax)/LOG(10#))
FOR idec=0 TO 10
 FOR i = 1 TO 10
  x=i*10^(lowdec+idec)
  ix=xs*(LOG(x)-LOG(x0))+i0
  IF ix>i0 AND ix <imax THEN
    Ltic=4
   IF i=1 THEN Ltic=11
   LINE (ix,j0)-(ix,j0-Ltic)
   LINE (ix,jmax)-(ix,jmax+Ltic)
  END IF
 NEXT i
NEXT idec
lowdec= INT(LOG(y0)/LOG(10#))
maxdex=INT(LOG(ymax/y0)/LOG(10!))+lowdec
FOR idec=0 TO 10
 FOR j = 1 TO 10
  y=j*10^(lowdec+idec)
  iy=ys*(LOG(y)-LOG(y0))+j0
  IF iy<j0 AND iy >jmax THEN
   Ltic=4
   IF j=1 THEN Ltic=11
   LINE (i0,iy)-(i0+Ltic,iy)
   LINE (imax,iy)-(imax-Ltic,iy)
  END IF
 NEXT j
NEXT idec

' axis numbering
LOCATE 23,6
DrawText STR$(x0)
LOCATE 23,61
DrawText  STR$(xmax)
LOCATE 22,3
DrawText STR$(y0)
LOCATE 3,3
DrawText STR$(ymax)
LOCATE 24,31
DrawText xlab$
LOCATE 10,2
DrawText ylab$
END SUB
```

```
 SUB rclasses(rL(),rrL(),d1,rg,nclass) STATIC
 PRINT " getting radius classes"
 rL(1)=0
 rL(2)=d1/2!
 rL(3)=d1*1!
 rL(4)=d1*1.5
 FOR L=5 TO nclass
  rL(L)=rL(4)*EXP( (L-4)/(nclass-4) *LOG(2!*rg/rL(4))   )
 NEXT L
 FOR L=1 TO nclass-1
  rrL(L)=(rL(L)+rL(L+1))/2!
  PRINT L,rL(L),rrL(L)
 NEXT L
 END SUB

 SUB sample3d(cl(),rncl(),gc,d1,npoints) STATIC
    FOR i=1 TO npoints
1    j=gc*RND+.499999
     IF(j=0) THEN GOTO 1
     CALL direction(dx,dy,dz)
     r=RND^.33333 *d1/2
     rncl(i,1)=cl(j,1)+dx*r
     rncl(i,2)=cl(j,2)+dy*r
     rncl(i,3)=cl(j,3)+dz*r
  NEXT i
END SUB

SUB direction(dx,dy,dz) STATIC
   dz=2*RND-1
   r=SQR(1-dz*dz)
   theta=RND*6.28318
   dx=r*COS(theta)
   dy=r*SIN(theta)
END SUB

SUB med(x(),n,xmed,sigx) STATIC
' resorts the real vector x so that x(1) is the largest value.
' return with the median and standard deviation about the median
IF n=1 THEN
   xmed=x(1)
   sigx=0
ELSE
'  First, sort:
   FOR j=1 TO n
    FOR i=1 TO n-1
     IF x(i)<x(i+1) THEN
        temp=x(i+1)
        x(i+1)=x(i)
        x(i)=temp
     END IF
   NEXT i
  NEXT j
' Next, find the median
   i1=n/2!-.499
   i2=n/2!+.501  ' remember: BASIC rounds integers
   xmed=(x(i1)+x(i2))/2!
   sigx=0
```

```
   FOR i=1 TO n
    sigx=sigx+(xmed-x(i))^2!/(n-1)
   NEXT i
   sigx=SQR(sigx)
 END IF
 END SUB

 SUB mean(x(),n,xmean,sigx) STATIC
 ' resorts the real vector x so that x(1) is the largest value.
 ' return with the median and standard deviation about the median
 IF n=1 THEN
   xmean=x(1)
   sigx=0
  ELSE
    xmean=0
    FOR i=1 TO n
       xmean=xmean+x(i)/n
    NEXT i
    sigx=0
    FOR i=1 TO n
     sigx=sigx+(xmean-x(i))^2!/(n-1)
    NEXT i
    sigx=SQR(sigx)
 END IF
 END SUB

 SUB cubic(xx,yy,zz,xy,xz,yz,y1,y2,y3) STATIC
 'given the moments and products of inertia
 ' for a body, find the three principle moments
 ' of inertia, y1,y2,y3.
 ' This is solved by getting the Eigenvalues of
 ' the inertia matrix
 ' The determinant of the 3x3 matix [inertia]-Iy is
 ' y^3+cp y^2+cq y+cr=0
  Pi!=3.14159265#
 ' nondimensionalize by the trace
  trace=(xx+yy+zz)
  cp=-1!
  cq=-(xz*xz+xy*xy+yz*yz-xx*zz-xx*yy-yy*zz)/trace^2
  cr=-(xx*yy*zz-2*xy*xz*yz-xy*xy*zz-xz*xz*yy-yz*yz*xx)/trace^3
  a=cq-cp*cp/3!
  b=(2!*cp^3-9!*cp*cq+27!*cr)/27!
  rad=2!*SQR(-a/3!)
  IF rad=0 THEN
    ctheta=0
   ELSE
    ctheta=3*b/a/rad
  END IF
  IF ctheta=0 THEN
     th=Pi!/6!
   ELSE
    IF ctheta>1 THEN ctheta=1
    IF ctheta<-1 THEN ctheta=-1
    IF ctheta>0 THEN
      tant=SQR(1-ctheta^2)/ctheta
       th=ATN(tant)/3!
       ELSE
      tant=SQR(1-ctheta^2)/ctheta
```

```
        th=Pi! -ATN(tant)/3!
      END IF
    END IF
    y1=trace*(3!*rad*COS(th)-cp)/3!
    y2=trace*(3!*rad*COS(th+2!/3!*Pi!)-cp)/3!
    y3=trace*(3!*rad*COS(th+4!/3!*Pi!)-cp)/3!
  ' sort so y1 is the largest, y3 the smallest
    IF y2>y1 THEN
      ytemp=y2
      y2=y1
      y1=ytemp
    END IF
    IF y3>y2 THEN
      ytemp=y3
      y3=y2
      y2=ytemp
    END IF
    IF y2>y1 THEN
      ytemp=y2
      y2=y1
      y1=ytemp
    END IF
  END SUB
```

```
12                                  'Sample Batch Input File
cit:cca00.xyz
cit:cca00.out
2000,40,.125,3
cit:cca01.xyz
cit:cca01.out
2000,40,.125,3
cit:cca6.xyz
cit:cca6.out
2000 ,40,.125,3
cit:cca7.xyz
cit:cca7.out
2000 ,40,.125,3
cit:cca8.xyz
cit:cca8.out
2000 ,40,.125,3
cit:cca9.xyz
cit:cca9.out
2000 ,40,.125,3
cit:cca10.xyz
cit:cca10.out
2000 ,40,.125,3
cit:cca11.xyz
cit:cca11.out
2000 ,40,.125,3
cit:cca12.xyz
cit:cca12.out
2000 ,40,.125,3
cit:cca13.xyz
cit:cca13.out
2000 ,40,.125,3
cit:cca14.xyz
cit:cca14.out
2000 ,40,.125,3
cit:cca15.xyz
cit:cca15.out
2000 ,40,.125,3
```

"CIT:beta0,.1.bat","02-01-1991" **Sample Batch Output File**

file	gc	rg3/d1	rg2/Rg3	area	coord#	aspect3	aspect2	DfC3	DfC2	Dfm3	Dfm2"
cca00.xyz	501.0	17.7	0.87	0.55	1.99	1.17	1.20	2.22	1.83	2.61	1.81
cca01.xyz	1024.0	22.8	0.94	0.50	2.06	1.45	1.52	2.40	1.79	2.31	1.88
cca6.xyz	108.0	11.2	0.78	0.61	1.56	1.56	1.51	1.80	1.66	2.14	1.90
cca7.xyz	108.0	14.2	0.90	0.70	1.77	2.15	3.87	1.63	1.34	1.85	1.39
cca8.xyz	108.0	10.5	0.84	0.60	1.75	1.34	2.11	1.88	1.59	2.15	1.82
cca9.xyz	108.0	12.1	0.86	0.74	1.59	2.07	2.29	1.84	1.58	2.04	1.94
cca10.xyz	108.0	11.6	0.76	0.65	1.55	1.80	1.76	1.84	1.65	2.21	1.90
cca11.xyz	726.0	24.1	0.88	0.55	1.98	1.28	1.38	2.01	1.69	2.11	1.67
cca12.xyz	726.0	27.0	0.87	0.59	1.91	1.32	1.40	1.92	1.68	2.25	1.95
cca13.xyz	726.0	33.6	0.82	0.57	1.98	1.78	1.94	1.83	1.60	2.14	1.61
cca14.xyz	726.0	39.3	0.88	0.67	2.05	1.52	1.31	1.70	1.51	1.86	1.66
cca15.xyz	726.0	27.3	0.87	0.61	1.93	1.39	1.85	2.00	1.77	2.17	1.92

Sample Output File for an Individual Cluster

cit:cca00.xyz

gc	2Rg3/d1	Dcorr 3-d	Dcum 3-d	Aspect
501.000	17.733	2.222	2.606	1.167

Dcum2	Dcorr2	area2	rg2	asp2
1.935	1.720	0.562	0.867	1.226
1.728	1.875	0.532	0.863	1.164
1.894	1.797	0.542	0.936	1.248
1.709	1.856	0.554	0.875	1.176
median values, sigs:				
1.811	1.827	0.548	0.871	1.204
0.115	0.072	0.013	0.038	0.040

2r/d1	Corr3(2r/d1)	Corr2(2r/d1)	m3(2r/d1)	m2(2r/d1)
0.50000	1.19000	1.60308	0.00200	0.00225
1.50000	0.07035	0.19883	0.00200	0.00900
2.50000	0.04572	0.11365	0.00300	0.02125
3.25039	0.03351	0.08059	0.00500	0.03350
3.79296	0.03348	0.07479	0.00900	0.04375
4.42610	0.02231	0.06063	0.01700	0.05875
5.16492	0.02248	0.04981	0.02500	0.08150
6.02708	0.01994	0.04085	0.04400	0.10825
7.03315	0.01769	0.03372	0.06800	0.14125
8.20716	0.01558	0.02795	0.10600	0.18425
9.57713	0.01358	0.02317	0.15200	0.24300
11.17580	0.01378	0.02006	0.21900	0.33375
13.04132	0.01322	0.01584	0.31300	0.43150
15.21824	0.01197	0.01231	0.41800	0.55200
17.75854	0.00940	0.00922	0.56300	0.67875
20.72289	0.00700	0.00625	0.70600	0.83100
24.18205	0.00434	0.00296	0.86900	0.94000
28.21864	0.00176	0.00057	0.96100	0.98450
32.92904	0.00000	0.00000	0.99900	1.00000

APPENDIX B PROGRAMS USED TO COMPUTE THE STOKES DRAG ON CLUSTERS

These files (FORCE.FOR, RNDSCALE.FOR, RANDOM.FOR and RADGYR.FOR) were linked and used to generate the results used in "StokesDrag on Self-Similar Clusters", version of Feb 1989.

```
      PROGRAM RNDSCALE
C PROGRAM TO COMPUTE DRAG FOR A 3-d CLUSTER
c  Version of Feb 8 1989
C  This program uses the assumption of self-similarity to compute
C the dynamic shape factor of aggregates of different sizes.  A basic
C unit of GC coordinates on an MxM or MxMxM lattice is read in and used
C as the basic structure for a selfsimilar fractal cluster.  We can
C introduce randomness by using one of NPERM configurations of the basic
C unit.  At each scale up, the cluster mass grows by a factor GC and
C its radius increases by a factor GC^(1/d), d=fractal dimension
c  The program runs in two modes:
c     1) regular- for RAND<0 .In this case the cluster is exactly
c                        self similar.
c     2) irregular- forRAND>=0  In this case the form of the basic
c                cluster may change randomly from scale to scale.
c    The program will perform the calculations for NFILE clusters
c and output the ensemble mean quantities as well as the NFILE
c data sets for each cluster of the ensemble.
c
c input variables:
c    BATCH   name of file containing the batch job information:
c       # of jobs NJOB, INNAME(1)..... INAME (NJOB)
c    INNAME  file containning the following information:
c    NITT    number of itterations used to compute the drag
c    GC      number of units in a basic structure
c    DP      primary particle diameter
c    NPERM   number of permutations allowed of the basic structure
c    NLL     number of scale levels condidered
c    DF      fractal or Hausdorf dimension
c    RAND    seed for random number (if RAND<0, the cluster is regular)
c    NFILE   # of clusters in the ensemble to be averaged
c    OUTNAME output file name (read in NFILE times for NFILE units)
c       CLUSTER(I,i,j) coordinates(I=1,2,3) for all the particles in the
c           basic unit (i=1..GC) for the NPERM variations of shape.
c output variables:
c    LL      current scale level (1<LL<NLL)
c    KDYN    shape factor (hydrodynamic radius/volume radius)
c    BT      length scale factor between largest and smallest scales
c    GL      number of primary particles in the current cluster
c    BETA    KSM/KDYN  (see notes below)
c    RGRH    radius of gyration/hydrodynmic radius
c variables passed to the subroutine FORCE
c     CL(I,i)=CLUSTER(I,i,j) for some particular j
```

```
c    DPL(i)  hyrdrodynamic diameter of a subcluster i at scale LL
c   GC,NITT,BT  as above
c    UX,UY,UZ  components of the cluster velocity U
c     TOTX...Z  sum DPL(i)*Vi where Vi is the subcluster virtual velocity
c          ( force X =3 PI VISC TOTX)
c internel variables:
c   NEXTDPL   DPL calculated for use at next highest scale level
c   RG        radius of gyration of  a subcluster
c   NEXTRG    RG calculated at the next scale level
c    KSM         outer radius / volume equivalent radius =N^(1/d-.333..)
c   ALF      mass scale factor = FLOAT(GC)
c   SBETA,SKDYN,SRGRH  accumulation registers for ensemble averaging
c   RANDOM    random integer generating function
c   IA,IC,MMAX parameters passed to RANDOM (see DATA statement below)
c    I,J,K,L,TRIAL,IFILE,II   subscripts.
c
C
*****************************************************************
C
C
    REAL CLUSTER,CL,DPL,NEXTDPL,RG,NEXTRG
    REAL BT,DP,KDYN,KSM,BETA,RGRH
    REAL DF,ALF
    REAL SBETA,SKDYN,SRGRH
    REAL TOTX,TOTY,TOTZ
    REAL UX,UY,UZ
    INTEGER*4 GC,NITT,LL,NLL,GL
    INTEGER*4 RAND,RANDOM,IA,IC,MMAX
    INTEGER NPERM,NJOB
     INTEGER I,J,K,L,TRIAL,NFILE,IFILE,II
    CHARACTER*20 INNAME,OUTNAME,BATCH
c
      DIMENSION CLUSTER(3,30,20),SBETA(22),SKDYN(22),SRGRH(22)
       DIMENSION CL(3,30),DPL(30),NEXTDPL(30),RG(30),NEXTRG(30)
C
         DATA IA/106/,IC/1283/,MMAX/6075/
C       parameters reccommended for the random number generator
c        for a overflow value of 2^20. (integer*4 -> 2^31 but
c       we do not need high resolution, long period random numbers)
c       (see documentaion for RANDOM)
C*****************************************************************
C       Input Data From Keyboard (*) and Coordinate File
C
      WRITE(*,10)
10     FORMAT(' Input batch file name BATCH ')
     READ(*,20) BATCH
20     FORMAT(A)
    OPEN(3,FILE=BATCH,STATUS='OLD')
     READ(3,50) NJOB
C*****************************************************************
C******************  LOOP  THROUGH  NJOB  JOBS  ******************
C*****************************************************************
    DO 9999 JOB=1,NJOB
     READ(3,20) INNAME
```

```
      OPEN(4,FILE=INNAME,STATUS='OLD')
        READ(4,50) NITT
 50      FORMAT(I4)
       READ(4,60) GC
 60      FORMAT(I4)
      ALF=FLOAT(GC)
        READ(4,70) DP
 70      FORMAT(F8.5)
       READ(4,80) NPERM
 80      FORMAT(I4)
       READ(4,90) NLL
 90      FORMAT(I4)
       READ(4,100) DF
 100     FORMAT(F8.3)
       READ(4,110) RAND
 110      FORMAT(I10)
       READ(4,120) NFILE
 120      FORMAT(I10)
       DO 140 II=5,NFILE+5
 C        the last unit number is the average file
        READ(4,130) OUTNAME
 130       FORMAT(A)
       OPEN(II,FILE=OUTNAME,STATUS='NEW')
 140   CONTINUE
 c now read in the cluster.  There will be NPERM variations which
 c can be used later as selected by a random number between 1 and NPERM
       DO 550 J=1,NPERM
       DO 500 I=1,GC
            READ(4,*) CLUSTER(1,I,J),CLUSTER(2,I,J),CLUSTER(3,I,J)
             WRITE(*,*) CLUSTER(1,I,J),CLUSTER(2,I,J),CLUSTER(3,I,J)
 500   CONTINUE
 550   CONTINUE
 C
      CLOSE(4)
 c**********************    finished   input   for   this   JOB   *********
      UX=1
      UY=0
      UZ=0
       U=SQRT(UX*UX+UY*UY+UZ+UZ)
      DO 600 LL=1,NLL
        SBETA(LL)=0.0
        SKDYN(LL)=0.0
        SRGRH(LL)=0.0
 600  CONTINUE
 C - - - - - - - - - - - - - - - - - - - - - - - - - - - - - - - - - - - - - - - - - - - - - -
 C---------------   CALULATIONS   FOR   NFILE   CLUSTERS   ---------------
 C - - - - - - - - - - - - - - - - - - - - - - - - - - - - - - - - - - - - - - - - - - - - - -
      DO 9000 II=1,NFILE
        IFILE=II+4
C         Initialize parameters for the smallest scale subcluster
       BT=1
      GL=GC
       DO 5000 I=1,GC
         DPL(I)=DP
```

```
          RG(I)=DP*.3873
C         the radius of gyration of a primary particle is sqrt(3/20)*DP
 5000    CONTINUE
C         (The first level uses the unscaled cluster moving with unit
C         velocity in the x direction)
c
C                          ------------------------------------------------------
c       Loop through all levels of scale
c                          ------------------------------------------------------
        DO 6000 LL=1,NLL
c       compute the asymptotic high DF shape factor KSM and the
c        volume equivalent diameter
            KSM=FLOAT(GL)**(1/DF-.3333333)
           DVOL=DP*(FLOAT(GL))**.333333
       IF(RAND.LT.0) THEN
C          regular cluster
          DO 5100 I=1,GC
             CL(1,I)=CLUSTER(1,I,II)
             CL(2,I)=CLUSTER(2,I,II)
             CL(3,I)=CLUSTER(3,I,II)
 5100      CONTINUE
         CALL RADGYR(CL,RG,GC,BT,II,NEXTRG)
         CALL FORCE(CL,DPL,GC,BT,UX,UY,UZ,NITT,TOTX,TOTY,TOTZ)
C         Compute the force on the cluster CL
         NEXTDPL(II)=SQRT(TOTX*TOTX+TOTY*TOTY+TOTZ*TOTZ)/U
            KDYN=NEXTDPL(II)/DVOL
           RGRH=NEXTRG(II)/NEXTDPL(II)*2
          DO 5200 J=1,GC
             DPL(J)=NEXTDPL(II)
            RG(J)=NEXTRG(II)
C             for the regular clusters all subclusters are the same
5200       CONTINUE
       ELSE
          DO 5500 TRIAL=1,GC
           RAND=RANDOM(RAND,IA,IC,MMAX)
                J=1+(NPERM)*(1.0*RAND)/(MMAX-1.0)
c           this is a random integer , 1<=J<=NPERM
            WRITE(*,*) LL,TRIAL,J
           DO 5250 I=1,GC
              CL(1,I)=CLUSTER(1,I,J)
              CL(2,I)=CLUSTER(2,I,J)
              CL(3,I)=CLUSTER(3,I,J)
 5250       CONTINUE
         CALL RADGYR(CL,RG,GC,BT,TRIAL,NEXTRG)
         CALL FORCE(CL,DPL,GC,BT,UX,UY,UZ,NITT,TOTX,TOTY,TOTZ)
C          Compute the force on the cluster CL
         NEXTDPL(TRIAL)=SQRT(TOTX*TOTX+TOTY*TOTY+TOTZ*TOTZ)/U
            KDYN=NEXTDPL(TRIAL)/DVOL
           RGRH=NEXTRG(TRIAL)/NEXTDPL(TRIAL)*2
5500       CONTINUE
         DO 5950 J=1,GC
            DPL(J)=NEXTDPL(J)
           RG(J)=NEXTRG(J)
5950       CONTINUE
```

```
        END IF
         BETA=KSM/KDYN
         SRGRH(LL)=SRGRH(LL)+RGRH
          SBETA(LL)=SBETA(LL)+BETA
          SKDYN(LL)=SKDYN(LL)+KDYN
          WRITE(IFILE,5900) LL,KDYN,BT,GL,BETA,RGRH
            WRITE(*,5900) LL,KDYN,BT,GL,BETA,RGRH
5900        FORMAT(/I5,2f10.2,I9,2F12.4)
c       For the next level we need new BT,GL
       GL=GL*GC
          BT=BT*ALF**(1./DF)
6000   CONTINUE
C                          ------------------------------------------------------
c       End of the scaling recursion
c                          ------------------------------------------------------
         WRITE(IFILE,6900)
 6900     FORMAT('  DP',4X,'NITT',2X,'NLL',4X,'INAME     FRACTAL DIM.')
         WRITE(IFILE,7000) DP,NITT,NLL,INNAME,DF
7000        FORMAT(F10.4,2I5,6X,A15,F10.3)
         WRITE(IFILE,7900)
 7900    FORMAT('  GC    NPERM       RAND')
        WRITE(IFILE,8000) GC,NPERM,RAND
 8000     FORMAT( 3I10)
       CLOSE (IFILE)
 9000  CONTINUE
C - - - - - - - - - - - - - - - - - - - - - - - - - - - - - - - - - - - - - - - - - - - - - - - - - - - - - - - - -
C--------  COMPUTATIONS  FOR  NFILE  CLUSTERS  FINISHED----------------
C - - - - - - - - - - - - - - - - - - - - - - - - - - - - - - - - - - - - - - - - - - - - - - - - - - - - - - - - -
      DO 9500 LL=1,NLL
       KDYN=SKDYN(LL)/NFILE
       BETA=SBETA(LL)/NFILE
      RGRH=SRGRH(LL)/NFILE
            BT=(ALF**(1.0/DF))**(LL-1)
      GL=GC**LL
       WRITE(NFILE+5,5900) LL,KDYN,BT,GL,BETA,RGRH
 9500  CONTINUE
     CLOSE (NFILE+5)
C * * * * * * * * * * * * * * * * * * * * * * * * * * * * * * * * * * * * * * * * * * * * * * * * * * * * * * * *
 9999 CONTINUE
C********************  ALL  JOBS  FINISHED  ********************
    CLOSE(3)
   STOP
   END


* * * * * * * * * * * * * * * * * * * * * * * * * * * * * * * * * * * * * * * * * * * * * * * * * * * * * * * * * * *
     SUBROUTINE FORCE(CLUSTER,DPL,GC,BT,UX,UY,UZ,NITT,TOTX,TOTY,TOTZ)
C  This subprogram takes a cluster whose particles have coordinates
C CLUSTER(K,J)*BT and whose hydodynamic diameters are stored in DPL.
c It then computes then computes the quantities TOTX..= sum Vi DPLi
c where Vi is the virtual velocity of particle i and DPLi is the
c hydrodynamic diameter or particle i. This quantity is proportiional
c to the force on the cluster in Stokes flow.  The computations are
c done for a cluster velocity of UX,UY,UZ.
```

```
C     November 2 1988 program by S. Rogak
**********************************************************************
C
      REAL CLUSTER,V,TXX,TXY,TXZ,TYY,TYZ,TZZ,DPL
C     cluster coordinates, virtual velocities and interaction tensor
      REAL A
C     primary particle hydrodynamic radius.
      REAL X,Y,Z
C     general coordinates of a particle relative to particle #1 or central
c          particle
      REAL F,G,H
C     intermediate results used in computing the interaction tensor TXX..
      REAL SX,SY,SZ,TOTX,TOTY,TOTZ,ERR,ERRX,ERRY,ERRZ
C     accumulated sums of virtual velocities used in computing interactions
      REAL UX,UY,UZ,BT
C     velocity of cluster, length scaling of coordinates
      INTEGER GC,ITT,NITT
C     number in cluster,current and maximum number of itterations,
      INTEGER I,J,K,L
C     general particle subscripts
c
        DIMENSION CLUSTER(3,30),V(3,30),TXX(30,30)
        DIMENSION TXY(30,30),TXZ(30,30),TYY(30,30)
       DIMENSION TYZ(30,30),TZZ(30,30)
      DIMENSION ERR(30),DPL(30)
C          ---------------------------------------------------------
       WRITE(*,*) ' in FORCE '
C     Compute the interaction tensor Tij; V @ i =Tij*V@j
      DO 3900 I=1,GC
       DO 3800 J=1,GC
        IF(I.EQ.J) THEN
          TXX(I,J)=0
            TXY(I,J)=0
            TXZ(I,J)=0
            TYY(I,J)=0
            TYZ(I,J)=0
            TZZ(I,J)=0
       ELSE
            X=(CLUSTER(1,I)-CLUSTER(1,J))*BT
            Y=(CLUSTER(2,I)-CLUSTER(2,J))*BT
            Z=(CLUSTER(3,I)-CLUSTER(3,J))*BT
C         the distances between points are scaled up by BT(LL)
             R=SQRT(X**2+Y**2+Z**2)
C         compute intermediate quantities.
C           note that the effective particle radius is A=DPL(J)/2
           A=DPL(J)/2.0
              F=-.5*A**2/R**4   *   (A/R -3*R/A)
             G=-.5*A/R**3   *   ( (A/R)**2 + 3)
          H=F+G/2
c         compute the 6 independent components of T
              TXX(I,J)=F*X**2  -  G*(Y**2+Z**2)/2
              TYY(I,J)=F*Y**2   -   G*(X**2+Z**2)/2
              TZZ(I,J)=F*Z**2  -  G*(X**2+Y**2)/2
            TXY(I,J)=X*Y*H
```

```
            TXZ(I,J)=X*Z*H
            TYZ(I,J)=Y*Z*h
        END IF
 3800    CONTINUE
 3900   CONTINUE
 C
          write(*,*) ' Tij computed'
 C - - - - - - - - - - - - - - - - - - - - - - - - - - - - - - - - - - - - - - - - - - - - - - - - - - - - - - - - - - - -
 c       COMPUTE KDYN
 C   Start by guessing the virtual velocity of particle #1
        V(1,1)=UX
        V(2,1)=UY
        V(3,1)=UZ
       DO 4800 K=2,GC
         DO 4600 ITT=1,NITT
          DO 4400 I=K,1,-1
         SX=0
            SY=0
            SZ=0
          DO 4300 L=1,K
                SX=SX+TXX(I,L)*V(1,L)+TXY(I,L)*V(2,L)+TXZ(I,L)*V(3,L)
                SY=SY+TXY(I,L)*V(1,L)+TYY(I,L)*V(2,L)+TYZ(I,L)*V(3,L)
                SZ=SZ+TXZ(I,L)*V(1,L)+TYZ(I,L)*V(2,L)+TZZ(I,L)*V(3,L)
 4300       CONTINUE
 c  If the velocity field at I due to the other particles in greater
 c than the unit cluster velocity then the itteration scheme becomes
 c unstable.  It can be made stable by reducing the correction to the
 c velocity of particle I
           IF(ABS(SX).GT.1.) SX=SX/ABS(SX)
             IF(ABS(SY).GT.1.) SY=SY/ABS(SY)
             IF(ABS(SZ).GT.1.) SZ=SZ/ABS(SZ)
           ERRX=UX-SX-V(1,I)
             ERRY=UY-SY-V(2,I)
             ERRZ=UZ-SZ-V(3,I)
             ERR(I)=SQRT(ERRX**2+ERRY**2+ERRZ**2)
             IF(ERR(I).GT.1.) WRITE(*,*) K,ITT,I,ERR(I)
           V(1,I)=UX-SX
             V(2,I)=UY-SY
             V(3,I)=UZ-SZ
 4400      CONTINUE
 4600      CONTINUE
 4800    CONTINUE
 C      next add up the particle virtual velocities
        TOTX=0
           TOTY=0
           TOTZ=0
         DO 4900 I=1,GC
            TOTX=TOTX+V(1,I)*DPL(I)
              TOTY=TOTY+V(2,I)*DPL(I)
              TOTZ=TOTZ*V(3,I)*DPL(I)
 4900      CONTINUE
       write(*,*) ' finished FORCE'
    RETURN
    END
```

```
C     ------------------------------------------------------------
      SUBROUTINE RADGYR(CL,RG,GC,BT,I,NEXTRG)
C       computes the radius of gyration of a cluster with coordinates
C         (CL(1,J)*BT,CL(2,J)*BT,CL(3,J)*BT).  BT is a scale factor depending
c       on the cluster size .  Each subcluster has a mass GL/GC.  The
c       result is placed in NEXTRG(I). Called by RNDSCALE.FOR
c        Feb. 8, 1989  Steven N. Rogak
c-------------------------------------------------------------------
        REAL CL(3,30),RG(30),BT,NEXTRG(30)
      INTEGER GC,I,J,K
      REAL INERTIA,X0,Y0,Z0,SR
C First find the centroid of the cluster, assuming that the centroid of
c the subclusters are at the points given by CL.
      X0=0
      Y0=0
      Z0=0
      DO 100 J=1,GC
         X0=X0+CL(1,J)/GC
         Y0=Y0+CL(2,J)/GC
         Z0=Z0+CL(2,J)/GC
 100  CONTINUE
C Next find the inertia of the cluster
      INERTIA=0
      DO 200 J=1,GC
                SR=(CL(1,J)-X0)**2+(CL(2,J)-Y0)**2+(CL(3,J)-Z0)**2
         INERTIA=INERTIA+RG(J)*RG(J)+SR*BT*BT
 200  CONTINUE
C The radius of gyration :
      NEXTRG(I)=SQRT(INERTIA/GC)
     RETURN
     END

      INTEGER*4 FUNCTION RANDOM(IRAND,A,C,MMAX)
C This routine uses a linear congruential generator to produce a
c random integer between 0 and MMAX. The parameters are obtained
c from Press,Flannery,Teukolsky and Vetterling NUMERICAL RECIPES
c in C page 211.  The overflow integer on the IBM fortran is
c 2^31 for INTEGER*4.
     INTEGER*4 IRAND,MMAX,A,C
C If integer*4 arthmatic is used then the following values of
c parameters are reccommended:a=4096  mmax=714025,  c=150889
      IRAND=IRAND*A+C
       RANDOM=IRAND-(IRAND/MMAX)*MMAX
     END
c OR                    a=9301 mmax=233280  c=49297
```

APPENDIX C

IMAGE PROCESSING

SOFTWARE

Transmission electron micrograph negatives of agglomerates were placed on a light-box. A video camera mounted above the light box was used to capture the image. Camera focus was adjusted while observing the live image on the Macintosh II screen, using the program Image. Once the focus was determined, the magnification was calibrated by placing a ruler in the image.

Particle lengths and areas were measured within Image, as it provides a convenient means of magnifying the image. Particles were also thresholded using this software package. First, the boundary of the agglomerate was highlighted manually using the "Pixel-Paint" tools that are built into Image. This process was tedious, requiring at least ten minutes per particle, but resulted in significantly more reproducible and accurate area measurements than any of the automated filtering procedures available with TCL-Image.

Thresholded (binary) images were saved in the Macintosh PICT format on 3.5" diskettes, compressed with STUFFIT. Structural measurements, including fractal dimensions, were performed by macros written in TCL-Image. The source code was included in a Department of Energy report [1] and is also available on the diskette "TCL-Image Programs." The program TCL Image and its documentation are available from the Material Science research group at Caltech. It should be noted that macros written in TCL-Image are extremely slow (10 minutes per image on a Mac-II), although there are many fast built-in image processing functions. Furthermore, recent versions of Image have a macro language that would allow similar measurements to be made in a more user-friendly environment.

---

[1] R.C. Flagan, X-M Li, B. Wong and S.N.Rogak (1990). Final report for the Department of Energy Grant No. DE-FG22-90PC90286.

DATABASE

Results from image processing for the first set of mobility experiments were entered into the Macintosh application IGOR, file name "summary data," on the "Drag-Paper" diskette. A printout of this data base was included with the DOE report[1] . Results from the second set of TiO_2 experiments are stored in the IGOR file "SEM/TEM data."

A statistical summary of the first data base is given below for the 13 TEM grids analyzed. The mean value, sample size n, standard deviation σ, and 95% confidence interval are given for each measurement. Note that other measurements included in the data base are not summarized below[1].

Skeleton (L_{sk} normalized by R_g)

grid	mean	n	σ	95%int
1	19.3	13	5.3	2.88
2	20.2	10	10.7	6.63
3	24	11	7.1	4.20
4				
5	15	20	4.2	1.84
6	14.3	15	6.1	3.09
7	7.4	6	4.9	3.92
8	15	12	7.9	4.47
9	12	10	3.7	2.29
11	11	9	4.7	3.07
12	12	14	4	2.10
13	18	17	5.8	2.76
Avg	15.29	12.5	5.854	3.436
SD	4.762	3.93	2.065	

Contour (normalized by R_g)

mean	n	σ	95%int
27	13	5.2	2.83
22	10	4.6	2.85
27	11	4.6	2.72
20	20	3.2	1.40
17	15	4.4	2.23
13	6	1	0.80
13	12	1.9	1.08
15	10	3.4	2.11
18	9	3.7	2.42
19	14	3.7	1.94
20.6	18	7.6	3.51
19.23	12.5	3.936	2.1048
4.826	4.06	1.727	

aspect ratio

grid	mean	n	σ	95%int
1	1.94	13	1	0.54
2	1.73	12	0.61	0.35
3	1.93	11	0.72	0.43
4	1.12	11	0.2	0.12
5	1.71	20	0.48	0.21
6	2.03	15	0.76	0.38
7	1.56	7	0.43	0.32
8	1.43	18	0.34	0.16
9	2.03	16	1.28	0.63
11	1.77	21	0.68	0.29
12	1.82	14	0.61	0.32
13	1.9	56	0.57	0.15
Avg	1.73	18.3	0.61	0.30
SD	0.27	13.2	0.28	0.15

D_{sq}

mean	n	σ	95%int
1.74	13	0.12	0.065
1.83	10	0.1	0.062
1.76	11	0.12	0.071
1.73	20	0.086	0.038
1.64	15	0.15	0.076
1.95	6	0.036	0.029
1.96	12	0.046	0.026
1.668	10	0.141	0.087
1.63	9	0.133	0.087
1.59	14	0.077	0.040
1.66	17	0.105	0.050
1.74	12	0.01	0.057
0.13	4.14	0.039	

d_{fine}(nm)				95%int
grid	mean	n	σ	%
1	8.7	9	2.9	22
2	7.2	12	1.5	12
3	8.9	11	2.8	19
4				
5	24	13	5.1	12
6	20	13	6	16
7	223	6	105	38
8	36	7	25	51
9	17	9	8.5	33
11	21	3	7.4	40
12	28	8	6.5	16
13	23	1	7	60
Avg	37.9	8.36	16.2	30
SD	62.0	3.93	30.1	

d_{coarse}(nm)			95%int
mean	n	σ	%
32	11	8	15
25	12	6.5	15
27	11	4.9	11
54	13	12	12
108	13	37	19
321	6	43	11
86	7	13	11
151	9	22	10
91	3	23	29
81	8	17	15
64	1	19	58
94.6	8.6	18.7	19
84.15	4.0	12.20	

D_{tile}				
grid	mean	n	σ	95%int
1	1.67	13	0.08	0.043
2	1.76	10	0.079	0.049
3	1.69	11	0.051	0.030
4				
5	1.68	20	0.056	0.025
6	1.65	15	0.06	0.030
7	1.86	6	0.027	0.022
8	1.82	12	0.051	0.029
9	1.64	10	0.075	0.046
11	1.54	9	0.062	0.041
12	1.58	14	0.061	0.032
13	1.59	17	0.094	0.045
Avg	1.681	12.4	0.062	0.035
SD	0.1047		4.14	0.0182

D_{cont}			
mean	n	σ	95%int
1.36	13	0.06	0.033
1.3	10	0.09	0.056
1.31	11	0.113	0.067
1.27	20	0.055	0.024
1.27	15	0.051	0.026
1.18	6	0.023	0.018
1.23	12	0.161	0.091
1.24	10	0.049	0.030
1.37	9	0.054	0.035
1.37	14	0.05	0.026
1.38	17	0.091	0.043
1.292	125	0.074	0.0417
0.067	4.14	0.0405	

APPENDIX D
CHARGING OF PROLATE SPHEROIDS

The charging theory developed by Laframboise and Chang (1977) was implemented in the program Shape.f, listed below. This function was called by Prochrg.f, which is used to calculate the steady-state charge distribution on a particle. The Fuchs attachment coefficients are modified by the factor calculated in Shape. The complete code is stored in the SUN directory aeolus\home\steve\charge. Copies of the code are also stored on the 3.5" Macintosh diskette titled " spheroid charge".

```
      REAL FUNCTION SHAPE(DMOB,D1,N,Q,IS,LION)
C     consider a prolate spheroid with mobility diameter DMOB,
c     minor axis D1, aspect ratio N, carrying Q (positive or neg.)
c     charges. The attachment rate to the spheroid will be different
c     from that of the sphere (diam. DMOB) by a factor SHAPE, according
c     to the theory of LAframboise and Chang, J. Aerosol Sci. 1977.
c     The ion of interest has sign IS (1=pos., 2=neg)
c     note that dmob is in microns and lion in meters
      IMPLICIT UNDEFINED(A-Z)
      DOUBLE PRECISION DMOB,I,IPHI,K,NS,DPHI,PHI
      DOUBLE PRECISION PHIMOB,KMOB,IMOB
      REAL*8 LION(2),D1,N,SIGN
      INTEGER IS,Q
      SIGN=-(IS-1.5)/ABS(IS-1.5)
      K=8./3.*LION(IS)/D1
      NS=DSQRT(N*N-1.)
      DPHI=2.*NS/ DLOG(  (N+NS)/(N-NS) )
      PHI=2.*55.3E-3*(DFLOAT(Q)+.00001)/(D1*DPHI)*SIGN
      CALL LAFR(N,K,PHI,I)
      IPHI=DPHI*PHI*DEXP(-PHI)/(1.-DEXP(-PHI)+K*PHI)
      PHIMOB=2.*55.3e-3*(DFLOAT(Q)+.00001)/DMOB*SIGN
      KMOB=8./3.*LION(IS)/DMOB
      IMOB=DMOB/D1*
     $    PHIMOB*DEXP(-PHIMOB)/(1.-DEXP(-PHIMOB)+KMOB*PHIMOB)
      shape=1.
c     shape=i/imob
      WRITE(3,20) N,DMOB/D1,DPHI,I/IPHI,I/IMOB,shape
20     FORMAT(F9.1,2F10.2,3f9.5)
      RETURN
      END

      SUBROUTINE LAFR(L,K,PHI,I)
      IMPLICIT UNDEFINED (A-Z)
      DOUBLE PRECISION I,I0,IS,F,PHI,A,B,AB,INTEG,L,K,MESS
      DOUBLE PRECISION ISL
      IS=PHI*DEXP(-PHI)/(1.-DEXP(-PHI)+K*PHI)
      MESS=(DSQRT(L+1.)+DSQRT(L-1.))/(DSQRT(L+1.)-DSQRT(L-1.))
```

```
 I0=DSQRT(L*L-1.)/DLOG(MESS) * PHI/(DEXP(PHI)-1.)
 A=(1.-DEXP(-PHI)) /PHI * DLOG(MESS)/K
 B=L/DSQRT(L*L-1.)
 AB=A*B
 IF(AB.LT.1.) THEN
  INTEG=2./DSQRT(1.-AB*AB) * DATAN(
$  DSQRT( (1.-AB*AB)*(L-1.)/(L+1.) )/(1.+AB)
$                        )
 ELSE
  INTEG=1./DSQRT(AB*AB-1.) * DLOG(
$  (DSQRT((AB+1.)*(L+1.)) + DSQRT((AB-1.)*(l-1.)) )/
$  (DSQRT((AB+1.)*(L+1.)) - DSQRT((AB-1.)*(l-1.)) )
$                        )
 ENDIF
 F=1.-DACOS(1./L)/A + INTEG/A
 I=I0*F
 ISL=L/DLOG(2.*L) * PHI*DEXP(-PHI)/
$  ( 1.-DEXP(-PHI)+3.14159/2.*PHI*K/DLOG(2.*L)  )
 RETURN
 END
```

APPENDIX E MODIFICATIONS TO DISC CODE

The following routines were used to compute the "sphere", "min" , "mid", and "max" coagulation kernel functions. The usage of the routines is essentially the same as described by Wu (Wu, J.J, Ph.D. thesis, California Institute of Technology, 1986). The new routines require a common block containing the fractal dimension and primary particle diameter. Modifications were confined to the main program "DISC" (file FDISC.for), NLIST.for, PRINTO.for ,ASKFOR.for and the BETA.for routines. The entire code is stored on both the Sun and Vax computers of the Air Pollution Group at Caltech, in the directories Steve\NEWDISC and STEVEN\NEWDISC.

The main module DISC was modified only so as to accommodate the transfer of the new variables associated with the fractal structure (see PHYSPT.INC).The data entry routine ASKFOR was changed so that the fractal dimension and primary particle size can be input, while NLIST was modified to output these parameters.

The size distribution out-put was considerably modified, however, so the full routine PRINTO is given below.

The routines used to calculate the upper, lower and mid. estimates of the coagulation kernel are identical except for several lines, so only the mid. routine is given completely.

```
      SUBROUTINE PRINTO(Q,TIME,VOLU,IFLAG,IPRNT)
C
C**********************************************************************
*
C
C PURPOSE:
C    This routine prints outs the size distribution
C    after each specified time is reached, #/dlogDp. The number con
c   concentration is in #/cc at STP. Distributions are based
c   on the mobility diameters and the volume equivalent diameters.
C
C ON ENTRY:
C  Q(i)                 Array of Sectional Mass Concentrations [kg/cu.m]
c         =Kg/Kg in sections for i=1..MS
c         =Kg/Kg of vapor for i=MS+1
c         =#/Kg  of particles in discrete sizes for i=MS+3..MS+2+NUMDIS
C       TIME          Current Time [sec]
C       VOLU                  Volume of Container [cu.m]
C       IFLAG                 Initialization Flag (1 if first call)
C       IPRNT                 Logical Unit Number of Output Device or File
Cc ****** WARNING ********
c      normally, the number of components is KC=1.  If this routine is
c     run for multi components, RECHECK it !!!!!!!!!!!!
c
C               Also numerous COMMON block variables must be set.
C
C ON RETURN:
C       All variables unchanged.
C INTERNEL VARIABLES
C     QNV= n/dLog(Dp) #/cc for vol. diameter
c       QNM= .....mobility diameter
```

```
c     DMOB= mean mobility diameter for size or section
c     DVOL= mean vol. equivalent diameter for each size or section
C     DLOGDV = dLog(DVOL)
C     DLOGDM = dLog(DMOB)
C  COMMENTS:
C       Set for 80 column wide output.
C       Modified November 28 by S. Rogak,  Now the mobility equivalent
c       diameters for each section boundary are printed out as well.
c       The routine DMOBIL computes this for fractal clusters using the
c       same theory used in the coagulation kernels.
C*************************************************************************
*
C
      include 'index.inc'          ! common for sectional pointers
      INCLUDE 'PARMK.INC'          ! Dimensioning
      INCLUDE 'PCONS.INC'          ! Numerical parameters (RGAS,PI)
      INCLUDE 'SIZES.INC'  ! COMMON for Sectional Sizes
      INCLUDE 'DEPSIT.INC'         ! COMMON for Deposited Mass Array
      INCLUDE 'GAS.INC'            ! COMMON for Gas Properties
      INCLUDE 'FLAGS.INC'          ! COMMON for Simulation Flags
     COMMON /CONDNS/ DELSAT,CONMW,GASMW
     COMMON /STOKES/ DENSTY
     COMMON /WALLS/ DELDEP
     COMMON /NUCL1/ SUE,RSCALE,TB,TS,DIMSOR,WEIGHT
     COMMON /NUCL2/ VL,VM,DIAM1,SAM,CS,VELQ,VPAT,DSMIN
      REAL DUMDIA,DLOGDV,DLOGDM,CUMNUM,OLDCUM
     DIMENSION Q(NEMAX),ddiam(nEmax),QNV(MMAX),QNM(MMAX)
     DIMENSION
QT(MMAX),QTV(MMAX),CUMDEP(8),QTN(MMAX),DMOB(MMAX)
      DIMENSION DVOL(MMAX)
     DATA DT0 / 0. /   ! Initial dimensionless time (assumes no vapor)
C
c
         nqmk=ms*kc
         nqv=nqmk+1
         nqn=nqmk+2
         neq=nqn+numdis
C
         vm=conmw/6.023e23*1.e-3          ! kg/molecule
         q(nqv)=q(nqn+1)*vm          ! kg/kg
     QVAP=Q(NQV)*DENAIR          ! Vapor Mass Concentration KG/Cu.m.
     QREF=WEIGHT*CS              ! Mass Density of Saturated Vapor
     DIN=DS(1)                   ! Boundary between nucleation and condensation
C
     IF (IFLAG.EQ.1) THEN ! IFLAG=1 to Initialize
      CUMTOT=ZERO
      DO I=1,KC
       CUMDEP(I)=ZERO     ! Initialize to no previous deposition
      END DO
     END IF
C
     SUM=0.
     COUNT=0.
     SURFAC=0.
```

```
      DAV=0.
      SMOMENT=0  ! To compute mass-average diam., accumulate
                 ! moments of distrubution in SMOMENT.
c First do DISCRETE SIZES.
C **** ASSUME THAT THE PARTICLES IN THE DISCRETE SIZES ARE
SPHERES ****
          do 5 J=NQN+1,NEQ
        DUMDIA=diam1*(J-nqn)**(1./3.)*1.e-2
          DVOL(J)=DUMDIA
        DMOB(J)=DUMDIA
        DLOGDV=ALOG10((J-NQN+0.5)/(J-NQN-0.5))/3.
       DLOGDM=DLOGDV
      QNV(J)=Q(J)*DENAIR*TEMP/295*101300./PRES/1.E6/DLOGDV
        QNM(J)=QNV(J)
          qt(J)=q(J)*vm*(J-nqn)
          sum=sum+qt(J)
          COUNT=COUNT+QNV(J)*DLOGDV
          surfac=surfac+q(J)*pi*DVOL(J)**2*1.e1  ! cm*cm/GM
          DAV=DAV+QNV(J)*DLOGDV*DVOL(J)
          SMOMENT=SMOMENT+QT(J)*DVOL(J) !increment in mass moment
5         continue
C SECTIONAL SIZE RANGES (may not be spherical)
     DO I=1,MS
       QT(I)=ZERO
c   add up the different components
        DO J=1,KC
         QT(I)=QT(I)+Q(J+KC*(I-1))
       END DO
       SUM=SUM+QT(I)                ! QT(I) units: Kg/KG total
       VHMEAN=ALOG(VS(I+1)/VS(I))/(1./VS(I)-1./VS(I+1))  ! kg mean particle
C  Remember: VS, VHMEAN is particle mass in Kilograms
       DVOL(I)=ALOG(DS(I+1)/DS(I))/(1./DS(I)-1./DS(I+1))
       DLOGDV=ALOG10(DS(I+1)/DS(I))
C DLOGDM is based on the mobility diameters of the section limits
       DUMDIA=DS(I)
       DMOB(I)=DMOBIL(DUMDIA,TGAS,PGAS)
       DUMDIA=DS(I+1)
       DMOB(I+1)=DMOBIL(DUMDIA,TGAS,PGAS)
       DLOGDM=ALOG10(DMOB(I+1)/DMOB(I))
c The mean mobility diameter is the mobility diameter of the mass-mean dia.
       DUMDIA=DVOL(I)
       DMOB(I)=DMOBIL(DUMDIA,TGAS,PGAS)
       FACTAV=6./DENSTY/DVOL(I)                    ! sq.m. / kg aerosol
       QNV(I)=QT(I)/VHMEAN*DENAIR/1.E6/DLOGDV  ! #/CC
    $ *TEMP*101300./295./PRES
       QNM(I)=QNV(I)*DLOGDV/DLOGDM
       COUNT=COUNT+QNV(I)*DLOGDV
       SURFAC=SURFAC+QT(I)*FACTAV*10.              ! cm*cm/GM
      DAV=DAV+QNV(I)*DVOL(I)*DLOGDV
      SMOMENT=SMOMENT+QT(I)*DVOL(I)
    END DO
    AVGDIA=SMOMENT/SUM ! mass averaged dia.
    DAV=DAV/COUNT      !number averaged dia.
```

```
c -------- now get the median diameter and geometric standard deviation  ---
      CUMNUM=0
      OLDCUM=0
      DVOLD=DVOL(NQN+1)
      DMOLD=DVOLD
c First do DISCRETE SIZES.
            do 555 J=NQN+1,NEQ
          CUMNUM=OLDCUM+Q(J)*DENAIR*TEMP/295*101300./PRES/1.E6/COUNT
           IF(CUMNUM.GT.0.159 .AND. OLDCUM.LT. 0.159) THEN
           DLOWV=(.159-OLDCUM)/(CUMNUM-OLDCUM) * (DVOL(J)-
DVOLD)+DVOLD
          DLOWM=(.159-OLDCUM)/(CUMNUM-OLDCUM) * (DMOB(J)-
DMOLD)+DMOLD
          END IF
             IF(CUMNUM.GT.0.5 .AND. OLDCUM.LT. 0.5) THEN
           DMEDV=(.5-OLDCUM)/(CUMNUM-OLDCUM) * (DVOL(J)-DVOLD)+DVOLD
           DMEDM=(.5-OLDCUM)/(CUMNUM-OLDCUM) * (DMOB(J)-
DMOLD)+DMOLD
          END IF
           IF(CUMNUM.GT.0.841 .AND. OLDCUM.LT. 0.841) THEN
          DHIGHV=(.841-OLDCUM)/(CUMNUM-OLDCUM) * (DVOL(J)-
DVOLD)+DVOLD
          DHIGHM=(.841-OLDCUM)/(CUMNUM-OLDCUM) * (DMOB(J)-
DMOLD)+DMOLD
          END IF
          OLDCUM=CUMNUM
          DVOLD=DVOL(J)
          DMOLD=DMOB(J)
555       continue
C SECTIONAL SIZE RANGES (may not be spherical)
     DO I=1,MS
       VHMEAN=ALOG(VS(I+1)/VS(I))/(1./VS(I)-1./VS(I+1))  ! kg mean particle
       CUMNUM=OLDCUM+QT(I)/VHMEAN*DENAIR/1.E6/COUNT
    $ *TEMP*101300./295./PRES
        IF(CUMNUM.GT.0.159 .AND. OLDCUM.LT. 0.159) THEN
        DLOWV=(.159-OLDCUM)/(CUMNUM-OLDCUM) * (DVOL(I)-
DVOLD)+DVOLD
        DLOWM=(.159-OLDCUM)/(CUMNUM-OLDCUM) * (DMOB(I)-
DMOLD)+DMOLD
       END IF
        IF(CUMNUM.GT.0.5 .AND. OLDCUM.LT. 0.5) THEN
        DMEDV=(.5-OLDCUM)/(CUMNUM-OLDCUM) * (DVOL(I)-DVOLD)+DVOLD
        DMEDM=(.5-OLDCUM)/(CUMNUM-OLDCUM) * (DMOB(I)-
DMOLD)+DMOLD
       END IF
       IF(CUMNUM.GT.0.841 .AND. OLDCUM.LT. 0.841) THEN
        DHIGHV=(.841-OLDCUM)/(CUMNUM-OLDCUM) * (DVOL(I)-
DVOLD)+DVOLD
        DHIGHM=(.841-OLDCUM)/(CUMNUM-OLDCUM) * (DMOB(I)-
DMOLD)+DMOLD
       END IF
      OLDCUM=CUMNUM
```

```
        DVOLD=DVOL(I)
        DMOLD=DMOB(I)
      END DO
      SIGMAM=SQRT(DHIGHM/DLOWM)
      SIGMAV=SQRT(DHIGHV/DLOWV)

c Print out the size distrubution
C     discrete:
       WRITE(IPRNT,10) TIME,SUM,(DVOL(I),DMOB(I)
     $  ,QNV(I),QNM(I),I=NQN+1,NEQ)
       TYPE 10,TIME,SUM,(DVOL(I),DMOB(I)
     $ ,QNV(i),QNM(i), i=nqn+1,neq)
C     sections:
      write(iprnt,12) (DVOL(I),DMOB(I),QNV(I),QNM(I),I=1,MS)
      TYPE 12, (DVOL(I),DMOB(I),QNV(I),QNM(I),I=1,MS)

10     FORMAT(///25X,' TIME =',1PG10.4,' SEC'//
     $ 8X,'TOTAL SUSPENDED MASS =',1PE11.4,' KG/KG'//
     $ 8X,'DIAMETER  vol., mob. (um)',6x,'dN/dlogDv #/cc','dN/dlogDm'/
     $ (1x,6pf11.5,6pf11.5,1PE12.3,1PE12.3))
12     format(1X,6Pf11.4,6Pf11.4,1PE13.3,1PE13.3)
c Miscelaneous output variables
      WRITE(IPRNT,13) COUNT,SURFAC
      TYPE 13,COUNT,SURFAC
13     FORMAT(/' TOTAL NUMBER =',1PE11.3,' #/CC',6X,
     $ 'TOTAL SURFACE AREA=',1PE11.3,' Sq.Cm./GM')
      WRITE(IPRNT,14) DENAIR,TEMP,FREEMP,VISCOS
      WRITE(IPRNT,66) DAV*1.E6,AVGDIA*1.E6
      WRITE(IPRNT,67) DMEDV*1.e6,DMEDM*1.e6,SIGMAV,SIGMAM
      TYPE 66, DAV*1.E6,AVGDIA*1.E6
66     format(' # AV. Dia=',f10.4,'uM   MASS AV. Dia=',f10.4,
     $ 'uM')
67     FORMAT(' med. Dvol',f10.4,'uM  med. Dmob',f10.4,
     $ 'uM  SIGg vol',f5.2,'  SIGg mob',f5.2)
      TYPE 14,DENAIR,temp,freemp,viscos
14      FORMAT(' GAS DENS Kg/m^3=',1pe12.3,4x,
     $ '   T=',1pe12.3,' K',/' gas mfp(m)=',1pe12.3,
     $ '   viscos  =',1pe12.3)
      RETURN
      END
```

ABSORBING SPHERE MODEL COAGULATION RATE
(MID. MODEL)

```
      REAL FUNCTION BETA(X,Y,TGAS,PGAS,NBTYPE)
C
C*********************************************************************
*
```

```
C
C PURPOSE:
C     To Calculate the Coagulation Coefficient
c     A simple model for fractal clusters is used. This geometric
c     model is used to calculate 1) the effective absorbing sphere
c     radius, 2) the appropriate area for computation of free molecule
c     drag and 3) the appropriate length scale for computing drag in the
C     continuum regime. This version assumes that the collision
c     diameter and the mobility diameter are the same.
c      -S Rogak May 31 90
C     Revised Aug. 22, 90. The lower limit of K is computed
c     as the lower of two "mobility" models. For the mobility
c     model, the absorbing cluster is assumed to be the sum of
c     the two mobility diameters.
c     The upper limit is computed by calculating the absorbing
c     cluster properties as before, using maximum and minimum
c     estimates for the mobility.
c
c     Revised Nov19,90. Only one mobility-structure model is used,
c     since uncertainty in this relation could be expressed by the
c     uncertainty in the fractal dimension. The relation between the
c     mobility diameter and collision diameter is considered. The
c     lower limit of the collision diameter is the mobility diameter.
c     the upper limit depends on the outer radius Rf.
C  ON ENTRY:
C     Y          Log Mass of first particle [ln(kg)]
C     X          Log Mass of second particle [ln(kg)]
C     TGAS          Gas Temperature [K]
C     PGAS          Gas Pressure, Total [Pa]
C     Dfrct       Fractal dimension of the aerosol population
c     Rprime      Radius of the primary particle
C  ON RETURN:
C     BETA          Coagulation Coefficient
C
C  LOCAL VARIABLES:
C     V,U         Particle Masses (of X and Y) [kg]
C     DX,DY          Particle Diameters (of X and Y) [m]
C     Uprime       Mass of the primary particle
c     UXY          U+V
C       AX              Primary particle diameter if NX is greater
c                       than 1; Rfx otherwise
c       N1,2         number of primary particles in a cluster
c     D1,2         Fractal dimension of the resulting agglomerate
c     Rs1,2        Radius of sphere with the same projected area
c     Rabs         Radius of the absorbing sphere
c     DIFFN          Diffusion coef. of the relative motion
c     CMEAN          Relative thermal speed of the two particles
c     KND          Knudsen number based on particle mean free paths
c     Dahneke       Transtion regime coagulation correction factor
c  SUBSCRIPTS (SUFFIXES)
c                 1 =  the larger of the two clusters,
c                 2 =  the smaller
c  The only difference between BETAMAX,BETAMID and BETAMIN is the
c  the name of the function. i.e. the variable of output.
```

```
C COMMENTS:
C      Note BETA is a symmetric function in X and Y, BEFORE it is
C       sectionalized.  NBTYPE =  4,5 retain this symmetry.
C     REFERENCES:  FUCHS,N.A. 'MECHANICS OF AEROSOLS', 291-294,
C     PERGAMON (1964).  GIESEKE,J.A., LEE,K.W. AND REED,L.D.,
C     'HAARM-3 USERS MANUAL', BMI-NUREG-1991 (1978).  DRAKE,R.L.
C    'A GENERAL MATHEMATICAL SURVEY OF THE COAGULATION
EQUATION,'
C     IN TOPICS IN CURRENT AEROSOL RESEARCH BY HIDY,G.M. AND
C     BROCK, J.R. (EDS.) VOL.3 PERGAMON, N.Y. 1972.
C
C*********************************************************************
*
C

      REAL U,V,X,Y,RPRIME,DFRCT,TGAS,PGAS,VISCOS,FREEMP,RHOX
     REAL KND,DAHNEKE,CMEAN,DIFFN,LAM
      REAL RS1,RS2,RC1,RC2
      REAL RCHAIN,RH1,RH2
      REAL A1,A2,D1,D2,UPRIME,N1,N2
      REAL KT,RF1,RF2,PI,RF,RSA,RSB
     REAL RC,RS,RHYD,RABS

     REAL BETAMAX,BETAMIN

     INCLUDE 'PCONS.INC'
     INCLUDE 'PHYSPT.INC'
     INCLUDE 'GAS.INC'
C Compute the geometric properties of the clusters
     kT=1.3805E-23*TGAS
     IF(X.LT.Y) THEN
      U=EXP(Y)
      V=EXP(X)
     ELSE
      U=EXP(X)
      V=EXP(Y)
     END IF
     RHOX=DENSTY
     UPRIME=RHOX*4.189*RPRIME**3
C
        IF(U.GT.UPRIME) THEN
         N1=U/UPRIME
         D1=DFRCT
         RF1=RPRIME*N1**(1.0/D1)
         A1=RPRIME
         RS1= MAX( A1*N1**0.333333, MIN(
   $         SQRT(1.+.6667*(N1-1))*A1, RF1*SQRT(D1/3.))   )
      RCHAIN=RF1/(LOG(2.*RF1/A1)+.3068528)
         RC1=MAX(RS1,RCHAIN,(0.5*( D1-1))**0.7 *RF1)
         RH1=RHYD(RS1,RC1,FREEMP)
        ELSE
         N1=1
         D1=3.0
         RF1=(U/UPRIME)**.3333*RPRIME
```

```
          A1=RF1
          RS1=RF1
          RC1=RF1
          RH1=RF1
         END IF
C
         IF(V.GT.UPRIME) THEN
          N2=V/UPRIME
          D2=DFRCT
          RF2=RPRIME*N2**(1.0/D2)
          A2=RPRIME
          RS2= MAX( A2*N2**0.333333, MIN(
     $         SQRT(1.+.6667*(N2-1))*A2, RF2*SQRT(D2/3.))   )
        RCHAIN=RF2/(LOG(2.*RF2/A2)+.3068528)
          RC2=MAX(RS2,RCHAIN,(0.5*( D2-1))**0.7 *RF2)
          RH2=RHYD(RS2,RC2,FREEMP)
         ELSE
          N2=1
          D2=3.0
          RF2=(V/UPRIME)**.3333*RPRIME
          A2=RF2
          RS2=RF2
          RC2=RF2
          RH2=RF2
         END IF

C CHECK THAT THE GAS PROPERTIES ARE CONSISTENT
         IF(TGAS.NE.TEMP.OR.PGAS.NE.PRES) THEN
          IF (TGAS.NE.TEMP) TYPE 21, TEMP,TGAS
21        FORMAT(/' WARNING:/GAS/ TEMP= ',F7.1,'WHILE TGAS=',F7.1/)
          IF(PGAS.NE.PRES) TYPE22,PRES,PGAS
22        FORMAT(/' WARNING:/GAS/ PRES=',1PE9.2,'WHILE PGAS=',E9.2/)
          CALL SETGAS(TGAS,PGAS)
         END IF

C Joint diffusivity and the relative mean free paths of the
c pair of clusters:
      DIFFN=KT/(6.*PI*VISCOS)*(
     $ (1.+FREEMP/RH2*(1.257+.4*EXP(-1.1*RH2/FREEMP)))/RH2+
     $ (1.+FREEMP/RH1*(1.257+.4*EXP(-1.1*RH1/FREEMP)))/RH1)
       CMEAN=5.9293E-12*SQRT(TGAS*(1/U+1/V))
      LAM=2*DIFFN/CMEAN
C Now estimate the properties of the "absorbing cluster". This
c will be used to get the upper limit on the coagulation frequency.
c  Outer radius:
      RF=RF1+RF2
c  Area equivalent radius:
      RS=MAX(RS1+RS2,MIN(SQRT((A1+RF2)**2.+.6667*(N1-1.)*A1*(A1+RF2)),
     $  SQRT(.32*D1)*RF))
C the continuum hydrodynamic radius is
      RCHAIN=RF/(LOG(2.*RF/(RF2+A1))+.3068528)
      RC=MAX(RS,RCHAIN,  (0.5*(D1-1))**0.7 *RF)
     RABS=RHYD(RS,RC,LAM)
```

```
C Knudsen number, Dahneke interpolation factor, coagulation frequency:
      KND=LAM/RABS
      DAHNEKE=(1+KND)/(1+2*KND*(1+KND))
      BETAMID=12.566*RABS*DIFFN*DAHNEKE
c Do the same for the lower limit:
      KND=LAM/(RH1+RH2)
      DAHNEKE=(1+KND)/(1+2*KND*(1+KND))
      BETAMIN=12.566*(RH1+RH2)*DIFFN*DAHNEKE
C And the upper limit:
     KND=LAM/(RF1+RF2)
     DAHNEKE=(1+KND)/(1+2.*KND*(1+KND))
     BETAMAX=12.566*(RF1+RF2)*DIFFN*DAHNEKE
C THIS IS BETAMID, SO
    BETA=BETAMID
C  For sectionalization, we need to keep x, y in order, since the kernel
C  is no longer symetric
      U=EXP(X)
      V=EXP(Y)
C INTERNAL CHECK FOR ERROR
       IF(BETA.EQ.ZERO) THEN
       TYPE 90,BETA,U,V,NBTYPE
90     FORMAT('  BETA=',1PE10.3,5X,'U=',E10.3,'V=',E10.3
   $     ,5X,'NBTYPE=',I2)
       STOP ' BETA=0 SHOULD NOT HAVE OCCURRED'
       END IF
C CONVERT TO THE MASS SECTIONALIZED BETA.
       GO TO (2,1,2,3,3,1,5,4),NBTYPE
1      BETA=BETA/V
       RETURN
2      BETA=BETA/U
       RETURN
3      BETA=BETA*(U+V)/U/V
       RETURN
4      BETA=BETA*(U+V)/U
5     return
    END
```

LOWER BOUND ON COAGULATION RATE
(lines differing from Absorbing Sphere model)

```
      REAL BETAMAX,BETAMIN
C     THIS IS BETAMIN, SO
      BETA=BETAMIN
```

UPPER BOUND ON COAGULATION RATE
(lines differing from Absorbing Sphere model)

```
      REAL BETAMAX,BETAMIN
C     THIS IS BETAMAX, SO
      BETA=BETAMAX
```

APPENDIX F

PRIMARY PARTICLE EVOLUTION

with H.V. Nguyen

Sectional or discrete-sectional models have been proposed previously to describe the evolution of aerosol size distributions. In these models, mass balance equations are written for each particle size "section". The same concepts may be used to follow the changes in the number of primary particle system, provided that a simple and physically reasonable model of the primary particle formation and loss is available. Such a model is described below. In the model, the number of primary particles in a size class is followed in addition to the mass in the class. Some collision events contribute to the number of primary particles in the section, while other types of events affect only the mass in the section. For example, condensation on an aerosol increases the mass of the particles without changing the number of particles. The key assumptions of the model are :

1. The variation in the primary particle size is small within a section, and thus an average primary particle size can be used for each section.
2. Particles smaller than some critical size x_0 completely coalesce with other particles.
3. Particles equal to or larger than x_0 coagulate with other particles and retain their identity, and thus contribute to the number of primary particles.

Before deriving the basic primary particle balance equations, the foundations of the discrete sectional model are briefly reviewed. The conventions used are similar to those used by J.J. Wu (Doctoral Thesis, California Institute of Technology, Pasadena (1986)).

Discrete Sectional Model

Notation:

r, s	sectional counting index
l	section in consideration
i, j	discrete counting indices
u, v	mass of a particle in a section or a discrete size
x	$\ln v$; $x_1 = \ln v_1$ used for size representation
x_0	size at or below which particles completely coalesce and form one new particle or behave as liquid droplets, and above which particles retain their identity

$$x_0 = \ln\left(\frac{\pi\, a_0^3\, \rho_p}{6}\right);\ x_0 = \ln v_0$$

Q_l total mass concentration of particles in section l

N_l total number concentration of particles in section l

N_{pl} total number concentration of primary particles in section l

$n_l(x) = \frac{e^x}{m_{pl}}$ number of primary particles in a particle of size x

k the cutoff size of the discrete regime; largest cluster size in the discrete regime

Ms total number of sections

m_{pl} average mass of a primary particle in section l

Following the Discrete-sectional representation and derivation, we have, for section l,

$$Q_l = \int_{x_{l-1}}^{x_l} q(x)dx$$

$q(x)$ mass density function $= \frac{dQ}{dx}$

$n(x)e^x$

$n(x)$ number density distribution function

In the sectional model, the mass-density function is assumed to be constant within each section,

$$q(x) = \frac{dQ}{dx} = \frac{q_l}{x_l - x_{l-1}};\ x_{l-1} \leqq x < x_l \tag{1}$$

$$N_l = \int_{x_{l-1}}^{x_l} n(x)dx = \int_{x_{l-1}}^{x_l} \frac{Q_l}{x_l - x_{l-1}} e^{-x}\, dx = Q_l \frac{e^{-x_{l-1}} - e^{-x_l}}{x_l - x_{l-1}}. \tag{2}$$

Derivation of Equations for N_{pl} (of section l) and book-keeping:

$$m_{pl} = \frac{Q_l}{N_{pl}};\ 1 \leqq l \leqq M_s\ . \tag{3}$$

1) Discrete Sizes

For the discrete sizes, the particles are single spheres, and thus

$$N_i = N_{pi}$$

$e^{x_i} = m_{pi}$.

2) Sections, particles smaller than x_0, ($1 \leqq l < rx_0$)

As was the case for discrete sizes, these small particles are expected to coalesce rapidly and completely, so

$$N_{pl} = N_l$$

$$N_l \bar{v}_l = Q_l ;$$

from (2) we have

$$\bar{v}_l = e^{\bar{x}_l} = \frac{x_l - x_{l-1}}{e^{-x_{l-1}} - e^{-x_l}} \tag{4}$$

$$\bar{x}_l = \ln(x_l - x_{l-1}) - \ln\left\{ e^{-x_{l-1}} - e^{-x_l} \right\}$$

$N_{pl}\, m_{pl} = Q_{pl}$; from (3)

therefore,

$$m_{pl} = \bar{v}_l .$$

We see that for the discrete sizes and sections $1 \leqq l < rx_0$, we do not need to keep track of N_{pi} and N_{pl} separately. The DISC code has already done that for us.

3) Particles in the section $l = rx_0$ where $x_{rx_0-1} \leqq x_0 < x_{rx_0}$

If initially we have zero particles in this section, then as soon as any mass enters the section, it is assumed to distribute evenly throughout the section (this is inevitable in the sectional model).

$$q_l(x) = \frac{Q_l}{x_l - x_{l-1}} \quad ; \quad l = rx_0 .$$

All of the particles entering this section must have come from lower sections; they are liquid spheres. Accordingly, we have

$$N_l = Q_l \frac{e^{-x_{rx_0-1}} - e^{-x_{rx_0}}}{x_{rx_0} - x_{rx_0-1}} \quad ; \quad l = rx_0 ,$$

where N_l is the number of solid spheres with an average particle size given by (4). Therefore, for the initial "inception" of particles in section $l = rx_0$,

$$N_{pl} = N_l$$

$$m_{pl} = \bar{v}_l \ .$$

We next consider the evolution of N_{pl} ($l = rx_0$) , with and without the use of the "geometric constraint" in the model.

With Geometric Constraint:

If we make full use of the geometric constraint and have as many sections per decade of diameter as possible, then we can have a maximum of 9 sections per decade of diameter, and if the sections are geometrically equally spaced, then narrowest possible section is

$$\frac{v_l}{v_{l-1}} = 1000^{1/9} = 2.1544 \ .$$

Thus, except for the particles near size x_{l-1}, self-coagulation of particles within the section leads to loss to higher section(s). Coagulation with particles in smaller sections, either with particles greater than or less than x_0 within section $l = rx_0$ does not change the number of primary particles within the section. The size of the primary particles is, thus, relatively constant throughout the whole section, and an average primary particle size for the whole section can still be used with relatively small error. The error reduces greatly for x_0 near the edge of the section, i.e., $x_0 \sim x_{rx_0-1}$ or $x_0 \sim x_{rx_0}$, and the behavior is similar to that of the upper ($r > rx_0$) and lower ($r < rx_0$) sections, respectively. Also, m_{pl} will be the same as $\bar{v}_l$ for $\frac{v_l}{v_{l-1}} = 2$ and very close to $\bar{v}_l$ for $\frac{v_l}{v_{l-1}} = 2.1544$, $N_l \sim N_{pl}$.

Without Geometric Constraint:

Again, coagulation with particles in sections $r < rx_0$ does not change N_{pl}. But now coagulation with particles or among particles within the section may reduce N_{pl}. N_{pl} is reduced because of the coagulation of particles smaller than x_0 even if the resulting particles

remain within section rx_0. Coagulation of particles smaller than x_0 with those of x_0 or larger also reduces N_{pl}, since a particle of size smaller than x_0 does not retain its identity. It is for coagulation of larger-sized particles that the present model and the original DISC model differ substantially.

4. Contribution to N_{pl} that is due to the Coagulation of Particles in the Discrete Regime:

$$\frac{dN_{pl}}{dt} = \frac{1}{2}\sum_{i=1}^{k}\sum_{j=1}^{k} \theta(k_{l-1} \leqq i + j < k_l)\beta_{ij}N_iN_j))$$

$$1 \leqq i, j \leqq k\ ;\ rx_0 \leqq l \leqq M_s$$

5. Contribution to N_{pl} that is due to the Coagulation of Particles in Lower Sections:

$$(\ 1 \leqq r, s \leqq l\text{-}1\ ;\ rx_0 \leqq l \leqq M_s)$$

$$\frac{dN_{pl}}{dt} = \frac{1}{2}\sum_{r=1}^{l-1}\sum_{s=1}^{l-1}\int_{u_{r-1}}^{u_r}\int_{v_{s-1}}^{v_s}\theta(u_{l-1} \leqq u + v < u_l)\alpha_{uv}\beta(u,v)n(u)n(v)dudv$$

$$= \frac{1}{2}\sum_{r=1}^{l-1}\sum_{s=1}^{l-1}\int_{x_{r-1}}^{x_r}\int_{x_{s-1}}^{x_s}\theta(u_{l-1} \leqq u + v < u_l)\alpha_{uv}\beta(u,v)\frac{Q_r \quad Q_s\,dxdy}{(x_r - x_{r-1})u(x_s - x_{s-1})v}$$

note: $u = u(x) = u(x_r)$

$$v = v(y) = v(y_s)$$

$$\frac{dN_{pl}}{dt} = \frac{1}{2}\sum_{r=1}^{l-1}\sum_{s=1}^{l-1}\int_{x_{r-1}}^{x_r}\int_{x_{s-1}}^{x_s}\frac{\theta(u_{l-1} \leqq u + v < u_l)\alpha_{uv}\beta(u,v)dxdy}{uv(x_r - x_{r-1})(x_s - x_{s-1})}Q_rQ_s)\ ,$$

where α_{uv} is defined as

$\alpha_{uv} = 1$ for $u < e^{x_0}$; $v < e^{x_0}$

$\alpha_{uv} = n_r(x) = \dfrac{u(x)}{m_{pr}}$ for $u > e^{x_0}$; $v < e^{x_0}$

$\alpha_{uv} = n_s(x) = \dfrac{v(x)}{m_{ps}}$ for $u < e^{x_0}$; $v > e^{x_0}$

$\alpha_{uv} = n_r(x) + n_s(x)$ for $u > e^{x_0}$; $v > e^{x_0}$

$$\frac{u(x)}{m_{pr}} = \frac{u(x)N_{pr}}{Q_r} = \frac{e^x N_{pr}}{Q_r}$$

$$\frac{v(y)}{m_{ps}} = \frac{v(y)N_{ps}}{Q_s} = \frac{e^y N_{ps}}{Q_s}$$

6. **Contribution to N_{pl} that is due to the coagulation of particles in lower sections with those in the Discrete Regime:**

$$\frac{dN_{pl}}{dt} = \sum_{i=1}^{k} \sum_{s=1}^{l-1} \int_{v_{s-1}}^{v_s} \alpha_{ui}\beta(u_{ci},v)\theta(v_{l-1} \leqq u_{ci} + v < u_l)N_i n(v)dv$$

$$\frac{dN_{pl}}{dt} = \sum_{i=1}^{k} \sum_{s=1}^{l-1} \int_{x_{s-1}}^{x_s} \theta(v_{l-1} \leqq u_{ci} + v < u_l)\alpha_{ui}\beta(u_{ci},v)N_i \frac{Q_s dy}{(x_s - x_{s-1})v}$$

$$\frac{dN_{pl}}{dt} = \sum_{i=1}^{k} N_i \sum_{s=1}^{l-1} Q_s \int_{x_{s-1}}^{x_s} \frac{\theta(v_{l-1} \leqq u_{ci} + v < u_l)\alpha_{ui}\beta(u_{ci},v)dy}{v(x_s - x_{s-1})},$$

where

$\alpha_{ui} = 1$ for $v < e^{x_0}$

$\alpha_{ui} = n_s(\,)$ for $v > e^{x_0}$

$1 \leqq i \leqq k$; $1 \leqq s \leqq l - 1$; $rx_0 \leqq l \leqq M_s$

7. **Contribution to N_{pl} that is due to the Coagulation of Particles within section l**

$(rx_0 \leqq l \leqq M_s)$

$$\frac{dN_{pl}}{dt} = -\frac{1}{2} \int_{u_{l-1}}^{u_l} \int_{v_{l-1}}^{v_l} \beta(u,v)\alpha_{ll} n(u)n(v)dudv$$

$$\frac{dN_{pl}}{dt} = -\frac{1}{2}\int_{x_{l-1}}^{x_l}\int_{x_{l-1}}^{x_l} \frac{\beta(u,v)\,\alpha_{ll}\,Q_l^2\,du dv}{(x_l-x_{l-1})^2 uv},$$

where

$\alpha_{ll} = \theta(u_{l-1} \leqq u+v < u_l)$ $\quad l=rx_0$ $\quad u<e^{x_0}$ or $v<e^{x_0}$

$\alpha_{ll} = 2\theta(u+v \leqq u_l)$ $\quad l=rx_0$ $\quad u<e^{x_0}$ or $v<e^{x_0}$

$\alpha_{ll} = (1+n_l(x))\theta(u_l \leqq u+v_l)$ $\quad l=rx_0$ $\quad u<e^{x_0}$ or $v>e^{x_0}$

$\alpha_{ll} = (n_l(y)+n_l(x))\theta(u_l \leqq u+v_l)$ $\quad l=rx_0$ $\quad u>e^{x_0}$ and $v>e^{x_0}$

8. **Contribution to N_{pl} that is due to the Coagulation of Particles of section l with particles of discrete regime i:**

$$\frac{dN_{pl}}{dt} = -\sum_{i=1}^{k}\int_{u_{l-1}}^{u_l} \beta(u,v)\,\alpha_{li}\,n(u)\,N_i\,du$$

$$\frac{dN_{pl}}{dt} = -Q_l\sum_{i=1}^{k} N_i \int_{u_{l-1}}^{u_l} \frac{\alpha_{li}\,\beta(u,v)}{(x_l - x_{l-1})\,v}\,du,$$

where

9. **Contribution to N_{pl} that is due to the Coagulation of Particles of section l with particles of in lower sections:**

$$\frac{dN_{pl}}{dt} = -Q_l\sum_{r=1}^{l-1} Q_r \int_{x_{r-1}}^{x_r}\int_{x_{l-1}}^{x_l} \frac{\alpha_{rl}\,\beta(u,v)}{(x_r - x_{r-1})\,u(x_l - x_{l-1})\,v}\,dx\,dy$$

$$\alpha_{rl} = \theta(u_l > u+v)\alpha_{rl1} \; - \; \theta(u_l > u+v)\alpha_{rl2}$$

$$\alpha_{rl1} = 1 \qquad u<e^{x_0}$$

$$\alpha_{rl1} = n_r(x) \qquad u>e^{x_0}$$

$$\alpha_{rl2} = 1 \qquad v<e^{x_0}$$

$$\alpha_{rl1} = n_1(y) \qquad v>e^{x_0}$$

10. Contribution to N_{pl} that is due to the Coagulation of Particles of section l with particles of in higher sections:

$$\frac{dN_{pl}}{dt} = - Q_l \sum_{r=l+1}^{M_S} Q_r \int_{x_{r-1}}^{x_r} \int_{x_{l-1}}^{x_l} \frac{\alpha_{rl}\,\beta(u,v)}{(x_r - x_{r-1})\,u(x_l - x_{l-1})\,v}\,dx\,dy\,,$$

where

$$\alpha_{rl3} = 1 \qquad v<e^{x_0}$$

$$\alpha_{rl3} = n_r(x) \qquad v>e^{x_0}$$

These equations were used in the FORTRAN code DISGLOM, based on the discrete sectional code of J.J. Wu's 1986 Caltech PhD thesis. Wu's code was extensively overhauled, including conversion of the equations to a non-dimensional form. Standard FORTRAN was used throughout so that the code should run on the Sun computer, although it was originally run on the Vax.

Particle size distributions from DISGLOM agreed very well with those from DISC. However, the primary particle balance did not evolve stably. At each printout time step (much longer than the integration time step), the coagulation coefficients were recomputed

on the basis of new estimates of the primary particle size. Smaller primary particles resulted in increased surface area, which in turn aided the deposition of fine particles on the larger agglomerates. This condensationlike growth resulted in much larger primary particle sizes by the next printout time. As a result, the average primary particle sizes oscillated with increasing amplitude.